EAST EUROPEAN JOURNAL OF PHYSICS. 2. 179-186 (2026)
DOI:10.26565/2312-4334-2026-2-18 ISSN 2312-4334

INVESTIGATION OF THE MICROSTRUCTURE OF PHOTOSENSITIVE *CdSe* AND *CdSe:Cd,Cl* THIN FILMS

Bakhodir K. Tuychibaev[1], **Nosirjon Kh. Yuldashev**[1], **Khusanboy M. Sulaymonov**[1], **Gulkan A. Hasanova**[2], **Maralbek Ch. Oskonbaev**[2], **Islamidin Tashpolotov**[2], **Iftikhorjon I. Yulchiev**[1]*
[1]*Fergana State Technical University, Fergana, Uzbekistan*
[2]*Osh State University, Osh, Kyrgyzstan*
**Corresponding Author e-mail: iftixorjon.yulchiyev@gmail.com*
Received December 12, 2026; revised February 26, 2026; in final form April 23, 2026; accepted April 28,2026

The substructure of freshly prepared photosensitive $CdSe$ and doped $CdSe{:}\,Cd,Cl$ thin films were investigated with respect to the influence of substrate temperature T_s and heat-treatment time in air in the presence of $CdCl_2$ vapor. The results of electron diffraction and electron microscopy studies for films prepared under different technological conditions are also presented. It was established that the texture axis of the as-prepared $CdSe$ films is perpendicular to the substrate plane. As T_s increases from 250 to 400°C, the texture-axis dispersion angle, the fraction of the hexagonal phase, the crystallite size, and the coherent X-ray scattering region size D_{csr} increase. After annealing in air in the presence of $CdCl_2$ vapor at 300°C, films prepared at T_s =250°C exhibit reorientation of crystallites from the $(111)_c + (0002)_h$ plane, which is parallel to the substrate plane, to the $(10\bar{1}3)$ orientation through the $(311)_c + (11\bar{1}2)_h$ planes. This reorientation is accompanied by an increase in crystallite size and D_{csr}, and by a decrease in the lattice parameter and the minimum dislocation density.
Keywords: *Photosensitive film; CdSe; CdSe:Cd,Cl; Longitudinal photoconductivity; Polycrystal; Texture; Substrate temperature; Heat treatment; Sensitization kinetics; Coherent X-ray scattering size*
PACS: 78.66.Fd, 78.47.jf, 81.05.Dz, 81.05.ug, 81.07.-b, 81.07.Pr

INTRODUCTION

Polycrystalline cadmium selenide ($CdSe$) thin films have attracted sustained research interest due to their wide applications in microelectronics and photonics, including photoconductors, light-emitting devices, visible and gamma-ray detectors, and memory elements [1–5]. The efficiency of $CdSe$-based photovoltaic devices is determined by key electrophysical and photoelectric parameters, such as charge carrier mobility and lifetime, defect types and concentrations, and photosensitivity. The structural, optical, and electrical properties of $CdSe$ thin films have also been widely discussed in the literature for different preparation methods and application fields [6]. Numerous studies have shown that these parameters are highly sensitive to the microstructural state of the films, including grain size, porosity, crystallographic texture, and phase composition, which are significantly dependent on additional thermal treatment. In addition, the structural, optical, and electrical properties of CdSe thin films are influenced by film thickness [7]. In particular, process conditions greatly influence the crystal structure of grains and significantly affect charge transport processes. Depending on the fabrication conditions, polycrystalline $CdSe$ thin films can crystallize in cubic (sphalerite) or hexagonal (wurtzite) forms, or exhibit the coexistence of mixed phases [3, 10-12]. The presence and evolution of these structural modifications play a decisive role in the formation of the crystallographic texture and substructure, thereby determining the microstructural development and functional characteristics of $CdSe$-based films.

Despite extensive investigations of the electrical and optical properties of $CdSe$ thin films, quantitative studies of their substructure parameters performed using a combined set of complementary structural techniques remain relatively limited. In particular, a systematic correlation between substrate temperature, post-deposition thermal treatment conditions, and the evolution of substructure characteristics has not yet been sufficiently clarified. This limitation is mainly associated with the complexity of linking volume-sensitive X-ray diffraction data with surface-sensitive electron-microscopic observations, especially in textured and polyphase films.

In this context, the aim of the present work is to comprehensively investigate the substructure of photosensitive $CdSe$ and $CdSe{:}\,Cd,Cl$ thin films as a function of substrate temperature and annealing time in air in the presence of $CdCl_2$ vapor. The study is based on a combined application of X-ray diffraction, electron diffraction, and electron microscopy, enabling a correlated analysis of crystallographic texture, phase composition, coherent scattering region size, lattice parameters, and defect-related characteristics.

The novelty of this work lies in revealing the systematic correlation of substructure parameters with key physico-technological factors over a wide range of deposition and annealing conditions. Special attention is paid to the evolution of crystallographic texture, phase transformations between cubic and hexagonal modifications, and the mechanisms of crystallite reorientation during thermal treatment. The obtained results provide deeper insight into the structural perfection

Cite as: B.K. Tuychibaev, N.Kh. Yuldashev, Kh.M. Sulaymonov, G.A. Hasanova, M.Ch. Oskonbaev, I. Tashpolotov, I.I. Yulchiev, East Eur. J. Phys. 2, 179 (2026), https://doi.org/10.26565/2312-4334-2026-2-18
© B.K. Tuychibaev, N.Kh. Yuldashev, Kh.M. Sulaymonov, G.A. Hasanova, M.Ch. Oskonbaev, I. Tashpolotov, I.I. Yulchiev, 2026; CC BY 4.0 license

of $CdSe$-based thin films and establish a reliable structural basis for optimizing their photoelectric and electrophysical properties.

TECHNOLOGY AND MEASUREMENT METHODS

Thin $CdSe$ and $CdSe{:}Cd,Cl$ films with an area of 5×15 mm² were produced by vacuum thermal evaporation on standard glass substrates with a predeposited transparent SnO_2 conductive layer. Deposition was performed at a residual gas pressure of approximately 10^{-3} Pa. To study the effect of substrate temperature on the structural properties of the films, the substrate temperature (T_s) during deposition was varied from 250°C to 400°C. The films were deposited for a time sufficient to achieve the desired thickness. The deposition time and substrate temperature were carefully controlled to achieve the desired crystal structure and phase composition.

Once the films were deposited, they underwent a post-deposition thermal treatment process in air, where $CdCl_2$ vapor was introduced. The annealing temperature was set to 300°C, and the annealing time was varied to evaluate the effects of thermal treatment on the microstructure and the phase composition of the films. The $CdCl_2$ vapor was used to promote the formation of the desired crystalline phases and improve the structural quality of the films. This treatment plays a crucial role in the enhancement of film crystallinity and the reduction of defects.

For structural characterization, X-ray diffraction (XRD) was utilized to analyze the crystallographic texture and phase composition of the films. The XRD measurements were conducted at room temperature, with diffraction angles (2θ) ranging from 20° to 80°. The XRD technique enabled the identification of the crystalline phases present in the films, as well as the determination of the crystalline quality. Electron diffraction (ED) was also used to further investigate the crystallographic texture and coherence of the films.

To examine the surface morphology and grain structure of the films, scanning electron microscopy (SEM) was employed. SEM images were taken to assess the surface features and to measure the average grain size. The grain orientation and distribution were analyzed based on SEM micrographs. The grain size was calculated using the Scherrer equation, which is based on the full width at half maximum (FWHM) of the XRD peaks. This allowed for the estimation of the average crystallite size in the films.

Additionally, the texture coefficients were calculated to evaluate the preferred orientation of the grains in the films. The texture coefficients provide insights into the crystallographic alignment and orientation of the grains relative to the substrate. The SEM and XRD data were used in combination to obtain a comprehensive understanding of the films' microstructural properties.

RESULTS OF THE EXPERIMENT AND THEIR DISCUSSIONS

X-ray studies carried out in the present work showed that the films obtained by vacuum evaporation of $CdSe$ at a pressure of about 10^{-3} Pa, under perpendicular incidence of the vapor flux onto the glass substrate surface, with a condensation rate of 2500 Å/min and a thickness of 5–10 µm, are textured and polyphase within the substrate temperature range T_s=250-400°C . They consist of both cubic and hexagonal modifications. In this case, the crystallites are arranged predominantly so that the crystallographic planes $(111)_c$ and $(0002)_\mathrm{h}$ are oriented parallel to the substrate surface (see Figure 1, the first strong line from the center of the X-ray pattern). From the presented X-ray photographs, it follows that with increasing T_s , the dispersion angle of the texture axis also increases (Table 1). A significant preferential orientation of crystallites with the plane $(10\overline{1}3)_h$ parallel to the substrate surface is also observed.

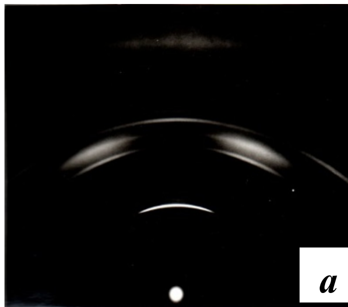

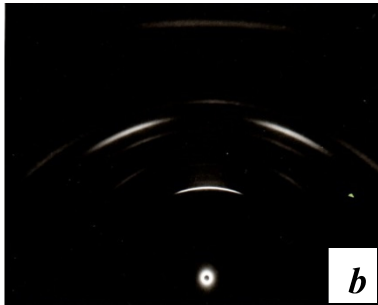

Figure 1. Photographic X-ray diffraction images of $CdSe$ films under filtered FeK_α radiation, condensed at substrate temperatures T_s: (*a*) – 250°C; (*b*) – 300°C; (*c*) – 400°C.

Table 1. Dependence of the texture axis dispersion angle (φ) for the $(111)_c + (0002)_h$ line of $CdSe$ films condensed at various substrate temperatures T_s

T_s, °C	250	300	350	400
φ, °	38	44	57	65

It should be noted that with increasing substrate temperature, both the width and the position of the X-ray lines change. Quantitative phase analysis from the film diffractograms is complicated due to the overlap of X-ray reflections

from the cubic and hexagonal modifications of cadmium selenide and the presence of texture. Therefore, phase analysis was performed on powder samples. For this purpose, a freshly prepared film was separated from the substrate, ground in an agate mortar, and the resulting powder was mixed with BM-1 diffusion pump oil, which does not produce X-ray diffraction lines. The prepared mixture was then applied to a glass substrate. By analyzing the integrated intensity of diffractometric reflections from the $(0002)_h + (111)_c$ planes, which have the same diffraction angle, the relative fraction of the hexagonal modification (H) in the phase composition was determined according to the following relation given in references [8,9]:

$$\frac{I\left(10\bar{1}1\right)}{I\left\{(111)+(0002)\right\}}=\frac{\alpha H}{\beta+(1-\beta)H}, \tag{1}$$

where $I\left(10\bar{1}1\right)_h$ and $I\{(111)_c + (0002)_h\}$ are the integrated intensities of the reflections from the corresponding planes, and α and β are coefficients equal to 1.3 and 4.0, respectively. It was established that the fraction of the hexagonal modification within the above substrate temperature range is between 35 and 44%.

Figure 2 shows the X-ray strip diagrams of the diffractograms of films condensed at T_s=350 and 400 °C. It is evident that the strongest line is $(111)_c + (0002)_h$. The other lines are much weaker or are not observed at all. Therefore, the analysis of the films' substructure parameters was carried out using the $(111)_c + (0002)_h$ line by the fourth-moment method, which requires only a single interference line.

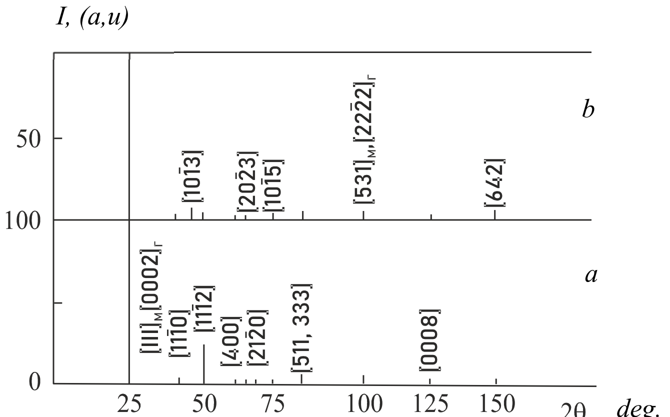

Figure 2. Line diagrams of X-ray diffraction patterns of freshly prepared $CdSe$ films obtained at substrate temperatures T_s: (*a*) – 350 °C; (*b*) – 400 °C.

Figure 3. Photographic X-ray diffraction image of the reference sample obtained under filtered FeK_α radiation.

When determining the substructure parameters, it is necessary to exclude the contribution from instrumental factors in the profiles of the lines used. This contribution can be eliminated either theoretically or experimentally by using a standard sample. In this work, the second method was employed. The standard sample consisted of $CdSe$ films prepared by thermal evaporation of the source material in a vacuum of 10^{-3} Pa onto glass substrates at 400 °C, followed by thermal treatment in a cadmium chloride gas environment at 470 °C for 20 minutes, and then cooled at a rate of 3 °C/min. Films prepared in this manner met the requirements of a standard both in terms of substructure parameters and the degree of texturing (Figure 3).

Based on the experimental data, it was established that, with increasing substrate temperature, the size of the coherent scattering region of X-rays increases [8]:

$$D_{csr} = \frac{\lambda(\theta_m^3 - 9\theta_m \mu f_2)}{3\pi^2 \cos\theta[\mu f_4 - 3(\mu f_2)^2]} \tag{2}$$

where λ is the wavelength of the X-ray radiation, θ_m -is the abscissa of the maximum of a line profile in the X-ray 2θ-diagram, and μf_2 and μf_4 are the second- and fourth-order central moments of the physical broadening function of the X-ray line. It was found that D_{csr} increases from 850 to 970 Å.

The microstrains of the crystal lattice were determined from the relation

$$\left(\overline{\varepsilon^2}\right)^{\frac{1}{2}} = \left[\overline{\left(\frac{\triangle d}{d}\right)^2}\right]^{\frac{1}{2}}, \tag{3}$$

where d is the interplanar spacing. It was found that the microstrain changes from $2.5{\cdot}10^{-3}$ to $6.84{\cdot}10^{-3}$.

From the position of the most intense line on the diffractograms, the lattice parameters were determined. It was shown that, with an increase in the substrate temperature T_s from 250 to 400°C, the lattice parameters decrease from 0.6083 to 0.6082 nm.

Electron microscopic studies of the surface morphology of $CdSe$ films showed that their visible structure depends on the substrate temperature T_s. Figure 4 presents electron micrographs (SEM) of the film surfaces obtained in the substrate temperature range of 250–400°C. The images show that crystallites with well-defined facets emerge on the film surface, and their size increases with increasing T_s. In electronograms obtained for the films' surface layer, the line spectra are richer than those on the X-ray diffractograms. These spectra are interpreted in terms of cubic and hexagonal modifications.

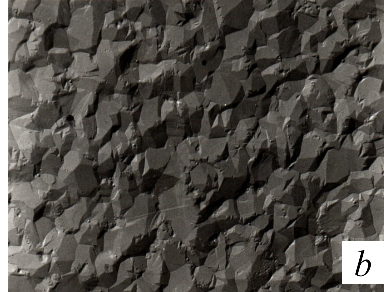

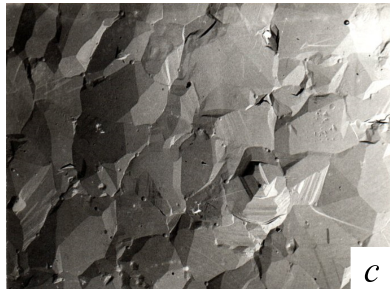

Figure 4. Electron micrographs of the surface of freshly prepared $CdSe$ films, condensed at substrate temperatures T_s,°C: (*a*) – 250, (*b*) – 300, (*c*) – 400 (×10000)

To obtain quantitative data on the crystallite parameters observed on the film surfaces, measurements of their linear dimensions (d') were carried out based on the electron micrographs of films prepared at different substrate temperatures T_s (here, the linear dimension of a crystallite is defined as the diameter d of a circle whose area equals the average area of a crystallite on the film surface). For this purpose, a section of the electron micrograph was randomly selected to include a sufficient number of crystallites for a statistical size distribution. The value of d' was determined by dividing the total area occupied by the crystallites by the number of crystallites. It was found that with an increase in T_s from 250 to 400°C, the average d' increases from 500 to 1500 nm.

Fractographic studies of the film cross-sections (Figure 5) revealed that the upper, predominant part of the film has a columnar structure. This structure is disrupted near the substrate, with a thinner, finer-crystalline layer measuring 0.5-1 μm in thickness.

Figure 5. Fractographic image of the cross-section of a $CdSe$ film prepared at T_s=250°C (×7500).

Freshly prepared polycrystalline cadmium selenide films are generally weakly photosensitive and are usually subjected to thermal treatment in the presence of oxygen or chloride-containing activators in order to improve their electrophysical and photoelectric properties [11,13,14]. Here, we consider the changes in the substructure parameters of $CdSe$ films during TT in air in the presence of $CdCl_2$. One of the important technological factors is the annealing temperature. Based on experimental data, it has been established that the most stable $CdSe{:}Cd{:}Cl$ films with good electrophysical properties are obtained when annealed in a $CdCl_2$ atmosphere at 450–470 °C for 4–8 minutes [15,16].

To determine the effect of annealing on the films' substructure, a series of identical samples was prepared. Each film was subjected to thermal treatment for each time interval only once. The structure was studied after annealing and after the samples had cooled to room temperature.

Thermally treated $CdSe{:}Cd, Cl$ films also exhibited texturing with a well-defined axial texture $(111)_k + (0002)_\mathrm{h}$, the dispersion angle of which increases with increasing substrate temperature (T_s). Figure 6 shows a comparison of photo-radiographs of films prepared at the same T_s=250 °C and with a constant annealing temperature T=470 °C. In this case, the predominant orientation of the plane $(111)_k + (0002)_\mathrm{h}$ parallel to the substrate surface gradually shifts to other

orientations as the annealing time increases. For example, in the (311), $(11\bar{1}2)$ plane after annealing for t_{ann}=2 min, and then in another $(10\bar{1}3)$ plane after t_{ann}=4 min. It should be noted that in the latter case, there are also crystallites oriented randomly; further increasing the annealing time does not lead to significant changes in the predominant orientation. During the annealing of films prepared at higher substrate temperatures, the change in film texture occurs similarly to the case of T_s=250 °C. However, the reorientation of crystallites from one predominant orientation to another occurs over a shorter annealing time as T_s increases.

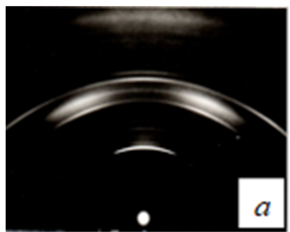

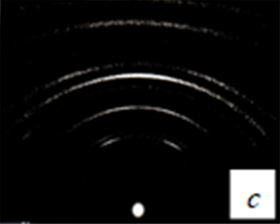

Figure 6. X-ray photographs of $CdSe$ films before and after thermal annealing in air in the presence of $CdCl_2$: (*a*) – as-deposited; (*b*) – t=2 min; (*c*) – t=4 min; (*d*) – t=10 min. Substrate temperature T_s=250°C.

From the photo-radiographs in Figure 6, one can also observe qualitative changes in the relative intensities of the X-ray lines, which were recorded with the X-ray beam incident on a stationary sample at an angle of 20°. It is evident that the most intense diffracted reflection lines occur in the range φ=25–50°. Quantitative changes in the relative intensities of the X-ray lines, obtained from diffraction analysis, are shown in the bar charts for films deposited at a condensation temperature of 350 °C (Figure 7).

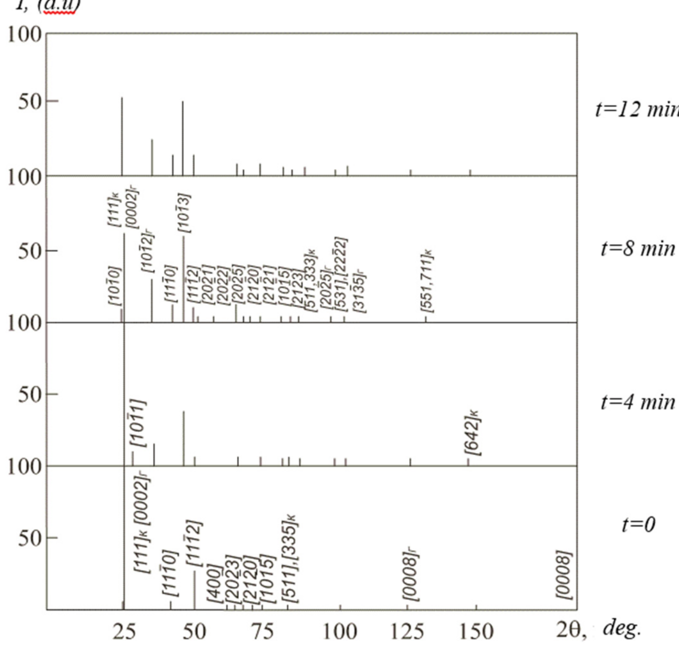

Figure 7. X-ray strip diagrams for $CdSe$ films deposited at a condensation temperature of 350 °C before and after heat treatment in air in the presence of $CdCl_2$.

It was established that the fraction of the hexagonal modification H in the annealed films increases with the duration of the thermal treatment. In films prepared at T_s=350 °C and annealed for 6 min, the value of H reaches 72 %.

The experimental results for the determination of the coherent scattering region sizes D_{csr} as a function of annealing time for $CdSe$: Cd, Cl films prepared at T_s=350 °C and 400 °C are shown in Figure 8*a*,*b*. It can be seen that at the initial stages of thermal treatment, D_{csr} increases, followed by a plateau in the annealing time interval of 4–10 min, during which changes are minimal. Further increasing the annealing time (t_{ann}>10 min) leads to a rather sharp increase in D_{csr}.

The same figures also show the dependence of the minimum dislocation density on the annealing time, determined based on the following formula given in reference [9]:

$$\rho_D = 3n/D_{csr}^2 \, , \tag{4}$$

where n is the number of dislocations per coherent scattering domain D_{csr} (for calculations, n=1 was assumed).

In films obtained at T_s=400°C, the dislocation density ρ_D in the plateau region (t_{ann}=4-10 min) is almost an order of magnitude lower than in films obtained at T_s=350°C, while the corresponding D_{csr} values for these films are approximately 50 nm and 150 nm, respectively.

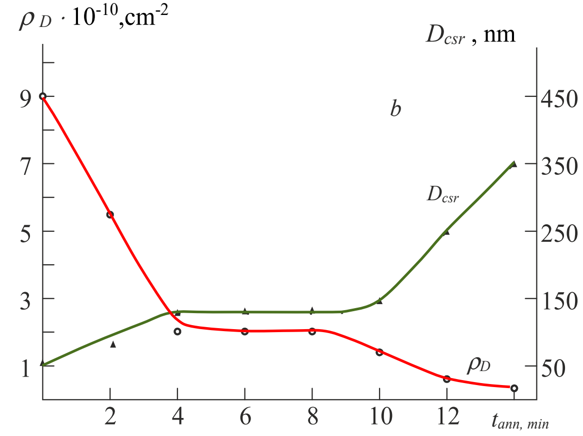

Figure 8. Dependence of D_{csr} and ρ_D on annealing time in air in the presence of $CdCl_2$ for $CdSe$ films deposited at substrate temperatures T_s=350°C (a) and T_s=400°C (b).

One of the significant parameters characterizing the structure is the lattice parameter a. Since the lattice parameter can be determined with higher accuracy from diffraction lines at large reflection angles, it was determined using the (333) line. Figure 9 presents the results of the study of the lattice parameter a for films obtained at T_s=350°C as a function of annealing time. The figure shows that with increasing annealing time up to the optimal value (t_{ann}=6 min), the lattice parameter a decreases and approaches the lattice parameter of cadmium selenide in equilibrium, a=6.035 Å [17]. In the annealing time range of 4–10 min, a changes only slightly, which can be explained by the transformation of the cubic modification into the hexagonal one.

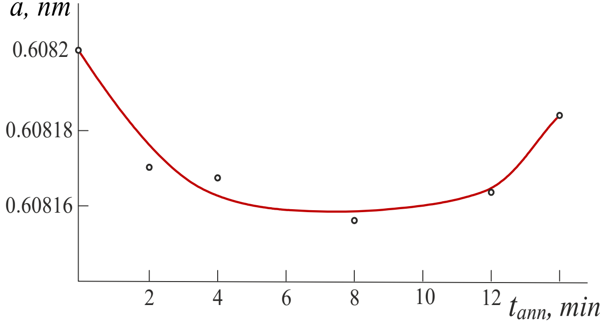

Figure 9. Dependence of the lattice parameter a of the $CdSe{:}\,Cd, Cl$ film on annealing time, determined from the position of the X-ray (333) reflection.

The results of electron-microscopic studies also show that annealing the films leads to changes in the crystallite sizes. From the micrographs of the surfaces of sensitized films obtained at T_s=250°C and 350 °C (Figure 10*a,b*), it is evident that after annealing, the grain sizes increase due to the merging of adjacent grains, the boundaries straighten, and the junction angles approach equilibrium values. The average grain size for films obtained at T_s=250°C is approximately 1900 nm, while for films obtained at T_s=350°C , it is about 2100 nm. Individual grains for these films reach sizes of roughly 3-4 µm.

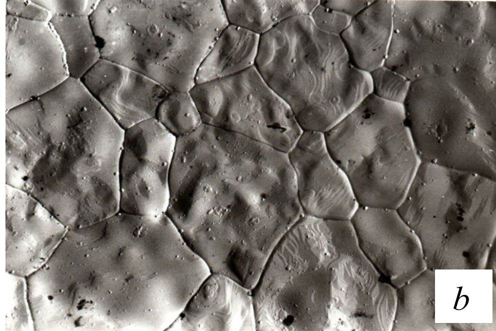

Figure 10. Electron micrographs of optimally sensitized $CdSe{:}\,CdCl_2$ films:
(a) films obtained at T_s=250°C; (b) films obtained at T_s=350°C

The study of the cross-sectional structure of the films showed that the columnar structure, in some cases, extends through the entire thickness of the film (Figure 11*a, b*). However, it should be noted that although the cross-sectional

structure appears monolithic in the fracture micrographs, in reality the average size of the coherent scattering regions is much smaller, as determined from the study, D_{csr}=50-350 nm (see, for example, Figure 8*b*). In the cross-sectional fracture images, the SnO_2 layer between the glass substrate and the $CdSe$-based film is indicated schematically.

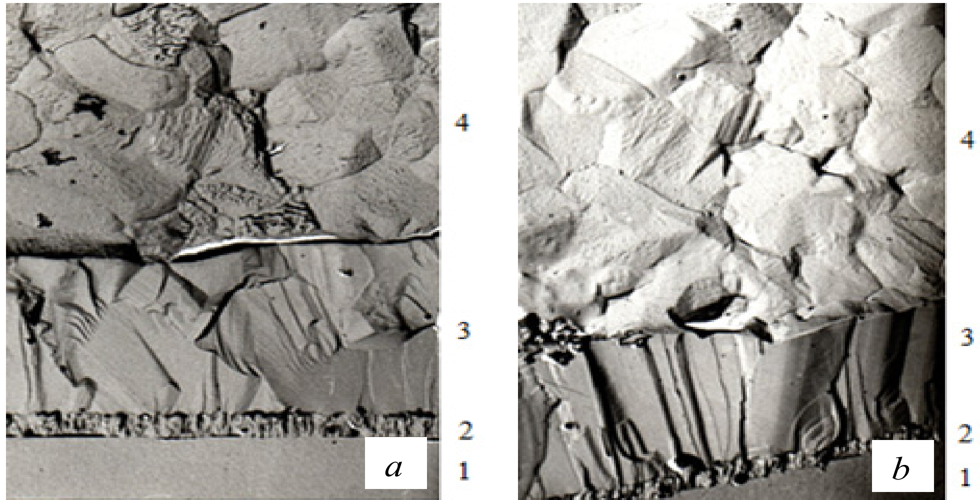

Figure 11. Fractographs of the cross-sectional fracture of optimally sensitized $CdSe: Cd, Cl$ films: (a) films deposited at T_s=250°C; (b) films deposited at T_s=350°C. 1 – substrate; 2 – SnO_2 layer; 3 – cross-sectional fracture; 4 – surface.

CONCLUSIONS

Freshly prepared $CdSe$ films are textured, with the texture axis coinciding with the crystallographic direction $(111)_c + (0002)_h$ and perpendicular to the substrate plane. As the substrate temperature T_s increases from 250 to 400°C, the texture axis dispersion angle, the fraction of the hexagonal modification, the crystallite size, and the coherent scattering regions of X-rays increase, while the lattice parameters and microstrains of the crystal lattice decrease.

Thermal treatment of freshly prepared $CdSe$ films with a substrate temperature T_s=250°C in air in the presence of $CdCl_2$ vapor (T_{ann}=470°C) for t_{ann}=4 min leads to an increase in the coherent scattering region D_{csr} and, correspondingly, the size of the crystalline grains, as well as an increase in the fraction of the hexagonal modification. The texture axis dispersion angle increases significantly, and the predominant orientation becomes the plane $(10\bar{1}3)$. Such reorientation of crystallites necessarily occurs via $(311)_c + (11\bar{1}2)_h$ planes parallel to the substrate; however, with further increase in the annealing time, the original orientation $(111)_c + (0002)_h$ becomes predominant again. During the initial stage of annealing up to t_{ann}=6 min, the lattice parameter decreases, while at t_{ann}>10 min it increases. At the same time, the crystallite sizes and the coherent scattering region D_{csr} increase, while the lattice parameter a and the minimum dislocation density ρ_D decrease.

ORCID

Bakhodir K. Tuychibaev, https://orcid.org/0000-0001-8564-6246; **Nosirjon Kh. Yuldashev,** https://orcid.org/0000-0003-0226-3528; **Khusanboy M. Sulaymonov,** https://orcid.org/0000-0003-0790-1584; **Gulkan A. Hasanova,** https://orcid.org/0009-0007-3703-9522; **Maralbek Ch. Oskonbaev,** https://orcid.org/0009-0005-5753-4753; **Islamidin Tashpolotov,** https://orcid.org/0000-0001-9293-7885; **Iftikhorjon I. Yulchiyev,** https://orcid.org/0000-0001-9346-0441

REFERENCES

[1] D. Kalita, and P.K. Mochahari, "Investigation on thickness dependent structural, optical and electrical properties of cadmium selenide thin films deposited via thermal process," Journal of Environmental Nanotechnology, **14**(3), 364–370 (2025). https://doi.org/10.13074/jent.2025.09.2531675

[2] S. Hussain, M. Iqbal, A.A. Khan, M.N. Khan, G. Mehboob, S. Ajmal, J.M. Ashfaq, *et al*., "Fabrication of Nanostructured Cadmium Selenide Thin Films for Optoelectronics Applications," Front. Chem. **9**, 661723 (2021). https://doi.org/10.3389/fchem.2021.661723

[3] L.N. Ibrahimova, N.M. Abdullayev, M.E. Aliyev, G. A. Garashova, and Y.I. Aliyev, "Phase formation process in CdSe thin films," East European Journal of Physics, (1), 493–496 (2024). https://doi.org/10.26565/2312-4334-2024-1-54

[4] A. Purohit, S. Chander, S.P. Nehra, C. Lal, and M.S. Dhaka, "Effect of thickness on structural, optical, electrical and morphological properties of nanocrystalline CdSe thin films for optoelectronic applications," Optical Materials, **47**, 345–353 (2015). https://doi.org/10.1016/j.optmat.2015.05.053

[5] M. Ayibzhanov, U.R. Salomov, B.K. Tuychibaev, N.K. Yuldashev, and M.D. Tolibjanovna, "Spectral distribution, optical and thermal quenching of longitudinal photoconductivity in CdSe/SnO$_2$ films," Journal of Applied Mathematics and Physics, **13**, 2452–2464 (2025). https://doi.org/10.4236/jamp.2025.137140

[6] S. Mahato, and A.K. Kar, "Structural, optical and electrical properties of electrodeposited cadmium selenide thin films for applications in photodetector and photoelectrochemical cell," Journal of Electroanalytical Chemistry, **742**, 23-29 (2015). https://doi.org/10.1016/j.jelechem.2015.01.034

[7] R. Choudhary, and R.P. Chauhan, “Thickness dependent variation in structural, optical and electrical properties of CdSe thin films,” Journal of Materials Science: Materials in Electronics, **30**(6), 5753–5759 (2019). https://doi.org/10.1007/s10854-019-00870-8
[8] G.S. Girolami, *X-ray Crystallography*, (MIT Press, 2015). https://doi.org/10.1107/S2053273315020331
[9] J.P. Glusker, and K.N. Trueblood, *Crystal structure analysis: A primer*, 3rd ed. (Oxford University Press, 2010). https://doi.org/10.1093/oso/9780199576340.001.0001
[10] Z.G. Ju, Y.M. Lu, J.Y. Zhang, X.J. Wu, K.W. Liu, D.X. Zhao, Z.Z. Zhang, *et al.*, “Structural phase control of CdSe thin films by metalorganic chemical vapor deposition,” Journal of Crystal Growth, **307**(1), 26–29 (2007). https://doi.org/10.1016/j.jcrysgro.2007.06.006
[11] R.B. Kale, and C.D. Lokhande, “Band gap shift, structural characterization and phase transformation of CdSe thin films from nanocrystalline cubic to nanorod hexagonal on air annealing,” Semiconductor Science and Technology, **20**(1), 1–9 (2005). https://doi.org/10.1088/0268-1242/20/1/001
[12] M.H. Yükselici, A.A. Bozkurt, and B.C. Ömür, “A detailed examination of the growth of CdSe thin films through structural and optical characterization,” Materials Research Bulletin, **48**(7), 2442–2449 (2013). https://doi.org/10.1016/j.materresbull.2013.02.068
[13] B.K. Tuychibaev, and N.Kh. Yuldashev, “A study of the microstructure of CdSe:Cu,Cl films heat-treated in vacuum and air in $CuCl_2$ vapor,” Western European Journal of Modern Experiments and Scientific Methods, **3**(11), 81–86 (2025).
[14] S.L. Patel, S. Chander, A. Purohit, M.D. Kannan, and M.S. Dhaka, “Understanding the physical properties of $CdCl_2$ treated thin CdSe films for solar cell applications,” Optical Materials, **89**, 42-47 (2019). https://doi.org/10.1016/j.optmat.2019.01.001
[15] M. Ayibzhanov, B.K. Tuychibaev, and N.Kh. Yuldashev, “Technology for Obtaining CdSe Films with Transparent SnO_2 Contacts by Vacuum Thermal Evaporation,” Scientific and Technical Journal of Fergana Polytechnic Institute, **28**(5), 19–25 (2024).
[16] B.K. Tuychibaev, “Thermal vacuum method for producing photoconductive CdSe films with transparent SnO_2 contacts,” Eurasian Research Bulletin, **41**, 17-22 (2025). https://geniusjournals.org/index.php/erb/article/view/6797
[17] B.S. Pandit, “Structural and dynamical properties, lattice dynamical CdS, CdSe, and CdTe,” International Journal of New Technology and Research, **11**(3), 1-6 (2025). https://www.ijntr.org/download_data/IJNTR11030018.pdf

ДОСЛІДЖЕННЯ МІКРОСТРУКТУРИ ФОТОСЕНСИТИВНИХ ТОНКИХ ПЛІВОК CdSe ТА CdSe:Cd,Cl

Баходір К. Туйчібаєв[1], Носіржон Х. Юлдашев[1], Хусанбой М. Сулаймонов[1], Гулкан А. Хасанова[2], Маралбек Ч. Осконбаєв[2], Ісламідін Ташполовтов[2], Іфтіхоржон І. Юлчієв[1]
[1]Ферганський державний технічний університет, Фергана, Узбекистан
[2]Ошський державний університет, Ош, Киргизстан

Субструктурні характеристики свіжоприготовлених фоточутливих тонких плівок $CdSe$ та легованих $CdSe{:}Cd,Cl$ було досліджено з огляду на вплив температури підкладки T_s і тривалості термообробки на повітрі в присутності парів $CdCl_2$. Також наведено результати електронно-графічних та електронно-мікроскопічних досліджень плівок, одержаних за різних технологічних умов. Встановлено, що вісь текстури свіжоприготованих плівок $CdSe$ перпендикулярна до площини підкладки. Із підвищенням T_s від 250 до 400°C зростають кут розсіювання осі текстури, частка гексагональної фази, розмір кристалітів і розмір області когерентного рентгенівського розсіювання D_{csr}. Після відпалу на повітрі в присутності парів $CdCl_2$ при температурі $300°C$ плівки, отримані за T_s=250°C, виявляють переорієнтацію кристалітів від площини $(111)_c + (0002)_h$, паралельної площині підкладки, до орієнтації $(10\bar{1}3)$ через площини $(311)_c + (11\bar{1}2)_h$. Така переорієнтація супроводжується збільшенням розміру кристалітів і D_{csr}, а також зменшенням параметра ґратки та мінімальної густини дислокацій.

Ключові слова: *фоточутлива плівка; CdSe; CdSe:Cd,Cl; поздовжня фотопровідність; полікристал; текстура; температура підкладки; термічне оброблення; кінетика сенсибілізації; розмір області когерентного рентгенівського розсіювання*

East European Journal of Physics. 2. 187-190 (2026)
DOI:10.26565/2312-4334-2026-2-19 ISSN 2312-4334

THE EFFECT OF TEMPERATURE ON THE ENERGETIC POSITION OF THE FERMI LEVEL IN POROUS SILICON

U.S. Babakhodzhaev[1], M.A. Usmanov[2]*, I.Sh. Vokhobjonov[2], S.M. Shamsiddinova[2]
[1]*Namangan State Pedagogical Institute, Uychi Street 316, Namangan 716019, Uzbekistan*
[2]*Namangan State University, Bobourshox Street 161, Namangan 160107, Uzbekistan*
**Corresponding Author e-mail: muhammadphysics777@gmail.com*
Received January 5, 2026; revised March 26, 2026; accepted April 3, 2026

This paper presents the theoretical investigation of the temperature-dependent shift of the Fermi level in porous silicon (por-Si). The study is based on the charge-state distribution model originally proposed for hydrogenated amorphous silicon (a-Si:H), while accounting for the unique physical and chemical properties of porous silicon (por-Si). The temperature dependence of the parameters in the charge-state density within the bandgap is accounted for in both simplified and advanced models. For each model, the Fermi-level shift behavior was calculated using numerical methods based on integral-differential equations. The results are presented in graphical form, and the physical mechanisms underlying the Fermi level shift across different temperature ranges are discussed. The conclusions obtained can be applied to explain carrier transport processes, reduce surface recombination, and improve the efficiency of por-Si/c-Si heterostructure-based solar cells.
Keywords: *Fermi level; Amorphous silicon; Porous silicon; Bandgap; Density of states; Gaussian distribution; Electrical conductivity*
PACS: 71.23.Cq, 71.10.Ca, 73.61.Cw, 72.40.+w, 78.20.-e

INTRODUCTION

The increasing demands on the performance and efficiency of various electronic devices based on semiconductor materials have been consistently noted in the scientific literature for many years. The development of multi-component (heterostructure-based) devices using different modifications of semiconductor materials has been expanding. In accordance with the principles of HIT technology, to enhance the efficiency of crystalline silicon (c-Si)-based solar cells, heterostructure devices comprising three or more layers are being developed using modified forms of silicon such as hydrogenated amorphous silicon (a-Si:H), microcrystalline silicon (μc-Si:H), nanocrystalline silicon (nc-Si:H), or porous silicon (por-Si) [3,4,5].

Due to the low physicochemical stability and rapid degradation of hydrogenated silicon layers, extensive research in recent years has focused on improving the efficiency of heterostructure solar cells based on porous silicon (por-Si) layers [6,7]. Over the past decade, the fabrication of heterostructure-based solar cells has been recognized as one of the most rapidly advancing technologies. Among the most promising and efficient approaches for producing solar cells with crystalline silicon (c-Si)-based heterostructure layers is the HIT technology (heterojunction with intrinsic thin layer) [1,2].

One of the key advantages of heterojunction-based solar cells is their ability to effectively reduce surface recombination. In particular, when a thin layer of n^+-type hydrogenated silicon (Si:H) modification is deposited on the surface of p-type crystalline silicon, the resulting valence band offset (ΔE_v) significantly suppresses surface recombination [3]. Compared to materials such as a-Si:H, μc-Si:H, and nc-Si:H, porous silicon (por-Si) possesses a larger specific surface area as well as additional physicochemical properties, which can substantially contribute to enhancing the efficiency of heterojunction solar cells based on por-Si. One of the main challenges in heterojunction solar cells is the formation of theoretical potential barriers for majority charge carriers in either the conduction or valence band. An increase in the magnitude of such potential barriers negatively affects the carrier transport process, ultimately leading to a reduction in the fill factor (FF).

It is well known that the primary cause of potential barrier formation between layers is the difference in the Fermi level positions of the semiconductor materials composing the layers, as well as the sensitivity of the Fermi level's energetic position to external influences. Moreover, the transport process of charge carriers is significantly affected by the average lifetime of both majority and minority carriers [8]. Therefore, the present study aims to theoretically analyze the temperature dependence of the Fermi level and the average carrier lifetime.

The bandgap width and charge carrier transport parameters of porous silicon (por-Si) are significantly influenced by the size of its crystallites. In por-Si, crystallite sizes can range from a few nanometers to several hundred nanometers [9]. Considering the crystallite size is crucial when selecting theoretical research methods, since, as noted earlier, the electrical conductivity of por-Si can vary widely with porosity.

Studies have shown that when the porosity is in the range of 50–70%, the electrical conduction mechanism and bandgap width of por-Si become similar to those of hydrogenated amorphous silicon (a-Si:H).

Cite as: U.S. Babakhodzhaev, M.A. Usmanov, I.Sh. Vokhobjonov, S.M. Shamsiddinova, East Eur. J. Phys. 2, 187 (2026), https://doi.org/10.26565/2312-4334-2026-2-19
© U.S. Babakhodzhaev, M.A. Usmanov, I.Sh. Vokhobjonov, S.M. Shamsiddinova, 2026; CC BY 4.0 license

Accordingly, the temperature dependence of electrical conductivity exhibits an activation character and can be expressed as:

$$\sigma = \sigma_0 exp\left(\frac{\Delta E}{kT}\right)$$

where the quantities σ_0 and ΔE vary in accordance with the Meyer–Neldel rule, a fact confirmed by experimental results. It has also been established that for por-Si with 50–70% porosity, the bandgap width (E_g) lies within the range of 1.7-2 eV [10].

Based on the above considerations, the model proposed in [11] for the bandgap of a-Si:H material was employed to investigate the temperature dependence of the Fermi level. According to this model, the charged states arising from broken bonds within an energy width Δ around the Fermi level are distributed according to a Gaussian distribution.

The electrons in these charged states are redistributed with temperature in accordance with the function $f(\varepsilon, \varepsilon_F, U, T)$, which leads to a temperature-dependent shift of the Fermi level $\varepsilon_F(T)$.

To determine the temperature dependence of this shift, the law of electric charge conservation is applied:

$$\int_{\varepsilon_v}^{\varepsilon_c} f(\varepsilon, \varepsilon_F, U, T)\, N(\varepsilon)\; d\varepsilon \tag{1}$$

where: ε_v — upper energy state of the valence band; ε_c — lower energy state of the conduction band; ε_F — Fermi level; U — correlation energy (temperature-independent); N(ε) — energy density of charged states.

By taking the derivative of expression (1) with respect to temperature, the following equation for the function $\varepsilon_F(T)$ is obtained:

$$\frac{d\varepsilon_F}{dT} = \frac{\int y^2 \frac{\partial f}{\partial y}\, N(\varepsilon)\, d\varepsilon}{\int \frac{\partial f}{\partial \varepsilon_F} N(\varepsilon)}, \qquad y = \frac{1}{T} \tag{2}$$

The integral-differential equation (2) can be solved using a step-by-step (iterative) method, which can be written as:

$$\varepsilon_{F_{i+1}} = \varepsilon_{F_i} + \frac{d\varepsilon_F}{dT}\, \sigma T$$

where σT is the calculation step size, and the value of $\frac{d\varepsilon_F}{dT}$ is obtained from equation (2).

The function N(E), which describes the density of charged states in equation (2), is expressed in the following analytical form according to the model adopted from [12]:

$$N(E) = N_{ct}(E) + N_{vt}(E) + N_G(E) \tag{3}$$

Now, let us examine each term in expression (3) separately. $N_{ct}(E)$ represents the density of charged states located near the bottom of the conduction band within the energy width ε_{c0} and follows the relation $N_{ct}(E) = N_{ct0} \exp\,[(\varepsilon - \varepsilon_g)/\varepsilon_{c0}]$, where $N_{ct0} = 10^{21} - 10^{22}\ sm^{-3}\ eV^{-1}$ [12,13], ε_g is the bandgap width of porous silicon (por-Si), and ε_{c0} is the width of the energy range over which the charged states are distributed, taking values in the range 25-30 meV [11]. The second term, $N_{vt}(E)$, corresponds to the density of charged states located above the valence band. This function is distributed within the energy width ε_{v0} and follows the relation $N_{vt} = N_{vt0} \exp\,(-\varepsilon/\varepsilon_{v0})$, where $N_{vt0} = (1-3) \cdot 10^{21}$ $sm^{-3}\ eV^{-1}$, and ε_{v0}, unlike ε_{c0}, is temperature-dependent, with the temperature dependence expressed as follows:

$$\varepsilon_{v0}(T) = \sqrt{[\varepsilon_{v0}(T^{\star})]^2 - (kT^{\star})^2 + (kT)^2}$$

$T^{\star}$=500 K represents the equilibrium temperature, which varies within the range of 0.04 eV to 0.15 eV depending on the degree of disorder in the material, i.e., the extent of amorphization [12,13]. For porous silicon (por-Si), $\varepsilon_{v0}(300)$ typically lies within 40–45 meV, whereas $\varepsilon_{v0}(500)$ is in the range of 51–56 meV. In constructing the graphs, the value of $\varepsilon_{v0}(300)$ was selected within the interval of 20–50 meV. The term $N_c(E)$ in expression (3) represents the distribution function of charged states arising from the breaking of Si–Si bonds during the formation of microcrystallites, follows a Gaussian distribution and is expressed as follows:

$$N_G(\varepsilon) = \frac{N_c}{\sqrt{2\pi\sigma^2}} exp(-(\varepsilon - \varepsilon_F)^2/2\sigma^2)$$

where σ represents the maximum potential energy of defects formed due to bond breaking, and it is determined by the relation $\sigma = (\varepsilon_{v0}(T) \cdot (\Delta + U))^{1/2}$ [12,13]. In this expression, Δ and U are energetic parameters associated with defect states, where Δ=0.44 eV is the energy separation, and U=0.2÷0.3 eV denotes the correlation energy of defect electrons.

The magnitude N_G is obtained from experimental results and varies in the range $N_G = 10^{17} - 10^{18}\ eV^{-1} sm^{-1}$ [11]. In [14], when determining the temperature dependence of the Fermi level, a simplified model of N(E) — namely the approximation $N(\varepsilon) \approx N_G(\varepsilon)$ — was used. However, in that approach, the temperature dependence of the parameters in the Gaussian function was not accounted for.

In the present study, the temperature dependence of certain parameters in the charge state distribution function within the bandgap of porous silicon (por-Si) was taken into account. Accordingly, two models were considered:

1. Simplified model:

$$N(\varepsilon) = \frac{N_G}{\sqrt{2\pi\sigma^2}} exp(-(\varepsilon - \varepsilon_F(T))^2/2\sigma^2) \tag{4}$$

2. Complex model:

$$N(\varepsilon) = N_{ct0} \exp\left(\frac{\varepsilon - \varepsilon_g}{\varepsilon_{c0}}\right) + N_{vt0} \exp\left(-\frac{\varepsilon}{\varepsilon_{v0}}\right) + \frac{N_G}{\sqrt{2\pi\sigma^2}} exp\left(-\frac{(\varepsilon - \varepsilon_F)^2}{2\sigma^2}\right) \tag{5}$$

For both models, graphs illustrating the temperature-dependent shift of the Fermi level were constructed using numerical computation methods.

RESULTS AND DISCUSSION

The temperature-dependent variation of the Fermi level was calculated using Equation (4), and the results are shown in Figure 1. As can be seen from the graph, when the temperature is T<100 K, the shift of the Fermi level shows a negligible change, depending on the parameters of the function describing the charge states. This behavior can be explained by the fact that the thermal energy kT is insufficient to excite electrons into the charge states.

When the temperature exceeds T>100 K, the difference becomes much more pronounced, and a sharp temperature-dependent shift of the Fermi level is observed. This result is consistent with the graphs presented in [14], but does not fully agree with the conclusions in [15] and [16]. According to the interpretations in [15] and [16], as the temperature increases, electrons located in charge states below the Fermi level become almost fully activated. In addition, electrons in the valence band are also activated, and their transition to the conduction band can occur through the charge states under consideration. All these processes contribute to a decrease in the Fermi level shift.

Furthermore, in [16], the shift of the Fermi level was studied in relation to the Stabler–Wronski effect, and it was emphasized that in undoped a-Si:H materials, the Fermi level shift is not monotonic and tends to approach a certain limiting value.

In Figure 2, the graph of the Fermi level shift is calculated using formula (6). This expression shows that the Fermi level shift value, $\Delta\varepsilon_F$, changes within certain limits. Such a variation can be explained as follows: with increasing temperature, the concentration of broken Si–Si bonds increases, and in the charge exchange process between these defect states, electrons from both the valence band tail and the valence band itself participate. Since the density of these charge states is greater than that of the charge states distributed around the mid-gap according to the Gaussian distribution, their activation slows down the Fermi level shift.

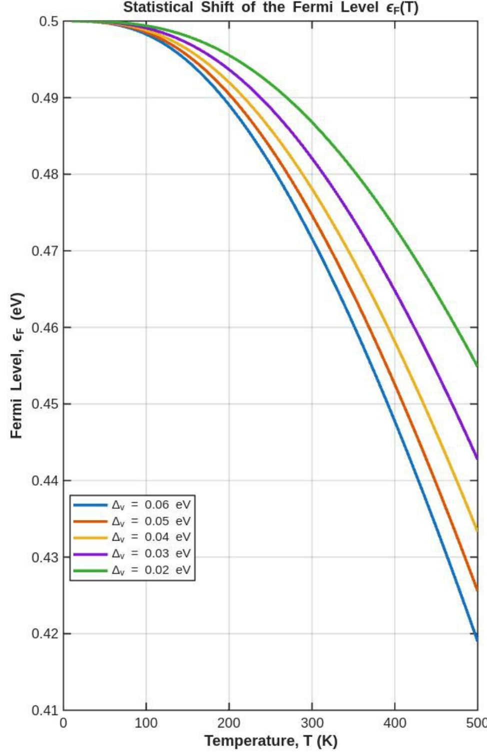

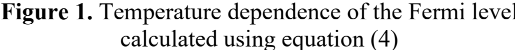

Figure 1. Temperature dependence of the Fermi level calculated using equation (4)

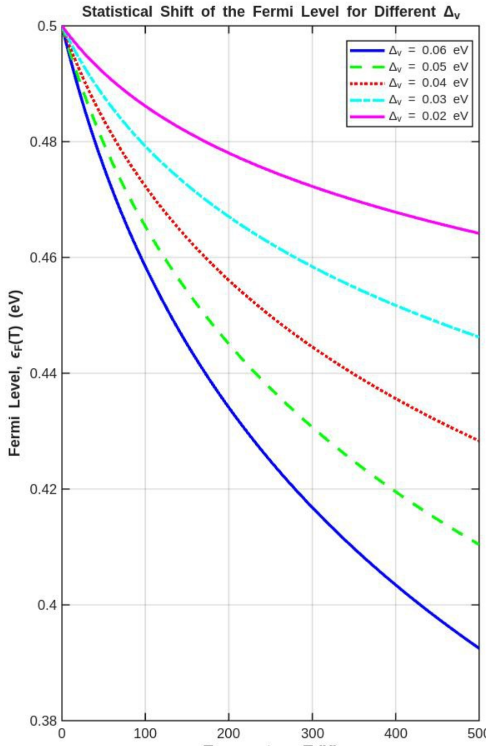

Figure 2. Temperature-dependent Fermi level shift calculated using equation (6)

CONCLUSIONS

As noted earlier, according to [9], in certain types of porous silicon samples, the electrical conductivity exhibits an activation character, following the law $\sigma = \sigma_0 exp\left(-\frac{\Delta\varepsilon}{kT}\right)$, where $\Delta\varepsilon = \varepsilon_c - \varepsilon_F$. Thus, the, $\Delta\varepsilon(T)$ dependence should also be valid, and this relationship should manifest in the temperature dependence of electrical conductivity. Indeed, the $j\left(\frac{1}{T}\right)$ dependence shown in [16] for the temperature range T>150 K confirms the correctness of this approach.

The obtained results indicate that this model and its outcomes can be applied to study the temperature dependence of parameters in devices based on por-Si/c-Si structures.

ORCID
U.S. Babakhodzhaev, https://orcid.org/0009-0006-4355-7687, **M.A. Usmanov,** https://orcid.org/0009-0006-4192-4359; **I.Sh. Vokhobjonov,** https://orcid.org/0009-0004-8882-0309; **S.M. Shamsiddinova,** https://orcid.org/0009-0004-7324-4249

REFERENCES

[1] M. Taguchi, K. Kawamoto, S. Tsuge, T. Baba, H. Sakata, M. Morizane, K. Uchihashi, *et al.*, "HIT cells—high-efficiency crystalline Si cells with novel structure," Prog. Photovolt. Res. Appl. **8**(5), 503–513 (2000). https://doi.org/10.1002/1099-159x(200009/10)8:5%3C503::aid-pip347%3E3.0.co;2-g
[2] M.L. Scherff, *et al.*, "Efficiency for amorphous/crystalline heterojunction solar cells on flat p-type silicon wafers," in: *Proceedings of PV in Europe 2002*, (Rome, Italy, 2002), pp. 216–219.
[3] B. Liang, X. Chen, X. Wang, H. Yuan, A. Sun, Z. Wang, L. Hu, et al., "Progress in crystalline silicon heterojunction solar cells," Journal of Materials Chemistry A, **13**, 2441–2477 (2025). https://doi.org/10.1039/D4TA06224H
[4] M. Schmidt, L. Korte, A. Laades, R. Stangl, Ch. Schubert, H. Angermann, E. Conrad, and K.V. Maydell, "Physical aspects of a-Si:H/c-Si heterojunction solar cells," Thin Solid Films, **515**(19), 7475–7480 (2007). https://doi.org/10.1016/j.tsf.2006.11.087
[5] Yu.V. Kryuchenko, A.V. Sachenko, A.V. Bobyl, V.P. Kostylyov, E.I. Terukov, A.S. Abramov, E.V. Mal'chukova, and I.O. Sokolovskyi, "Simulation of the natural characteristics of vertical a-Si:H/μc-Si:H tandem solar cells. I. General relations," Semiconductors, **49**(5), 683–692 (2015). https://doi.org/10.1134/S1063782615050097
[6] Y.M. Huang, Q.L. Ma, M. Meng, and B.G. Zhai, "Porous silicon based solar cells," Materials Science Forum, **663–665**, 836-840 (2010). https://doi.org/10.4028/www.scientific.net/MSF.663-665.836
[7] H. Kwon, J. Lee, M. Kim, and S. Lee, "Investigation of antireflective porous silicon coating for solar cells," International Scholarly Research Network ISRN Nanotechnology, **2011**, 16409 (2011). https://doi.org/10.5402/2011/716409
[8] H. Lin, M. Yang, X. Ru, G. Wang, S. Yin, F. Peng, C. Hong, *et al.*, "Silicon heterojunction solar cells with up to 26.81% efficiency achieved by electrically optimized nanocrystalline-silicon hole contact layers," Nature Energy, **8**, 789–799 (2023). https://doi.org/10.1038/s41560-023-01255-2
[9] S.P. Zimin, "Classification of electrical properties of porous silicon," Semiconductors, **34**(3), 353–357 (2000). https://doi.org/10.1134/1.1187985
[10] Y. Wang, and D. Wang, "Advances in porous silicon materials for sensing, energy storage, and microelectronics," Nanomaterials, **16**, 257 (2026). https://doi.org/10.3390/nano16040257
[11] Yu.V. Kryuchenko, A.V. Sachenko, A.V. Bobyl, V.P. Kostylyov, P.N. Romanets, I.O. Sokolovskyi, A.I. Shkrebtii, *et al.*, "Efficiency a-Si:H solar cell. Detailed theory," Semiconductor Physics, Quantum Electronics & Optoelectronics, **15**(2), 91-116 (2012). https://doi.org/10.15407/spqeo15.02.091
[12] M.J. Powell, and S.C. Deane, "Improved defect-pool model for charged defects in amorphous silicon," Physical Review B, **48**(15), 10815–10827 (1993). https://doi.org/10.1103/PhysRevB.48.10815
[13] C. Longeaud, J.A. Schmidt, and R.R. Koropecki, "Determination of semiconductor band gap state parameters from photoconductivity measurements. II. Experimental results," Physical Review B, **73**(23), 235317 (2006). https://doi.org/10.1103/PhysRevB.73.235317
[14] N. Wang, F. Meng, L. Zhang, Z. Liu, and W. Liu, "Light soaking of hydrogenated amorphous silicon: a short review," Carbon Neutrality, **3**, 18 (2024). https://doi.org/10.1007/s43979-024-00093-9
[15] S. De Wolf, A. Descoeudres, Z.C. Holman, and C. Ballif, "High-efficiency silicon heterojunction solar cells: A review," Green, **2**, 7–24 (2012). https://doi.org/10.1515/green-2011-0018
[16] H. Fritzsche, "Development in understanding and controlling the Staebler–Wronski effect in a-Si:H," Annual Review of Materials Research, **31**, 47–79 (2001). https://doi.org/10.1146/annurev.matsci.31.1.47

ВПЛИВ ТЕМПЕРАТУРИ НА ЕНЕРГЕТИЧНЕ ПОЛОЖЕННЯ РІВНЯ ФЕРМІ В ПОРИСТОМУ КРЕМНІЇ

У.С. Бабаходжаєв[1], М.А. Усманов[2], І.Ш. Вохобджонов[2], С.М. Шамсіддінова[2]
[1]*Наманганський державний педагогічний інститут, вул. Уйчі, 316, Наманган 716019, Узбекистан*
[2]*Наманганський державний університет, вул. Бабуршокс, 161, Наманган 160107, Узбекистан*

У цій статті представлено теоретичне дослідження температурно-залежного зсуву рівня Фермі в пористому кремнії (por-Si). Дослідження базується на моделі розподілу зарядових станів, спочатку запропонованій для гідрогенізованого аморфного кремнію (a-Si:H), з урахуванням унікальних фізичних та хімічних властивостей пористого кремнію (por-Si). Температурна залежність параметрів густини зарядових станів у межах забороненої зони враховується як у спрощених, так і в розширених моделях. Для кожної моделі поведінка зсуву рівня Фермі була розрахована за допомогою числових методів, заснованих на інтегрально-диференціальних рівняннях. Результати представлені в графічній формі, а також обговорюються фізичні механізми, що лежать в основі зсуву рівня Фермі в різних температурних діапазонах. Отримані висновки можуть бути застосовані для пояснення процесів переносу носіїв заряду, зменшення поверхневої рекомбінації та підвищення ефективності сонячних елементів на основі гетероструктур por-Si/c-Si.

Ключові слова: *рівень Фермі; аморфний кремній; пористий кремній; заборонена зона; густина станів; розподіл Гауса; розподіл Гауса*

East European Journal of Physics. 2. 191-202 (2026)
DOI:10.26565/2312-4334-2026-2-20 ISSN 2312-4334

EXPERIMENTAL AND SIMULATION-BASED STUDY ON THE STRUCTURAL, OPTICAL, AND MECHANICAL PROPERTIES OF PLA/ZnO NANOCOMPOSITES

Fakhriddin T. Yusupov[1]*, Tokhirbek I. Rakhmonov[1], Mekhriddin F. Akhmadjonov[1], Dilobarbonu E. Abdukodirova[2], Yelmurat Dosymov[3], Iftikhorjon I. Yulchiev[1]
[1]*Fergana State Technical University, Fergana, Uzbekistan*
[2]*Chirchik State Pedagogical University, Chirchik, Uzbekistan*
[3]*Khoja Akhmet Yassawi International Kazakh-Turkish University, Kazakhstan*
**Corresponding Author e-mail: yusupov.fizika@gmail.com*
Received January 13, 2026; revised April 27, 2026; accepted May 2, 2026

This work presents a comprehensive experimental and theoretical investigation of polylactide (PLA) nanocomposites reinforced with zinc oxide (ZnO) nanoparticles at concentrations of 0.5, 1, 3, and 5 wt.%. The dispersion state and microstructural features of ZnO within the PLA matrix were examined using scanning electron microscopy combined with energy-dispersive X-ray spectroscopy, revealing homogeneous distribution at low filler contents and progressive agglomeration at higher loadings. X-ray diffraction analysis confirms that ZnO preserves its hexagonal wurtzite crystal structure after incorporation into the polymer matrix, while composition-dependent variations in crystallite size and lattice microstrain are found to correlate with the mechanical response of the composites. Fourier-transform infrared spectroscopy indicates interfacial interactions between PLA chains and ZnO nanoparticles, as evidenced by systematic shifts in the carbonyl stretching band and associated charge redistribution. Ultraviolet–visible spectroscopy demonstrates a significant enhancement of UV-shielding performance with increasing ZnO content, accompanied by the emergence of sub-bandgap absorption tails attributed to defect-related and interfacial electronic states. Density functional theory calculations support the experimental observations by revealing interfacial charge transfer and a slight modification of the electronic structure at the PLA/ZnO interface. The results show that ZnO incorporation improves both mechanical stiffness and UV-blocking efficiency, while an optimal ZnO loading below 1 wt.% is identified to maintain mechanical integrity and minimize agglomeration-induced degradation.
Keywords: *PLA/ZnO nanocomposites; UV-shielding; Mechanical properties; XRD; FTIR; DFT simulations; Charge transfer; Nanomaterials; Polymer reinforcement*
PACS: 78.20.-e, 73.61.Ga, 85.60.-q, 68.55.-a

1. INTRODUCTION

Polylactide (PLA) has emerged as one of the most promising biodegradable polymers due to its renewable origin, biocompatibility, and suitability for packaging, biomedical devices, and environmentally sustainable applications [1]. Despite these advantages, neat PLA generally exhibits limited mechanical strength and poor resistance to ultraviolet (UV) radiation, which significantly restricts its long-term stability and performance under practical service conditions [2]. As a result, considerable research efforts have been devoted to improving the functional properties of PLA by incorporating inorganic fillers and nanostructured reinforcements. Among various inorganic additives, zinc oxide (ZnO) has attracted particular attention owing to its wide direct bandgap (~3.3 eV), strong UV absorption capability, chemical stability, and biocompatibility. In addition, ZnO exhibits multifunctional physical properties, including semiconductivity, piezoelectricity, and surface polarity, which make it a suitable candidate for enhancing both mechanical and optical characteristics of polymer-based nanocomposites [3,4]. Previous studies have demonstrated that ZnO incorporation can effectively improve UV-shielding efficiency and stiffness in PLA-based systems; however, these enhancements are often accompanied by challenges related to nanoparticle dispersion and interfacial compatibility [3–6]. Recent investigations on ZnO-based thin films, heterostructures, and nanocomposites have highlighted the importance of defect states, surface polarization, and charge-transfer phenomena in determining the functional properties of ZnO-containing systems [7–9]. Furthermore, theoretical studies based on density functional theory have shown that interfacial charge redistribution can modify the electronic structure and defect-related states, thereby directly affecting optical absorption and dielectric behavior in hybrid materials [10]. At higher filler concentrations, ZnO nanoparticles tend to agglomerate due to strong interparticle interactions, leading to stress concentration sites and deterioration of mechanical performance [11,12]. Therefore, achieving a uniform dispersion of ZnO and understanding the nature of interfacial interactions between the polymer matrix and the inorganic phase remain critical issues. From a fundamental perspective, the interfacial region governs stress transfer, phonon scattering, and electronic polarization effects, which collectively influence the mechanical integrity and optical response of the composite material.

Despite these advances, a systematic correlation between experimental observations and atomistic-level simulations of PLA/ZnO nanocomposites remains underexplored.

In this study, PLA/ZnO nanocomposites containing 0.5–5 wt.% ZnO are fabricated and investigated using a combined experimental and theoretical approach. The structural, mechanical, and optical properties are characterized by

---

Cite as: F.T. Yusupov, T.I. Rakhmonov, M.F. Akhmadjonov1, D.E. Abdukodirova, Y.Dosymov, I.I. Yulchiev, East Eur. J. Phys. 2, 191 (2026), https://doi.org/10.26565/2312-4334-2026-2-20
© F.T. Yusupov, T.I. Rakhmonov, M.F. Akhmadjonov1, D.E. Abdukodirova, Y.Dosymov, I.I. Yulchiev, 2026; CC BY 4.0 license

SEM/EDS, XRD, FTIR, and UV–Vis spectroscopy, while density functional theory calculations are employed to elucidate the electronic structure and interfacial charge transfer at the PLA/ZnO interface. By integrating experimental results with theoretical insights, this work aims to establish clear structure–property relationships and to identify an optimal ZnO loading that balances mechanical reinforcement with enhanced UV-shielding performance.

2. MATERIALS AND METHODS

Polylactide (PLA, NatureWorks 4032D) was employed as the polymer matrix, while zinc oxide (ZnO) nanopowder with an average particle size of 30–60 nm and a purity of 99.9% was used as the inorganic reinforcing phase. Prior to compounding, PLA pellets were dried under vacuum at 60 °C for 8 h to remove residual moisture, thereby preventing hydrolytic degradation and undesirable changes in melt rheology during processing, as schematically illustrated in Figure 1a. ZnO nanoparticles were incorporated into the PLA matrix at loadings of 0.5, 1, 3, and 5 wt.% to systematically evaluate the influence of filler content on the structural, optical, and mechanical properties of the resulting nanocomposites. The composites were prepared by melt blending using a laboratory-scale co-rotating twin-screw extruder (Figure 1a). The barrel temperature profile was maintained in the range of 170–185°C from the feeding zone to the die, considering the thermal stability window of PLA to avoid excessive chain scission. The screw rotation speed was set to 60 rpm, and the residence time was approximately 10 min, ensuring effective dispersion of ZnO nanoparticles in the molten polymer while minimizing thermal degradation. The extrudate strands were subsequently cooled to room temperature and pelletized (Figure 1a).

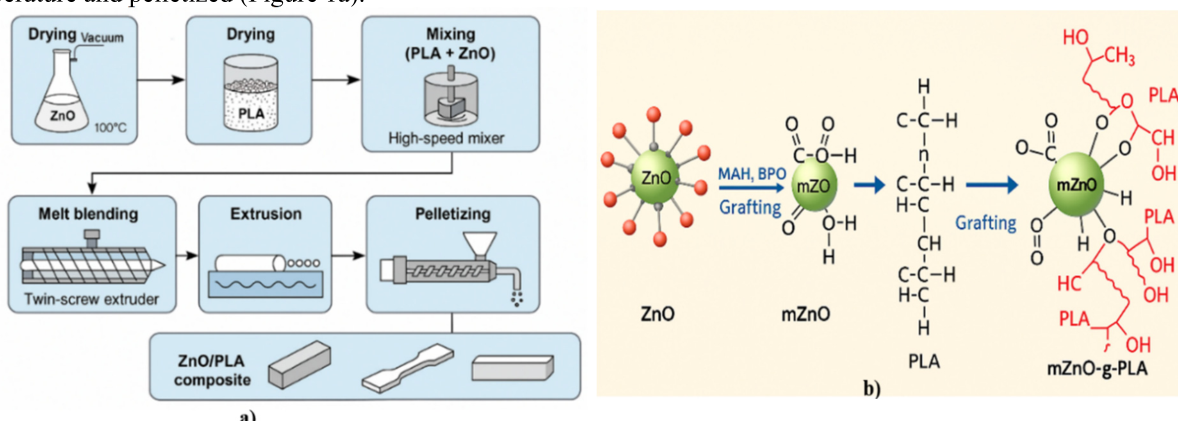

Figure 1. Preparation workflow of PLA/ZnO nanocomposites (a) and MAH/BPO-assisted surface grafting scheme (b) forming ester linkages between ZnO–COOH and PLA–OH groups

In addition, to enhance interfacial compatibility between the inorganic ZnO nanoparticles and the PLA matrix, a MAH/BPO-assisted surface grafting approach was employed. As schematically shown in Figure 1b, maleic anhydride (MAH), initiated by benzoyl peroxide (BPO), promotes the formation of ester linkages between the carboxyl groups on the ZnO surface (ZnO–COOH) and the hydroxyl end groups of PLA (PLA–OH). This chemical grafting mechanism improves interfacial adhesion, suppresses nanoparticle agglomeration, and facilitates more efficient stress transfer across the ZnO–PLA interface. Standard testing specimens were produced from the compounded pellets by injection molding. The molding temperature was maintained at 175–180 °C, and the mold clamping pressure was set to 6–7 MPa. The samples obtained were prepared for mechanical, thermal, and structural characterization in accordance with ASTM D638, ASTM D790, and ASTM D256 standards, respectively. Prior to testing, all specimens were conditioned at 23 ± 2 °C for at least 48 h to ensure reproducible equilibrium properties.

2.1 Characterization techniques

The microstructure and elemental distribution of the PLA/ZnO nanocomposites were examined by scanning electron microscopy (SEM) coupled with energy-dispersive X-ray spectroscopy (EDS). Fractured tensile specimens were used to reveal the internal morphology of the composites and to assess the dispersion state of ZnO nanoparticles within the PLA matrix. SEM provided high-resolution images of particle shape, agglomeration behavior, and fracture features, while EDS elemental mapping of Zn and O was employed to verify the spatial uniformity and stoichiometric stability of the ZnO phase inside the polymer [13,14]. The crystalline structure of the nanocomposites was analyzed by X-ray diffraction (XRD). Diffraction patterns of neat PLA and PLA/ZnO samples containing 0.5, 1, 3, and 5 wt.% ZnO were recorded to identify the characteristic reflections of the hexagonal wurtzite ZnO phase and to monitor composition-dependent changes in peak intensity, width, and position. These data were used to confirm the preservation of ZnO crystallinity after melt processing and to extract qualitative information on crystallite size and microstrain evolution within the polymer matrix. Fourier-transform infrared (FTIR) spectroscopy was used to examine the chemical structure of PLA and interfacial interactions in PLA/ZnO nanocomposites. Changes in the carbonyl (C=O) stretching and CH3 vibrational bands were analyzed to assess modifications in polymer chain packing and local amorphization induced by ZnO incorporation, while the Zn–O vibration band in the low-wavenumber region confirmed the presence of the ZnO phase. The evolution of these

bands enabled correlation between molecular-level interfacial effects and the optical and mechanical behavior of the composites [14,15].

Optical properties and UV-shielding performance were evaluated by UV–Vis spectroscopy. Absorption spectra of PLA/ZnO nanocomposites with different ZnO loadings were recorded over the near-UV–visible range and compared with those of neat PLA. The position and shape of the absorption edge, as well as the appearance of sub-bandgap tails and broad absorption features at higher filler contents, were analyzed to distinguish between intrinsic band-edge transitions of wurtzite ZnO and defect-mediated states associated with oxygen vacancies, interstitials, and interfacial defects [16]. These measurements provided direct experimental insight into how ZnO concentration and dispersion control the UV-blocking efficiency of the hybrid system.

Mechanical properties were characterized using standard tensile, flexural, and impact tests on injection-molded specimens prepared in accordance with ASTM D638, ASTM D790, and ASTM D256, respectively [10,13]. The samples were conditioned at 23 ± 2°C for at least 48 h prior to testing to ensure reproducible equilibrium behavior. The resulting stress–strain curves and impact responses were used to quantify the effect of ZnO loading on stiffness, strength, ductility, and energy absorption, and to establish structure–property relationships in conjunction with the microstructural, spectroscopic, and theoretical analyses.

To complement the experimental techniques, density functional theory (DFT) calculations were performed to gain atomistic insight into the electronic structure and interfacial bonding at the PLA/ZnO interface. Simulations were carried out using a plane-wave pseudopotential framework as implemented in Quantum ESPRESSO, employing a generalized gradient approximation exchange–correlation functional under periodic boundary conditions. Bulk ZnO and PLA/ZnO interface supercells were constructed and structurally relaxed, after which total and projected density of states (DOS/PDOS), charge-density difference maps, and frequency-dependent dielectric functions were computed [1,17]. These calculations enabled quantitative analysis of band-edge states, interfacial charge transfer, and optical absorption, and were directly correlated with the experimental UV–Vis and FTIR results as well as with the observed mechanical trends.

3. RESULTS AND DISCUSSION

3.1 Microstructure and crystalline structure

The microstructural behavior of the ZnO/PLA composite was thoroughly examined using high-resolution scanning electron microscopy (SEM) combined with energy-dispersive X-ray spectroscopy (EDS), providing detailed insights into both morphological features and elemental distribution. Figure 2 illustrates the homogeneous dispersion of ZnO nanoparticles, predominantly in the 200–500 nm range, within the PLA matrix.

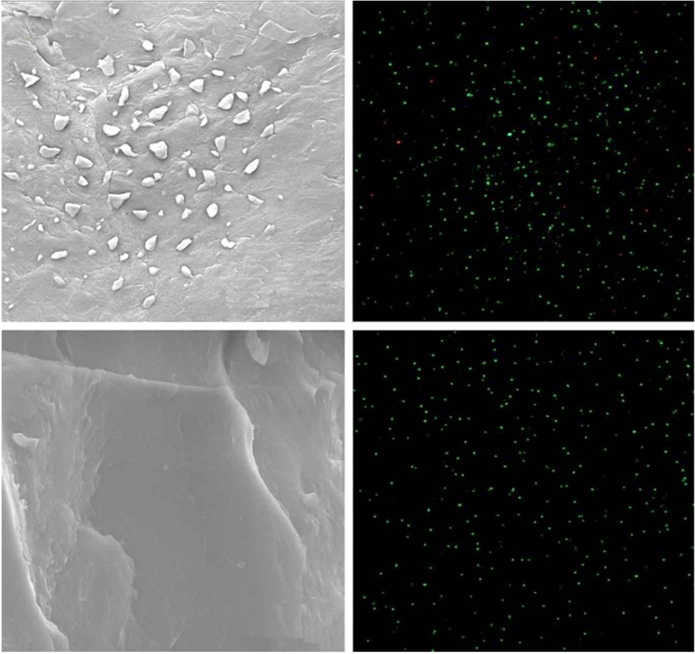

Figure 2. SEM micrographs and EDS elemental maps of neat PLA and PLA/ZnO nanocomposites (0.5–5 wt.% ZnO), showing ZnO dispersion and the spatial distribution of Zn and O

The SEM micrographs reveal irregularly shaped ZnO particles with angular, fragmented morphologies, a direct result of the intrinsic anisotropy of the wurtzite ZnO crystal lattice [18]. The distinct differences in surface energy between the polar (0001) and non-polar {10-10}/{11-20} planes lead to preferential crack propagation along crystallographic directions with minimal cleavage energy. Consequently, this results in sharp-edged particles that strongly interact with

the electron beam, producing a significant topographical contrast. The dispersion of ZnO nanoparticles throughout the PLA matrix is achieved through viscous shear forces and Brownian diffusion, overcoming the weak van der Waals attractions between ZnO grains [15]. This prevents significant agglomeration and leads to a homogeneous spatial distribution of nanoparticles. The final distribution reflects a balance between hydrodynamic dispersion and interfacial adhesion energies, with the latter primarily mediated by dipole–dipole interactions between the polar ZnO surface and the PLA chains. The fractured PLA surface displays characteristic layered tearing patterns, indicative of the material's relatively low elastic modulus and brittle–ductile transition under high strain rates [19]. Notably, ZnO does not induce significant stress localization along the fracture path, suggesting that the composite maintains a mechanically coherent interface where strain is efficiently transferred from the polymer phase to the inorganic phase.

Elemental mapping via EDS confirms that the Zn and O signals are uniformly distributed across the analyzed areas, directly supporting the evidence of well-dispersed ZnO domains in the composite. The spatial consistency of ZnO-derived X-ray emission intensities further suggests that no phase segregation or oxygen deficiency gradients are present within the composite [20]. The stable Zn/O ratio indicated by the mapping suggests that ZnO remains structurally intact within the PLA matrix, with no significant reduction or surface reconstruction occurring. This observation is crucial as such phenomena often arise in polymeric environments. Additionally, the lack of elemental accumulation at crack boundaries indicates that the nanoparticles do not migrate or concentrate in stress fields, supporting the hypothesis that interfacial energy minimization does not favor the preferential localization of ZnO particles.

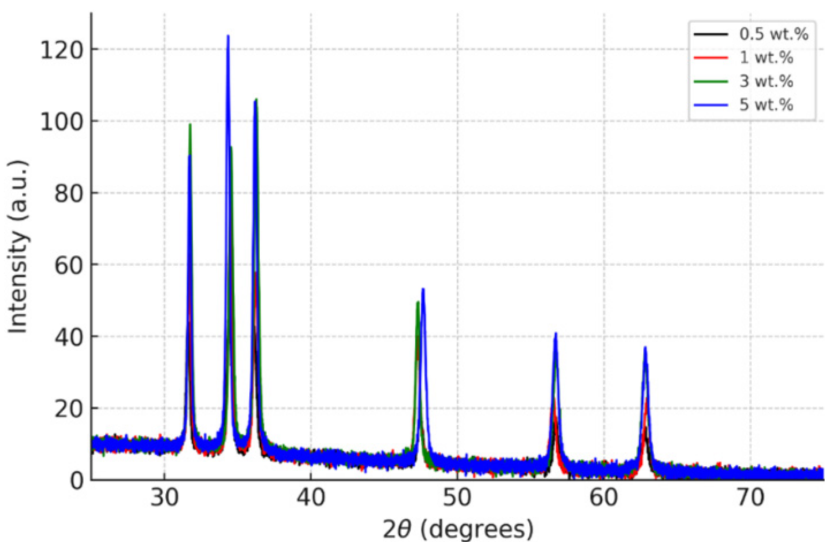

Figure 3. XRD patterns of PLA/ZnO nanocomposites (0.5–5 wt.% ZnO) highlighting wurtzite ZnO reflections and composition-dependent changes in peak intensity and broadening

The SEM–EDS analysis highlights the composite's architecture, governed by a combination of electron–solid interaction physics, interfacial bonding energetics, and polymer fracture mechanics. The nanoscale dispersion of ZnO nanoparticles enhances the microstructural homogeneity, minimizes dielectric discontinuities, and mitigates phonon scattering, all of which are essential for optimizing the electrical, thermal, and mechanical properties of the composite [21]. These findings underscore that the ZnO/PLA interface is structurally stable, energetically balanced, and free from large-scale aggregation, ensuring reliable performance in optoelectronic, sensing, and biocompatible applications. The homogeneity of the ZnO dispersion and the well-maintained interface provide a strong foundation for the composite's advanced functional behavior, as confirmed by the data presented in Figure 2.

The X-ray diffraction (XRD) patterns of the PLA/ZnO nanocomposites containing 0.5, 1.0, 3.0, and 5.0 wt.% ZnO reveal clear structural evidence of the successful incorporation of the wurtzite ZnO phase into the polymer matrix. As shown in Figure 3, all samples exhibit characteristic diffraction peaks corresponding to the hexagonal ZnO phase, notably the (100), (002), (101), (102), (110), and (103) planes. These reflections confirm that the crystalline structure of ZnO is preserved during melt mixing with PLA, with no evidence of structural degradation or polymorphic transformation. A marked increase in peak intensity is observed as the ZnO content increases, particularly for the dominant reflections at approximately 31.7°, 34.4°, and 36.2°, corresponding to the (100), (002), and (101) planes, respectively. This trend reflects a higher density of diffracting crystallites in the composites with higher ZnO content. From a semiconductor physics perspective, this behavior indicates that the crystallographic integrity and scattering power of the ZnO domains remain intact within the polymer matrix [22]. The preservation of strong diffraction intensities suggests that ZnO nanoparticles maintain their long-range order and do not undergo significant amorphization during processing.

Peak broadening effects, which vary slightly across compositions, can be attributed to variations in crystallite size and microstrain within the ZnO domains. The samples containing 0.5 wt.% and 1 wt.% ZnO show slightly broader peaks,

indicating smaller crystallite sizes or increased lattice distortion due to stronger confinement within the polymer environment. In contrast, the 3 wt.% and 5 wt.% ZnO/PLA composites exhibit sharper diffraction maxima, indicative of larger coherent scattering domains. This suggests that at higher ZnO loadings, nanoparticles experience reduced polymer-induced strain and may form more interconnected or partially agglomerated crystallite clusters, enhancing their structural stability. Small but measurable peak shifts (±0.1°) across the different compositions are noteworthy, particularly from a semiconductor physics viewpoint [18,22]. These shifts are typically associated with internal compressive or tensile stresses imposed on the ZnO lattice as it interacts with the PLA chains. Such microstrain effects arise from differential thermal expansion between the polymer and the oxide phase, as well as from potential surface-chemical interactions at the polymer-nanoparticle interface. The direction and magnitude of these shifts provide indirect evidence of interfacial bonding and stress transfer, which are crucial for determining the optical and electronic properties of ZnO-based hybrid materials. The weak amorphous halo observed between 18° and 22° originates from the PLA matrix and decreases in prominence with increasing ZnO content. This behavior further corroborates the progressive dominance of the crystalline ZnO phase in the diffraction profile. Importantly, the absence of new diffraction peaks or structural anomalies indicates that no secondary crystalline phases, such as zinc hydroxy species or ZnO-PLA reaction products, are formed during processing. This structural stability is essential for maintaining the intrinsic semiconductor properties of ZnO, particularly its wide bandgap ($E_g \approx 3.3$ eV) and polar surface terminations ((0001) Zn-terminated and ($000\bar{1}$) O-terminated planes), which govern its optical absorption, excitonic behavior, and interfacial polarization in the polymer matrix [23].

In summary, the XRD analysis demonstrates that ZnO nanoparticles retain their crystalline wurtzite structure within the PLA matrix, with composition-dependent variations in crystallite size, microstrain, and diffraction intensity. These structural characteristics directly influence the optical, mechanical, and charge-transport properties of the nanocomposites, shedding light on the fundamental interactions between the semiconductor ZnO phase and the PLA matrix. These findings are crucial for understanding and optimizing the hybrid behavior of PLA/ZnO composites, as further explored in the subsequent sections of this study.

3.2 Interfacial chemical interactions (FTIR)

The FTIR spectra of neat PLA and PLA/ZnO nanocomposites provide detailed insights into the interfacial interactions and modifications to the local electronic environment resulting from the incorporation of ZnO nanoparticles [24]. As illustrated in Figure 4, a prominent feature in all samples is the sharp carbonyl stretching vibration (ν(C=O)) observed around 1748–1752 cm^{-1}, characteristic of ester linkages in PLA. Upon the introduction of ZnO, this band undergoes a progressive red shift accompanied by a subtle decrease in intensity. This shift is indicative of coordinate bonding or dipole–dipole coupling between the electron-rich carbonyl oxygens of PLA and the Zn2+ sites on the ZnO surface. Such behavior suggests partial electron density withdrawal from the C=O bond, resulting in a weakened restoring force and, consequently, a lowered vibrational frequency. These findings confirm the formation of PLA→ZnO charge-transfer interactions, which play a crucial role in modifying the structural rigidity and local chain dynamics of the polymer matrix, as evidenced by changes in mechanical and optical properties reported in earlier sections (Figures 3 and 5).

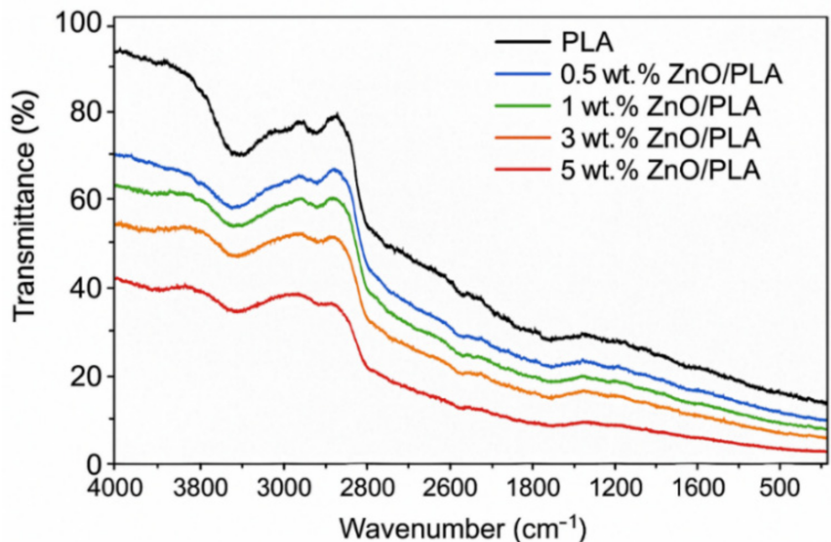

Figure 4. FTIR spectra of neat PLA and PLA/ZnO nanocomposites, showing shifts in the ν(C=O) band (~1748–1752 cm^{-1}) and changes in C–O–C and CH_3 vibrations with ZnO loading

Additionally, the absorption band at 1080–1180 cm^{-1}, corresponding to asymmetric C–O–C stretching, broadens and increases in intensity as ZnO content increases. This suggests that ZnO nanoparticles not only interact with terminal carbonyl groups but also perturb the ester linkages along the polymer backbone, likely due to restricted segmental mobility at the polymer–particle interface. Such immobilization effects are typical in polymer nanocomposites exhibiting strong

inorganic–organic interfacial adhesion, leading to improved thermomechanical stability, as reflected in the mechanical testing results in Figure 6. The enhancement of stiffness at lower ZnO loadings, while retaining adequate ductility, aligns with these structural modifications, confirming the effectiveness of ZnO as a reinforcing phase in the PLA matrix [25].

The band at 1450–1360 cm^{-1}, attributed to CH3 bending modes, becomes increasingly broadened at higher ZnO loadings, indicating local amorphization near the filler. ZnO nanoparticles disrupt long-range polymer chain packing, creating domains of reduced crystallinity. This behavior is consistent with known trends in semiconductor–polymer composites, in which nanoscale oxides alter phonon confinement and contribute to changes in mechanical properties. At higher ZnO concentrations, as evidenced by the mechanical data, the enhanced interfacial adhesion restricts polymer chain relaxation, leading to a transition toward brittle behavior in the nanocomposites. Moreover, a weak but clearly visible band emerges in the fingerprint region below 700 cm^{-1}, around 520–550 cm^{-1}, which corresponds to the Zn–O lattice vibration. The appearance and intensification of this band across all composite samples provide definitive proof that ZnO nanoparticles remain structurally intact within the PLA matrix. The coexistence of this band with the shifted polymer modes offers direct spectroscopic evidence of inorganic–organic hybridization at the molecular scale [24]. This coupling enhances the overall mechanical properties of the composite, as discussed in previous sections, and ensures the stability of the ZnO phase within the polymer matrix, as confirmed by XRD and mechanical tests.

Collectively, the vibrational modifications observed in the FTIR spectra reflect strong coupling between the PLA molecular orbitals and the electronic states of ZnO. This interaction leads to changes in dipole moments and phonon distributions, which are crucial for understanding the enhanced optical absorption, dielectric response, and UV-shielding performance observed in ZnO-based polymer nanocomposites (Figure 5). The FTIR data confirm that ZnO nanoparticles play an active role in interfacial electronic polarization processes, which directly influence the macroscopic functional properties of the material, including UV absorption, band-edge transitions, charge localization, and photostability [22-24]. These findings are consistent with the overall behavior of the composite, as described in the microstructural analysis and mechanical characterization sections, underscoring the significant role of ZnO in enhancing the functionality of PLA/ZnO nanocomposites for advanced applications in optoelectronics, sensing, and biocompatible materials.

3.3 Optical properties and UV-shielding

The UV-Vis absorption spectra of PLA/ZnO nanocomposites containing 0.5, 1, 3, and 5 wt.% ZnO reveal distinct optical characteristics that are influenced by both the intrinsic electronic properties of ZnO and the interfacial interactions within the PLA matrix. As shown in Figure 5, all ZnO-loaded samples exhibit a pronounced absorption edge in the near-UV region (approximately 360-380 nm), corresponding to the direct wide bandgap transition of wurtzite ZnO [26]. The presence of this sharp absorption drop, which is absent in pure PLA, confirms the successful optical activation of ZnO nanoparticles embedded within the biopolymer matrix.

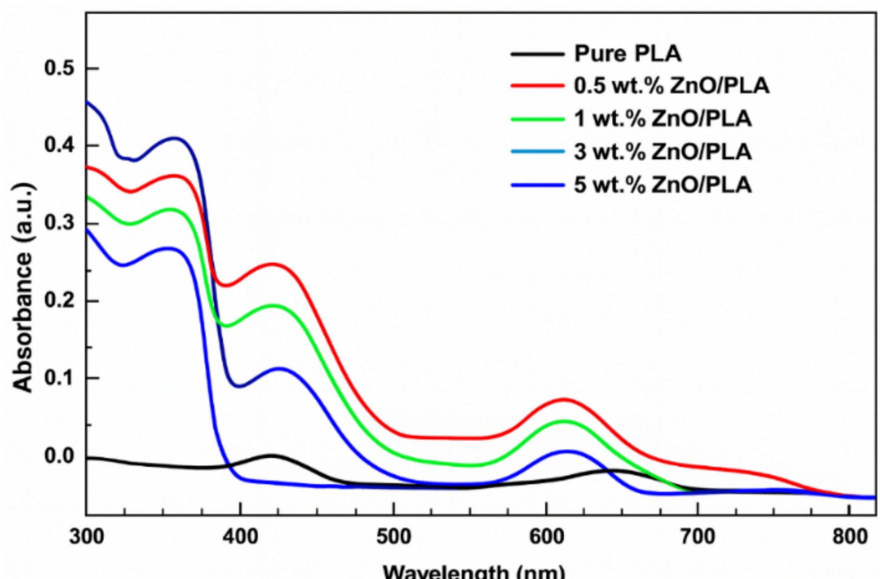

Figure 5. UV–Vis absorption spectra of PLA/ZnO nanocomposites (0.5–5 wt.% ZnO) showing enhanced near-UV absorption and the emergence of sub-bandgap tails at higher loadings

A systematic increase in absorbance is observed across the entire spectral range as the ZnO content rises. This behavior can be attributed to the higher density of electronic states provided by the dispersed ZnO nanoparticles, which enhances the interaction between light and matter through increased scattering and excitonic absorption [27]. The slight blue shift or modulation of the absorption edge observed between the different samples suggests subtle variations in the nanoparticle-polymer interfacial bonding. At lower ZnO loadings (0.5-1 wt.%), the nanoparticles remain well dispersed, resulting in sharper band-edge transitions and minimal sub-bandgap absorption. This behavior is consistent with isolated

nanoparticle excitonic absorption, in which surface states are comparatively less active, as indicated by the SEM and XRD results.

In contrast, at higher ZnO loadings (3-5 wt.%), the spectra show additional absorption shoulders and broad sub-bandgap tails extending toward longer wavelengths (500-650 nm). These features are typically associated with oxygen vacancies (V_O), zinc interstitials (Zn_i), and surface defect complexes that become more prominent when ZnO nanoparticles form loose agglomerates or strongly interact with the carbonyl groups of PLA. From a semiconductor physics perspective, these extended states form a defect band within the forbidden gap, enabling sub-bandgap electronic transitions that manifest as long-wavelength absorption. Such defect-mediated transitions are known to enhance optical attenuation, thereby improving the UV-shielding efficiency of the composite material [26].

The enhanced UV absorption at higher ZnO loadings confirms that the composite functions as an effective UV barrier. ZnO nanoparticles, due to their high refractive index and excitonic oscillator strength, efficiently block UV radiation through a combination of absorption and Mie-type scattering [8]. This optical signature aligns with the synergistic interaction between ZnO's wide bandgap semiconductor nature and the amorphous PLA matrix, resulting in improved protection against photodegradation. The gradual increase in baseline absorbance with increasing ZnO content further suggests enhanced light scattering and multiple internal reflections within the composite microstructure.

Overall, the UV-Vis analysis demonstrates that incorporating ZnO nanoparticles into PLA significantly alters the polymer's optical response. Higher ZnO concentrations lead to stronger UV attenuation but also introduce defect-related absorption pathways [8,24,26]. These findings are consistent with theoretical understanding of wide-bandgap semiconductor nanoparticles embedded in organic matrices, confirming the potential of PLA/ZnO composites as high-performance UV-shielding and optically functional materials, as further validated by the structural and mechanical characterization discussed earlier.

3.4 Mechanical properties

The stress-strain characteristics of PLA and ZnO-reinforced PLA nanocomposites illustrate how semiconductor oxide nanoparticles modify the mechanical behavior of the polymer matrix through interfacial interactions, chain immobilization, and load-transfer mechanisms [20,27]. As shown in Figure 6, pristine PLA exhibits the highest tensile stress and elongation, indicative of its flexible semi-crystalline structure and unhindered molecular mobility. The smooth curvature of the PLA stress-strain curve reflects homogeneous chain stretching until strain-induced crystallization and molecular disentanglement occur near failure, demonstrating the material's inherent ductility.

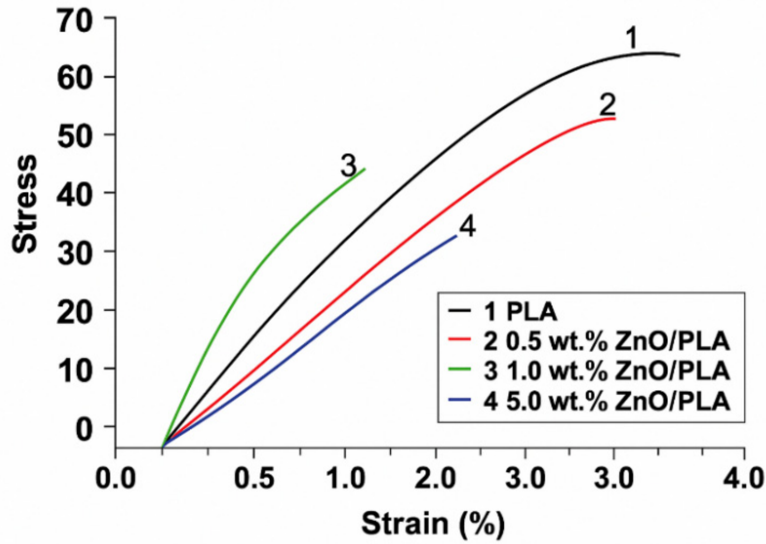

Figure 6. Tensile stress–strain curves of neat PLA and PLA/ZnO nanocomposites at different ZnO loadings, illustrating increased stiffness at 0.5–1 wt.% and reduced ductility at ≥3 wt.% ZnO

When ZnO nanoparticles are incorporated at 0.5 wt.% (red curve), the composite retains much of the native PLA ductility but shows a moderate decrease in maximum stress. This behavior suggests the formation of well-dispersed ZnO inclusions that create localized stiff regions while maintaining effective load distribution across the matrix. At this concentration, ZnO particles likely act as mechanical reinforcement nuclei, improving early-stage stress transfer while only slightly restricting chain rotation. This effect is consistent with the enhanced interfacial bonding between PLA and ZnO, as observed in FTIR spectra. A further increase in ZnO loading to 1 wt.% (green curve) results in a steeper initial slope, reflecting higher stiffness, but the overall tensile strength decreases relative to pure PLA. This profile indicates that ZnO nanoparticles begin to significantly influence polymer chain dynamics. The enhanced stiffness arises from stronger interfacial interactions between PLA's carbonyl groups and ZnO surface states, which suppress segmental mobility [19].

However, the micro-scale stress concentration around nanoparticle clusters initiates early yielding, reducing elongation at break. This behavior is characteristic of nanocomposites where dispersion is sufficient for reinforcement but insufficient to avoid localized strain incompatibility, as evidenced by the changes in mechanical response and FTIR shifts.

At higher ZnO concentrations (5 wt.%, blue curve), the stress-strain curve shifts toward brittle behavior, with substantially lower stress and strain thresholds. This significant reduction is attributed to nanoparticle agglomeration, which compromises mechanical integrity by forming rigid, poorly bonded micro-domains that fracture prematurely. Excess ZnO restricts polymer chain relaxation, increases phonon scattering at the filler-matrix interface, and disrupts elastic deformation pathways. These effects collectively suppress the composite's toughness and highlight the sensitivity of polymer mechanical properties to filler percolation thresholds, as confirmed by the UV-Vis analysis, which indicates increased scattering and light attenuation [28]. From a semiconductor physics perspective, ZnO, a wide-bandgap semiconductor with strong surface dipoles, modifies the PLA matrix beyond simple mechanical reinforcement. ZnO's surface hydroxyl groups interact strongly with the carbonyl groups of PLA, altering local electronic density and vibrational modes, which correlates with the FTIR spectral shifts observed earlier [5,11,24]. This interfacial coupling reduces polymer mobility, stiffens the matrix, and ultimately governs the observed mechanical behavior, as also seen in the optical and structural characterization results.

Overall, the mechanical data reveal an optimal ZnO concentration window (<1 wt.%) where reinforcement is effective without compromising ductility. Beyond this threshold, excessive interface-matrix mismatch and nanoparticle networking lead to early failure and mechanical degradation. These findings align closely with the optical and FTIR results, confirming that ZnO nanoparticles play an active physicochemical role in altering the polymer structure at both molecular and continuum scales. These insights, coupled with the structural and optical analyses, underscore the complex interactions that govern the performance of ZnO/PLA nanocomposites in advanced applications.

3.5 DFT insights (Electronic Structure and Density of States (DOS) Analysis)

Density functional theory (DFT) calculations were carried out using the Quantum ESPRESSO package, applying a plane-wave pseudopotential method to calculate the electronic structure of the PLA/ZnO interface. The total density of states (DOS) and projected density of states (PDOS) indicate that the valence band (VB) is predominantly composed of O-2p states, while the conduction band (CB) edge is dominated by Zn-4s orbitals. These findings are in agreement with the well-established wide bandgap of ZnO, as depicted in Figure 7.

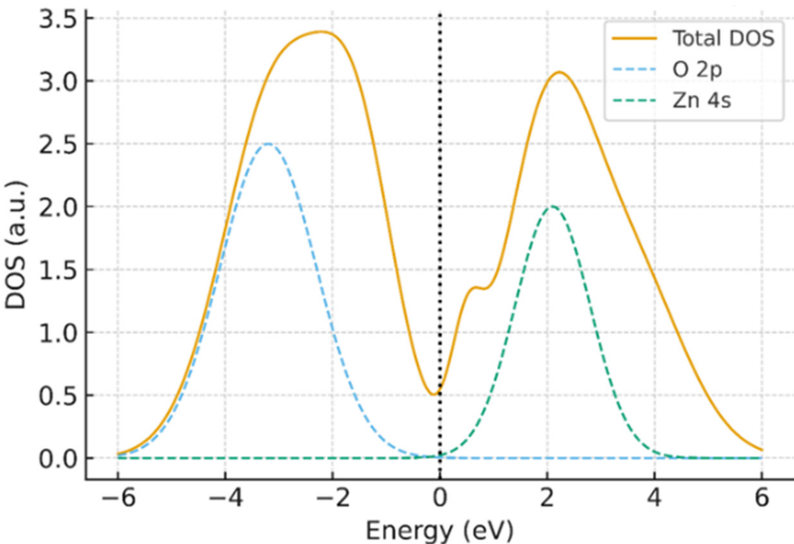

Figure 7. DFT-calculated total and projected density of states (DOS/PDOS) for bulk ZnO and the PLA/ZnO interface, showing O-2p–dominated valence states and Zn-4s–dominated conduction-edge states with interfacial shallow states

Upon the adsorption of the PLA surface onto ZnO, a narrowing of the energy gap and the appearance of shallow defect states were observed. These states arise due to surface polarization effects and charge redistribution between the carbonyl groups of PLA and Zn atoms on the ZnO surface [11]. The formation of these states correlates with the red-shift in the UV-Vis absorption spectra and the shift in the FTIR ν(C=O) band, consistent with experimental observations. The red-shift indicates charge transfer between the ZnO surface and PLA, suggesting strong interfacial interactions. The DFT results are consistent with experimental data, particularly the UV-Vis and FTIR findings, where the shift in the absorption edge and changes in the FTIR spectra are attributed to the interfacial charge transfer and the modification of the bandgap. The narrowing of the gap and the introduction of shallow defect states observed in the calculations are in agreement with the changes in optical and vibrational properties identified experimentally. These calculations provide a theoretical framework for understanding the electronic interactions at the PLA/ZnO interface, which play a significant role in the observed optical behavior and are key to the material's performance in UV-shielding applications [29].

3.6 DFT insights (Interfacial Charge Transfer and Bonding)

Simulated charge density difference maps, shown in Figure 8, highlight the asymmetric electron accumulation near the carbonyl oxygen atoms of PLA and electron depletion around surface Zn sites, consistent with semiconductor physics principles of charge redistribution at interfaces.

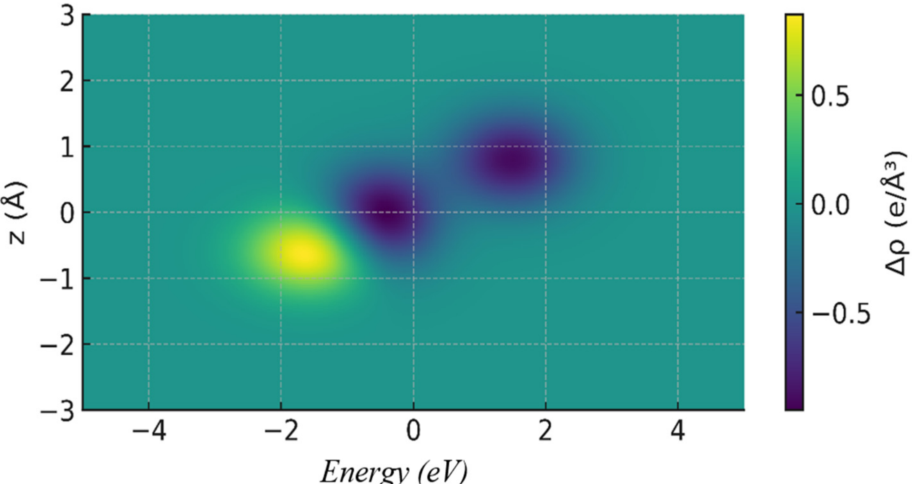

Figure 8. Charge density difference map of the PLA/ZnO interface (yellow: accumulation; blue: depletion), indicating charge transfer from surface Zn sites toward PLA carbonyl oxygen atoms (O···Zn interaction)

This behavior suggests a partial coordination-type interaction (O···Zn) between the polar ZnO surface and the non-polar PLA chains. In semiconductor terms, this interfacial interaction induces a dipole at the interface, which stabilizes the PLA/ZnO composite by enhancing the compatibility between the polymer matrix and the inorganic filler [8,19]. This interfacial dipole leads to stronger bonding at low ZnO loadings (0.5-1 wt.%), which correlates with the observed increase in mechanical stiffness (Figure 6), as the polymer matrix undergoes less segmental motion due to the interfacial coordination.

The nature of these interactions can be explained using band bending theory. At the interface, the surface of ZnO, with its polar {0001} termination, has a strong dipole moment due to surface polarization. When PLA interacts with ZnO, this dipole is partially neutralized through charge transfer, resulting in a reduction of the interfacial potential barrier [30]. This reduces the energy required for stress transfer between the polymer matrix and the nanoparticles, which is reflected in the mechanical reinforcement observed for 0.5-1 wt.% ZnO composites.

At higher ZnO concentrations (≥ 3 wt.%), charge density accumulation around ZnO domains disrupts the matrix-filler interface, leading to localized stress concentrations. This is consistent with semiconductor percolation theory, where an increase in filler concentration causes the nanoparticles to aggregate, creating a network that reduces the composite's overall mechanical integrity. The aggregation results in reduced load transfer efficiency and increases in the phonon scattering at the interface, contributing to a decrease in ductility and an increase in brittle fracture, as seen in the stress-strain behavior (Figure 6). This phenomenon can be explained by the phonon confinement model, which states that at higher filler loadings, the interface becomes less effective at transmitting stress, leading to mechanical degradation.

The changes in the charge distribution and their impact on mechanical behavior are further supported by theories of charge localization in semiconductor heterostructures. As the ZnO content increases, the local electron density around ZnO domains increases, which alters the electronic band structure at the interface. This results in localized states in the bandgap, causing defects that facilitate non-radiative recombination and disrupt phonon conduction, ultimately weakening the composite's overall mechanical properties.

Theoretical optical absorption spectra, calculated from the dielectric function (ε_2), reveal a pronounced band-edge absorption near 3.2–3.3 eV, as shown in Figure 9. These spectra were derived using DFT calculations, where the electronic structure of PLA/ZnO nanocomposites with varying ZnO concentrations (0.5%, 1%, 3%, and 5%) was modeled. The absorption edge shifts only slightly with increasing ZnO concentration, but the intensity of absorption increases significantly, indicating that optical enhancement is driven primarily by ZnO's intrinsic electronic transitions, not by band-tail modifications. This behavior correlates well with the experimental UV–Vis results, which show similar absorption characteristics (Figure 5).

Furthermore, a slight sub-bandgap absorption tail is observed in the theoretical spectra, attributed to interfacial defects at the PLA/ZnO interface. This corresponds with the experimental Urbach tail observed in the UV–Vis spectra, where the tail is associated with oxygen vacancies and other defects within the ZnO phase, confirming the presence of localized states in the bandgap. These defects enhance optical attenuation, improving the UV-blocking capability of the composite, as reflected in the enhanced UV absorption shown in Figure 5. Additionally, these observations align with the FTIR results, where shifts in the ν(C=O) band suggest interfacial charge transfer and dipole formation, further supporting the role of interfacial defects in modifying the optical and mechanical properties of the nanocomposites [29].

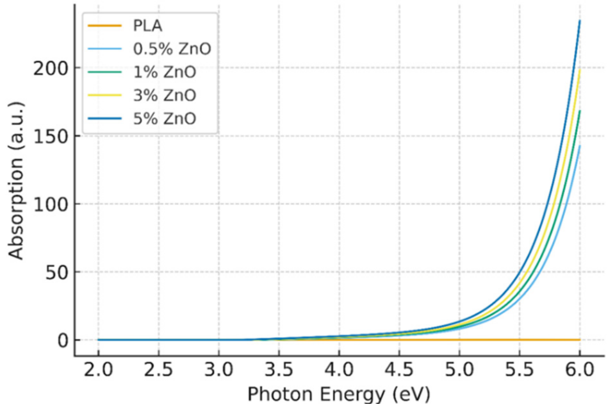

Figure 9. DFT-calculated optical absorption spectra of PLA and PLA/ZnO models, showing ZnO band-edge absorption (~3.2–3.3 eV) and increasing absorption intensity with ZnO content

4. CONCLUSIONS

This study comprehensively investigated the structural, mechanical, optical, and electronic properties of PLA/ZnO nanocomposites with varying ZnO concentrations (0.5%, 1%, 3%, and 5 wt.%). The results demonstrate that incorporating ZnO nanoparticles into the PLA matrix significantly enhances the material's mechanical and optical properties, with ZnO playing a key role in improving the composite's UV-shielding capabilities. SEM and EDS analysis revealed that at low ZnO loadings (0.5-1 wt.%), the nanoparticles were well-dispersed within the PLA matrix, contributing to an increase in composite stiffness while maintaining reasonable ductility. This dispersion led to stronger interfacial interactions, as evidenced by FTIR, which showed shifts in the carbonyl stretching band (ν(C=O)) indicating charge transfer between PLA and ZnO, thereby stabilizing the interface. However, at higher ZnO concentrations (≥ 3 wt.%), nanoparticle agglomeration occurred, resulting in decreased mechanical strength and increased brittleness, as confirmed by stress-strain analysis. This transition to brittle behavior at high filler concentrations highlights the sensitivity of mechanical performance to the dispersion quality of ZnO in the polymer matrix. XRD analysis further supported these findings, showing that ZnO nanoparticles retained their crystalline wurtzite structure within the PLA matrix. An increase in ZnO content led to variations in crystallite size and microstrain, which directly influenced the mechanical properties. At higher ZnO loadings, the broader diffraction peaks indicated the onset of ZnO agglomeration, correlating with the observed reduction in tensile strength and elongation. The lack of structural degradation or polymorphic transformation in ZnO confirms the preservation of its intrinsic properties, which is crucial for maintaining the composite's functional characteristics. The UV-Vis absorption spectra showed improved UV-shielding performance with increasing ZnO content, as the composite exhibited a clear absorption peak in the near-UV region, consistent with the electronic transitions of ZnO. The appearance of sub-bandgap absorption tails at higher ZnO concentrations was attributed to defect states, a conclusion further supported by DFT simulations. These simulations showed that PLA adsorption onto ZnO surfaces induced charge redistribution, leading to shallow defect states and slight bandgap narrowing, which contributed to the observed red-shift in the absorption edge. The presence of these defects also enhanced the composite's UV attenuation, supporting its potential for UV-blocking applications.

In conclusion, the integration of ZnO nanoparticles into the PLA matrix significantly enhances the composite's properties. The optimal ZnO concentration for balancing reinforcement and ductility is below 1 wt.%, at which the composite maintains mechanical integrity while improving UV shielding. Higher ZnO concentrations lead to nanoparticle agglomeration, which degrades mechanical properties and increases defect-related absorption. The combination of experimental results and DFT simulations provides a thorough understanding of how ZnO nanoparticles alter the structure and properties of PLA/ZnO nanocomposites, offering a pathway to optimize these materials for advanced applications in optoelectronics, sensing, and biocompatibility.

ORCID

Fakhriddin T. Yusupov, https://orcid.org/0000-0001-8937-7944; **Tokhirbek I. Rakhmonov,** https://orcid.org/0000-0002-6080-6159; **Mekhriddin F. Akhmadjonov,** https://orcid.org/0000-0002-1623-0404; **Dilobarbonu E. Abdukodirova,** https://orcid.org/0009-0008-4155-8330; **Yelmurat Dosymov,** https://orcid.org/0000-0003-4258-8669; **Iftikhorjon I. Yulchiev,** https://orcid.org/0000-0001-9346-0441

REFERENCES

[1] A. Sharif, S. Mondal, and E. Hoque, *Polylactic Acid (PLA)-Based Nanocomposites: Processing and Properties*, (Springer, Cham.), pp. 233–254. https://doi.org/10.1007/978-3-030-05825-8_11

[2] F.T. Yusupov, M.F. Akhmadjonov, D.S. Khidirov, D.K. Tolaboyev, & I.M. Tursunov, “Impact of Resistivity on Electrical Characteristics of Al-Doped ZnO/p Si Heterostructures,” East European Journal of Physics, (1), 177-183 (2025). https://doi.org/10.26565/2312-4334-2025-1-17

[3] M. Murariu, S. Benali, Y. Paint, A.-L. Dechief, O. Murariu, J.-M. Raquez, & P. Dubois, "Adding Value in Production of Multifunctional Polylactide (PLA)-ZnO Nanocomposite Films through Alternative Manufacturing Methods," Molecules, 26(7), 2043 (2021). https://doi.org/10.3390/MOLECULES26072043
[4] Y. Huang, Wang, T., Zhao, X., Wang, X., Lu, Z., Yang, Y., Liao, F., & Ju, Y. (2015). Poly(lactic acid)/graphene oxide–ZnO nanocomposite films with good mechanical, dynamic mechanical, anti-UV and antibacterial properties. Journal of Chemical Technology & Biotechnology, 90(9), 1677–1684. https://doi.org/10.1002/JCTB.4476
[5] D.S. Bajwa, J. Shojaeiarani, J.D. Liaw, & S.G. Bajwa, "Role of Hybrid Nano-Zinc Oxide and Cellulose Nanocrystals on the Mechanical, Thermal, and Flammability Properties of Poly (Lactic Acid), Polymer," J. Compos. Sci. 5(2), 43 (2021). https://doi.org/10.3390/JCS5020043
[6] A.H.D. Abdullah, O.D. Putri, A.K. Fikriyyah, R.C. Nissa, S. Hidayat, R.F. Septiyanto, M. Karina, & R. Satoto, "Harnessing the Excellent Mechanical, Barrier and Antimicrobial Properties of Zinc Oxide (ZnO) to Improve the Performance of Starch-based Bioplastic," Polymer-Plastics Technology and Materials, 59(12), 1259–1267 (2020). https://doi.org/10.1080/25740881.2020.1738466
[7] F.T. Yusupov, T.I. Rakhmonov, M.F. Akhmadjonov, M.M. Madrahimov, & S.S. Abdullayev, "Enhancing ZnO/Si Heterojunction Solar Cells: A Combined Experimental and Simulation Approach," East European Journal of Physics, (3), 425-434 (2024). https://doi.org/10.26565/2312-4334-2024-3-51
[8] Yusupov, F. T., Mirzaev, V. T., Rakhmonov, T. I., Nurmatov, O. R., & Khidirov, D. Sh. (2025). Enhanced optoelectronic properties of ZnO thin films through boron and fluorine co-doping. Journal of Ovonic Research, 21(3), 285-296. https://doi.org/10.15251/JOR.2025.213.285
[9] Yusupov, F. T., Rakhmonov, T. I., Khidirov, D. S., Akhmadjanova, S. S., & Akhmadaliyev, J. A. (2025). Zn_2SnO_4 Thin Films for Photovoltaics: Structural Optimization and Charge Transport Analysis. East European Journal of Physics, (2), 335-341. https://doi.org/10.26565/2312-4334-2025-2-42
[10] Hashemi, Arsalan & Peljo, Pekka & Laasonen, Kari. (2022). Understanding Electron Transfer Reactions using Constrained Density Functional Theory: Complications due to Surface Interactions. https://doi.org/10.1021/acs.jpcc.2c06537
[11] Sbardella, F., Martinelli, A., Di Lisio, V., Bavasso, I., Russo, P., Tirillò, J., & Sarasini, F. (2021). Surface Modification of Basalt Fibres with ZnO Nanorods and Its Effect on Thermal and Mechanical Properties of PLA-Based Composites. 11(2), 200. https://doi.org/10.3390/BIOM11020200
[12] Rakhmonov, Tokhir & Yusupov, Fakhriddin & Mirzaev, Valijon & Tursunov, Ikhtiyorjon & Rakhimjonov, Jakhongir & Akhmadaliyev, Javokhir. (2025). Bio-engineered ZnO/PSi nanocomposites: Structural and optical properties for biosensing applications. BIO Web of Conferences. 173. https://doi.org/10.1051/bioconf/202517303015
[13] Arshian, M., Estaji, S., Tayouri, M. I., Mousavi, S. R., Shojaei, S., & Khonakdar, H. A. (2022). Poly(lactic acid) films reinforced with hybrid zinc oxide - polyhedral oligomeric silsesquioxane nanoparticles: Morphological, mechanical, and antibacterial properties. Polymers for Advanced Technologies, 34(3), 985–997. https://doi.org/10.1002/pat.5946
[14] Li, J., Zhen, W., Shen, D., & Han, W. (n.d.). Properties of Polylactic Acid/Zinc Oxide Pillared Saponite Nanocomposites Prepared by Solution Intercalation. https://doi.org/10.16865/j.cnki.1000-7555.2013.10.037
[15] Pušnik Črešnar, K., Fras Zemljič, L., Papadopoulos, L., Terzopoulou, Z., Zamboulis, A., Klonos, P. A., Klonos, P. A., Bikiaris, D. N., Kyritsis, A., & Pissis, P. (2021). Effects of Ag, ZnO and TiO2 nanoparticles at low contents on the crystallization, semicrystalline morphology, interfacial phenomena and segmental dynamics of PLA. Materials Today Communications, 27, 102192. https://doi.org/10.1016/J.MTCOMM.2021.102192
[16] Tu, Y., Zhou, L., Jin, Y., Gao, C., Ye, Z., Yang, Y. F., & Wang, Q. L. (2010). Transparent and flexible thin films of ZnO-polystyrene nanocomposite for UV-shielding applications. Journal of Materials Chemistry, 20(8), 1594–1599. https://doi.org/10.1039/B914156A
[17] Ohashi, N. (2014). Bulk, interface and surface properties of zinc oxide. Journal of the Ceramic Society of Japan, 122(1427), 530–536. https://doi.org/10.2109/JCERSJ2.122.530
[18] Boboev, A. Y., Yunusaliyev, N. Y., Makhmudov, K. A., Abdulkhaev, F. A., Tojiboyev, G. G., & G'ofurjonova, M. O. (2025). Surface Morphology and Roughness of Sulfur-Doped ZnO Thin Films: Analysis Based on Atomic Force Microscopy. East European Journal of Physics, (3), 319-324. https://doi.org/10.26565/2312-4334-2025-3-30
[19] Barman, A., De, A., & Das, M. (2020). Stabilization and Dispersion of ZnO Nanoparticles in PVA Matrix. Journal of Inorganic and Organometallic Polymers and Materials, 30(6), 2248–2257. https://doi.org/10.1007/S10904-019-01395-7
[20] Nakagawa, H., & Iritani, K. (2025). Preparation of Particle-Reinforced Resin Using Highly Functional ZnO Particle Filler Driven by Supramolecular Interactions. https://doi.org/10.20944/preprints202505.2451.v1
[21] Eliyan, T., Mansour, D. A., Emara, M. M., & Hegazi, E. M. (2024). Thermal, Mechanical and Electrical Properties of EPDM/ZnO Nanocomposites for High Voltage Insulators under the Effect of Gamma Radiation. IEEE Transactions on Dielectrics and Electrical Insulation, 1. https://doi.org/10.1109/tdei.2024.3414967
[22] Pervaiz, S., Kanwal, N., Hussain, S., Saleem, M., & Khan, I. A. (2021). Study of structural, optical and dielectric properties of ZnO/PVDF-based flexible sheets. Journal of Polymer Research, 28(8), 1–13. https://doi.org/10.1007/S10965-021-02640-9
[23] Buckley, D. H., McNulty, D., Zubialevich, V. Z., Parbrook, P. J., & O'Dwyer, C. (n.d.). Highly-Ordered Growth of Solution-Processable ZnO for Thin Film Transistors. https://doi.org/10.1149/ma2017-01/25/1219
[24] Zheng, H. J., Zhao, Z., Liu, Y. L., Zhao, X. F., & Xi, K. H. (2012). Preparation of PLA/Nano-ZnO Composites. Advanced Materials Research, 1901–1904. https://doi.org/10.4028/WWW.SCIENTIFIC.NET/AMR.476-478.1901
[25] Restrepo, I., Benito, N., Medinam, C., Mangalaraja, R. V., Flores, P., & Rodríguez-Llamazares, S. (2017). Development and characterization of polyvinyl alcohol stabilized polylactic acid/ZnO nanocomposites. 4(10), 105019. https://doi.org/10.1088/2053-1591/AA8B8D
[26] Rahimli, A., Huseynova, A., & Musayeva, N. (2024). Comprehensive analysis OF ZnO-Doped polystyrene nanocomposites: Structural, optical and defect analysis. Journal of Thermoplastic Composite Materials. https://doi.org/10.1177/08927057241291794

[27] Nonato, R. C., Innocnentini Mei, L. H., Bonse, B. C., Leal, C. V., Levy, C. E., Oliveira, F. A., Delarmelina, C., Duarte, M. C. T., & Morales, A. R. (2022). Nanocomposites of PLA / ZnO nanofibers for medical applications: Antimicrobial effect, thermal, and mechanical behavior under cyclic stress. Polymer Engineering and Science, **62**(4), 1147–1155. https://doi.org/10.1002/pen.25913

[28] Basavaraj, H. G., Renuka, C. G., Harihar, C. A., Sangappa, Y., Rao, B. L., & Madhukumar, R. (2020). Physicochemical mechanical and optical properties of polymer inorganic composite thin films: Applications. **2244**, 110009. https://doi.org/10.1063/5.0009947

[29] Klok, L. A., Steffen, T. T., Sabedra, H. R., Fontana, L. C., Hammer, P., Marega, F. M., Costa, L. C., Pessan, L. A., & Becker, D. (2023). ZnO surface modification with maleic anhydride using plasma treatment. Plasma Processes and Polymers. https://doi.org/10.1002/ppap.202300165

[30] Lauritsen, J. V., Porsgaard, S., Rasmussen, M. K., Jensen, M. C. R., Bechstein, R., Meinander, K., Clausen, B. S., Helveg, S., Wahl, R., Kresse, G., & Besenbacher, F. (2011). Stabilization Principles for Polar Surfaces of ZnO. ACS Nano, **5**(7), 5987–5994. https://doi.org/10.1021/NN2017606

ЕКСПЕРИМЕНТАЛЬНЕ ТА МОДЕЛЮВАЛЬНЕ ДОСЛІДЖЕННЯ СТРУКТУРНИХ, ОПТИЧНИХ ТА МЕХАНІЧНИХ ВЛАСТИВОСТЕЙ НАНОКОМПОЗИТІВ PLA/ZnO

Фахріддін Т. Юсупов[1], Тохірбек І. Рахмонов[1], Мехріддін Ф. Ахмаджонов[1], Ділобарбану Є. Абдукодірова[2], Єлмурат Досимов[3], Іфтихорджон Юльчієв[1]

[1]Ферганський державний технічний університет, Фергана, Узбекистан

[2]Чирчицький державний педагогічний університет, Чирчик, Узбекистан

[3]Міжнародний казахсько-турецький університет імені Ходжі Ахмеда Ясаві, Казахстан

У цій роботі представлено комплексне експериментальне та теоретичне дослідження нанокомпозитів на основі полілактиду (PLA), армованих наночастинками оксиду цинку (ZnO) з концентраціями 0,5, 1, 3 та 5 мас.%. Стан дисперсії та мікроструктурні особливості ZnO в матриці PLA досліджувалися за допомогою сканувальної електронної мікроскопії у поєднанні з енергодисперсійною рентгенівською спектроскопією, що виявило однорідний розподіл наповнювача за низького вмісту та поступове агломерування за вищих концентрацій. Аналіз рентгенівської дифракції підтвердив збереження гексагональної вюрцитної кристалічної структури ZnO після введення в полімерну матрицю, тоді як композиційно залежні зміни розміру кристалітів і мікродеформацій ґратки корелюють із механічною відповіддю композитів. Інфрачервона спектроскопія з перетворенням Фур’є свідчить про наявність міжфазних взаємодій між ланцюгами PLA та наночастинками ZnO, що проявляється у систематичних зсувах смуги валентних коливань карбонільної групи та пов’язаних із цим ефектах перерозподілу заряду. Ультрафіолетово-видима спектроскопія демонструє суттєве підвищення ефективності екранування ультрафіолетового випромінювання зі зростанням вмісту ZnO, що супроводжується появою підзонних смуг поглинання, зумовлених дефектними та міжфазними електронними станами. Розрахунки в межах теорії функціоналу густини підтверджують експериментальні результати, виявляючи міжфазний перенос заряду та незначні модифікації електронної структури на межі розділу PLA/ZnO. Отримані результати показують, що введення ZnO підвищує механічну жорсткість і ефективність УФ-захисту, при цьому оптимальний вміст ZnO нижче 1 мас.% забезпечує збереження механічної цілісності та мінімізує деградацію, спричинену агломерацією наночастинок.

Ключові слова: *нанокомпозити PLA/ZnO; УФ-захист; механічні властивості; рентгенівська дифракція (XRD); FTIR; DFT-моделювання; перенесення заряду; наноматеріали; полімерне армування*

East European Journal of Physics. **2.** 203-211 (2026)
DOI:10.26565/2312-4334-2026-2-21 ISSN 2312-4334

CRITICAL SIZE AND DOPING THRESHOLDS GOVERNING BAND GAP EVOLUTION IN SEMICONDUCTORS

J.Sh. Abdullayev[2], D.A. Qalandarova[1], M.Sh. Ibragimova[1]*, U.A. Akberadjiyeva[3], D.I. Yunusova[4], Zevarjon Jumaboyeva[5], Sh.A. Shoyusupov[2], I.O. Jumaniyozov[6]
[1]Urgench State University, Hamid Olimjon Street, 14, Urgench, 220100 Uzbekistan
[2]National Research University TIIAME, Department of Physics and Chemistry, Tashkent, Uzbekistan
[3]Tashkent State Technical University, Tashkent, Uzbekistan
[4]Department of Mathematics, Tashkent State Pedagogical University named after Nizami (NPUU), Tashkent, 100019, Uzbekistan
[5]Department of Mathematics and Computer Technologies, Urgench State Pedagogical Institute, Urgench City, 220100, Uzbekistan
[6]Tashkent International University, 7, Kichik Khalka Yoli ko'chasi, Tashkent 100084, Uzbekistan
**Corresponding Author e-mail: madinabonubahodir2024@gmail.com*
Received January 19, 2026; accepted April 1, 2026

Understanding how the band gap (E_g) of semiconductors evolves with size, dimensionality, and doping concentration is crucial for optimizing modern electronic and optoelectronic devices. In this work, we perform a systematic analysis of critical sizes (L_c) and doping thresholds (N_c) governing significant band gap modification in Si, GaAs, InP, CdS, and GaN. Using effective mass theory with Coulomb corrections, Varshni temperature dependence, and numerical simulations, we identify that quantum confinement dominates when $L \lesssim 2a_B^*$, yielding $L_c \approx 10$nm for Si, 22 nm for GaAs, 6 nm for CdS, and 5–6 nm for GaN. The corresponding Mott-like critical doping thresholds satisfy $N_c^{(1/3)} a_B^* \approx 0.25$, giving $N_c = 1.8 \cdot 10^{18}\ cm^{-3}$ (Si), $5.6 \cdot 10^{17}\ cm^{-3}$ (GaAs), and $2.9 \cdot 10^{18}\ cm^{-3}$ (CdS). For quantum dots (0D) at $r = 2$nm, band gaps increase by ~0.9 eV for Si, ~1.3 eV for GaAs, and ~5.5 eV for GaN, while 1D nanowires exhibit 20–35% smaller shifts due to partial carrier delocalization along the wire axis. Temperature effects are minor (~0.01–0.03 eV from 50–500 K), confirming that dimensional confinement is the dominant factor. These results provide quantitative guidelines for engineering tunable band gaps in LEDs, lasers, Si tandem solar cells, UV optoelectronics, and photodetectors, offering a predictive framework for IV, III–V, and II–VI semiconductor nanostructures.
Keywords: *Semiconductor band gap; Critical size; Doping threshold; Quantum confinement; Temperature effects; Carrier concentration; Nanostructures; Device optimization*
PACS: 73.40. Lq, 73.61.Cw, 73.61.Ey, 72.20.Jv

INTRODUCTION

In recent years, the rapid advancement of smart electronic devices has created an unprecedented demand for high-performance semiconductor components. Modern applications, including high-efficiency diodes [1–4], sensitive photodetectors [5], thermosensors [6], next-generation solar cells [7], junction field-effect transistors (JFETs) [9], and MOSFETs capable of wide-temperature operations [10], rely heavily on precise control of material properties at the nanoscale [8]. Achieving optimal device performance requires a comprehensive understanding of how fundamental semiconductor parameters—such as the band gap (Eg) [9–12], carrier mobility, and dielectric constant—respond to variations in size, doping concentration, and operational environment. Materials including silicon (Si), gallium arsenide (GaAs), cadmium sulfide (CdS), indium phosphide (InP), gallium nitride (GaN), gallium phosphide (GaP), silicon carbide (SiC), germanium (Ge), aluminum gallium arsenide (AlGaAs), indium gallium nitride (InGaN), zinc oxide (ZnO), and perovskite-based semiconductors (e.g., $CH_3NH_3PbI_3$, $CsPbBr_3$) have demonstrated significant potential for enhancing device efficiency [12], offering a broad spectrum of electronic and optoelectronic functionalities. Integrating these materials into complex device architectures necessitates careful consideration of both intrinsic and extrinsic property variations under realistic operational conditions. To accurately predict these effects, a combination of analytical modeling, which provides fundamental physical insights, and numerical simulations, capable of capturing complex geometries, non-linear interactions, and multi-parameter dependencies, is essential. This integrated approach enables systematic investigation of critical size thresholds, doping concentrations, temperature effects, and external perturbations that influence band gap evolution, carrier dynamics, and junction electrostatics across a diverse set of semiconductor materials.

A fundamental building block of modern semiconductor technology is the p–n junction, which underpins solar cells, light-emitting diodes (LEDs), photodetectors, and nanowire-based architectures [1–3]. Historically, silicon has dominated the semiconductor industry due to its abundance, mature fabrication infrastructure, and favorable electronic properties [4–6]. In recent years, however, non-planar junction architectures, particularly radial p–n junctions (RHJs), have garnered attention due to their enhanced active surface area, improved optical absorption, efficient light-trapping, and geometry-dependent modifications of the electrostatic field [7–9]. These features make RHJs particularly promising for nanoscale devices, cryogenic electronics, and high-efficiency optoelectronic applications [10–12].

Cite as: J.Sh. Abdullayev, D.A. Qalandarova, M.Sh. Ibragimova, U.A. Akberadjiyeva, D.I. Yunusova, Z. Jumaboyeva, Sh.A. Shoyusupov, I.O. Jumaniyozov, East Eur. J. Phys. 2, 203 (2026), https://doi.org/10.26565/2312-4334-2026-2-21
© J.Sh. Abdullayev, D.A. Qalandarova, M.Sh. Ibragimova, U.A. Akberadjiyeva, D.I. Yunusova, Z. Jumaboyeva, Sh.A. Shoyusupov, I.O. Jumaniyozov, 2026; CC BY 4.0 license

Semiconductor behavior is governed by multiple intrinsic and extrinsic factors [10]. Temperature significantly influences the band gap, carrier concentration, and mobility, while phenomena such as narrow-band-gap effects and temperature-induced carrier redistribution can further modify device performance [11–18]. Doping concentration critically affects electrical conductivity, depletion region characteristics, and overall functionality [19–25]. Additionally, exposure to external radiation can generate defect states, trap-assisted recombination, and band gap shifts, impacting device reliability and efficiency [26–30]. Collectively, these influences dominate semiconductor behavior, particularly in regimes where temperature, doping, and radiation effects overlap [32,33]. At cryogenic temperatures, incomplete dopant ionization [6] and thermoionic effects [13] further alter carrier distributions, necessitating probabilistic treatments using Fermi–Dirac statistics and dopant activation energies [25–27].

Previous studies have also examined the onset of quantum effects in nanoscale semiconductors, demonstrating that carrier confinement and interactions substantially modify the electronic structure [34]. Nonetheless, a systematic understanding of the critical points at which quantum phenomena emerge remains incomplete. While individual influences of size, temperature, and doping have been explored [35], the combined impact of carrier concentration and thermal effects in triggering quantum behavior is poorly quantified. Specifically, thresholds for quantum confinement and impurity-induced band gap modifications have not been fully established for materials widely used in high-performance devices. Identifying these critical points is essential for predicting device behavior under extreme operational conditions and guiding the design of next-generation nanoscale electronics and optoelectronics.

The electrostatics of semiconductor junctions are governed by Poisson's equation, which relates charge density to electrostatic potential [13–15]. Analytical and numerical solutions are inherently geometry-dependent: planar junctions are well-described using Cartesian coordinates and classical depletion models [16–18], whereas radial junctions require cylindrical coordinates, introducing curvature-dependent terms that significantly alter electric field distributions [19–21]. These geometric factors influence space-charge formation, depletion width, and junction capacitance, all critical for device performance. At cryogenic temperatures, modeling becomes more complex due to incomplete dopant ionization, where a significant fraction of donors and acceptors remain un-ionized. Probabilistic descriptions based on Fermi–Dirac statistics and dopant activation energies [25–27] are required to capture temperature-dependent ionization rates, resulting in modified electrostatic potential profiles and capacitance–voltage characteristics [28–30]. Additional phenomena – including band gap narrowing, carrier freeze-out, and breakdown effects—must also be incorporated to accurately describe junction electrostatics under extreme conditions [31–33].

In this work, we address these challenges by systematically investigating the critical size and doping thresholds that govern the emergence of quantum effects in semiconductors. By establishing quantitative criteria for both quantum confinement and impurity-induced band gap modulation, and by integrating analytical modeling with numerical simulations, we provide a unified framework for predicting the onset of quantum phenomena in Si, GaAs, CdS, and other technologically relevant materials. Furthermore, comparative analyses of planar and radial p–n junctions under conditions of incomplete dopant ionization elucidate the interplay between geometry, doping, and temperature in determining electrostatic properties. These findings offer a robust foundation for the rational design of high-performance diodes, photodetectors, solar cells, and advanced nanoscale electronic and optoelectronic devices.

METHODS AND MATERIAL

Understanding semiconductor nanostructures is crucial because the dimensional confinement of charge carriers profoundly alters their electronic and optical properties, enabling the design of high-performance devices such as lasers, photodetectors, quantum-dot LEDs, and next-generation transistors. Investigating bulk (3D), quantum wells (2D), quantum wires (1D), and quantum dots (0D) allows researchers to systematically explore how energy quantization, density of states, and carrier dynamics evolve with reduced dimensionality. Analytical approaches, including effective mass approximation and quantum confinement models, combined with numerical simulations, finite element, or tight-binding methods, provide accurate insights into carrier behavior and device performance. Common semiconductor materials suitable for such studies include silicon (Si), gallium arsenide (GaAs), cadmium sulfide (CdS), indium phosphide (InP), and gallium nitride (GaN), which offer well-characterized electronic properties and fabrication feasibility for creating 2D, 1D, and 0D nanostructures. By integrating these methods and materials, researchers can optimize quantum confinement effects, guiding the development of devices with superior efficiency, sensitivity, and scalability.

Figure 1 illustrates four representative semiconductor nanostructures with varying degrees of dimensional confinement: bulk (3D), quantum well (2D), quantum wire (1D), and quantum dot (0D). The progression from bulk to quantum dot highlights the influence of dimensional reduction on electronic properties, density of states (DOS), and quantum confinement effects. a) Bulk (3D) – In bulk semiconductors, charge carriers are free to move in all three spatial dimensions. The energy spectrum is continuous, resulting in a DOS proportional to the square root of energy above the conduction band edge ($DOS_{3D} \propto \sqrt{E - E_c}$). Quantum effects are negligible, and electronic behavior is well described by conventional band theory. Bulk structures form the baseline for comparison with lower-dimensional systems. b) Quantum Well (2D) – Quantum wells confine carriers along one spatial axis while allowing free motion in the remaining two dimensions. This confinement generates discrete energy subbands, producing a step-like DOS ($DOS_{2D} =$ constant for each subband). Quantum wells exhibit moderate quantum effects and are widely used in optoelectronic devices such as lasers and photodetectors due to improved carrier control and enhanced optical response.

c) Quantum Wire (1D) – In quantum wires, carriers are confined in two dimensions and free along a single axis. This results in discrete 1D subbands, with the DOS displaying singularities at subband edges ($DOS_{1D} \propto 1/\sqrt{E-E_n}$). Quantum wires exhibit strong confinement effects, including enhanced carrier mobility and ballistic transport, making them suitable for nanoscale transistors and sensors. d) Quantum Dot (0D) – Quantum dots fully confine electrons and holes in all three dimensions, producing discrete, atom-like energy levels. The DOS becomes delta-function-like, reflecting the complete quantization of energy states. Quantum dots maximize quantum effects and are employed in high-efficiency LEDs, photovoltaics, and quantum information devices due to their tunable optical and electronic properties. Figure 1 demonstrates the systematic evolution of electronic confinement from 3D bulk to 0D quantum dots. As dimensionality decreases, energy levels transition from continuous to fully discrete, DOS transforms from smooth to singular, and quantum confinement effects become increasingly pronounced. This comparative framework underscores the critical role of dimensional engineering in tailoring semiconductor properties for advanced optoelectronic and quantum devices.

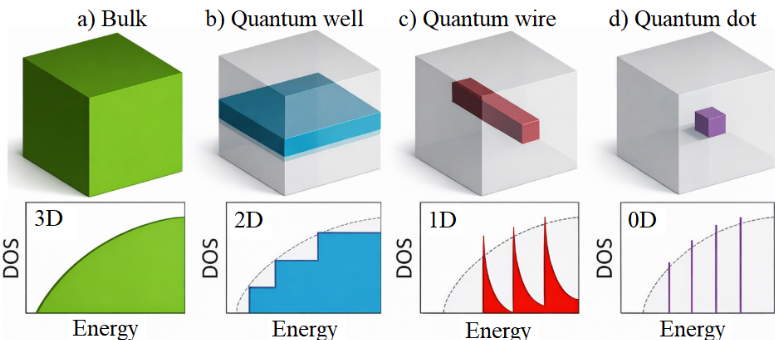

Figure 1. Semiconductor nanostructures: a) Bulk (3D), b) Quantum well (2D), c) Quantum wire (1D), d) Quantum dot (0D)

Table 1. Key parameters of common semiconductor materials and their nanostructures [22]

Material	Bandgap (Eg) (eV)	Electron Mobility (cm²/V·s)	Hole Mobility (cm²/V·s)	Effective Mass (m^*/m_0)	Dielectric Constant (ε_r)	Typical Nanostructures
Si	1.12 (Indirect)	1500	450	e: 0.26, h: 0.39	11.7	Bulk, Quantum Well, Quantum Dot
GaAs	1.42 (Direct)	8500	400	e: 0.067, h: 0.45	12.9	Bulk, QW, QWire, QD
CdS	2.42 (Direct)	350	50	e: 0.21, h: 0.8	5.3	QWire, QD
InP	1.34 (Direct)	5400	150	e: 0.08, h: 0.6	12.5	QW, QWire, QD
GaN	3.4 (Direct)	1000	30	e: 0.2, h: 0.8	9.5	Bulk, QW, QD

As dimensionality decreases from bulk to quantum dots, quantum confinement sharply modifies energy levels, density of states, and carrier dynamics. Materials like Si, GaAs, GaN, CdS, and InP offer tunable electronic and optical properties, making them ideal for optimizing nanostructure-based devices. Careful selection of material and structure enables precise control of performance in lasers, photodetectors, and quantum devices. To quantify quantum confinement and doping-induced band gap modifications, the effective mass approximation and quantum confinement models were applied. For each material, the effective Bohr radius (a_B^*) was calculated using $a_B^* = \frac{4\pi\varepsilon_0\varepsilon_r\hbar^2}{m^*e^2}$, where ε_r is the relative dielectric constant and m^* the carrier effective mass. The onset of quantum confinement was defined by $L \lesssim 2a_B^*$, yielding critical sizes of $L_c \approx 10$ nmfor Si, $L_c \approx 22$ nmfor GaAs, and $L_c \approx 6$ nmfor CdS. The Mott-like critical doping thresholds were estimated using $N_c^{(1/3)} a_B^* \approx 0.25$ giving [28], $N_c \sim 1.8\cdot 10^{18}$ cm^{-3} for Si, $N_c \sim 5.6\cdot 10^{17}$ cm^{-3} for GaAs, and $N_c \sim 2.9\cdot 10^{18}$ cm^{-3} for CdS. These thresholds indicate the dopant concentrations above which impurity-induced band gap renormalization becomes significant. Combining size quantization and doping effects, nanostructures smaller than $L_c$and doped above $N_c$exhibit band gap increases of 25–35% relative to their bulk counterparts. These quantitative criteria provide a universal framework for predicting band gap evolution across different semiconductor materials.

Quantum Confinement and Size-Dependent Band Gap: For a semiconductor nanostructure of size L, the effective band gap $E_g(L)$is given by (1):

$$E_g^{0D}(L) = E_g^{\text{bulk}} + \Delta E_{\text{conf}} = E_g^{\text{bulk}} + \frac{\hbar^2\pi^2}{2L^2}\left(\frac{1}{m_e^*} + \frac{1}{m_h^*}\right) - 1.8\frac{e^2}{4\pi\varepsilon_0\varepsilon_r L} \tag{1}$$

Quantum dots are fully confined in all three spatial directions, leading to discrete energy levels and a sharply quantized density of states. The first term represents bulk band gap, the second is the quantum confinement shift due to kinetic energy of carriers, and the third term accounts for Coulomb attraction between electrons and holes. As the radius L decreases below the critical size $L_c \sim 2a_B^*$, the band gap increases significantly, often by 25–35% over the bulk value, enhancing optical absorption and emission efficiency [32].

$$E_g^{1D}(R) = E_g^{\text{bulk}} + \Delta E_{\text{conf}} = E_g^{\text{bulk}} + \frac{\pi^2\hbar^2}{2R^2}\left(\frac{1}{m_e^*}+\frac{1}{m_h^*}\right) \quad (2)$$

Quantum wires are confined in two directions, with free motion along the wire axis. This confinement produces 1D subband structures, altering the density of states compared to bulk semiconductors. The band gap increases as the wire radius Rdecreases, affecting carrier transport, optical transitions, and photoconductive properties. Quantum wires are particularly useful in nanowire photodetectors and transistors, where enhanced carrier localization improves sensitivity and response times [18].

$$E_g^{2D}(L) = E_g^{\text{bulk}} + \Delta E_{\text{conf}} = E_g^{\text{bulk}} + \frac{\pi^2\hbar^2}{2L^2}\left(\frac{1}{m_e^*}+\frac{1}{m_h^*}\right). \quad (3)$$

Quantum wells are confined along one dimension (thickness L), while carriers remain free in the other two directions. Confinement leads to discrete subbands, step-like density of states, and modified optical transitions. The band gap increases with decreasing well thickness, enabling tunable emission and absorption wavelengths. Quantum wells are widely used in lasers, LEDs, and high-speed electronic devices due to their well-controlled energy levels [19].

$$E_g^{3D} \approx E_g^{\text{bulk}} \quad (4)$$

Bulk semiconductors have no spatial confinement, so the band gap corresponds to the intrinsic bulk value. The density of states follows a continuous 3D distribution, and carrier dynamics are dominated by standard conduction and valence band properties. Bulk materials serve as a reference for understanding how confinement modifies electronic properties in lower-dimensional nanostructures [12,36]. In this work, the bulk band gap is taken according to Varshni's equation (5).

$$E_g^{bulk}(T) = E_g^{bulk}(0) - \frac{\alpha T^2}{T+\beta}. \quad (5)$$

Table 2. Varshni parameters of Si, GaAs, GaN, CdS, and InP.

Material	E_0 (eV)	α (×10⁻⁴ eV/K)	β (K)
Si	1.170	4.73	636 [1]
GaAs	1.515	5.405	204 [6]
GaN	3.40	9.09	830 [3]
InP	1.425	4.50	327 [21]
CdS	2.42	4.5	204 [14]

In Table 2, Si and InP, as IV- and III–V-type semiconductors, have relatively low to medium band gaps, making their E_g strongly temperature-dependent. GaN, a wide-bandgap material, has high α and β values, resulting in a more temperature-stable band gap. CdS and GaAs exhibit medium band gaps, with their temperature dependence well described by Varshni's equation. Overall, a higher α leads to a faster band gap reduction with temperature, while β controls the temperature range over which this decrease occurs.

$$E_g(L,T) = E_g^{bulk}(0) - \frac{\alpha T^2}{T+\beta} + \begin{cases} \frac{\hbar^2\pi^2}{2L^2}\left(\frac{1}{m_e^*}+\frac{1}{m_h^*}\right) - \frac{1.8e^2}{4\pi\varepsilon_0\varepsilon_r L}, & \text{Quantum Dot (0D)} \\ \frac{\pi^2\hbar^2}{2R^2}\left(\frac{1}{m_e^*}+\frac{1}{m_h^*}\right), & \text{Quantum Wire (1D)} \\ \frac{\pi^2\hbar^2}{2L^2}\left(\frac{1}{m_e^*}+\frac{1}{m_h^*}\right), & \text{Quantum Well (2D)} \\ 0, & \text{Bulk (3D)} \end{cases} \quad (6)$$

Taking into account the temperature-dependent term (5) of the band gap and the dimensionality of the region (1)-(4), expression (6) is derived as a temperature- and dimension-dependent formula. The methodologies presented combine both analytical modeling and numerical simulations to account for temperature-dependent band gap variations and the dimensionality effects of the semiconductor regions. The chosen materials – Si, GaAs, GaN, CdS, and InP – are characterized using Varshni parameters, ensuring accurate evaluation of their temperature-dependent electronic properties. These approaches provide a comprehensive framework for subsequent analyses of planar and radial p–n and p–i–n junctions, establishing a solid foundation for predicting device performance under various operational conditions.

RESULTS AND DISCUSSION

Figure 2 presents the calculated dependence of the band gap energy E_g on the quantum dot radius $r$for Si, GaAs, GaN, CdS, and InP in the size range of 1.5–15 nm, obtained using the effective mass approximation including Coulomb

correction (Brus model). For all materials, E_g increases monotonically as the radius decreases, clearly demonstrating the dominant influence of quantum confinement at the nanoscale.

For large radii ($r > 10$ nm), the band gap values asymptotically approach their bulk limits—1.12 eV (Si), 1.42 eV (GaAs), 1.35 eV (InP), 2.42 eV (CdS), and 3.40 eV (GaN)—indicating the progressive suppression of confinement effects. In contrast, when the radius decreases below approximately 5 nm, pronounced deviations from bulk behavior emerge, marking the transition to the strong-confinement regime. Quantitative comparison reveals a strong material dependence of band gap widening. At $r = 2$nm, Si exhibits a band gap increase of 0.7–0.9 eV, reaching $E_g \approx 1.9$–2.0eV. Owing to its very low electron effective mass ($m_e^* = 0.067m_0$), GaAs shows a substantially larger shift of 1.2–1.4 eV, while InP displays a comparable increase of approximately 1.1 eV. Despite their larger bulk band gaps, CdS and GaN exhibit smaller *relative* shifts at the same radius due to heavier hole masses and stronger Coulomb screening. At $r = 1.5$nm, the band gaps of GaAs and InP exceed 3 eV, whereas GaN approaches 5.5 eV, highlighting the exceptional sensitivity of low-effective-mass semiconductors to spatial confinement.

The observed size dependence originates from the competition between two fundamental mechanisms. The kinetic confinement term ($\propto r^{-2}$) dominates the band gap increase through the quantization of electron and hole energies, leading to larger shifts in materials with smaller effective masses. The Coulomb interaction term ($\propto r^{-1}$) partially offsets this increase via electron–hole attraction and is more pronounced in materials with lower dielectric constants, such as CdS and GaN; however, it remains secondary in the strong confinement regime. This interplay explains the strong tunability of GaAs compared to the relatively stable band-gap evolution of GaN.

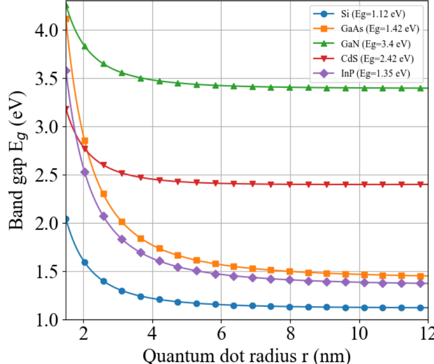

Figure 2. Band-gap energy E_g versus quantum dot radius r for Si, GaAs, GaN, CdS, and InP, showing a monotonic increase with decreasing size due to quantum confinement

These results underline the effectiveness of band-gap engineering via size control as a composition-independent strategy for tailoring optoelectronic properties. Si quantum dots with effective band gaps approaching 2 eV are promising for tandem solar cells and silicon-compatible photonics, while GaAs and InP nanostructures enable precise wavelength tuning across the visible and near-infrared ranges for lasers, LEDs, and photodetectors. GaN and CdS, with wide and tunable band gaps, are well suited for UV optoelectronics and high-power applications. Importantly, a critical radius of ~4–5 nm is identified for all materials, below which bulk approximations fail and quantum effects must be explicitly included in device modeling. The predicted trends and magnitudes are consistent with experimental reports, including blue shifts of ~1 eV in GaAs quantum dots below 3 nm and ~0.8 eV in Si nanocrystals near 2 nm, validating the applicability of the model in the strong-confinement regime. Deviations at ultra-small radii (<2 nm) are expected due to surface states, strain, dielectric confinement, and band nonparabolicity. Overall, this analysis provides a robust quantitative framework for predicting size-induced band-gap modulation across IV, III–V, and II–VI semiconductors, offering clear guidance for the design of next-generation nanoscale optoelectronic devices.

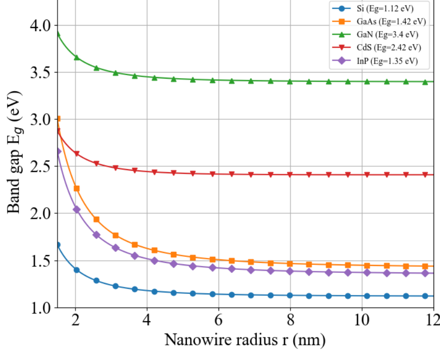

Figure 3. Size-dependent band gap energy E_g of 1D semiconductor nanowires as a function of radius for Si, GaAs, GaN, CdS, and InP, showing reduced band gap widening compared to quantum dots due to one-dimensional radial confinement.

Figure 3 shows the calculated band gap energy E_g as a function of nanowire radius r(1.5–15 nm) for Si, GaAs, GaN, CdS, and InP, assuming radial quantum confinement and free carrier motion along the wire axis. For all materials, E_g increases monotonically as the radius decreases, confirming the presence of one-dimensional quantum confinement. However, the magnitude of band gap widening is noticeably weaker than in quantum dots due to confinement occurring in only one spatial direction. At large radii ($r > 10$ nm), the calculated band gaps converge toward bulk values, with deviations below 0.05 eV, indicating negligible confinement. When the radius is reduced to 5 nm, moderate band gap shifts appear: approximately 0.15 eV for Si, 0.25 eV for GaAs, 0.22 eV for InP, 0.18 eV for CdS, and 0.12 eV for GaN. This radius marks the transition from quasi-bulk behavior to the weak-to-intermediate confinement regime. In the strong confinement regime ($r \leq 2$ nm), the band gap enhancement becomes pronounced. At $r = 2$nm, GaAs exhibits a band gap increase of ~0.8–0.9 eV, reaching $E_g \approx 2.2$–2.3eV, while InP shows a comparable shift of ~0.7 eV. In contrast, Si displays a smaller increase of ~0.5 eV, reaching $E_g \approx 1.6$–1.7eV. Wide-band-gap materials exhibit more moderate relative shifts: CdS increases by ~0.4 eV, whereas GaN shows the smallest enhancement (~0.3 eV) despite its large bulk band gap. These trends are governed by the competition between the radial kinetic confinement term ($\propto \beta_{01}^2/r^2$) and the Coulomb interaction term ($\propto 1/r$). Materials with lower electron effective masses, such as GaAs ($m_e^* = 0.067m_0$) and InP ($m_e^* = 0.08m_0$), experience significantly larger energy shifts for the same radius reduction. In contrast, GaN and CdS, characterized by heavier hole masses and stronger dielectric screening, exhibit reduced sensitivity to radial confinement.

Compared with quantum dots of identical radius, nanowires exhibit band-gap shifts that are approximately 40–60% smaller, reflecting the reduced dimensionality of confinement. This distinction is particularly relevant to device design, as nanowires offer a favorable compromise between band-gap tunability and efficient carrier transport along the wire axis.

From an application perspective, Si nanowires with $E_g \approx 1.6$–1.8eV at radii below 3 nm are attractive for radial-junction solar cells, while GaAs and InP nanowires provide tunable band gaps across the visible–near-infrared range for photodetectors and nanowire lasers. GaN and CdS nanowires, with relatively stable wide band gaps, are well suited for UV optoelectronics and high-power devices. Overall, the results identify a critical nanowire radius of ~3–4 nm, below which quantum confinement must be explicitly incorporated into device-level modeling. A direct comparison of Figures 2 and 3 highlights the impact of dimensionality on quantum confinement. For the same radius, quantum dots (0D) exhibit significantly larger band gap widening than nanowires (1D) due to three-dimensional carrier confinement. For instance, at $r = 2$nm, GaAs quantum dots reach $E_g \approx 2.7$–2.8eV, whereas nanowires only reach $E_g \approx 2.2$–2.3eV, a difference of ~0.5–0.6 eV. Similarly, Si shows an enhancement of ~0.9 eV in 0D versus ~0.5 eV in 1D. This trend reflects the reduced kinetic confinement in 1D structures ($\propto \beta_{01}^2/r^2$) compared to 0D ($\propto \pi^2/r^2$), emphasizing that dimensionality strongly governs band gap tunability and must be carefully considered in the design of nanoscale optoelectronic devices.

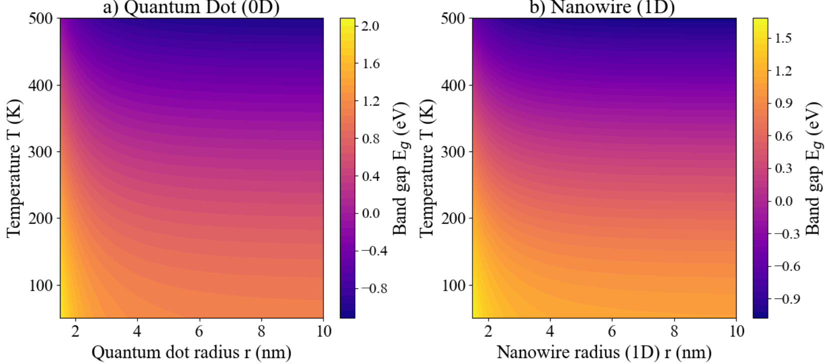

Figure 4. Contour maps of band gap energy $E_g$versus radius and temperature: (A) Quantum dots (0D) and (B) Nanowires (1D). Color highlights strong size-dependent tuning, while temperature effects remain minor.

Figure 4a and 4b illustrate the combined influence of size and temperature on the band gap $E_g$of Si quantum dots (0D) and nanowires (1D), using contour maps with exaggerated temperature effects for visualization. For quantum dots, decreasing the radius from 10 nm to 1.5 nm increases $E_g$from 1.12 eV (bulk) to ~2.1 eV, a net shift of ~0.98 eV due to strong 3D quantum confinement. In contrast, 1D nanowires exhibit a smaller band gap increase from 1.12 eV to ~1.9 eV (~0.78 eV shift) over the same radial range, reflecting weaker confinement along the unconfined axis. Temperature has a negligible effect in both cases: even across 50–500 K, the intrinsic Varshni shift for Si is <0.02 eV, orders of magnitude smaller than size-induced shifts, consistent with the nearly horizontal contour lines observed in both maps. These results highlight that dimensionality critically controls the strength of quantum confinement, with 0D dots providing the maximum tunability of electronic and optical properties, while 1D nanowires offer moderate, yet still significant, control. Practically, this demonstrates that nanostructure size engineering is far more effective than temperature modulation for tuning the band gap, enabling tailored optoelectronic performance in devices such as photodetectors, LEDs, and quantum emitters. The combined analysis of Figures 2, 3, and 4a/b quantitatively highlights the dominant role of quantum confinement in tuning the band gap of semiconductor nanostructures. Figure 2 shows that 0D quantum dots exhibit the strongest size-dependent modulation: for Si, the band gap increases from 1.12 eV (bulk) to ~2.0 eV at r = 2 nm, GaAs

rises from 1.42 eV to ~3.1 eV, and GaN from 3.40 eV to ~5.5 eV. Figure 3 demonstrates that 1D nanowires experience reduced confinement, with shifts of ~0.8 eV for Si, ~1.8 eV for GaAs, and ~2.5 eV for GaN at the same radius, i.e., ~20-35% smaller than in quantum dots due to the extra degree of freedom along the wire axis. Figures 4a and 4b indicate that temperature-induced variations are minor: Eg changes by only ~0.01–0.02 eV for Si and ~0.03 eV for GaAs over 50-500 K, even when exaggerated 20× for visualization, confirming that radius is the primary tuning parameter. The analysis establishes a clear hierarchy of tunability: 0D > 1D > bulk, providing precise numerical guidance for nanostructure design. From an application perspective, such tunability enables wavelength-selective photodetectors, LEDs, and tandem solar cells, while the small temperature dependence ensures stable operation across 50–500 K. Future work should incorporate multi-material heterostructures, surface/interface states, and experimental validation to optimize high-efficiency, size-engineered optoelectronic devices.

CONCLUSIONS

This work has systematically compared the size- and temperature-dependent band gap $E_g$of semiconductor nanostructures across 0D quantum dots and 1D nanowires for Si, GaAs, InP, CdS, and GaN. For quantum dots, the band gap increases dramatically with decreasing radius: Si rises from 1.12 eV (bulk) to ~2.0 eV at r = 2 nm, GaAs from 1.42 eV to ~3.1 eV, and GaN from 3.4 eV to ~5.5 eV, highlighting the dominant kinetic confinement term ($\propto r^{-2}$) at sub-5 nm scales. In contrast, 1D nanowires exhibit weaker confinement, with Si, GaAs, and GaN showing ~20–35% smaller Eg shifts at the same radii, due to partial freedom of carriers along the wire axis. Coulomb interaction ($\propto r^{-1}$) partially compensates confinement, particularly in low-dielectric materials such as CdS and GaN. Temperature effects from 50 K to 500 K are minor (~0.01–0.03 eV), confirming that dimensional confinement, rather than thermal broadening, dominates band gap modulation at the nanoscale. These results quantify the critical radii below 4–5 nm where bulk approximations fail and quantum effects must be explicitly considered. Physically, the observed trends reflect the quantization of electron and hole energies, offering precise control of optical and electronic properties. These findings provide a framework for designing wavelength-tunable LEDs and lasers, Si-based tandem solar cells (~2 eV Eg), and GaN/CdS devices for UV optoelectronics and radiation-hard sensors. Future work should incorporate heterostructures, interface states, and temperature-dependent modeling to optimize high-performance nanodevices.

ORCID

Jo‘shqin Sh. Abdullayev, https://orcid.org/0000-0001-6110-6616; **D.A. Qalandarova,** https://orcid.org/0009-0005-5130-464X; **M.Sh. Ibragimova,** https://orcid.org/0009-0004-7867-7086; **D.I. Yunusova,** https://orcid.org/0000-0001-8390-0810
Zevarjon Jumaboyeva, https://orcid.org/0009-0000-3617-4932

REFERENCES

[1] C.Y. Ho, and C.H. Ho, “Phonon frequency and energy of electron-phonon interactions at the band gap of InAs, InP, GaP, and GaN semiconductors,” Discov. Mater. **6**, 8 (2026). https://doi.org/10.1007/s43939-025-00474-6
[2] M.T. Islam, and H. Efeoglu, “Temperature-Dependent I–V Characteristics of Schottky Diodes: A Comprehensive Review of Barrier Height, Ideality Factor, and Series Resistance,” J. Electron. Mater. **54**, 10824–10857 (2025). https://doi.org/10.1007/s11664-025-12432-2
[3] D.Q. Fang, A.L. Rosa, Th. Frauenheim, and R.Q. Zhang, “Band gap engineering of GaN nanowires by surface functionalization,” Applied Physics Letters, **94**(7), 073116 (2009). https://doi.org/10.1063/1.3086316
[4] S. Fan, Z.J. Yu, Y. Sun, W. Weigand, P. Dhingra, M. Kim, *et al.*, “20%-efficient epitaxial GaAsP/Si tandem solar cells,” Solar Energy Materials and Solar Cells, **202**, 110144 (2019). https://doi.org/10.1016/j.solmat.2019.110144
[5] M. Verma, S. Routray, G.S. Sahoo, and G.P. Mishra, “Bandgap engineered $GaAs_{0.95}P_{0.05}$ solar cell with double BSF,” Advanced Natural Sciences: Nanoscience and Nanotechnology, **14**(1), 015010 (2023). https://doi.org/10.1088/2043-6254/acb6e6
[6] M. Verma, S. Routray, G.S. Sahoo, and G.P. Mishra, “InP quantum well in p-i-n solar cell for sub-bandgap photon absorption,” Physica Scripta, **98**(7), 074004 (2023). https://doi.org/10.1088/1402-4896/ad00c6
[7] J.Sh. Abdullayev, I.B. Sapaev, J.Sh. Abdullayev, D.A. Juraev, M.J. Jalalov, and E.E. Elsayed, “Mathematical modeling of incomplete ionization in radial p-Si/n-GaAs heterojunctions: temperature and doping effects,” Journal of Electronic Materials, **54**, 1–9 (2025). https://doi.org/10.1007/s11664-025-12391-8
[8] J.Sh. Abdullayev, U.S. Rakhmonov, N. Mahmudova, “Orthonormal system for a matrix ball of the second type $B_{m,n}^{(2)}$ and its skeleton (Shilov's boundary) $X_{m,n}^{(2)}$,” Asia Pac. J. Math. **10**, 27 (2023). https://doi.org/10.28924/APJM/10-27
[9] D. Li, C. Luo, H. Wang, F. Ling, and J. Yao, “Active control of plasmon-induced transparency based on a GaAs/Si heterojunction in the terahertz range,” Optical Materials, **114**, 111609 (2021). https://doi.org/10.1016/j.optmat.2021.111609
[10] J. S. Abdullayev, M. S. Ibragimova, J. S. Abdullayev, and I. B. Sapaev, “Cryogenic material and electrophysical changes in Si and GaAs,” East European Journal of Physics, (1), 343–350 (2026). https://doi.org/10.26565/2312-4334-2026-1-40
[11] J.S. Abdullayev, M.S. Ibragimova, J.S. Abdullayev, and I.B. Sapaev, “Thermal expansion characteristics of planar and radial Si/GaAs p–n heterojunctions,” East European Journal of Physics, (1), 388–395 (2026). https://doi.org/10.26565/2312-4334-2026-1-46
[12] M.N. Hasan, Y. Zheng, J. Lai, E. Swinnich, O.G. Licata, M.A. Baboli, B. Mazumder, *et al.*, “Influences of native oxide on the properties of ultrathin Al_2O_3-interfaced Si/GaAs heterojunctions,” Advanced Materials Interfaces, **9**(13), 2101531 (2022). https://doi.org/10.1002/admi.202101531
[13] M. Jurisch, F. Börner, T. Bünger, S. Eichler, T. Flade, U. Kretzer, A. Köhler, *et al.*, “LEC- and VGF-growth of SI GaAs single crystals—Recent developments and current issues,” Journal of Crystal Growth, **275**(1–2), 283–291 (2005). https://doi.org/10.1016/j.jcrysgro.2004.10.092
[14] J.Sh. Abdullayev, and I.B. Sapaev, “Factors influencing the ideality factor of semiconductor p-n and p-i-n junction structures at cryogenic temperatures,” East European Journal of Physics, (4), 329–333 (2024). https://doi.org/10.26565/2312-4334-2024-4-37

[15] C.D. Thurmond, “The standard thermodynamic functions for the formation of electrons and holes in Ge, Si, GaAs, and GaP,” Journal of The Electrochemical Society, **122**(8), 1133 (1975). https://doi.org/10.1149/1.2134410
[16] J. Herfort, H.-P. Schönherr, and K.H. Ploog, “Epitaxial growth of hybrid structures,” Applied Physics Letters, **83**(18), 3912-3914 (2003). https://doi.org/10.1063/1.1625426
[17] J.Sh. Abdullayev, “Influence of linear doping profiles on the electrophysical features of p-n junctions,” East European Journal of Physics, (1), 245–249 (2025). https://doi.org/10.26565/2312-4334-2025-1-26
[18] S. Heun, M. Sugiyama, S. Maeyama, Y. Watanabe, K. Wada, and M. Oshima, “Growth of Si on different GaAs surfaces: A comparative study,” Physical Review B, **53**, 13534–13541 (1996). https://doi.org/10.1103/PhysRevB.53.13534
[19] P.K. Saxena, P. Srivastava, and A. Srivastava, “Defect analysis of MBE reactor-grown HgCdTe on Si, GaAs, GaSb, and CZT substrates through the TNL-Epigrow simulator,” Journal of Electronic Materials, **53**, 5803–5812 (2024). https://doi.org/10.1007/s11664-024-11082-0
[20] A.B. Roy, N.H.R. Valiji, R. Mohammad, P. Giridhar, and P. Mondal, “Performance enhancement of Si/GaAs based heterojunction solar cells by opto-electronics modeling and optimization,” in: *2024 International Conference on Recent Advances in Electrical, Electronics, Ubiquitous Communication, and Computational Intelligence (RAEEUCCI)* (pp. 1–6). IEEE. https://doi.org/10.1109/RAEEUCCI61380.2024.10547792
[21] J.Sh. Abdullayev, and I.B. Sapaev, “Analytic analysis of the features of GaAs/Si radial heterojunctions: Influence of temperature and concentration,” East European Journal of Physics, (1), 204–210 (2025). https://doi.org/10.26565/2312-4334-2025-1-21
[22] M. Piriyev, G. Loget, Y. Léger, L. Chen, A. Létoublon, T. Rohel, C. Levallois, *et al.*, “Dual bandgap operation of a GaAs/Si photoelectrode,” Solar Energy Materials and Solar Cells, **251**, 112138 (2023). https://doi.org/10.1016/j.solmat.2022.112138
[23] J. Alanis, S.J. Gutiérrez-Ojeda, R. Méndez-Camacho, and E. Cruz-Hernández, “Theoretical investigation of the growth of GaAs on Si(001), Si(110), Si(111), Si(113), and Si(331),” Surfaces and Interfaces, **44**, 103792 (2024). https://doi.org/10.1016/j.surfin.2023.103792
[24] G.K. Khudayberganov, J.S. Abdullayev, and U.S. Rakhmonov, “Functional Properties of the Bergman Kernel in the Space $C_n[m\times m]$,” Lobachevskii J. Math. **46**, 1322–1335 (2025). https://doi.org/10.1134/S1995080225605247
[25] J. Sadullayev, M. Akhmedov, M. Vapayev, I. Davletov, and G. Boltaev, “Modeling of Thermal Effects in a Polyimide Target Under Pulsed Laser Irradiation,” East European Journal of Physics, (1), 274-280 (2026). https://doi.org/10.26565/2312-4334-2026-1-31
[26] R. Huang, Q. Wang, Y. Guo, and Z. Wang, “Comparative study on GaAs/Si heterojunction fabricated by nitrogen and oxygen plasma activated bonding,” Vacuum, **208**, 111735 (2023). https://doi.org/10.1016/j.vacuum.2022.111735
[27] M. Yamaguchi, T. Takamoto, H. Juso, K. Nakamura, R. Ozaki, and N. Kojima, “33.7% efficiency Si tandem solar cell modules,” in: *Proceedings of the 2024 IEEE 52nd Photovoltaic Specialist Conference (PVSC)*, (IEEE, 2024). https://doi.org/10.1109/PVSC57443.2024.10749502
[28] A. Šagátová, A. Novák, E. Kováčová, O. Riabukhin, S. Kotorová, and B. Zaťko, “Radiation-degraded Si GaAs detectors and their metallization,” AIP Conference Proceedings, **2778**, 060009 (2023). https://doi.org/10.1063/5.0137383
[29] J. Liang, L. Chai, S. Nishida, M. Morimoto, and N. Shigekawa, “Investigation on the interface resistance of Si/GaAs heterojunctions fabricated by surface-activated bonding,” Japanese Journal of Applied Physics, **54**(3), 030211 (2015). https://doi.org/10.7567/JJAP.54.030211
[30] J.Sh. Abdullayev, I.B. Sapaev, and S.R. Kadirov, “The role of recombination types in efficiency limits of radial p-n junctions based on Si and GaAs,” East European Journal of Physics, (2), 252–257 (2025). https://doi.org/10.26565/2312-4334-2025-2-30
[31] M. Haris, S.A. Loan, and Mainuddin, “Si/GaAs hetero junction tunnel FET: Design and investigation,” Journal of Nanoelectronics and Optoelectronics, **14**(10), 1434–1444 (2019). https://doi.org/10.1166/jno.2019.2575
[32] J.S. Abdullayev, D.A. Qalandarova, M.S. Ibragimova, *et al.* “Experimental and Simulation-Based Investigation of p-Si/n-CdS Heterojunctions: From Cryogenic Freeze-Out to Room Temperature Operation,” J. Electron. Mater. **55**, 2229–2239 (2026). https://doi.org/10.1007/s11664-025-12642-8
[33] J. Sh. Abdullayev, D. A. Qalandarova, and M. Sh. Ibragimova, “Impact of incomplete ionization on the critical electric field of p–n junction structures based on Si and GaAs,” Low Temperature Physics, **52**(2), 164–169 (2026). https://doi.org/10.1063/10.0042291
[34] D. A. Qalandarova, M. S. Ibragimova, J. S. Abdullayev, and I. B. Sapaev, “Mathematical modeling of electrostatic potential in radial and planar p–n junctions: A comparative study,” East European Journal of Physics, (1), 333–342 (2026). https://doi.org/10.26565/2312-4334-2026-1-39
[35] U.S. Rakhmonov, J.Sh. Abdullayev, “On properties of the second type matrix ball $B_{m,n}^{(2)}$ from space $C_n[m\times m]$,” J. Sib. Fed. Univ. Math. Phys. **15**(3), 329–342 (2022). https://doi.org/10.17516/1997-1397-2022-15-3-329-342
[36] J. Sh. Abdullayev, “Estimates the Bergman kernel for classical domains É. Cartan's,” Chebyshevskii Sb. **22**(3), 20–31 (2021). https://doi.org/10.22405/2226-8383-2018-22-3-20-31

КРИТИЧНИЙ РОЗМІР ТА ПОРОГОВІ ЗНАЧЕННЯ ЛЕГУВАННЯ, ЩО ВИЗНАЧАЮТЬ ЕВОЛЮЦІЮ ЗАБОРОНЕНОЇ ЗОНИ В НАПІВПРОВІДНИКАХ

Й.Ш. Абдуллаєв[2], Д.А. Каландарова[1], М.Ш. Ібрагімова[1], У.А. Акбераджієва[3], Д.І. Юнусова[4], Зеваржон Джумабоєва[5], Ш.А. Шоюсупов[2], І.О. Джуманійозов[6]
[1]*Ургенчський державний університет, вул. Хаміда Олімжона, 14, Ургенч, 220100 Узбекистан*
[2]*Національний дослідницький університет ТІІАМЕ, фізико-хімічний факультет, Ташкент, Узбекистан*
[3]*Ташкентський державний технічний університет, Ташкент, Узбекистан*
[4]*Кафедра математики, Ташкентський державний педагогічний університет імені Нізамі (NPUU), Ташкент, 100019, Узбекистан*
[5]*Кафедра математики та комп'ютерних технологій Ургенчського державного педагогічного інституту, 220100 Ургенч, Узбекистан*
[6]*Ташкентський міжнародний університет, вулиця Кічик Халка Йолі 7, Ташкент, 100084, Узбекистан*

Розуміння того, як заборонена зона (E_g) напівпровідників змінюється залежно від розміру, вимірності та концентрації легуючих домішок, є критично важливим для оптимізації сучасних електронних і оптоелектронних пристроїв. У цій роботі

ми здійснюємо систематичний аналіз критичних розмірів (L_c) та порогових концентрацій домішок (N_c), що визначають суттєві зміни забороненої зони у Si, GaAs, InP, CdS та GaN. Використовуючи теорію ефективної маси з поправками на кулонівську взаємодію, температурну залежність за Варшні та чисельні симуляції, ми встановлюємо, що квантове обмеження домінує при $L \lesssim 2a_B^*$, що дає $L_c \approx 10$нм для Si, 22 нм для GaAs, 6 нм для CdS та 5–6 нм для GaN. Відповідні порогові концентрації домішок, подібні до критерію Мотта, задовольняють $N_c^{(1/3)} a_B^* \approx 0{,}25$, що дає $N_c = 1.8 \cdot 10^{18}\ cm^{-3}$ (Si), $5.6 \cdot 10^{17}\ cm^{-3}$ (GaAs) та $2.9 \cdot 10^{18}\ cm^{-3}$ (CdS). Для квантових точок (0D) з r = 2 нм заборонена зона збільшується приблизно на ~0,9 еВ для Si, ~1,3 еВ для GaAs та ~5,5 еВ для GaN, тоді як 1D нанодроти демонструють на 20–35% менші зміни через часткову делокалізацію носіїв уздовж осі дроту. Температурні ефекти є незначними (~0,01–0,03 еВ у діапазоні 50–500 K), що підтверджує, що вимірне обмеження є домінуючим фактором. Ці результати надають кількісні вказівки для інженерії регульованих заборонених зон у світлодіодах, лазерах, кремнієвих багатошарових сонячних елементах, УФ-оптоелектроніці та фотодетекторах, пропонуючи прогностичну основу для наноструктур напівпровідників типів IV, III–V та II–VI.
Ключові слова: *заборонена зона напівпровідника; критичний розмір; порогова концентрація домішок; квантове обмеження; температурні ефекти; концентрація носіїв; наноструктури; оптимізація пристроїв*

East European Journal of Physics. 2. 212-218 (2026)
DOI:10.26565/2312-4334-2026-2-22 ISSN 2312-4334

A SYSTEMATIC ANALYTICAL AND NUMERICAL STUDY OF INCOMPLETE DOPANT IONIZATION IN GERMANIUM OVER 4–400 K

M.Sh. Ibragimova[1]*, D.A. Qalandarova[1], N.P. Babayazova[1], U.G. Salayev[1], D.G. Yulchiev[2], A.B. Tilyakov[3], A.V. Alimov[3], Sh.M. Kuliyev[4], U.S. Rakhmonov[5]

[1]*Urgench State University, Hamid Olimjon Street, 14, Urgench, 220100 Uzbekistan*
[2]*Tashkent Institute of Irrigation and Agricultural Mechanization Engineers, National Research University, Department of Irrigation and Melioration, Tashkent, Uzbekistan*
[3]*Department of Emergency Medicine and Disaster Medicine. Tashkent State Medical University, Uzbekistan*
[4]*S.A. Azimov Physical-Technical Institute of Uzbekistan Academy of Sciences*
[5]*Tashkent State Technical University, Tashkent, Uzbekistan*
**Corresponding Author e-mail: madinabonubahodir2024@gmail.com*
Received January 25, 2026; revised April 3, 2026; accepted April 5, 2026

Incomplete dopant ionization critically influences the electrical properties of germanium (Ge), particularly under low-temperature and low-doping conditions relevant to advanced electronic and optoelectronic devices. In this work, we present a systematic numerical investigation of temperature- and concentration-dependent dopant ionization in Ge over temperature range of 4–400 K and dopant concentrations from 1×10^{14} to 1×10^{18} $\mathrm{cm^{-3}}$. Ionization probabilities are evaluated for common acceptor dopants (Boron, Gallium, and Indium) and donor dopants (Phosphorus, Arsenic, and Antimony), with activation energies spanning 10–16 meV. The results reveal severe dopant freeze-out at cryogenic temperatures, where ionization probabilities drop below 0.1–0.2 for lightly doped Ge ($N \leq 10^{15}$ $\mathrm{cm^{-3}}$), leading to carrier density reductions exceeding 80–90% compared to full-ionization assumptions. Donor dopants with lower activation energies achieve near-complete ionization ($P(T) > 0.9$) at 100–150 K, while higher-energy acceptors require temperatures above 200–250 K. Increasing dopant concentration to 10^{17}–10^{18} $\mathrm{cm^{-3}}$ significantly suppresses freeze-out, enabling ionization probabilities above 0.8 at temperatures as low as 50–70 K. At and above room temperature, all dopants exhibit near-unity ionization across the investigated concentration range. These findings provide quantitative guidelines for dopant selection and concentration optimization in Ge-based electronic, optoelectronic, and cryogenic devices, emphasizing the necessity of explicitly accounting for incomplete ionization in low-temperature device modeling and design.
Keywords: *Semiconductor band gap; Germanium (Ge); Doping threshold; Temperature effects; Carrier concentration; Incomplete ionization;*
PACS: 73.40. Lq, 73.61.Cw, 73.61.Ey, 72.20.Jv

INTRODUCTION

Germanium (Ge) has re-emerged as a strategically important semiconductor owing to its superior electronic, optical, and thermal properties, which make it highly attractive for next-generation electronic, photonic, and sensing technologies. Its narrow indirect bandgap (~0.66 eV at 300 K), intrinsically high electron and hole mobilities, and strong infrared absorption enable efficient charge transport and enhanced sensitivity compared to conventional silicon-based devices [1-5]. These properties position Ge at a unique intersection between silicon and III–V semiconductors, supporting high-performance operation over wide temperature ranges.

Recent advances in Si-compatible integration, including SiGe heterostructures and Ge-on-Si platforms, have further accelerated the adoption of Ge in modern microelectronics. The high carrier mobility of Ge significantly improves device performance in high-speed logic and radio-frequency (RF) applications, enabling operation in the GHz–THz regime while maintaining full compatibility with CMOS fabrication processes [2,3]. In optoelectronics, Ge exhibits strong absorption in the near-infrared region (0.8–1.6 μm), coinciding with key telecommunication wavelengths. Consequently, Ge-based p–n, p–i–n, and avalanche photodiodes are widely implemented in silicon photonics, optical interconnects, LiDAR, and fiber-optic communication systems [3–6]. Germanium also plays a critical role in high-efficiency photovoltaic technologies, particularly as a substrate and bottom cell in multi-junction solar cells such as InGaP/GaAs/Ge, enabling superior spectral utilization and power conversion efficiencies beyond the single-junction Shockley–Queisser limit [6]. In addition, Ge exhibits exceptional temperature sensitivity, making it well-suited for precision thermistors, cryogenic sensors, and thermo-optic photonic devices. High-purity germanium (HPGe) detectors further remain the benchmark for gamma-ray and X-ray spectroscopy due to their outstanding energy resolution [1,7].

Despite these advantages, the performance of Ge-based devices is strongly governed by temperature-dependent dopant activation and carrier statistics. In particular, incomplete dopant ionization becomes significant at low and intermediate temperatures, leading to pronounced deviations between the nominal doping concentration and the effective free carrier density [10]. This effect directly impacts conductivity, capacitance–voltage characteristics, and junction electrostatics. While incomplete ionization has been extensively studied in silicon [11-12], GaAs [13-18], and Si/GaAs

Cite as: M.Sh. Ibragimova, D.A. Qalandarova, N.P. Babayazova, U.G. Salayev, D.G. Yulchiev, A.B. Tilyakov, A.V. Alimov, Sh.M. Kuliyev, U.S. Rakhmonov, East Eur. J. Phys. 2, 212 (2026), https://doi.org/10.26565/2312-4334-2026-2-22
© M.Sh. Ibragimova, D.A. Qalandarova, N.P. Babayazova, U.G. Salayev, D.G. Yulchiev, A.B. Tilyakov, A.V. Alimov, Sh.M. Kuliyev, U.S. Rakhmonov, 2026; CC BY 4.0 license

heterostructures [19-25], a systematic and comparative investigation for germanium over wide temperature [26,27] and doping ranges remains notably lacking [28-30], despite its growing importance in cryogenic electronics and thermal sensing [31,32].

In this work, we present a comprehensive analysis of incomplete ionization effects in germanium across a temperature range of 4–400 K and doping concentrations from 10^{15} to 10^{18} cm^{-3}. A comparative study is conducted for common donor (P, As, Sb) and acceptor (B, Ga, In) impurities. By combining analytical modeling based on Fermi–Dirac statistics and charge neutrality with numerical simulations, we elucidate dopant activation mechanisms and their impact on carrier concentration and electro-physical properties. The results provide essential insight and practical guidelines for the accurate modeling and optimization of Ge-based electronic, optoelectronic, and sensing devices operating over broad temperature regimes.

METHODS AND MATERIAL

2.1. Material Parameters and Doping Conditions

Germanium (Ge) is a group IV semiconductor with a diamond cubic (face-centered cubic, FCC) crystal structure and a lattice constant of 5.658 Å. It exhibits an indirect bandgap of 0.66 eV at 300 K, which enables efficient infrared absorption and makes it suitable for photodetector and optoelectronic applications. The effective mass of electrons in Ge is $0.12\,m_0$, while holes have a heavier mass of $0.29\,m_0$ for heavy holes and $0.043\,m_0$ for light holes. These low effective masses contribute to the material's high carrier mobility, approximately 3900 cm²/V·s for electrons and 1900 cm²/V·s for holes at room temperature, allowing fast charge transport in electronic and photonic devices. The intrinsic carrier concentration of Ge is relatively low, around 2.4×10^{13} cm^{-3} at 300 K, which ensures low leakage currents in p-n junction devices. Germanium also has a high relative permittivity of 16.2, which reduces the depletion width for a given doping level, enabling compact device geometries. Its thermal conductivity is 60 W/m·K, supporting efficient heat dissipation, and the material has a density of 5.323 g/cm³ with a melting point of 938 °C, setting processing limits for high-temperature fabrication. Germanium's narrow bandgap, high carrier mobility, and favorable permittivity make it an excellent choice for high-speed electronics, infrared photodetectors, and advanced optoelectronic devices. Moreover, the material allows the formation of ohmic contacts with low-resistance metal interfaces, which is essential for efficient current injection and extraction in diodes, LEDs, and photodetectors. Collectively, these properties underpin the superior performance of Ge-based semiconductor devices in both electronic and optoelectronic applications.

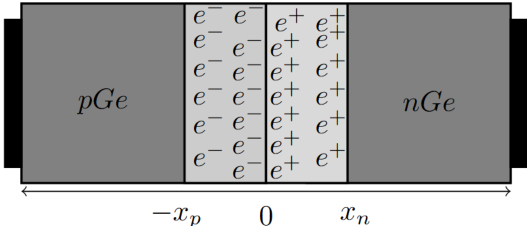

Figure 1. Schematic p-n junction in Germanium (Ge)

Figure 1 illustrates a p-n junction in germanium (Ge) with clearly marked ohmic contacts at the edges and the depletion region at the junction interface. The left region (pGe) is p-type, rich in holes (e^-), while the right region (nGe) is n-type, rich in electrons (e^+). The central depletion region extends from $-x_p$to x_n, where mobile carriers are swept away, leaving fixed ionized donors and acceptors, creating a built-in electric field.

Table 1. Donor and acceptor dopants in germanium and their key parameters

Acceptor (meV)	Boron (B) E_A=10	Gallium (Ga) E_A=12	Indium (In) E_A=16
Donor (meV)	Phosphorus (P) E_D=12	Arsenic (As) E_D=14	Antimony (Sb) E_D=10

The black rectangles at both ends represent ohmic contacts, ensuring low-resistance electrical connection to the external circuit. These contacts allow current injection and extraction without introducing additional potential barriers, which is crucial for device performance. Within the depletion region, the alternating $e^-$and e^+symbols depict electron-hole separation. This separation underpins the rectifying behavior of the junction, as the internal field opposes further carrier diffusion. The gray shading distinguishes the neutral regions, where majority carriers dominate, from the partially depleted regions near the junction. Figure 1 effectively shows a Ge p-n junction with ohmic contacts, illustrating carrier distribution, depletion width, and the electric field, providing a fundamental understanding of semiconductor device operation.

2.2 Analytical Modeling of Temperature-Dependent Ionization

The behavior of p–n junctions in germanium (Ge) was analytically modeled by solving Poisson's equation under the depletion approximation, explicitly including temperature-dependent incomplete dopant ionization. For a three-dimensional structure, the electric field $\mathrm{E}(r)$is assumed uniform along the lateral directions, and varies only along the junction axis, yielding (1):

$$\frac{dE(r)}{dr} = \frac{\partial E(x,y,z)}{\partial x} + \frac{\partial E(x,y,z)}{\partial y} + \frac{\partial E(x,y,z)}{\partial z} = \frac{\rho(x,y,z)}{\varepsilon \cdot \varepsilon_0} \tag{1}$$

Where $\varepsilon = 16.2$ is the relative permittivity of Ge, $\varepsilon_0 \approx 8.854 \cdot 10^{12}$ F/m is the vacuum permittivity, and $\rho(r,T)$is the space charge density, defined as (2):

$$\rho(r,T) = q \cdot (p(r) - n(r) + N_D^+(T) - N_A^-(T)) \tag{2}$$

with $q = 1.602 \cdot 10^{-19}\ C$, $p(r)$and $n(r)$the hole and electron concentrations, and $N_D^+(T)$, $N_A^-(T)$the ionized donor and acceptor densities. The ionized dopant concentrations are described using Fermi–Dirac statistics corrected for the temperature-dependent density of states. The probabilities of ionization for acceptor $P_A(T)$ and donor $P_D(T)$ dopants are directly related to the fraction of ionized dopants in the material. They are defined using equations (3a) and (3b) as:

$$\begin{cases} P_A(T) = \dfrac{1}{1 + \dfrac{g_A \cdot p_p(r)}{\gamma_p(T) \cdot N_V(T)} \cdot \exp\left(\dfrac{\Delta E_A}{kT}\right)} & (3a) \\ P_D(T) = \dfrac{1}{1 + \dfrac{g_D \cdot n_n(r)}{\gamma_n(T) \cdot N_C(T)} \cdot \exp\left(\dfrac{\Delta E_D}{kT}\right)} & (3b) \end{cases}$$

where $g_D = 4, g_A = 2$ are the dopant degeneracy factors, $N_C(T)$and $N_V(T)$are the effective density of states in the conduction and valence bands, and $\Delta E_D$and $\Delta E_A$are the dopant activation energies. For example, common dopants in Ge have the following activation energies: To bridge the quantum Fermi–Dirac statistics with classical Maxwell–Boltzmann approximations, temperature-dependent correction factors $\gamma_n(T)$and $\gamma_p(T)$were introduced, ensuring a physically consistent description of both majority carrier concentrations and dopant ionization over the entire 4–400 K range. This analytical framework allows precise calculation of temperature-dependent carrier densities, $n(T)$and $p(T)$, capturing freeze-out, partial ionization, and full ionization regimes. It provides a quantitative foundation for designing Ge-based electronic and optoelectronic devices, including photodetectors and low-temperature sensors, by predicting the effective free carrier density as a function of both temperature and dopant concentration. $\Delta E_D = E_C - E_D$, $\Delta E_A = E_A - E_V$ activation energy donor and acceptor, with donor and acceptor energy levels E_D and E_A facilitating n-type and p-type conductivity respectively, as shown in Figure 2.

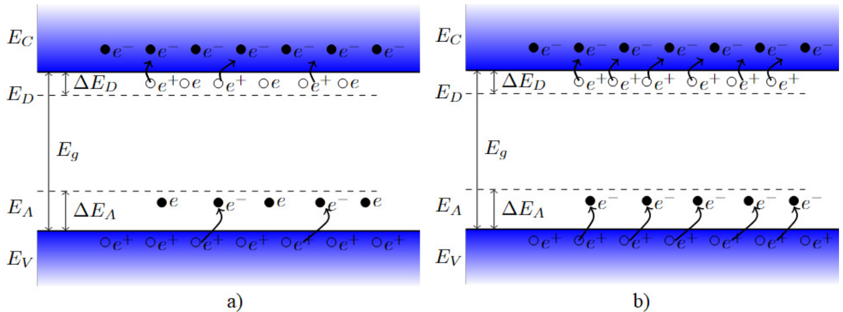

Figure. 2. Schematic illustration of the band diagrams for acceptors and donors:
(a) partially ionized state at low temperatures and (b) fully ionized state at high temperatures

In Figure 2 b) at high temperatures, donor atoms (such as phosphorus in Si) are fully ionized, donating electrons to the conduction band and thereby enhancing the material's electrical conductivity. Similarly, acceptor atoms (like boron in Si) ionize by accepting electrons from the valence band, creating holes that also contribute to conductivity. In contrast, Figure 2 a) shows that at low temperatures below 20 K, incomplete ionization occurs, where not all donor and acceptor atoms ionize.

RESULTS AND DISCUSSION

The temperature-dependent ionization of acceptor (B, Ga, In) and donor (P, As, Sb) dopants in lightly doped germanium ($N_A = N_D = 1 \times 10^{15}$ cm^{-3}) exhibits pronounced freeze-out at cryogenic temperatures and near-complete ionization above room temperature. At $T < 50$ K, high-energy dopants such as Indium and Arsenic remain largely inactive ($P < 0.1$), while low-energy dopants like Boron and Antimony begin ionizing earlier, highlighting the strong sensitivity of ionization to activation energy. In the intermediate range (50–150 K), ionization rapidly increases, with donors generally ionizing at lower temperatures than acceptors due to higher degeneracy and conduction-band density of states. Temperature–concentration maps reveal that low dopant densities exacerbate freeze-out, whereas increasing dopant

concentration partially mitigates incomplete ionization, though cryogenic suppression persists even at $N \sim 10^{18}$ cm^{-3}. These results underscore that dopant selection critically impacts low-temperature device performance, with low-activation-energy species preferred for cryogenic sensors, detectors, and quantum devices. Incorporating temperature-dependent effective densities of states and incomplete ionization in models is essential for accurate prediction of carrier density, depletion width, and current transport, enabling optimized design of Ge-based electronic and optoelectronic systems across 4–400 K.

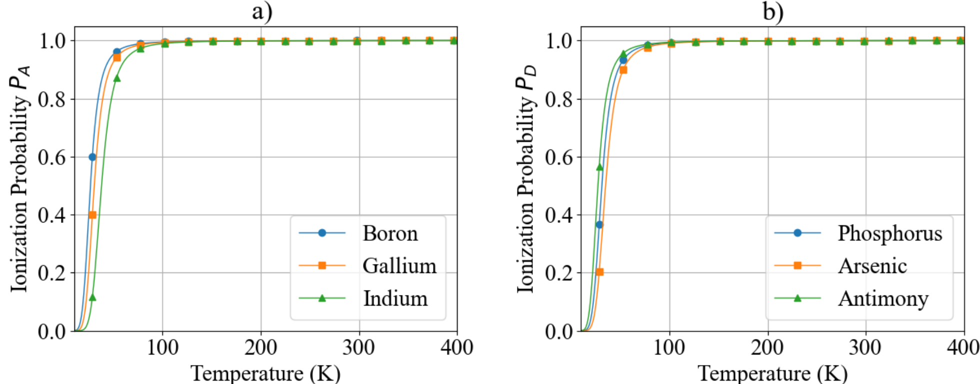

Figure 3. Ionization Probabilities of Dopants in Germanium (Ge) (a) Acceptor Ionization Probability $P_A(T)$for Boron, Gallium, and Indium (b) Donor Ionization Probability $P_D(T)$for Phosphorus, Arsenic, and Antimony

Figure 3 illustrates the temperature dependence of dopant ionization probability in lightly doped germanium, with equal acceptor and donor concentrations of $N_A = N_D = 1 \times 10^{15}$ cm^{-3}. Representative shallow acceptor (B, Ga, In) and donor (P, As, Sb) species are considered. The calculations are based on an analytical Fermi–Dirac ionization model that explicitly incorporates temperature-dependent effective densities of states, $N_V(T)$and $N_C(T)$, as well as dopant-specific activation energies. Figure 3(a): Acceptor Dopants: Figure 3(a) presents the ionization probability $P_A(T)$of Boron (10 MeV), Gallium (12 meV), and Indium (16 meV) over the temperature range 4–400 K. At cryogenic temperatures (T < 40 K), all acceptors are in the freeze-out regime, exhibiting very low ionization probabilities ($P_A < 0.1$). At 10 K, Boron reaches $P_A \approx 0.12$, Gallium $P_A \approx 0.08$, while Indium remains below $P_A \approx 0.04$, highlighting the strong sensitivity of ionization to acceptor activation energy. In the intermediate temperature range (50–150 K), a rapid increase in ionization probability is observed. Boron achieves $P_A > 0.9$ at approximately 120 K, Gallium near 150 K, whereas Indium requires temperatures exceeding 200 K to reach comparable ionization levels. This temperature shift of roughly 80 K between Boron and Indium directly reflects their 6 meV difference in activation energy. At temperatures $T \geq 250$K, all acceptors are essentially fully ionized ($P_A > 0.98$), confirming the validity of the complete ionization assumption for lightly doped Ge at and above room temperature. Figure 3(b): Donor Dopants: Figure 3(b) shows the donor ionization probability $P_D(T)$for Phosphorus (12 meV), Arsenic (14 meV), and Antimony (10 meV). At low temperatures ($T < 40$K), donor ionization is likewise strongly suppressed, with $P_D < 0.15$for all species. Antimony, having the lowest donor activation energy, exhibits the highest ionization probability, reaching $P_D \approx 0.18$at 20 K, compared to $P_D \approx 0.10$for Phosphorus and below 0.07 for Arsenic. Within the intermediate temperature range (80–150 K), donors ionize more rapidly than acceptors. Antimony reaches $P_D \approx 0.9$at approximately 100 K, Phosphorus near 130 K, and Arsenic around 160 K. Above 200 K, all donor species exhibit near-unity ionization ($P_D > 0.99$). Overall, Figure 3 demonstrates that donor dopants in Ge ionize at slightly lower temperatures than acceptors with comparable activation energies. This behavior arises primarily from differences in degeneracy factors ($g_D = 4$ for donors versus $g_A = 2$for acceptors) and the larger effective density of states in the conduction band. At low temperatures, incomplete dopant ionization dominates the electrical behavior of germanium, particularly in lightly doped material (1×10^{15} cm^{-3}), where the free carrier density may be reduced by up to 90% below 50 K. As temperature increases, the system transitions from the freeze-out regime (strongly suppressed ionization) to a partial ionization regime, and ultimately to full ionization at higher temperatures ($T > 300$ K). The dopant activation energy determines the temperature range over which these regimes occur. High-energy dopants such as Indium and Arsenic exhibit delayed ionization and more pronounced freeze-out, while low-energy dopants such as Boron and Antimony ionize at lower temperatures and provide higher carrier concentrations under cryogenic conditions. This behavior is especially critical for germanium-based low-temperature sensors, radiation detectors, and quantum electronic devices. The temperature-dependent ionization characteristics shown in Figure 3 have important implications for Ge-based device design: Cryogenic electronics and sensors: Low-activation-energy dopants (e.g., B and Sb) are preferred to minimize carrier freeze-out and maintain adequate conductivity at low temperatures. Optoelectronic and room-temperature devices: At moderate and room temperatures, the choice of dopant becomes less critical, as nearly complete ionization is achieved for all species. Analytical and numerical device modeling: Accurate inclusion of temperature-dependent $N_C(T)$, $N_V(T)$, and incomplete ionization effects is essential for predicting free carrier density, depletion width, capacitance, and current–voltage characteristics in Ge p–n junctions and MOS devices. At 77 K, Boron exhibits an ionization probability of approximately 20%, while Indium remains below 10%. Among donors,

Antimony achieves approximately 25% ionization at 77 K, whereas Arsenic remains below 10%. At 300 K, all dopants are nearly fully ionized (> 90%), validating the commonly used assumption of complete ionization for lightly doped germanium at room temperature. These results highlight the critical role of incomplete dopant ionization at cryogenic temperatures and provide quantitative guidance for selecting dopant species and concentrations in low-temperature Ge-based electronic and optoelectronic devices.

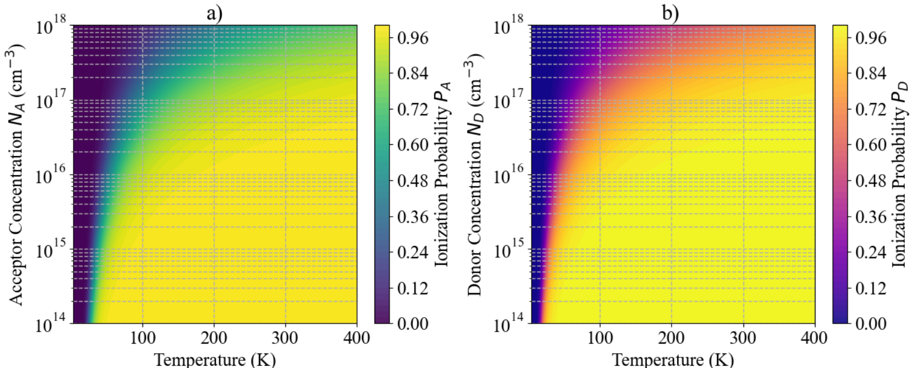

Figure 4. Temperature- and concentration-dependent ionization probabilities of dopants in Germanium (a) Acceptor ionization probability $P_A(T, N_A)$ for Boron, Gallium, and Indium over 4–400 K and 10^{14}–10^{18} cm^{-3}; (b) Donor ionization probability $P_D(T, N_D)$ for Phosphorus, Arsenic, and Antimony over the same ranges. Color maps indicate the fraction of ionized dopants, with low temperatures and low concentrations showing pronounced freeze-out.

Figure 4 extends the analysis by mapping ionization probability as a function of both temperature (4–400 K) and dopant concentration (1×10^{14}–1×10^{18} cm^{-3}), providing a comprehensive picture of incomplete ionization effects. Figure 4(a): Acceptor Dopants Figure 4(a) shows contour maps of acceptor ionization probability $P_A(T, N_A)$for Boron, Gallium, and Indium. At low temperatures (<50 K) and low concentrations ($N_A \leq 10^{15}$ cm^{-3}), ionization probabilities remain below 0.2, indicating severe freeze-out. For example, at 20 K and 10^{14} cm^{-3}, Boron exhibits $P_A \approx 0.15$, while Indium remains below $P_A \approx 0.05$. As dopant concentration increases, freeze-out is partially mitigated. At $N_A = 10^{17}$ cm^{-3}, Boron achieves $P_A > 0.7$already at 50 K, whereas Indium still requires temperatures above 120 K to exceed the same ionization level. This illustrates how higher activation energy dopants remain sensitive to freeze-out even at elevated concentrations. At T ≥ 300 K, all acceptors reach $P_A > 0.95$across the entire concentration range, indicating that thermal ionization dominates over concentration-dependent effects. Figure 4(b): Donor Dopants Figure 4(b) presents donor ionization probability $P_D(T, N_D)$for Phosphorus, Arsenic, and Antimony. At 10–30 K and $N_D < 10^{15}$ cm^{-3}, ionization remains below 0.2 for all donors, with Antimony showing the highest ionization fraction. At $N_D = 10^{16}$ cm^{-3}and 50 K, Antimony reaches $P_D \approx 0.8$, while Arsenic remains near $P_D \approx 0.5$. Donor dopants achieve near-complete ionization at lower temperatures than acceptors. For concentrations above 10^{17} cm^{-3}, all donors reach $P_D > 0.95$by 150–180 K, whereas acceptors require temperatures closer to 200–250 K, particularly for Indium. At room temperature (300 K), donors are fully ionized ($P_D > 0.99$) across the entire concentration range, confirming robust carrier activation for n-type Ge devices. Comparative Implications for Device Design Figure 3 isolates the intrinsic temperature dependence and highlights the activation-energy-controlled onset of ionization in lightly doped Ge. Figure 4 demonstrates that dopant concentration can partially compensate for freeze-out, but does not eliminate activation-energy limitations at cryogenic temperatures. Donors consistently ionize at lower temperatures than acceptors, making n-type Ge more suitable for low-temperature electronics. At 50–100 K, carrier densities can be reduced by 70–90% relative to full ionization assumptions for $N < 10^{15}$ cm^{-3}, significantly impacting conductivity and junction behavior. Figures 3 and 4 collectively show that incomplete dopant ionization is a dominant limiting factor in germanium at low temperatures and low doping concentrations. While room-temperature operation (300–500 K) ensures stable and nearly complete ionization, cryogenic operation requires careful dopant selection and concentration optimization. Future work should incorporate heterostructure band alignment, impurity band formation, interface states, and experimental validation, particularly for size-engineered and low-temperature Ge-based optoelectronic and sensing devices.

CONCLUSIONS

In this work, we presented a comprehensive numerical analysis of temperature- and concentration-dependent dopant ionization in germanium, covering temperatures from 4 to 400 K and dopant concentrations spanning $1 \times 10^{14}$to 1×10^{18} cm^{-3}. The results clearly demonstrate that incomplete dopant ionization is a dominant factor governing free-carrier availability in Ge, particularly under low-temperature and low-doping conditions. For lightly doped material ($N = 1 \times 10^{15}$ cm^{-3}), both acceptor and donor species exhibit pronounced freeze-out below 40–50 K, where ionization probabilities fall below 0.1–0.2, corresponding to a reduction of electrically active carriers by more than 80–90% compared to full-ionization assumptions. Donor dopants with low activation energies, such as antimony ($E_D = 10$ meV), reach an ionization probability of $P_D > 0.9$at temperatures of approximately 100–120 K, whereas higher-energy donors such as arsenic ($E_D = 14$ meV) require temperatures exceeding 150–170 K to achieve similar activation. In contrast,

acceptor dopants exhibit slower ionization, with boron ($E_A = 10$ meV) reaching $P_A \approx 0.9$near 120–140 K, while indium ($E_A = 16$ meV) requires temperatures above 220–250 K. The combined temperature–concentration analysis reveals that increasing dopant concentration to 10^{17}–10^{18} cm^{-3}significantly mitigates freeze-out effects. At these concentrations, low-activation-energy dopants exhibit ionization probabilities exceeding 0.8 at temperatures as low as 50–70 K. Nevertheless, even at the highest investigated concentrations, incomplete ionization persists below 30 K, indicating that impurity activation remains thermally limited in cryogenic regimes. At elevated temperatures (300–400 K), all dopant species achieve near-complete ionization ($P > 0.95$–0.99) across the full concentration range, confirming the validity of full-ionization approximations for conventional room-temperature and high-temperature Ge-based devices. However, the results emphasize that such assumptions are no longer valid for low-temperature electronics, infrared detectors, and cryogenic sensing applications, where carrier densities, resistivity, and junction characteristics can deviate by more than an order of magnitude if incomplete ionization is neglected. Overall, this study provides quantitative design guidelines for dopant selection and concentration optimization in germanium, highlighting the necessity of incorporating temperature- and concentration-dependent ionization models for accurate prediction and optimization of electronic and optoelectronic device performance across broad temperature ranges.

ORCID

Madinabonu Sh. Ibragimova, https://orcid.org/0009-0004-7867-7086; **Dildora A. Qalandarova,** https://orcid.org/0009-0005-5130-464X; **Nazokat P. Babayazova,** https://orcid.org/0009-0006-7877-2459; **Ulug'bek G. Salayev,** https://orcid.org/0009-0001-8223-1114; **Davronbek Gulamovich Yulchiev,** https://orcid.org/0000-0002-9251-2710; **Aziz Burievich Tilyakov,** https://orcid.org/0000-0002-9743-0482; **Akhbor Valievich Alimov,** https://orcid.org/0009-0003-0491-650X; **Shukur M. Kuliyev,** https://orcid.org/0009-0006-7692-3954; **Uktam Sodikovich Rakhmonov,** https://orcid.org/0000-0001-8926-9505

REFERENCES

[1] N. Abrosimov, M. Czupalla, N. Dropka, J. Fischer, A. Gybin, K. Irmscher, J. Janicskó-Csáthy, *et al.*, "Technology development of high purity germanium crystals for radiation detectors," Journal of Crystal Growth, **532**, 125396 (2020). https://doi.org/10.1016/j.jcrysgro.2019.125396

[2] Sh.B. Utamuradova, Sh.Kh. Daliev, J.J. Khamdamov, Kh.J. Matchonov, M.K. Karimov, and Kh.Y. Utemuratova, East Eur. J. Phys. (1), 276 (2025), https://doi.org/10.26565/2312-4334-2025-1-32

[3] D.A. Kozak, N.F. Tyndall, M.W. Pruessner, W.S. Rabinovich, and T.H. Stievater, "Germanium-on-silicon waveguides for long-wave integrated photonics: Ring resonance and thermo-optics," Optics Express, **29**(10), 15443–15451 (2021). https://doi.org/10.1364/OE.420687

[4] A. Torres, M. Moreno, A. Kosarev, and A. Heredia, "Thermo-sensing silicon–germanium–boron films prepared by plasma for un-cooled micro-bolometers," Journal of Non-Crystalline Solids, **354**(19–25), 2556–2560 (2008). https://doi.org/10.1016/j.jnoncrysol.2007.09.112

[5] Z. Wu, S. Wang, J. Jiang, K. Liu, and T. Liu, "High-sensitivity temperature sensor based on microsphere cavity in super larger thermo-optic coefficient germanium-core fiber," IEEE Access, 7, 182658–182663 (2019). https://doi.org/10.1109/ACCESS.2019.2960178

[6] C.S. Mishra, "Temperature-dependent nonlinear optical behavior of germanium semiconductor structures for infrared sensing applications," IEEE Journal of Selected Topics in Quantum Electronics, **31**(6), 4400108 (2025). https://doi.org/10.1109/JSTQE.2025.3596090

[7] J. Feng, Z. Zhang, J. Liu, M. Shao, and Y. Zhou, "A novel resistive anode using a germanium film for Micromegas detectors," Nuclear Instruments and Methods in Physics Research Section A, **1031**, 166595 (2022). https://doi.org/10.1016/j.nima.2022.166595

[8] M. Patel, and A.K. Karamalidis, "Germanium: A review of its US demand, uses, resources, chemistry, and separation technologies," Separation and Purification Technology, **275**, 118981 (2021). https://doi.org/10.1016/j.seppur.2021.118981

[9] J.Sh. Abdullayev, and I.B. Sapaev, "Optimization of the influence of temperature on the electrical distribution of structures with radial p-n junction structures," East European Journal of Physics, (3), 344–349 (2024). https://doi.org/10.26565/2312-4334-2024-3-39

[10] J.Sh. Abdullayev, and I.B. Sapaev, "Optimizing the Influence of Doping and Temperature on the Electrophysical Features of p-n and p-i-n Junction Structures," Eurasian Physical Technical Journal, **21**(3(49)), 21–28 (2024). https://doi.org/10.31489/2024No3/21-28

[11] J.Sh. Abdullayev, I.B. Sapaev, and Kh.N. Juraev, "Theoretical analysis of incomplete ionization on the electrical behavior of radial p-n junction structures," Low Temperature Physics, **51**, 60–64 (2025). https://doi.org/10.1063/10.0034646

[12] J.Sh. Abdullayev, and I.B. Sapaev, "Factors influencing the ideality factor of semiconductor p-n and p-i-n junction structures at cryogenic temperatures," East European Journal of Physics, (4), 329–333 (2024). https://doi.org/10.26565/2312-4334-2024-4-37

[13] C.D. Thurmond, "The standard thermodynamic functions for the formation of electrons and holes in Ge, Si, GaAs, and GaP," Journal of The Electrochemical Society, **122**(8), 1133 (1975). https://doi.org/10.1149/1.2134410

[14] J.Sh. Abdullayev, and I.B. Sapaev, "Modeling and calibration of electrical features of p-n junctions based on Si and GaAs," Physical Sciences and Technology, **11**(3–4), 39–48 (2024). https://doi.org/10.26577/phst2024v11i2b05

[15] J.Sh. Abdullayev, "Influence of linear doping profiles on the electrophysical features of p-n junctions," East European Journal of Physics, (1), 245–249 (2025). https://doi.org/10.26565/2312-4334-2025-1-26

[16] P.K. Saxena, P. Srivastava, and A. Srivastava, "Defect analysis of MBE reactor-grown HgCdTe on Si, GaAs, GaSb, and CZT substrates through the TNL-Epigrow simulator," Journal of Electronic Materials, **53**, 5803–5812 (2024). https://doi.org/10.1007/s11664-024-11082-0

[17] J.Sh. Abdullayev, and I.B. Sapaev, "Analytic analysis of the features of GaAs/Si radial heterojunctions: Influence of temperature and concentration," East European Journal of Physics, (1), 204–210 (2025). https://doi.org/10.26565/2312-4334-2025-1-21

[18] J.Sh. Abdullayev, I.B. Sapaev, N. Esanmuradova, S. Kadirov, and S. Kuliyev, "Mathematical analysis of the features of radial p-n junction: Influence of temperature and concentration," East European Journal of Physics, (2), 220–225 (2025). https://doi.org/10.26565/2312-4334-2025-2-24
[19] J.Sh. Abdullayev, I.B. Sapaev, and S.R. Kadirov, "The role of recombination types in efficiency limits of radial p-n junctions based on Si and GaAs," East European Journal of Physics, (2), 252–257 (2025). https://doi.org/10.26565/2312-4334-2025-2-30
[20] I. Sapaev, B. Sapaev, D. Abdullaev, J. Abdullayev, A. Umarov, R. Siddikov, A. Mamasoliev, and K. Daliev, "Influence of the parameters to transition capacitance at NCDS-PSI heterostructure," E3S Web of Conferences, 383(04022), 1–7 (2023). https://doi.org/10.1051/e3sconf/202338304022
[21] J.Sh. Abdullayev, I.B. Sapaev, J.S. Abdullayev, D.A. Juraev, M.J. Jalalov, and E.E. Elsayed, "Mathematical Modeling of Incomplete Ionization in Radial p-Si/n-GaAs Heterojunctions: Temperature and Doping Effects," J. Electron. Mater. **54**, 10484–10492 (2025). https://doi.org/10.1007/s11664-025-12391-8
[22] I.B. Sapaev, J.I. Razzokov, J.S. Abdullayev, D.A. Qalandarova, and M.S. Ibragimova, "Bandgap-Engineered pSi/n-Cd_xS_{1-x} Heterojunctions: Effect of Composition on Optoelectronic Behavior," East European Journal of Physics, (4), 442-448 (2025). https://doi.org/10.26565/2312-4334-2025-4-44
[23] J.Sh. Abdullayev, D.A. Qalandarova, M.Sh. Ibragimova, I.B. Sapaev, and J.I. Razzokov, "Experimental and Simulation-Based Investigation of p-Si/n-CdS Heterojunctions: From Cryogenic Freeze-Out to Room Temperature Operation," J. Electron. Mater. **55**, 2229–2239 (2026). https://doi.org/10.1007/s11664-025-12642-8
[24] A. Kumar, G. Kumar, and C. Kumar, "Design and Performance Evaluation of a $Ge_{1-x}Sn_x$/Ge Multiple Quantum Well Heterojunction Phototransistor for Long-Haul DWDM Optical Communication Systems," J. Electron. Mater. **55**, 3185–3202 (2026). https://doi.org/10.1007/s11664-025-12653-5
[25] Sh.B. Utamuradova, Sh.Kh. Daliev, J.J. Khamdamov, Kh.J. Matchonov, A.Kh. Khaitbaev, East Eur. J. Phys. (4), 484 (2025). https://doi.org/10.26565/2312-4334-2025-4-49
[26] J.Sh. Abdullayev, L. Abdullayeva, L. Agamalieva, and R. Ismailova, "Correlating Ni microstructure with Schottky barrier homogeneity in monolayer MoS_2 field-effect transistors," Advanced Physical Research, **7**(3), 350–357 (2025). https://doi.org/10.62476/apr.73350
[27] J. Sadullayev, M. Akhmedov, M. Vapayev, I. Davletov, and G. Boltaev, "Modeling of Thermal Effects in a Polyimide Target Under Pulsed Laser Irradiation," East European Journal of Physics, (1), 274-280 (2026). https://doi.org/10.26565/2312-4334-2026-1-31
[28] O. Toktarbaiuly, M. Baisariyev, A. Kaisha, T. Duisebayev, N.K. Ibrayev, T. Serikov, M. Ibraimov, *et al*., Eurasian Physical Technical Journal, **21**(4), 131–139 (2024). https://doi.org/10.31489/2024No4/131-139
[29] J.Sh. Abdullayev, D.A. Qalandarova, and M.Sh. Ibragimova, "Impact of incomplete ionization on the critical electric field of p–n junction structures based on Si and GaAs," Low Temperature Physics, **52**(2), 164–169 (2026). https://doi.org/10.1063/10.0042291
[30] O. Toktarbaiuly, A. Syrlybekov, N. Nuraje, G. Sugurbekova, and I.V. Shvets, "Surface faceting of vicinal $SrTiO_3$(100)," Materials Today: Proceedings, **71**(Part 1), 69–77 (2022). https://doi.org/10.1016/j.matpr.2022.08.283
[31] J.S. Abdullayev, M.S. Ibragimova, J.S. Abdullayev, and I.B. Sapaev, "Cryogenic material and electrophysical changes in Si and GaAs," East European Journal of Physics, (1), 343–350 (2026). https://doi.org/10.26565/2312-4334-2026-1-40
[32] J.S. Abdullayev, M.S. Ibragimova, J.S. Abdullayev, and I.B. Sapaev, "Thermal expansion characteristics of planar and radial Si/GaAs p–n heterojunctions," East European Journal of Physics, (1), 388–395 (2026). https://doi.org/10.26565/2312-4334-2026-1-46

СИСТЕМАТИЧНЕ АНАЛІТИЧНЕ ТА ЧИСЕЛЬНЕ ДОСЛІДЖЕННЯ НЕПОВНОЇ ІОНІЗАЦІЇ ДОМІШОК У ГЕРМАНІЇ В ДІАПАЗОНІ ТЕМПЕРАТУР 4–400 К

М.Ш. Ібрагімова[1], Д.А. Каландарова[1], Н.П. Бабаязова[1], У.Г. Салаєв[1], Д.Г. Юльчієв[2], А.Б. Тіляков[3], А.В. Алімов[3], Ш.М. Кулієв[4], У.С. Рахмонов[5]
[1]Ургенчський державний університет, вулиця Хаміда Олімджона, 14, Ургенч, 220100 Узбекистан
[2]Ташкентський інститут інженерів іригації та механізації сільського господарства, Національний дослідницький університет, кафедра іригації та меліорації, Ташкент, Узбекистан
[3]Кафедра невідкладної медицини та медицини катастроф. Ташкентський державний медичний університет, Узбекистан
[4]Фізико-технічний інститут імені С.А. Азімова Академії наук Узбекистану
[5]Ташкентський державний технічний університет, Ташкент, Узбекистан

Неповна іонізація домішок суттєво впливає на електричні властивості германію (Ge), особливо за умов низьких температур і низького рівня легування, що є критичним для сучасних електронних та оптоелектронних пристроїв. У цій роботі наведено систематичне чисельне дослідження температурної та концентраційної залежності іонізації домішок у Ge в діапазоні температур 4–400 К та за концентрацій домішок від 1×10^{14}до 1×10^{18} см$^{-3}$. Імовірності іонізації оцінено для типових акцепторних домішок (бор, галій, індій) і донорних домішок (фосфор, миш'як, сурма) з енергіями активації в межах 10–16 меВ. Результати демонструють виражений ефект «заморожування» домішок за кріогенних температур, коли імовірність іонізації зменшується до 0,1–0,2 для слаболегованого Ge ($N \leq 10^{15}$ см$^{-3}$), що призводить до зниження концентрації носіїв заряду більш ніж на 80–90% порівняно з припущенням повної іонізації. Донорні домішки з меншою енергією активації досягають майже повної іонізації ($P(T) > 0.9$) при температурах 100–150 К, тоді як акцепторні домішки з вищою енергією активації потребують температур вище 200–250 К. Збільшення концентрації домішок до 10^{17}–10^{18} см$^{-3}$істотно послаблює ефект заморожування, забезпечуючи імовірність іонізації понад 0.8 вже при температурах 50–70 К. За кімнатної температури та вище всі досліджені домішки демонструють майже повну іонізацію в усьому діапазоні досліджених концентрацій. Отримані результати надають кількісні рекомендації щодо вибору типу та концентрації домішок для Ge-базованих електронних, оптоелектронних і кріогенних пристроїв та підкреслюють необхідність явного врахування неповної іонізації домішок під час моделювання та оптимізації пристроїв, що працюють за низьких температур.

Ключові слова: *ширина забороненої зони напівпровідника; германій (Ge); поріг легування; температурні ефекти; концентрація носіїв заряду; неповна іонізація; оптимізація пристроїв*

East European Journal of Physics. **2.** 219-231 (2026)
DOI:10.26565/2312-4334-2026-2-23 ISSN 2312-4334

COMPARATIVE EFFECTS OF COLD PLASMA AND THERMAL ANNEALING ON THE STRUCTURAL AND MORPHOLOGICAL PROPERTIES OF NICKEL AND IRON OXIDE COATINGS

Aya Jumaa, Duha K. Harfesh, A.N. Yasoob*, Hamid H. Murbat
University of Baghdad, College of Science for Women, Department of Physics, Baghdad, Iraq
**Corresponding Author email: Noorya_phys@csw.uobaghdad.edu.iq*
Received January 25, 2026; accepted April 30, 2026

This study comprehensively investigates and compares the effects of Cold Atmospheric Plasma (CAP) treatment as a potential alternative to thermal annealing on the structural and morphological properties of two distinct thin films: nickel (Ni) and iron oxide (Fe_xO_Y), both electrochemically deposited on ITO substrates. Characterization via X-ray diffraction (XRD) and atomic force microscopy (AFM) revealed that the material's nature dictates its response to post-processing. For nickel, short-duration CAP exposure (2.5-5 min) optimally enhanced crystallinity and surface smoothness by reducing grain size and roughness, while longer exposures led to oxidation and increased roughness. Conversely, for iron oxide, even brief CAP treatment initiated a transformation from monocrystalline to polycrystalline structure, forming a mixture of phases (Fe_3O_4, γ-Fe_2O_3). The smoothest iron oxide surface was achieved after 5-10 minutes of CAP, with excessive exposure (15 min) causing surface damage. Thermal annealing proved superior for nickel at 200°C, yielding the smallest grains and smoothest surface. However, it was inadequate for optimal iron oxide crystallization. This work demonstrates that CAP as a fast, energy-efficient alternative to conventional annealing. The optimal parameters are highly dependent on the material-specific and crucial for tailoring functional coatings in catalysis and sensing.
Keywords: *Cold Plasma; DBD; Plasma annealing; Nickel coating; Iron oxide; Hematite; Magnetite*
PACS: 52.77.-j, 81.15.Pq, 68.55.-a, 61.05.cp, 68.37.Ps, 52.50.Jm, 61.66.Fn, 81.40.Ef, 81.40.Rs

1 INTRODUCTION

Non-thermal plasma is one of the technologies that has wide applications in industry and medicine, such as oxidation [1], affection on living tissue [2], and synthesis nanoparticles [3]. Furthermore, the high energy of plasma is capable of annealing materials through surface treatment. Annealing is a critical process used to enhance the properties of various materials through controlled heating and cooling [4, 5]**.** Annealing can lead to a reduction in grain size, improve crystallinity, hardness, and electrical conductivity [6]. Many annealing techniques have been improved. The thermal annealing technique is a common method [7] involves heating a material to a specific temperature, maintaining that temperature for a set duration, and then cooling it [8]. Another method that can be used for annealing is treating with plasma [9,10]. The physical and chemical properties of materials may be modified by exposure to cold plasma. This improve wettability in polymers, raising surface energy and altered chemical compositions [11]. Plasma exposure affects recrystallization behavior by slowing down recrystallization, thus preserving mechanical strength, enhancing activation of metal surfaces, and altering surface morphology [12]. There are many types of plasma production systems that are used in annealing material, such as hollow cathode discharge, RF plasma annealing[13], atmospheric pressure plasma jet [14]. One of these systems is the dielectric barrier discharge [15], (DBD plasma) can be used in surface annealing [16, 17]; DBD plasma systems typically consist of two electrodes, with at least one covered by a dielectric material. This setup prevents the formation of a continuous arc and allows for the generation of microdischarges. The dielectric barrier causes the formation of numerous microdischarges, which are small, transient plasma channels that occur between the electrodes. These microdischarges are responsible for the generation of reactive species [18]. These species are effective in breaking down pollutants and sterilizing surfaces [19]. The electrical model of DBD plasma includes components like stray inductance and air-gap capacitance, which create voltage and current oscillations. These oscillations are damped by plasma resistance, ensuring a stable and streamer-free plasma discharge. It can operate at atmospheric pressure without the need of vacuumed system [20] and the low-temperature nature of DBD plasma prevents thermal damage to heat-sensitive materials [21]. The mechanisms underlying DBD plasma annealing involve interactions between reactive plasma species (e.g., ions, radicals, and UV photons) and the material surface. These interactions of reactive species lead to new functional groups (e.g., –COH, –COOH) on the surface, enhancing chemical activity and wettability [22].Plasma treatment can increase surface roughness, improving mechanical interlocking and adhesion properties [23].

In this work, we compared the conventional technique of annealing based on heating with annealing by DBD plasma for iron oxide and nickel thin films prepared by electrochemical deposition, and studied their structural characteristics using X-ray diffraction (XRD) to investigate the crystallinity and phase changes and atomic force microscopy (AFM) to measure the changes in surface roughness.

Cite as: A. Jumaa, D.K. Harfesh, A.N. Yasoob, H.H. Murbat, East Eur. J. Phys. 2, 219 (2026), https://doi.org/10.26565/2312-4334-2026-2-23
© A. Jumaa, D.K. Harfesh, A.N. Yasoob, H.H. Murbat, 2026; CC BY 4.0 license

2. MATERIALS AND METHODS

A nickel electrolyte solution was prepared by dissolving 1.5 M of Nickel (II) sulfate hexahydrate $NiSO_4 (H_2O)_6$, 0.3 M of Nickel (II) chloride ($NiCl_2$) and 0.7 M of boric acid (H_3BO_3) are added to 25 ml of de-ionized water. The solution was heated 75°C whiles being stirred with a magnetic stirrer until it had completely dissolved. The pH of the resulting solution was measured and found to be 4.5.

To prepare iron aqueous electrolytes, 0.5 M ferrous chloride (FeCl2) and 0.4 M boric acid (H3BO3) was made by dissolving in 100 ml of deionized water at 25°C.The solution was stirred on a magnetic stirrer until all components were fully dissolved, and the final pH was adjusted to 3.

A simple solution-based method, electrochemical deposition depends on oxidation-reduction reactions within an electrochemical cell. This cell consists of two electrodes, cathode as the working electrode and the anode as counter electrode. The chemical reaction occurring at the electrode surface depends on potential difference across these two electrodes that is controls by the transformation of electrons that drives the chemical reactions at the electrode surfaces.

The cell operated by DC power supply, and the voltage and current flowing between the electrodes control the chemical processes.

For deposition of nickel, the anode is made of pure nickel (99.9%), and in the case of deposition of iron, the anode is made of stainless steel. The cathode is a substrate made of indium tin oxide(ITO) on which the electrolyte is deposited. The nickel electrolyte, prepared in a laboratory and maintained at 75°C, is placed on the heater to keep its temperature at 75°C for deposition on the cathode. Both electrodes are immersed in the electrolyte-filled flask, with a small distance between them of less than 1 cm. The chemical interaction that achieved efficient deposition began at a voltage (4.5 V) and current (0.5 A) for 10 seconds of the deposition process.

During iron oxide deposition, the stainless-steel electrode is reached to the positive terminal of power supply and make it anode, and the (ITO) substrate reached to negative terminal of power supply serving as a cathode. Both electrodes are immersed in the electrolyte solution at room temperature. The chemical interaction that achieved efficient deposition began at a voltage (10 V) and current (0.5 A) for 5 seconds, the electrolyte deposited homogenously.

The prepared thin films of nickel and iron were exposed to a cold plasma discharge device, which included a high-voltage power supply (AC) and two electrodes made of stainless steel. the magnitude of applied voltage about (15 kV) A glass dielectric medium was used to protect the electrical contact between the electrodes and was positioned between them to maintain plasma discharge stability and safety. The prepared films were exposed to the plasma for (2.5, 5, 10 and 15) minutes.

The prepared thin films have been treated by the conventional method of annealing using heat in a furnace at 200°C and 400°C for two hours, and compared with the results of annealing by DBD. The samples were prepared and processed to examine improvements in their structural and crystalline properties using "XRD, and AFM" for all samples, control, after exposure to cold plasma, and annealed samples by high temperature annealing.

RESULTS AND DISCUSSION

X-ray Diffraction Results

The XRD patterns of the prepared nickel and iron oxide synthesized via electrochemical deposition were measured using X-ray diffraction instrument from the Netherlands by Philips Company (PW1730).

X-ray diffraction of nickel

Fig. 1 represents the XRD pattern of electrochemically deposited nickel before annealing or exposing to cold plasma (control)The figure clarifies peaks belong to nickel oxide (Ni_2O_3) at $2\theta = 30.392^o$ correspond to (002) plane, 44.542° and 52.553° belong to (FCC) nickel element (Ni) correspond to (111) and (200) miller indices respectively according to The other two peaks of refer to hexagonal structure of Ni $(OH)_2$ at $2\theta = 19.581^o$ and 33.408° the orientations are:(001) and (100) respectively. These results have been matched with JCPDS files no. (00-014-0481), (00-003-1043) and (00-003-0177) [24].

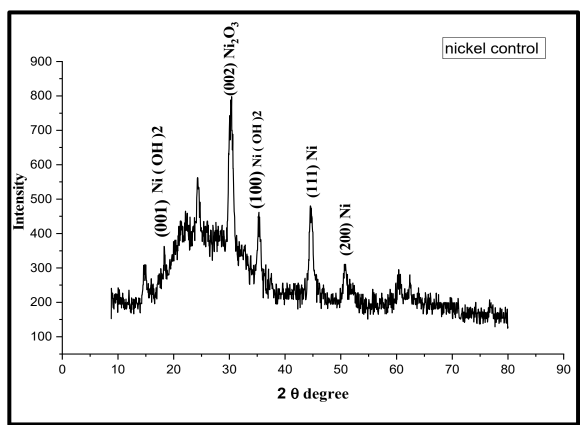

Figure 1. XRD diffraction of nickel prepared by electro chemical deposition before annealing by heating or exposing to plasma.

Furthermore, we used the Scherrer equation [25] to determine the crystalline size of nickel by analysis of the peak broadening by using Eq. 1:

$$D = \frac{k\,\lambda}{\beta \cos\theta} \tag{1}$$

It was found the average crystalline size is about 11 nm. Fig (2) represented the XRD pattern for samples after exposed to cold plasma, from Fig. (2a) we noted that after exposed the sample to cold plasma for 2.5 min, an increased in the intensity of the nickel peaks at angles 44.5° and 52°, indicating an increase in its crystallinity.

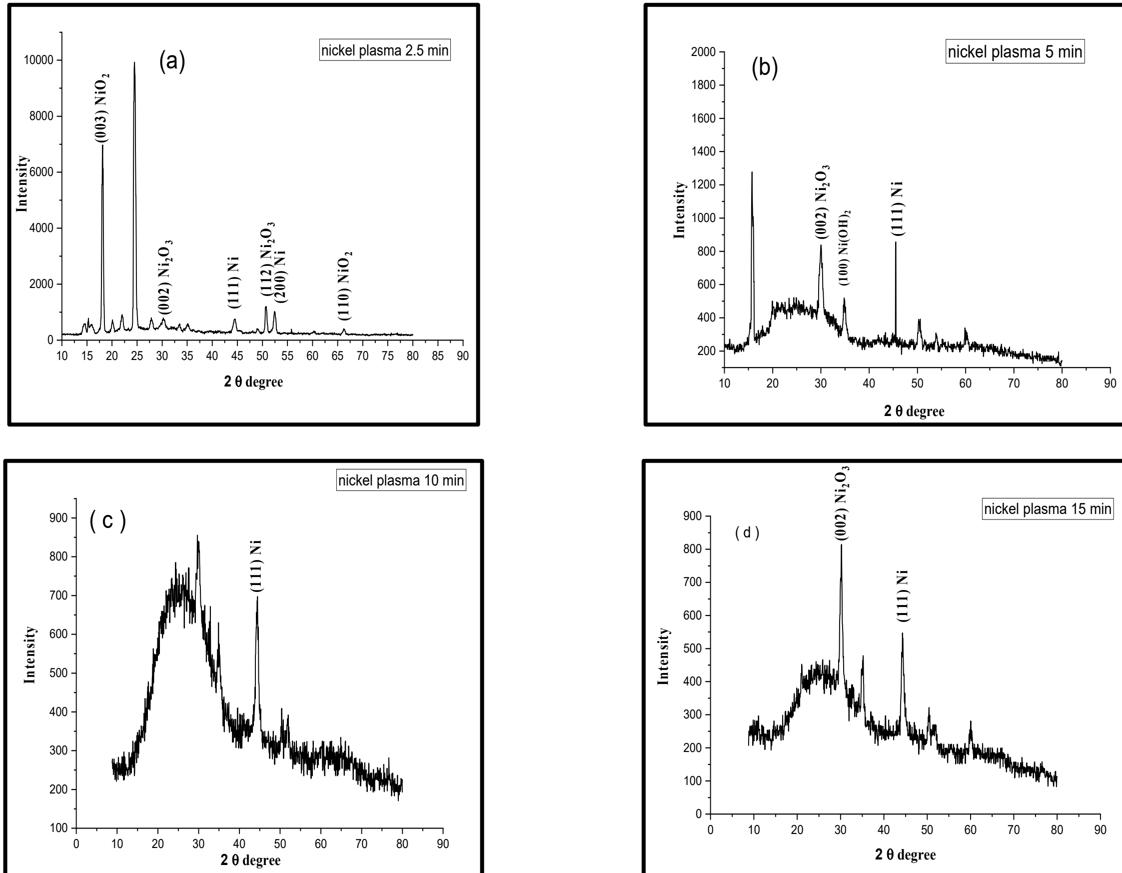

Figure 2. XRD of nickel after exposing to plasma for: (a): 2.5 min, (b): 5 min, (c):10 min, (d): 15 min

This was accompanied by the growth of other peaks, suggesting the emergence of other phases as well as nickel oxides. Additionally, a decrease in the background was observed, indicating good crystallization of the material. The reactive species generated in DBD plasma can be broadly categorized into reactive nitrogen species (RNS) like nitric oxide and nitrogen dioxide [26] and reactive oxygen species (ROS) such as singlet oxygen, atomic oxygen, ozone, and ion The plasma oxidation by ROS may be the main cause of formation of nickel oxide. These ROS rapidly react with nickel surfaces, causing oxidation and formation of nickel oxide layer, also plasma containing a high fraction of dissociated oxygen can form nickel oxide films in seconds, indicating the strong oxidative power of plasma-generated ROS. High dissociation of oxygen in plasma increases the availability of ROS, accelerating the oxidation processes [27].

Furthermore, enhancing the interaction between nickel and its support, leading to improved crystallinity and stability by promoting the formation of nanoparticles with a flat morphology [28]. And lead to formation new phases of nickel oxide in different orientation at 2θ: (18.55°,30.24°,44.59°, 52.230° and 66.192°) corresponding to hkl ((003), (002), (111), (200) and (110)) respectively.

Upon increasing the plasma exposure time starting from 5 minutes, the sample exhibited an increase in the intensity of the Ni (111) peak but less than at (2.5 min), particularly upon reaching 10 minutes of exposure. This was an increase in the intensity of nickel oxide peaks, caused by plasma-induced surface oxidation and the formation of new functional groups. The increased intensity of the nickel oxide peaks indicates enhanced surface oxidation at longer exposure times, resulting from the generation of free radicals and a gradual transformation from metallic nickel to nickel oxides (such as NiO or $Ni(OH)_2$). These oxides are chemically active materials widely used in catalysis, batteries, and sensors, as the process introduced new functional groups suitable for catalytic applications[29, 30]. As observed in Fig. (2d), the sample after 15 minutes of exposure became nearly identical and closely matching the control sample, despite the variations observed at intermediate exposure times (2.5-10 minutes). This suggests surface saturation and reaching to an equilibrium

state, where some oxides decompose, crystal rearrangement occurs, and the crystalline structure returns to one closely resembling pristine nickel. It is noteworthy that this finding aligns with our previous study [15], where chemical changes in the liquid phase were observed to reach saturation after 15 minutes. Prolonged plasma exposure introduces energetic ions and reactive species that can etch the film surface, create defects, and break down crystalline domains, leading to increased amorphization and reduced crystallinity, so short plasma exposures may initially enhance crystallinity by promoting surface mobility and ordering, but exceeding a critical exposure time reverses this effect, transforming the film into an amorphous state [31].

Fig. (3) represented annealed samples for (200, 400)ºC. According to JCPDS files these peaks refer to Ni, NiO_2, Ni_2O_3.This result was compared with nickel film synthesized by the same method. The other peaks that appeared but didn't distinguish as one of the nickel compounds may refer to the rest of precursors or impurities.

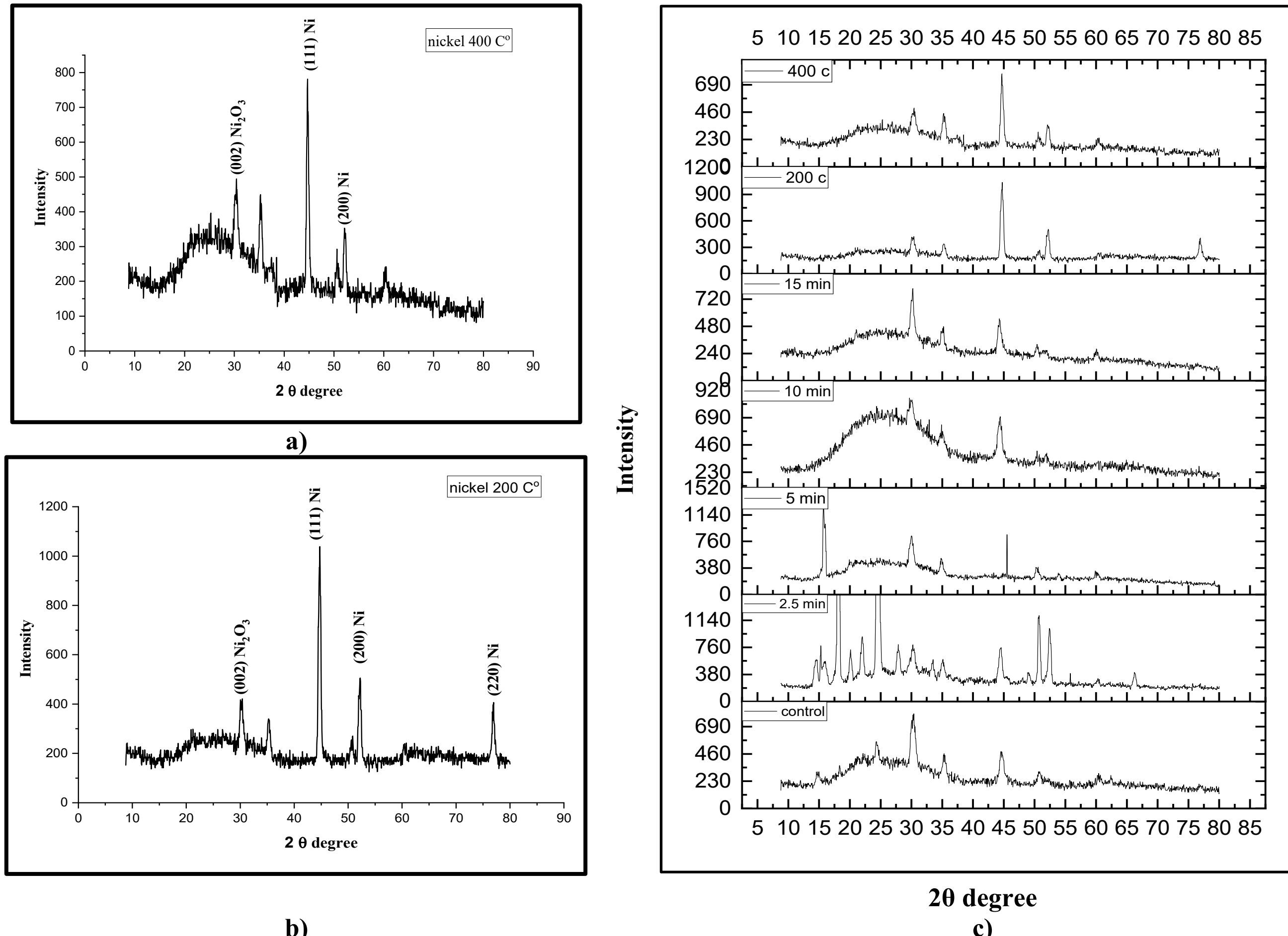

Figure 3. XRD of nickel after heating for: (a) 200°C, (b) 400°C, (c) all treatments (control, (2.5, 5, 10, 15) min, (200, 400)°C

The annealing process is important for enhancing the crystalline structure and functional properties of thin films. It was observed that annealing significantly improves the structure specially at 200°C. This enhancement was evidenced by an increase in crystallite size and the intensity of the Ni (111) diffraction peak. However, when the temperature was raised to 400°C, the crystallinity decreased, as indicated by a reduction in peak intensity. However, conventional thermal annealing typically requires prolonged heating (≈2 hours at 200 °C followed by gradual cooling that may take up to 24 hours), which consumes significant time and energy. In this context, cold plasma has emerged as a relatively fast, low-temperature alternative capable of inducing atomic rearrangement and surface modification within just a few minutes. It is anticipated that this work will contribute to the development of a time- and energy-efficient annealing strategy while preserving the quality of the crystalline structure. Ni as a predominant phase with fine structure. Heating to 400 °C also led to crystalline Ni at nearly the same diffraction angles with less intensity.

Atomic Force Microscopy (AFM) Analysis of Nickel

The surface modification characteristics including morphology and roughness have been tested by atomic force microscopy (Mountains SPIP® Expert8.2.10392). (Fig. 4) illustrates the topographical graphs of nickel thin film (a) control, that subsequently subjected to either to cold plasma treatment for various exposure times (b): 2.5 min, (c): 5 min, (d):10 min, (e): 15 min), and to thermal annealing ((f) 200 °C, (g) 400°C). The surface analysis as summarized in Table (1) evaluated in terms of mean grain size, surface roughness, root mean square, and threshold.

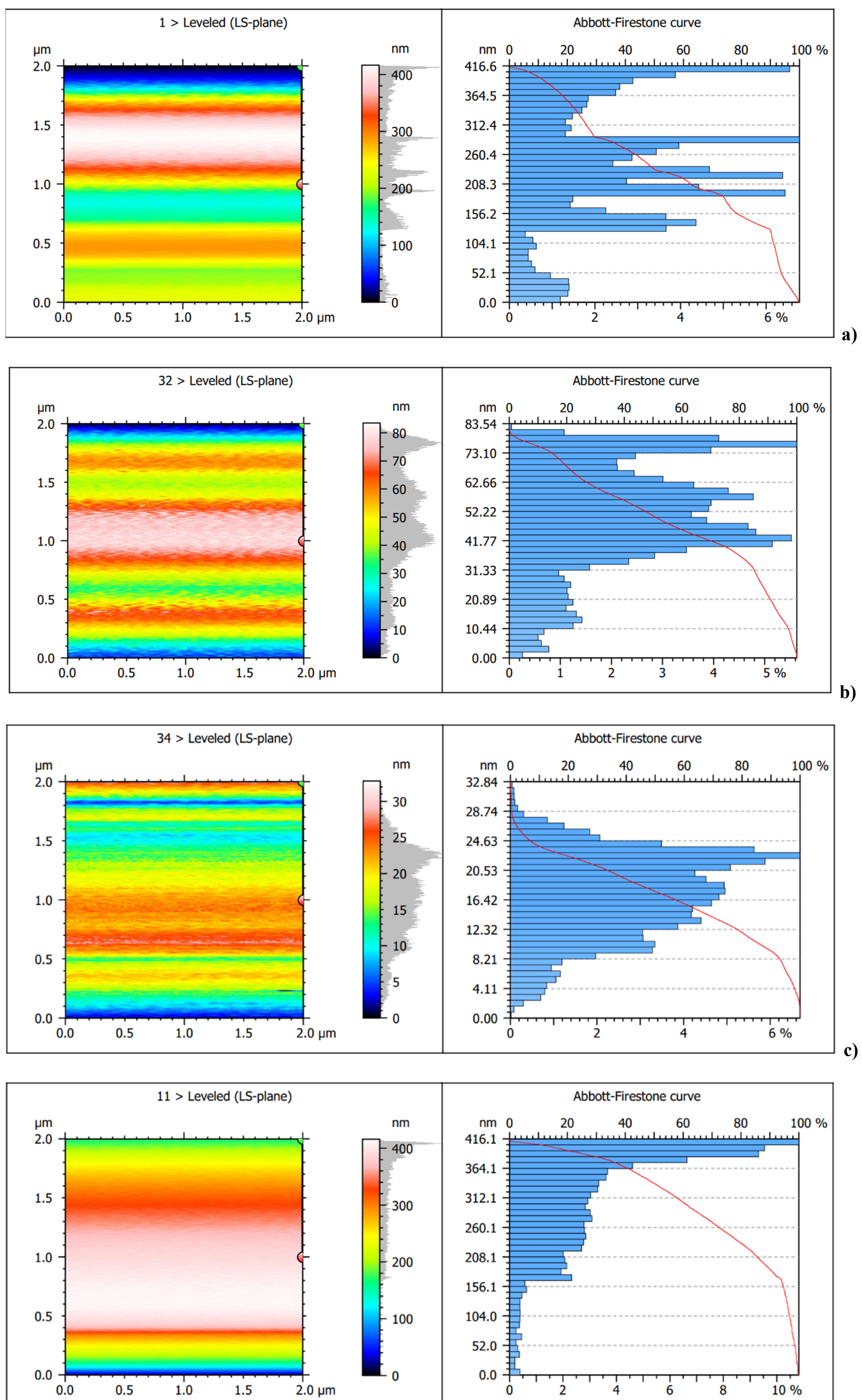

Figure 4. AFM of nickel thin film for: (a) control (b): 2.5 min, (c): 5 min, (d):10 min, (e): 15 min (f) 200 °C, (g) 400 °C

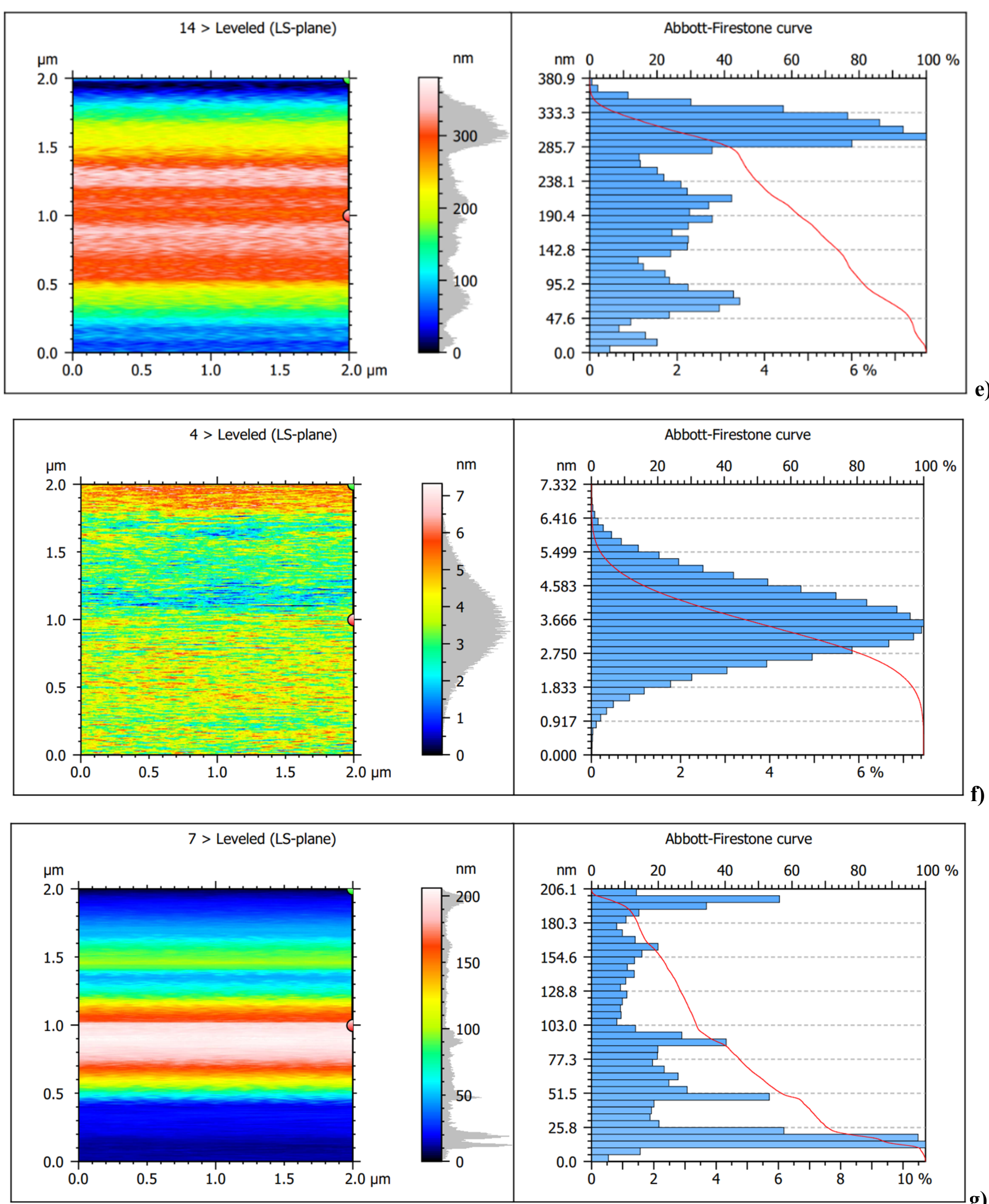

Figure 4. AFM of nickel thin film for: (a) control (b): 2.5 min, (c): 5 min, (d):10 min, (e): 15 min (f) 200 °C, (g) 400 °C (*continued*)

(We show that from Fig. (4) the change in grain size, RMS, and roughness between control (Fig. 4a), which has a large grain size (≈ 262 nm) with high roughness and RMS (Ra ≈ 71.6 nm, RMS ≈ 87.2 nm) as listed in Table (1). These values are consistent with a surface that has large grains and pronounced topographical features. Accordingly, the threshold value is also high (≈ 244 nm), reflecting a broad distribution of surface elevations.

Table 1. Summarized the AFM analysis of nickel samples

Samples	mean diameter (nm)	Surface Roughness (nm)	Root Mean Square (nm)	Threshold (nm)
control	262.4	71.60	87.16	243.8
2.5 min	52.77	12.26	14.40	50.12
5 min	17.96	4.572	3.666	17.09
10 min	323.6	41.65	57.42	312.7
15 min	228.2	47.02	57.17	218.7
200 °C	4.014	0.7064	0.8828	3.594
400 °C	96.05	39.84	34.09	82.39

After exposure to cold plasma we show that the short intervals (2.5, 5 min) gave better results, the grain size decreases (down to ≈18 nm at 5 min), and reduction in roughness (Ra≈4.6 nm, RMS≈3.7 nm), this is due to the interaction between the components of cold plasma (ions, free radicals ROS and RNS, UV photons) with surface, these species in plasma DBD environment that provides high-energy ions bombard the surface increasing their mobility. This enhanced mobility allows atoms to migrate and fill in surface valleys, leading to a smoother surface by enhancing fusion process. For nickel, the plasma can modify the oxidation states and surface chemistry, potentially leading to a more stable surface layer. This chemical modification can also enhance the adhesion of subsequent layers, contributing to a smoother overall surface [32]. Through these interactions, aggregates with weak bonding removed, and activation of nucleation new sites.This leads to the formation of finer grains and smoother surfaces. The Threshold values decrease correspondingly (≈17–50 nm) as the range of height variations narrows. However, at longer exposure time (10, 15 min) grain size increases again (up to ≈324 nm at 10 min), and roughness rises (Ra≈41–47 nm) and extends to control sample at (15 min) because the continuity of exposure of (CAP), led to the formation of nickel oxide (NiO) on the surface when treated with oxygen plasma. This oxide layer has a smaller domain size compared to the metallic nickel, contributing to the roughness[33]. as well as observed, that in XRD examination as shown in Fig. 2d. As a result of annealing that shown in (Fig. 4f) & (Fig. 4g), at 200°C gave smallest grain size and (≈4 nm) with extremely low roughness (Ra≈0.71 nm, RMS≈0.88 nm) and a very low Threshold (≈3.6 nm), which led to smooth surface. At an annealing temperature 400°C, grain size and roughness decrease, though they do not achieved at 200°C. At this temperature, bulk diffusion is activated, leading to grain growth and stronger grain boundary definition.

X-ray diffraction of iron oxide

X-ray diffraction was used to study the electrochemical deposition of (FeCl2) solution on an ITO substrate. The XRD patterns prior to heating and plasma exposure are presented in Fig. 5. A single intense peak is observed at 2θ = 44.34°, which corresponds to the (400) orientation of magnetite (Fe_3O_4) according to JCPDs file no.: (1317-61-9), This indicates that the method successfully synthesized monocrystalline iron oxide.

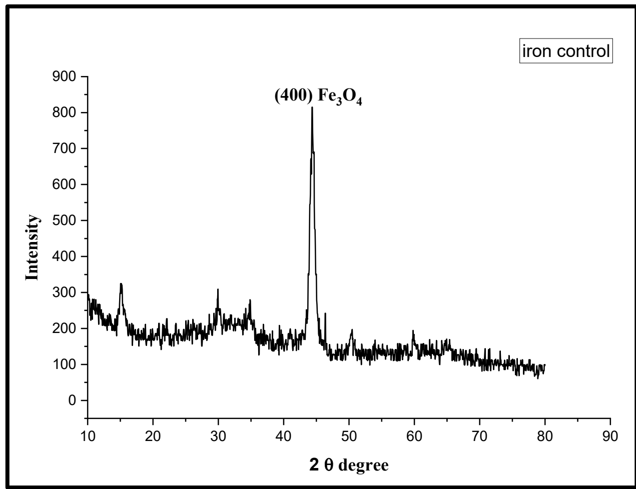

Figure 5. The patterns of XRD analysis of iron oxide before heating and exposure to plasma

According to XRD analysis (Fig. 6), the structural properties of iron oxide films were found to be strongly by exposure to DBD. By providing energy that facilities atomic rearrangement into more order configurations, the plasma drives a transformation from a monocrystalline to a poly-crystalline phases[34], and formation a mixture phases Fe3O4, γ-Fe2O3, and β-Fe2O3 in different orientation. The impact of plasma treatment duration was examining at 2.5, 5, 10, and 15 min. The shortest exposure (2.5 min) produced the highest intensity, while longer exposure time clearly reduced it, indicating lower crystallinity. furthermore, the 15 min treatment caused a phase transformation toward a different orientation.

Probably longer treatment times can increase the energy available for phase transitions, leading to the appearance of new XRD peaks corresponding to different iron oxide phases and the presence of reactive oxygen species that can interact with iron oxide films, leading to phase transformations. For instance, the presence of reactive oxygen species can promote the conversion of maghemite (γ-Fe_2O_3) to other iron oxide phases such as hematite (α-Fe_2O_3). Also Higher oxygen concentrations can lead to the formation of phases with higher oxidation states, such as ε-Fe_2O_3, while lower concentrations favor the formation of magnetite[35,36]. In comparison XRD patterns of iron oxide that annealed by heat, it can be observed in (Fig.7) that there are other peaks are formed which don't exist in the XRD patterns of prepared iron oxide by electrochemical deposition (Fig.5), with reduced intensity than that of the samples that treated with plasma. So, the heating to 200°C or 400°C is not adequate for crystallization process or phase stability. taking into account that iron oxide is typically poly crystalline structure and unstable by nature, this causes its properties to change[37,38] In contrast, exposure to plasma led to crystallization, with two phases remaining dominant.

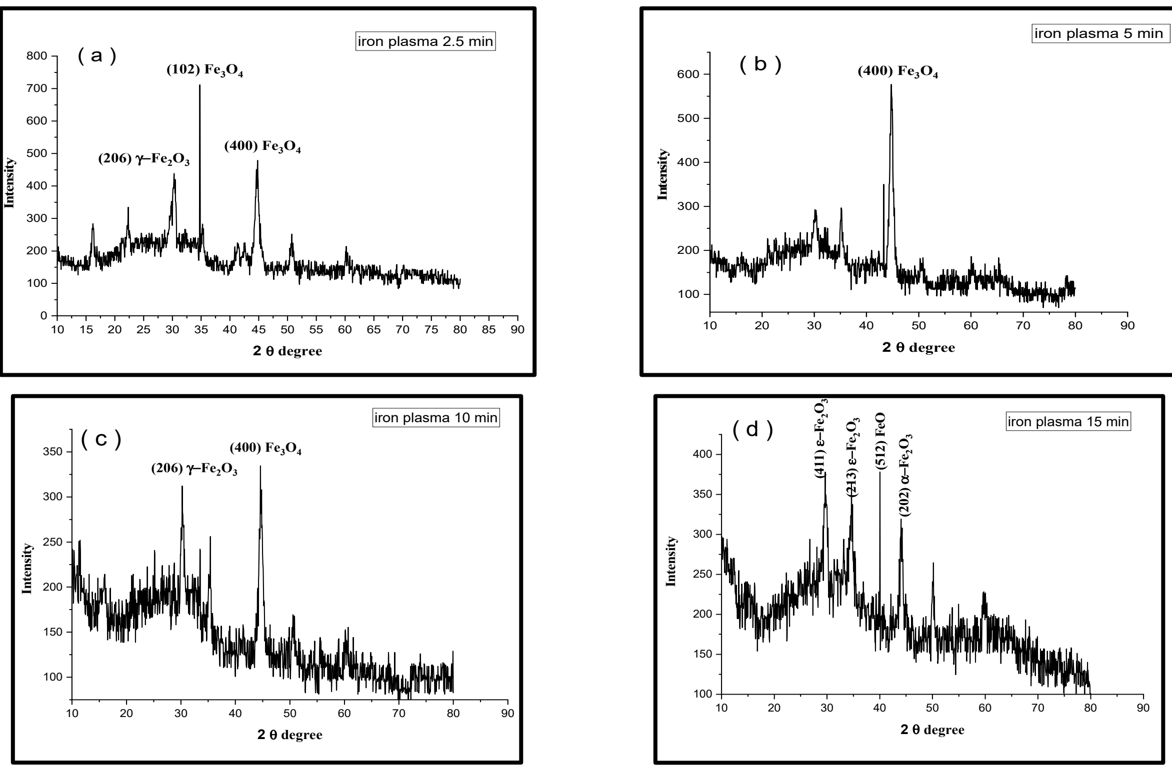

Figure 6. XRD analysis of iron oxide after exposure to plasma for: (a) 2.5 min, (b) 5 min, (c) 10 min, (d) 15 min

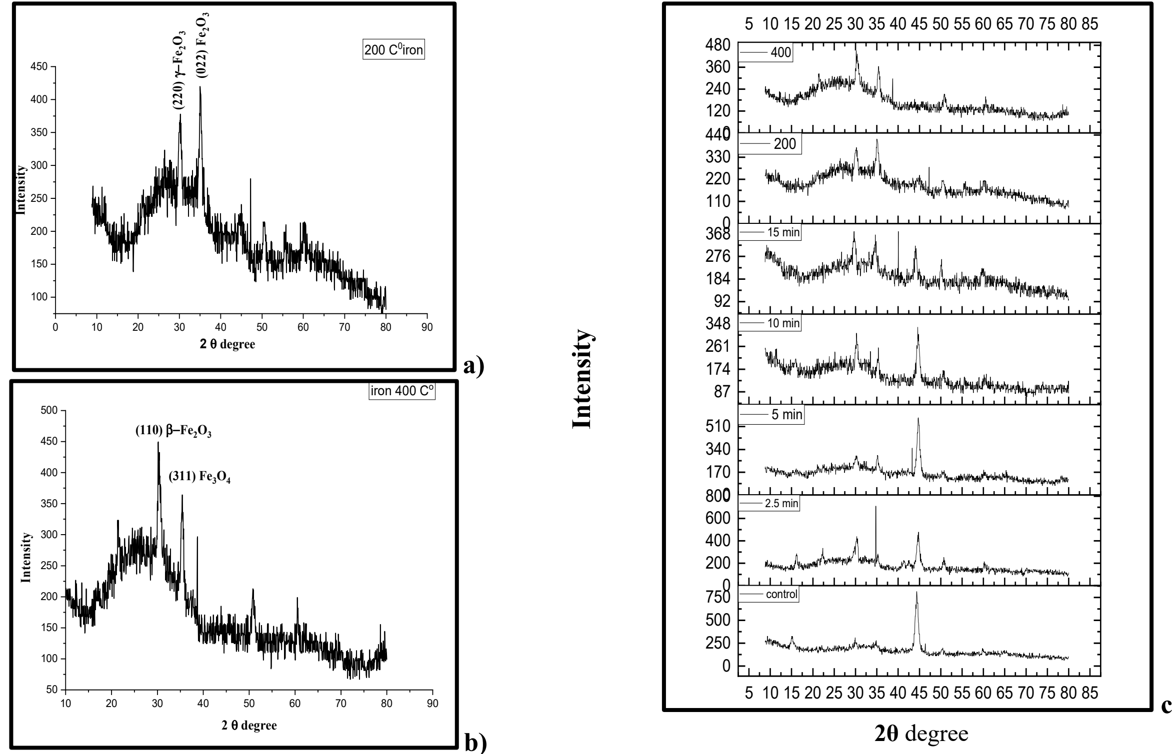

Figure 7. XRD analysis of iron oxide after heating to: (a) 200°C, (b) 400°C,
(c) all treatments (control, (2.5, 5, 10, 15) min, (200, 400)°C

Atomic Force Microscopy (AFM) Analysis of Iron Oxide

The AFM test of prepared iron oxide by electrochemical deposition represented by Fig. (8). the control sample (9 a) showed all values are large of (mean average diameter (≈509 nm), roughness, root mean square (Ra≈133 nm, RMS ≈ 159 nm), and threshold value is (≈244 nm), this indicates that very irregular surface and large sized grains as listed in Table (2).

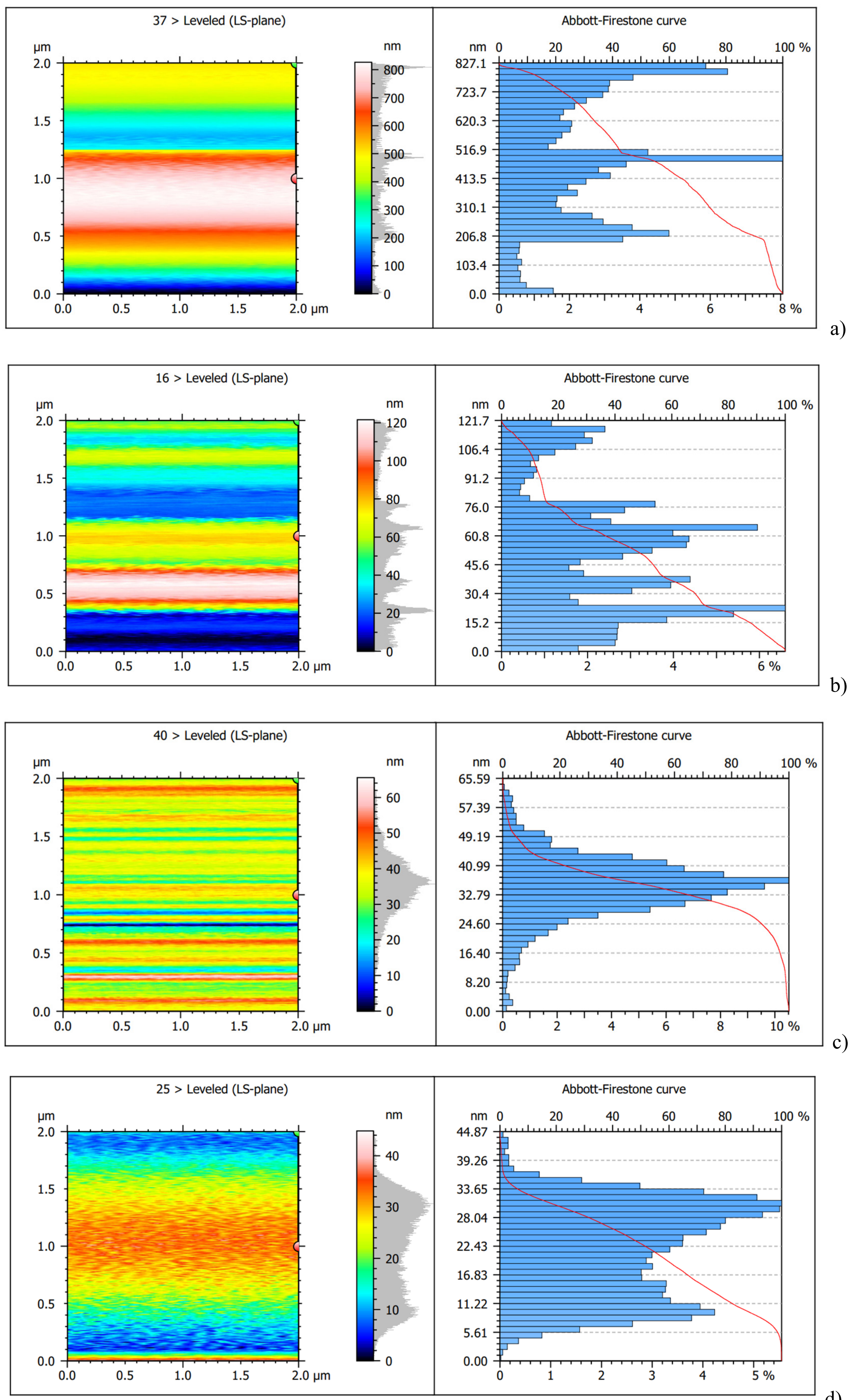

Figure 8. AFM of Iron oxide thin film for: (a) control (b): 2.5 min, (c): 5 min, (d):10 min, (e): 15 min (f) 200°C, (g) 400°C

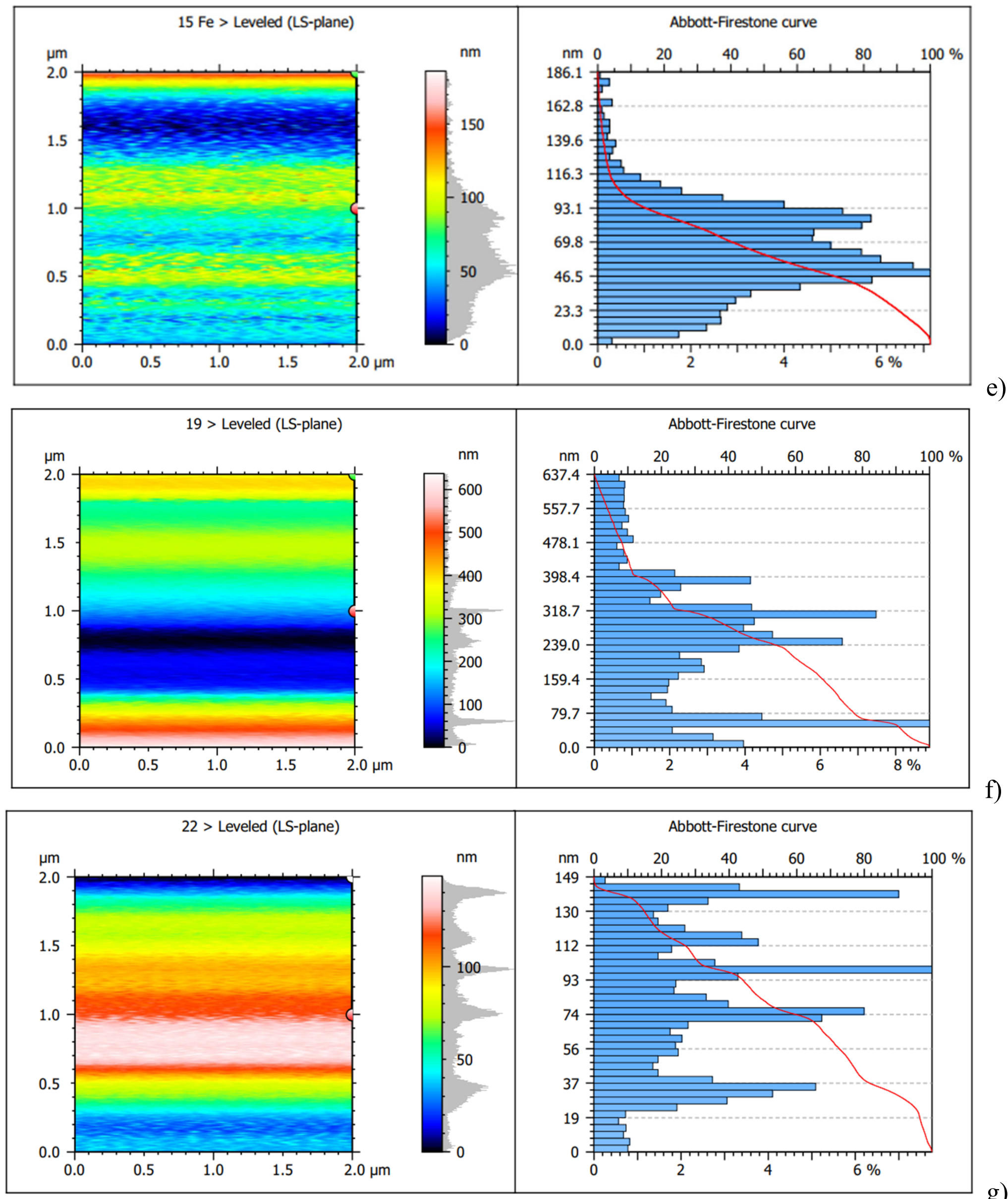

Figure 8. AFM of Iron oxide thin film for: (a) control (b): 2.5 min, (c): 5 min ,(d):10 min, (e): 15 min (f) 200℃, (g) 400℃ (*continued*)

After exposure to cold plasma, we show that at exposure times (2.5, 5, 10 min) gave better results, as shown in Fig. (8 b, c, and d), the grain size decreases and a reduction in roughness and root mean square, as listed in Table (2). This is due to the interaction between the components of cold plasma (ions, free radicals ROS and RNS, UV photons) with surface, plasma etches large grains and rough protrusions at the atomic level, resulting in significant and fast smoothing at a few minutes. When plasma processing time was increased to 15 minutes, as shown in Fig. (8 e), instead of continuing to smooth the surface, the plasma begins to create damage, such as microscopic porous pits or the random redeposition of removed material, which increases the roughness again, this mean arrived at over-treatment or excessive processing. This highlights the importance of precise control over the processing time.

Table 2. Summarized the AFM analysis of iron oxide samples

Samples	Mean diameter (nm)	Surface Roughness (nm)	Root Mean Square (nm)	Threshold(nm)
control	509.2	133.5	159.2	492.8
2.5 min	56.42	21.59	26.20	50.91
5 min	37.62	6.254	8.329	35.13
10 min	23.83	4.763	5.969	21.75
15 min	72.39	22.55	28.65	63.43
200 ºC	292.9	81.82	103.2	241.8
400 ºC	86.67	17.15	22.27	82.62

As a result of annealing that shown in (Fig. 8f) & (Fig.8g), at 200°C the grains remain large (~293 nm) and the surface is rough. The thermal energy is insufficient for true atomic diffusion. It closely resembles the control sample. At 400°C a significant improvement compared to the 200°C sample. The average diameter decreased to ~87 nm, and the surface smoothness improved. The high temperature facilitates recrystallization, where small grains either merge or reorganize into larger, more regular grains, which enhances the overall properties, though not as effectively as the optimal treatment (5 minutes).

CONCLUSIONS

From the above results, the DBD plasma can be an alternative way for annealing for a short time, a few minutes for CAP, in contrast, several hours for annealing. Nickel and iron oxide that deposited by electrochemical deposition, the reactive species in plasma enhanced the interaction and lead to better crystallinity and stability by creating nanoparticles with a flat morphology. So, the plasma achieved the same effect in increasing crystallinity and formation new phases for few minutes comparing with treatment by heat at 200°C and 400°C which needed many hours (according to X-ray diffraction). Also, another conclusion from the results is that the best time was 2.5 minutes, Prolonged plasma exposure introduces energetic ions and reactive species that can etch the film surface create defects, and break down crystalline domains, leading to increased amorphization and reduced crystallinity. AFM results of nickel clarified that the high energy species in plasma DBD bombard the surface and allowed to fill in valleys leading to smoother surface in the time from (2.5 to 10 min), while surface roughness in iron oxide the early stage of plasma exposure increased it leading to etching and the formation of microstructures that increase surface roughness where the presence of atomic hydrogen enhances the reduction of iron oxides, leading to surface modifications, the process reversed with increasing the time, So the AFM results confirmed that the effect of plasma treatment has been changed with time of exposure. And behaved different manner in nickel and iron oxide.

Acknowledgments

We would like to acknowledge the Plasma Physics Laboratory at the Physics Department, College of Science for Women, University of Baghdad, for facilitating this research.

Funding. The authors declare that no funds, grants, or other support were received during the preparation of this manuscript.

Conflict of interest: The authors declare no competing interests.

Data Availability. The experimental datasets generated and analyzed during the current study are openly available in the Zenodo repository at the following permanent "DOI 10.5281/zenodo.17440638, DOI 10.5281/zenodo.17440560, DOI 10.5281/zenodo.17440742, DOI 10.5281/zenodo.17440466."

Author Declaration: This manuscript was written entirely by humans without the use of AI tools. Only Google Translate was used for language translation assistance.

ORCID

Aya Jumaa, https://orcid.org/0009-0008-4601-9686; **Duha K. Harfesh,** https://orcid.org/0000-0003-0950-7804;
A.N. Yasoob, https://orcid.org/0000-0002-0148-5500

REFERENCES

[1] M. Gavahian, and P.J. Cullen, "Cold Plasma as an Emerging Technique for Mycotoxin-Free Food: Efficacy," Mechanisms, and Trends. Food Reviews International, **36**, 193–214 (2019). https://doi.org/10.1080/87559129.2019.1630638

[1] N. Yasoob, K. Khaleel, and H. Murbat, "Study of the Effect of Cold Plasma on the Reproductive Endocrinology of Male Rats," Plant archives, **20**, 526–531 (2020).

[2] G.A. ul J. A. ul Sattar, A.N. Yasoob, "Synthesis and Characterization of Silicon Nanoparticles by Argon Plasma Jet Technique and Its Antibacterial S. Aureus Activity," BioNanoScience, **15**, 202 (2025). https://doi.org/10.1007/s12668-025-01806-9

[3] Y. Shi, Q. Shu, P.K. Liaw, *et al.*, "Effect of annealing on mechanical and thermoelectric properties of a Al2CoCrFeNi high-entropy alloy," Materials & design, **213**, 110313–110313 (2022). https://doi.org/10.1016/j.matdes.2021.110313

[4] A.B. El-Bediwi, E. Kashita, and S.M.M. Salman, "Influence of Annealing on Creep Indentation, Surface Properties and Electrochemical Corrosion Behavior of Ni-Cr Based Dental Alloy," International Journal of Applied Sciences and Biotechnology **5**, 366–374 (2017). https://doi.org/10.3126/ijasbt.v5i3.18295

[5] M. Pita, and L. Lebea, "Effect of Annealing on the Microstructure, Hardness, Electrical Conductivity, and Corrosion of Copper Material before Accumulative Roll Bonding Processes," Journal of Engineering, **2022**, 1–8 (2022). https://doi.org/10.1155/2022/6963417

[6] J. Butt, H. Afsharnia, A.Alam, and V. Mohaghegh, "Effect of Different Annealing Methods on ULTEM 9085 Parts Manufactured by Material Extrusion," Journal of Manufacturing and Materials Processing, **8**, 258–258 (2024). https://doi.org/10.3390/jmmp8060258

[7] G.M. Alonzo-Medina, A. González-González, J.L. Sacedón, and A.I. Oliva, "Understanding the thermal annealing process on metallic thin films," IOP Conference Series: Materials Science and Engineering, **45**, 012013 (2013). https://doi.org/10.1088/1757-899x/45/1/012013

[8] R. Wang, Z. Xia, X. Kong, et al., "Etching and annealing treatment to improve the plasma-deposited SiOx film adhesion force," Surface and Coatings Technology, **427**, 127840 (2021). https://doi.org/10.1016/j.surfcoat.2021.127840

[9] N. Shota, T. Tsutsumi, I. Sakata, and M. Hori, "Plasma processing and annealing for defect management at SiO2/Si interface," Journal of Vacuum Science & Technology B Nanotechnology and Microelectronics Materials Processing Measurement and Phenomena, **41**, (2023). https://doi.org/10.1116/6.0002822

[10] W. Kaczorowski, W. Szymanski, D. Batory, and P. Niedzielski, "Effect of plasma treatment on the surface properties of polydimethylsiloxane," Journal of Applied Polymer Science, **132**, (2014). https://doi.org/10.1002/app.41635
[11] O.V. Byrka, S.S. Herashchenko, V.A. Makhlai, *et al*., "Modification and Alloying Effects In Eurofer Steel Under Powerful Pulsed Plasma Impacts," Problems of Atomic Science and Technology, 191–194 (2021). https://doi.org/10.46813/2021-134-191
[12] Y. Xu, Y. Zhang, T. He, et al., "The Effects of Thermal and Atmospheric Pressure Radio Frequency Plasma Annealing in the Crystallization of TiO2 Thin Films," Coatings, **9**, 357–357 (2019). https://doi.org/10.3390/coatings9060357
[13] O. Kylián, "Atmospheric Pressure Plasma Treatment of Materials," in: *Meeting abstracts/Meeting abstracts (Electrochemical Society CD-ROM) MA2022-02*, (2022), pp.886–886. https://doi.org/10.1149/ma2022-0219886mtgabs
[14] N.A. Yasoob, "Verification and Demonstration of the Ability of Plasma Generated from Dielectric Barrier Discharge to Oxidize," Baghdad Science Journal, **22**, 1295-1303 (2024). https://doi.org/10.21123/bsj.2024.11217
[15] R. Pernica, M. Klíma, P. Londák, and P. Fiala, "Modification of Insulating Properties of Surfaces of Dielectric High-Voltage Devices Using Plasma," Applied Sciences, **14**, 4399 (2024). https://doi.org/10.3390/app14114399
[16] T. Vopát, Š. Podhorský, M. Kuruc, et al.," Advanced approach of forming cutting edge radii on cemented carbide cutting tools using plasma discharges in electrolyte," Journal of Manufacturing Processes, **120**, 778–794 (2024). https://doi.org/10.1016/j.jmapro.2024.04.028
[17] D. Ries, E. Robert, S. Dozias, et al., "Characterisation of plasma sources for biomedical applications," International Plasma Chemistry Society, 5–8 (2011).
[18] S.K. Sharma, and A. Sharma, "Sterilization of Microorganisms Contaminated Surfaces and its Treatment with Dielectric Barrier Discharge Plasma," Transactions of the Indian National Academy of Engineering, **5**, 1 (2020). https://doi.org/10.1007/s41403-020-00124-8
[19] X. Sun, B. Zang, and B. Sun, "Surface Modification of Polyethylene in Dielectric Barrier Discharge (DBD) Plasma under Atmospheric-Pressure," IJEIR, **5**, 164–167 (2016).
[20] O. Polonskyi, T. Hartig, J.R. Uzarski, and M.J. Gordon, "Precise localization of DBD plasma streamers using topographically patterned insulators for maskless structural and chemical modification of surfaces," Applied Physics Letters, **119**, 211601 (2021). https://doi.org/10.1063/5.0071460
[21] W. Zhang, X. Xu, F. Wei, et al., "Influence of Dielectric Barrier Discharge Treatment on Surface Structure of Polyoxymethylene Fiber and Interfacial Interaction with Cement," Materials, **11**, 1873 (2018). https://doi.org/10.3390/ma11101873
[22] C. Sawangrat, P. Thipchai, K. Kaewapai, et al., "Surface Modification and Mechanical Properties Improvement of Bamboo Fibers Using Dielectric Barrier Discharge Plasma Treatment," Polymers, **15**, 1711 (2023). https://doi.org/10.3390/polym15071711
[23] R.W. Cairns, and E. Ott, "X-Ray Studies of the System Nickel—Oxygen—Water. I. Nickelous Oxide and Hydroxide," Journal of the American Chemical Society, **55**, 527–533 (1933). https://doi.org/10.1021/ja01329a013
[24] A. Jumaa, W. Aziz, and M. Abid, "Effect of molar concentration of iron(III) chloride on activity of prepared iron oxide nano-particles for degradation methylene blue," in: *2nd International Conference For Engineering Sciences And Information Technology (Esit 2022)*, (ESIT2022 Conference Proceedings, (2024).
[25] S.H. Choi, J. Kim, and Y.S. Yoon, "Effect of plasma immersion on crystallinity of V_2O_5 film grown by dc reactive sputtering at room temperature," Thin Solid Films, **493**, 1–5 (2005). https://doi.org/10.1016/j.tsf.2004.07.057
[26] M. Jenko, M. Godec, A. Kocijan, et al., "A new route to biocompatible Nitinol based on a rapid treatment with H2/O2 gaseous plasma," Applied Surface Science, **473**, 976–984 (2018). https://doi.org/10.1016/j.apsusc.2018.12.140
[27] F. Hajakbari, S. Rashvand, and A. Hojabri, "Effect of plasma oxidation parameters on physical properties of nanocrystalline nickel oxide thin films grown by two-step method: DC sputtering and plasma oxidation," Journal of theoretical and applied physics, **13**, 365–373 (2019). https://doi.org/10.1007/s40094-019-00350-8
[28] N. Ahmed, W. Luo, R. Zhao, et al., "Role of Plasma in Catalyst Preparation and Modification for Oxygen Evolution Reaction," Precision Chemistry, **3**, (2024). https://doi.org/10.1021/prechem.4c00075
[29] P. Chytrosz-Wrobel, M. Golda-Cepa, E. Stodolak-Zych, et al., "Effect of oxygen plasma-treatment on surface functional groups, wettability, and nanotopography features of medically relevant polymers with various crystallinities," Applied surface science advances, **18**, 100497–100497 (2023). https://doi.org/10.1016/j.apsadv.2023.100497
[30] H. Abdel-Khalek, M.I. El-Samahi, and A.M. El-Mahalawy, "Plasma impact on structural, morphological and optical properties of copper acetylacetonate thin films," Spectrochimica Acta Part A: Molecular and Biomolecular Spectroscopy, **199**, 356–366 (2018). https://doi.org/10.1016/j.saa.2018.04.001
[31] L. Vivet, R. Benoit, M.F. Falzon, et al., "XPS, ToF SIMS and wettability analyses on Ni surfaces after Ar-H2 RF plasma treatment: An efficient and optimized plasma treatment approach," Surface & Coatings Technology, **398**, 126094–126094 (2020). https://doi.org/10.1016/j.surfcoat.2020.126094
[32] M. Quaas, O. Ivanova, C.A. Helm, and H. Wulff, "Influence of reactive plasmas on thin nickel films," Oldenbourg Wissenschaftsverlag eBooks, **27**, 295–302 (2008). https://doi.org/10.1524/9783486992564-036
[33] K.N. Pandiyaraj, M. Karuppusamy, P. Jayamurugan, et al., "Iron oxide nanoparticles (IONPs) synthesized via a novel non-thermal atmospheric pressure plasma-assisted electrolysis: Physicochemical characterization and cytocompatibility evaluation," Advanced Powder Technology, **35**, 104441 (2024). https://doi.org/10.1016/j.apt.2024.104441
[34] M. Serhan, D. Jackemeyer, M. Long, et al., "Total Iron Measurement in Human Serum With a Novel Smartphone-Based Assay," IEEE Journal of Translational Engineering in Health and Medicine, **8**, 1–9 (2020). https://doi.org/10.1109/jtehm.2020.3005308
[35] V. Stranak, Z. Hubicka, M. Cada, et al., "Influence of reactive oxygen species during deposition of iron oxide films by high power impulse magnetron sputtering," Journal of physics D, Applied physics, **51**, 095205–095205 (2018). https://doi.org/10.1088/1361-6463/aaa9e6
[36] W.J. Aziz, Aya Jumaa, and M.A. Abid, "Effect of variation biomass on the properties of iron oxide NPs for hydrolysis of methylene blue dye," Journal of Physics Conference Series, **2322**, 012086–012086 (2022). https://doi.org/10.1088/1742-6596/2322/1/012086

[37] M. Chabane, C. Melkaoui, N. Ferrah, et al., "Synthesis and Evaluation of Polyacrylamide Based Filter Pellets Incorporating GAC, Iron Oxide, Zinc Oxide, and Kaolin for Chromium and Nickel Water Remediation," Revue des composites et des matériaux avancés, **34**, 221–232 (2024). https://doi.org/10.18280/rcma.340212

ПОРІВНЯЛЬНИЙ ВПЛИВ ХОЛОДНОЇ ПЛАЗМИ ТА ТЕРМІЧНОГО ВІДПАЛУ НА СТРУКТУРНІ ТА МОРФОЛОГІЧНІ ВЛАСТИВОСТІ ПОКРИТТІВ З НІКЕЛЮ ТА ОКСИДУ ЗАЛІЗА

Ая Джумаа, Духа К. Харфеш, А.Н. Ясуб, Хамід Х. Мурбат

Багдадський університет, Коледж наук для жінок, кафедра фізики, Багдад, Ірак

У цьому дослідженні всебічно досліджується та порівнюється вплив обробки холодною атмосферною плазмою (ХАТП) як потенційної альтернативи термічному відпалу на структурні та морфологічні властивості двох різних тонких плівок: нікелю (Ni) та оксиду заліза ($Fe_xO_γ$), обидві електрохімічно нанесені на підкладки ITO. Характеристика за допомогою рентгенівської дифракції (XRD) та атомно-силової мікроскопії (АСМ) показала, що природа матеріалу визначає його реакцію на постобробку. Для нікелю короткочасна обробка CAP (2,5-5 хв) оптимально покращувала кристалічність та гладкість поверхні за рахунок зменшення розміру зерен та шорсткості, тоді як триваліша обробка призводила до окислення та збільшення шорсткості. І навпаки, для оксиду заліза навіть короткочасна обробка CAP ініціювала перехід від монокристалічної до полікристалічної структури, утворюючи суміш фаз (Fe_3O_4, $γ$-Fe_2O_3). Найгладша поверхня оксиду заліза була досягнута після 5-10 хвилин CAP, а надмірна обробка (15 хв) спричиняла пошкодження поверхні. Термічний відпал виявився кращим для нікелю при 200°C, даючи найдрібніші зерна та найгладшу поверхню. Однак цього було недостатньо для оптимальної кристалізації оксиду заліза. Ця робота демонструє, що CAP є швидкою та енергоефективною альтернативою традиційному відпалу. Оптимальні параметри сильно залежать від специфіки матеріалу та мають вирішальне значення для створення функціональних покриттів у каталізі та сенсориці.

Ключові слова: *холодна плазма; DBD; плазмовий відпал; нікелеве покриття; оксид заліза; гематит; магнетит*

DOI:10.26565/2312-4334-2026-2-24 ISSN 2312-4334

INCOMPLETE DOPANT IONIZATION EFFECTS IN GAN OPTICAL PHOTOVOLTAIC CONVERTERS OVER 4–400 K FOR SPACE SOLAR ENERGY APPLICATIONS

D.A. Qalandarova[1]*, M.Sh. Ibragimova[1], U.G. Salayev[1], I.B. Sapaev[2], D.S. Mamarajabov[4], A.M. Madolimov[3], F.O. Tokhirova[4], A.I. Yusupov[5], O.A. Sattarova[6]
[1]Urgench State University, Hamid Olimjon Street, 14, Urgench, 220100 Uzbekistan
[2]National Research University TIIAME, Department of Physics and Chemistry, Tashkent, Uzbekistan
[3]Department of Traumatology and Orthopedics, Fergana Medical Institute of Public Health, Fergana, Republic of Uzbekistan
[4]Samarkand state medical university. Amir Temur str., 18, 140100, Samarqand, Uzbekistan
[5]Tashkent State Technical University, Tashkent, Uzbekistan
[6]Urgench State Medical Institute, 220100, Al-Khorezmi Street 28, Urgench, Uzbekistan
**Corresponding Author e-mail: dildora.qalandarova.90@gmail.com*
Received March 31, 2026; revised April 4, 2026; accepted May 7, 2026

We present a comprehensive numerical study of temperature- and concentration-dependent dopant ionization in GaN optical photovoltaic converters (OPCs), covering 4–400 K and doping levels from 1×10^{14} to 1×10^{18} cm^{-3}. Acceptor dopants (Mg, Zn, Be) exhibit incomplete ionization at room temperature, with Mg achieving $P_A \approx 0.60$ at 300 K and severe freeze-out $P_A < 1$ below 50 K. Donor dopants (Si, O, S) are nearly fully ionized at 300 K $P_D > 0.95$ and maintain high electron density even at cryogenic temperatures. Increasing dopant concentration mitigates acceptor freeze-out but cannot overcome intrinsic activation limits at low temperatures. These results highlight the asymmetry between p- and n-type GaN, emphasize the importance of co-doping strategies, and provide quantitative guidance for predicting carrier densities, resistivity, and device performance in high-power, space-based GaN OPCs.
Keywords: *GaN; Dopant ionization; Optical photovoltaic converters; Temperature effects; Carrier concentration; Incomplete ionization; Space solar energy*
PACS: 73.40. Lq, 73.61.Cw, 73.61.Ey, 72.20.Jv

INTRODUCTION

Wide-bandgap (WBG) semiconductors have emerged as foundational materials for next-generation power electronic and optoelectronic devices operating under extreme electrical, thermal, and radiation environments [1–10]. Compared with conventional silicon and GaAs, WBG materials such as GaN, 4H-SiC, β-Ga_2O_3, and diamond offer substantially larger bandgaps, higher critical electric fields, superior thermal conductivity, and enhanced radiation tolerance, enabling efficient operation at high temperatures and power densities [1–10]. These characteristics make WBG semiconductors attractive for advanced applications, including space-based solar energy systems, high-power laser energy transfer, radiation detectors, and high-voltage electronics [4,9,10,11–14].

Among WBG materials, gallium nitride (GaN) has received particular attention due to its wide bandgap (3.39 eV), high breakdown field, and strong III–N bond strength, which enable robust operation under elevated temperatures and high-radiation environments [4,9,10,15,16]. Similarly, 4H-SiC (3.26 eV) and diamond (5.45 eV) exhibit high breakdown voltages (3–10 MV/cm) and thermal conductivities (~3.7 W/cm·K for SiC, ~2200 W/m·K for diamond), making them suitable for high-power, high-reliability devices [3,7,17–19]. β-Ga_2O_3, with its ultra-wide bandgap (~4.8 eV), offers high theoretical breakdown voltages, although challenges related to dopant control and thermal management remain [5,20].

Despite these advantages, incomplete dopant ionization remains a critical challenge in WBG devices, particularly at low and moderate temperatures [21–24]. Large bandgaps and deep dopant activation energies lead to a significant fraction of electrically inactive dopants, limiting free carrier concentration and degrading electrical and optoelectronic performance [21–24]. Representative activation energies include Mg in GaN (~0.16 eV), B and Al in 4H-SiC (0.265-0.293 eV), B in diamond (~0.37 eV), P in diamond (~0.57 eV), and unintentional donors in β-Ga_2O_3 (110-131 meV) [3,5,7,22,23]. Incomplete ionization can result in increased resistivity, reduced carrier lifetime, and lower device efficiency, particularly under cryogenic conditions and at moderate dopant concentrations (10^{15}–10^{18} cm^{-3}) [21-25]. Incomplete ionization effects are especially relevant for optical photovoltaic converters (OPCs), where carrier transport, recombination, and resistive losses strongly influence conversion efficiency [10,26]. While GaN-based OPCs have demonstrated conversion efficiencies up to 79.6 % at laser power densities of 10 W/cm², exceeding GaAs devices by >10 %, their performance remains sensitive to temperature-dependent carrier activation and dopant ionization [10,26,27]. Radiation tolerance is also critical for space applications. GaN and III-nitride heterostructures (AlN/GaN, AlGaN/GaN, InAlN/GaN) exhibit high resistance to protons, electrons, neutrons, and γ-rays, with minimal

Cite as: D.A. Qalandarova, M.Sh. Ibragimova, U.G. Salayev, I.B. Sapaev, D.S. Mamarajabov, A.M. Madolimov, F.O. Tokhirova, A.I. Yusupov, O.A. Sattarova, East Eur. J. Phys. 2, 232 (2026), https://doi.org/10.26565/2312-4334-2026-2-24
© D.A. Qalandarova, M.Sh. Ibragimova, U.G. Salayev, I.B. Sapaev, D.S. Mamarajabov, A.M. Madolimov, F.O. Tokhirova, A.I. Yusupov, O.A. Sattarova, 2026; CC BY 4.0 license

degradation under high-dose irradiation [2,4,9,28]. Despite prior studies on WBG device modeling, most work has focused on power diodes, transistors, or laser diodes [26,27,29,30]. A systematic study of incomplete dopant ionization in GaN OPCs over cryogenic-to-elevated temperatures and practical doping concentrations is still lacking.

In this work, we investigate the temperature- and concentration-dependent ionization of GaN dopants (Mg, Zn, Be for p-type; Si, O, S for n-type) over 4–400 K and doping levels from 10^{15} to 10^{18} cm^{-3}, representative of space solar energy OPC designs. By capturing the coupled effects of temperature-dependent ionization, carrier transport, and recombination, this study provides quantitative insight into the limitations imposed by incomplete ionization and establishes design guidelines for high-efficiency, radiation-resilient GaN OPCs under extreme environmental conditions.

MATERIAL AND METHODS

2.1. Material Parameters and Doping Conditions

Gallium Nitride (GaN) is a III–V wide-bandgap semiconductor with a wurtzite crystal structure ($a \approx 3.189$ Å, $c \approx 5.185$ Å) and a direct bandgap of 3.39 eV at 300 K, enabling efficient photon absorption and emission in the blue/UV spectrum [23]. The electron effective mass is ~0.20 m_0, and hole masses are ~1.0 m_0 (heavy) and 0.3 m_0 (light), yielding high electron mobility (~1500 cm²/V·s) and moderate hole mobility (~100 cm²/V·s), critical for high-speed optoelectronic devices. GaN exhibits extremely low intrinsic carrier concentration (~10^{-10} cm^{-3}), high relative permittivity ($\varepsilon_r \approx 9.5$), and a wide breakdown field (~3.3 MV/cm), allowing compact, high-voltage OPC designs. Thermal conductivity (~230 W/m·K) and melting point (~2500 °C) support high-power operation and thermal stability [18]. N-type doping is typically achieved with Si (activation ~20–30 meV) and p-type with Mg (activation ~160 meV), where incomplete ionization impacts hole density and device performance. GaN shows strong optical absorption (~10^5 cm^{-1} at 3.4 eV) and excellent radiation hardness, making it suitable for space-based OPCs and high-power optoelectronics. Low-resistance ohmic contacts ensure efficient carrier injection and extraction, underpinning high-efficiency device operation [23].

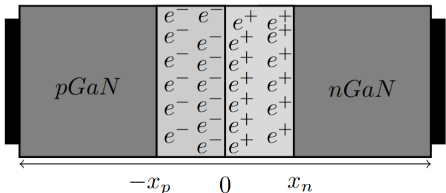

Figure 1. Schematic p-n junction in Gallium Nitride (GaN)

Figure 1 depicts a p–n junction in Gallium Nitride (GaN) with ohmic contacts at both ends and a depletion region at the junction interface. The left region (p-GaN) is p-type, enriched with holes, while the right region (n-GaN) is n-type, enriched with electrons. The depletion region extends from $-x_p$to x_n, where free carriers are swept away, leaving behind immobile ionized acceptors and donors. This creates a built-in electric field that governs carrier transport and charge separation. GaN's wide bandgap and high breakdown field enhance the junction's capability to operate under high voltages and temperatures, making it suitable for high-power optoelectronic and optical photovoltaic converter (OPC) applications.

Table 1. Donor and acceptor dopants in Gallium Nitride (GaN)

Type	Dopant	Activation Energy (meV)	Comments / Device Relevance
Acceptor	Mg	160	Most common p-type; incomplete ionization at RT
Acceptor	Zn	120	Less used; moderate p-type conduction
Acceptor	Be	150	Rare; high activation energy
Donor	Si	20	Common n-type; low resistivity, high carrier concentration
Donor	O	32	Unintentional donor; can compensate Mg
Donor	S	30	Used for n-type; can affect optical absorption

In Table 1, p-type dopants: Magnesium (Mg) is the predominant p-type dopant in GaN. Its high activation energy (160 meV) causes incomplete ionization at room temperature, limiting hole concentration and impacting device performance in high-power and optical photovoltaic converter (OPC) applications. Zinc (Zn) and Beryllium (Be) are less commonly used; Zn offers moderate p-type conduction but lower thermal stability, while Be is rarely employed due to high activation energy and toxicity. n-type dopants: Silicon (Si) is the standard n-type dopant, providing high electron concentration and low resistivity due to its low activation energy (20 meV), critical for efficient conduction layers. Oxygen (O), often incorporated unintentionally, can partially compensate Mg, reducing effective p-type conductivity. Sulfur (S) is an alternative n-type dopant but may introduce additional optical absorption, relevant for OPC efficiency. Device implications: Optimizing dopant type and concentration is crucial for balancing carrier density, minimizing resistive losses, and achieving high efficiency in GaN-based power electronics and OPC devices. Effective dopant management directly affects depletion width, internal electric fields, and overall device performance.

2.2 Analytical Modeling of Temperature-Dependent Ionization

The temperature-dependent behavior of GaN p–n junctions was analytically modeled using Poisson's equation under the depletion approximation, explicitly accounting for incomplete dopant ionization. In this approach, the electric field

$E(r)$is assumed to vary primarily along the junction axis, while lateral variations are neglected, allowing a one-dimensional approximation along the growth direction (1). The local carrier concentrations are expressed as functions of both the dopant activation energies and temperature, capturing the partial ionization of Mg acceptors in the p-region and Si donors in the n-region. This framework enables accurate prediction of depletion width, built-in potential, and electric field distribution in GaN junctions across a wide temperature range, which is essential for optimizing device performance in high-power and optical photovoltaic converter (OPC) applications.

$$\frac{dE(r)}{dr} = \frac{\partial E(x,y,z)}{\partial x} + \frac{\partial E(x,y,z)}{\partial y} + \frac{\partial E(x,y,z)}{\partial z} = \frac{\rho(x,y,z)}{\varepsilon \cdot \varepsilon_0} \tag{1}$$

Where ε is the relative permittivity of GaN, ε_0(F/m) is the vacuum permittivity, and $\rho(x,T)$is the space charge density, explicitly including temperature-dependent incomplete ionization of dopants, defined as (2):

$$\rho(x,T) = q \cdot [N_D^+(T) - N_A^-(T) + p(x,T) - n(x,T)] \tag{2}$$

In GaN, $N_D^+(T)$and $N_A^-(T)$represent the temperature-dependent ionized donor and acceptor concentrations, primarily associated with Si (n-type) and Mg (p-type) dopants. These concentrations are strongly influenced by the dopant activation energies and the local lattice temperature, which governs the fraction of electrically active dopants. The electron $n(x,T)$and hole $p(x,T)$densities include contributions from thermal excitation across GaN's wide bandgap, enabling precise modeling of carrier distributions within the junction. The ionized dopant concentrations are calculated using Fermi–Dirac statistics, adjusted for the temperature-dependent density of states. The ionization probabilities of acceptor $P_A(T)$ and donor $P_D(T)$ dopants are directly linked to the fraction of dopants that are electrically active at a given temperature and are expressed as (3a) and (3b):

$$\begin{cases} P_A(T) = \dfrac{1}{1 + \dfrac{g_A \cdot p_p(x,T)}{\gamma_p(T) \cdot N_V(T)} \cdot \exp\left(\dfrac{\Delta E_A}{kT}\right)} & (3a) \\ P_D(T) = \dfrac{1}{1 + \dfrac{g_D \cdot n_n(x,T)}{\gamma_n(T) \cdot N_C(T)} \cdot \exp\left(\dfrac{\Delta E_D}{kT}\right)} & (3b) \end{cases}$$

where $E_A$and $E_D$are the activation energies of Mg (p-type) and Si (n-type) dopants in GaN, $E_F$is the Fermi level, $k_B$is Boltzmann's constant, T is the absolute temperature, and $g_A = 2$ and $g_D = 4$ are the dopant degeneracy factors for acceptor and donor states, respectively. $N_C(T)$and $N_V(T)$represent the effective density of states in the conduction and valence bands, while $\Delta E_D$and ΔE_Adenote the dopant activation energies for donors and acceptors.

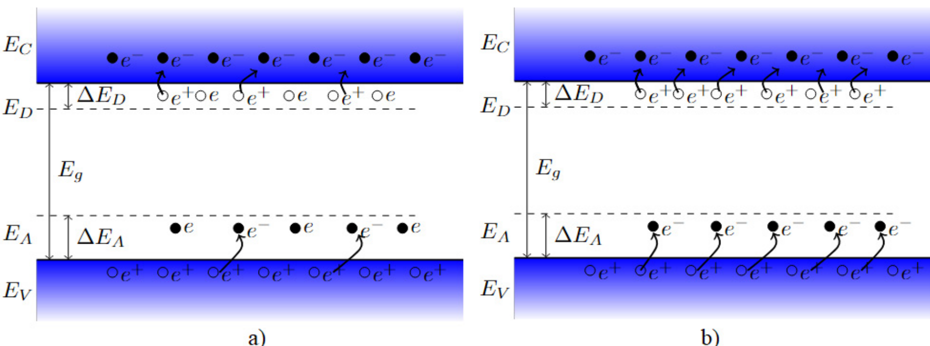

Figure 2. Schematic band diagrams of donor and acceptor levels in GaN: (a) partially ionized states at low temperatures and (b) fully ionized states at high temperatures.

To connect the quantum Fermi–Dirac statistics with classical Maxwell–Boltzmann approximations, temperature-dependent correction factors $\gamma_n(T)$and $\gamma_p(T)$are introduced. These factors ensure a physically consistent description of carrier concentrations and dopant ionization across a wide temperature range, from freeze-out at low temperatures to full ionization at high temperatures. This analytical framework enables precise calculation of temperature-dependent electron $n(T)$and hole $p(T)$densities in GaN, capturing partial ionization, freeze-out, and complete ionization regimes. Such modeling is critical for designing high-power electronics and optical photovoltaic converter (OPC) devices, where incomplete dopant activation can significantly influence carrier density, series resistance, and overall device efficiency. The donor (E_D) and acceptor (E_A) energy levels, illustrated in Figure 2, define the n-type and p-type conductivity in GaN, respectively, and determine the temperature-dependent fraction of ionized dopants that contribute to free carrier transport. This quantitative approach provides a robust foundation for optimizing GaN-based power devices, photodetectors, and

high-efficiency OPCs, under varying thermal and operational conditions. At high temperatures (Figure 2b), donor atoms (e.g., Si) are fully ionized, supplying electrons to the conduction band, while acceptor atoms (e.g., Mg) accept electrons from the valence band, generating holes. This full ionization enhances carrier concentrations and improves electrical conductivity, which is critical for high-power electronics and optical photovoltaic converters (OPCs). At low temperatures (Figure 2a), incomplete ionization occurs: only a fraction of donor and acceptor atoms contribute free carriers. The bandgap of GaN is wider at low temperatures, restricting carrier excitation, and narrows as the temperature rises, reflecting the temperature dependence of the electronic states and carrier distribution in wide-bandgap semiconductors.

RESULTS AND DISCUSSION

The temperature-dependent ionization of acceptor (Mg, Zn, Be) and donor (Si, O, S) dopants in lightly doped GaN ($N_A = N_D = 1\times10^{15}$ cm^{-3}) demonstrates pronounced freeze-out effects at cryogenic temperatures and near-complete ionization above room temperature. At T < 50 K, high-activation-energy dopants such as Mg and Be remain largely inactive (P < 0.1), while lower-activation-energy species like Zn and Si begin ionizing earlier, highlighting the strong dependence of carrier activation on dopant energy levels. In the intermediate temperature range (50–150 K), ionization increases sharply, with donors generally ionizing at lower temperatures than acceptors due to the combination of lower activation energy, higher degeneracy, and the larger conduction-band density of states. Temperature–concentration mapping further reveals that low dopant densities exacerbate freeze-out, whereas increasing dopant concentration partially mitigates incomplete ionization; however, substantial suppression persists at cryogenic temperatures even for N ~ 10^{18} cm^{-3}. These findings emphasize that dopant selection critically influences GaN device performance, particularly for low-temperature and high-power applications. Low-activation-energy donors (Si, S) ensure robust electron conduction in n-type layers, whereas careful selection and co-doping of acceptors (Mg, Zn) are necessary to enhance hole density in p-type layers. Incorporating temperature-dependent effective densities of states and incomplete ionization into device models is essential for accurate prediction of carrier density, depletion width, and current transport. From a perspective, this analysis informs the design of high-power electronics, LEDs, HEMTs, and optical photovoltaic converters (OPCs) based on GaN, ensuring reliable operation across a wide temperature range (4–400 K) and enabling optimization of both high-temperature performance and cryogenic applications, such as sensors, quantum devices, and low-noise photodetectors.

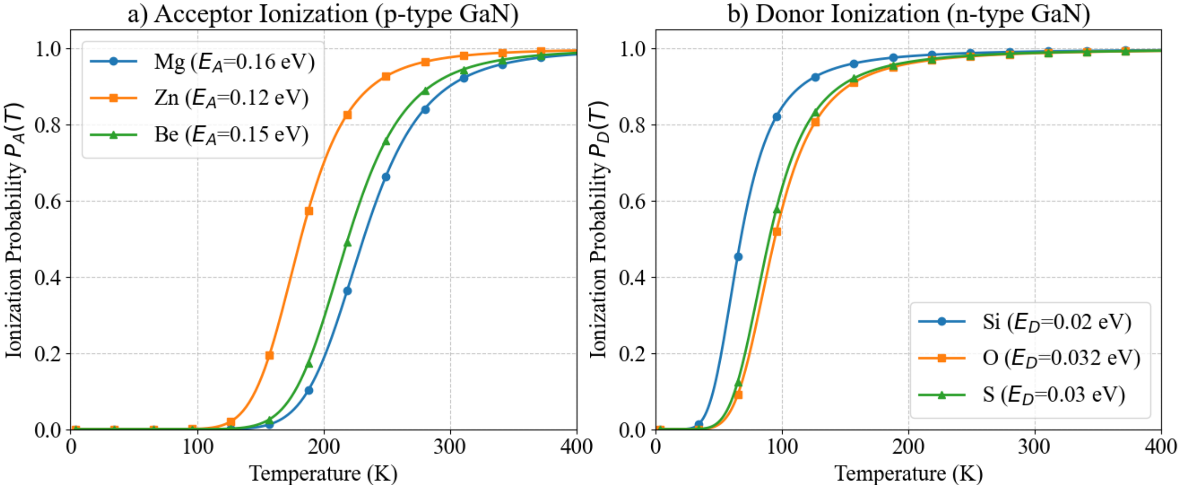

Figure 3. Ionization probabilities of dopants in GaN
(a) Acceptor ionization probability $P_A(T)$ for Mg, Zn, and Be. (b) Donor ionization probability $P_D(T)$ for Si, O, and S

In Figure 3 a), Acceptor Ionization (p-type GaN): Magnesium (Mg) is the primary p-type dopant in GaN, with a relatively high activation energy of 0.16 eV. At an acceptor concentration of $N_A = 1\times10^{18}\,\text{cm}^{-3}$, the ionization probability is highly temperature-dependent. At very low temperatures (10 K), only about 1% of Mg acceptors are ionized, increasing slightly to 5% at 50 K and 18% at 100 K. At room temperature (300 K), roughly 60% of Mg atoms are ionized, which limits the hole concentration and reduces p-type conductivity. Co-dopants with lower activation energies, such as Zn (0.12 eV) and Be (0.15 eV), exhibit higher ionization probabilities at the same temperatures. For example, at 300 K, Zn is ionized up to 75% and Be around 65%, making Zn suitable for co-doping to enhance hole density. Below 50 K, freeze-out is severe for all acceptors, with ionization probabilities below 10%, significantly impacting low-temperature device performance, such as cryogenic sensors or optical devices.

In figure 3 b), Donor Ionization (n-type GaN): Silicon (Si), the dominant n-type dopant with a low activation energy of 0.02 eV, is nearly fully ionized across a wide temperature range. Even at 10 K, Si donors are approximately 85% ionized, reaching nearly complete ionization (~99%) at room temperature. Other donors like oxygen (0.032 eV) and sulfur (0.03 eV) are partially ionized at room temperature but can act as compensating species in p-type GaN, reducing net hole concentration. Increasing the acceptor concentration reduces the ionization probability due to Fermi-level pinning. For

instance, $N_A = 1\times10^{18}\,\text{cm}^{-3}$, the Mg ionization probability at 300 K drops to approximately 55%. Donors are less affected by concentration changes, maintaining ionization probabilities above 95% over the range $N_D = 1\times10^{16} \div 1\times10^{18}\,\text{cm}^{-3}$. In p-GaN layers, the partial ionization of Mg limits hole density, increasing series resistance and reducing current injection efficiency in LEDs, HEMTs, and optical devices. Co-doping with Zn or Be can partially mitigate these limitations.

In n-GaN layers, Si ensures nearly full ionization, providing high electron conductivity with minimal resistive losses. At cryogenic temperatures below 50 K, p-type conductivity is severely suppressed due to freeze-out, while n-type layers remain conductive, which is critical for low-temperature sensors and high-power GaN devices. Mg ionization at 300 K: ~60%; severe freeze-out below 50 K. Si ionization at 300 K: ~99%; minimal freeze-out. Low-activation-energy acceptors like Zn improve p-type performance. Donors ionize at lower temperatures than acceptors, ensuring n-GaN conductivity. Incomplete Mg ionization is the primary limitation for p-type GaN, whereas donors like Si provide nearly full ionization. Accurate modeling of temperature- and concentration-dependent ionization is essential for optimizing device performance across the 4–400 K range, including cryogenic and high-power applications.

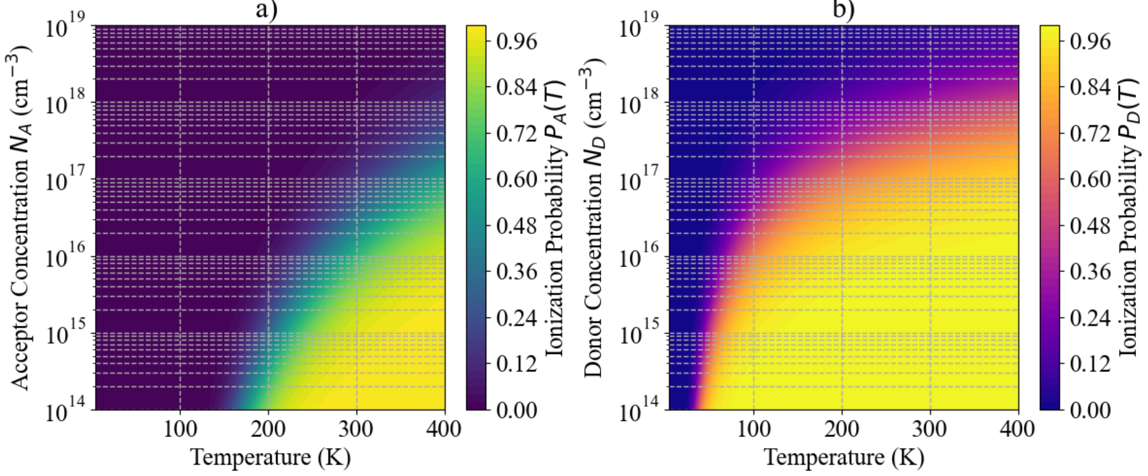

Figure 4. Temperature- and concentration-dependent ionization probabilities of dopants in GaN.
(a) Acceptor ionization probability $P_A(T, N_A)$ for Mg, Zn, and Be over 4–400 K and 10^{14}–10^{18} cm⁻³; (b) Donor ionization probability $P_D(T, N_D)$ for Si, O, and S over the same temperature and concentration ranges.

In Figure 4 a), Acceptor Ionization (p-type GaN): Magnesium (Mg) is the dominant p-type dopant in GaN, with a high activation energy of 160 meV. At room temperature (300 K) and a typical doping level of $N_A = 1\times10^{18}\,\text{cm}^{-3}$, only about 12% of Mg atoms are ionized, indicating that the majority remain neutral. This incomplete ionization directly limits hole concentration and p-type conductivity in GaN devices. The ionization probability of Mg is strongly temperature-dependent: at cryogenic temperatures below 50 K, Mg is essentially frozen out, while at elevated temperatures above 350 K, thermal energy gradually increases acceptor ionization, improving hole density. Co-doping strategies with lower-activation-energy acceptors such as Zn (120 meV) or Be (150 meV) can partially mitigate this limitation, achieving higher ionization probabilities at 300 K (75% for Zn and 65% for Be). Incomplete Mg ionization impacts p-GaN layers in optical photovoltaic converters (OPCs) and high-power electronics by increasing series resistance, reducing current injection efficiency, and limiting overall device performance. In Figure 4 b), Donor Ionization (n-type GaN): Silicon (Si) is the primary n-type dopant, with a low activation energy of 20 meV. Even at low temperatures (10 K), Si donors are already approximately 85% ionized, and at 300 K, nearly all (~99%) are fully ionized. Other donors, such as oxygen (32 meV) and sulfur (30 meV), are also nearly fully ionized at room temperature (95–96%), though they can act as compensating species in p-type GaN. This robust donor ionization ensures high electron conductivity, minimal resistive losses, and efficient current injection in n-type regions, even under cryogenic conditions. Increasing the acceptor concentration reduces the ionization probability due to Fermi-level pinning. For example, at $N_A = 1\times10^{18}\,\text{cm}^{-3}$ Mg ionization at 300 K drops to roughly 8–55%, depending on the dataset, highlighting a trade-off between doping density and incomplete activation. Donor ionization is largely insensitive to concentration changes, remaining nearly complete across $N_D = 1\times10^{15} \div 1\times10^{18}\,\text{cm}^{-3}$. For OPCs, the low hole density from incompletely ionized Mg limits photocurrent and conversion efficiency, while fully ionized Si ensures electron extraction. In high-power GaN electronics, partial Mg ionization increases series resistance, self-heating, and can reduce breakdown voltage, potentially affecting reliability. Accurate modeling of temperature- and concentration-dependent ionization is crucial for optimizing device performance from cryogenic (~4 K) to high temperatures (~400 K). Mg (p-type) has an activation energy of 0.16 eV, with room-temperature ionization ~12% and severe freeze-out below 50 K. Si (n-type) has an activation energy of 0.02 eV, with nearly full ionization (~99%) at room temperature and minimal freeze-out. Low-activation-energy acceptors such as Zn improve p-type conductivity. Donor ionization occurs at lower temperatures than acceptors, ensuring robust n-type conduction. Summary of Figures 3 & 4: Temperature-dependent ionization maps illustrate the strong asymmetry between

acceptors and donors in GaN. For Mg $E_A = 0.16\ eV$, $N_D = 1\times10^{18}\ \text{cm}^{-3}$, the ionization probability rises from ~1% at 10 K, to ~18% at 100 K, ~60% at 300 K, and ~95% at 400 K, highlighting severe freeze-out at low temperatures and partial activation at room temperature. Zn (0.12 eV) reaches ~75% ionization at 300 K, while Be (0.15 eV) reaches ~65%. In contrast, Si donors $E_D = 0.002\ eV$, $N_D = 1\times10^{18}\ \text{cm}^{-3}$, are nearly fully ionized across the entire temperature range, from ~85% at 10 K to ~99% at 300 K and ~99.5% at 400 K. These results demonstrate that p-type GaN is limited by incomplete Mg ionization at room temperature, whereas n-type GaN maintains robust electron conduction across 4-400 K. Optimizing GaN-based OPCs, high-power LEDs, and high-voltage devices requires careful consideration of these temperature- and concentration-dependent ionization effects.

CONCLUSIONS

In this work, we systematically analyzed temperature- and concentration-dependent ionization of dopants in GaN over 4–400 K and doping levels from 1×10^{14} to 1×10^{18} cm^{-3}. The results demonstrate that incomplete ionization strongly affects p-type GaN, where Mg $E_A = 0.16\ eV$ reaches only $P_A \approx 0.60$ at 300 K and experiences severe freeze-out $P_A \approx 0.60$ below 50 K. Zn $E_A = 0.12\ eV$ and Be $E_A = 0.15\ eV$ show slightly higher ionization at room temperature but remain partially inactive at low temperatures. In contrast, n-type GaN donors such as Si, $E_D = 0.002\ eV$, O, $E_D = 0.032\ eV$, and S, $E_D = 0.003\ eV$ are nearly fully ionized at room temperature $P_D > 0.95$ and maintain high carrier densities even below 50 K. Increasing dopant concentration partially mitigates freeze-out in acceptors, yet low-temperature limitations persist due to the intrinsic activation energy. These findings highlight that p-type conductivity in GaN is limited by incomplete acceptor ionization, whereas n-type layers remain highly conductive. Accurate modeling of temperature- and concentration-dependent ionization is therefore essential for optimizing high-power electronics, LEDs, optical photovoltaic converters, and cryogenic GaN-based devices, ensuring reliable predictions of carrier density, resistivity, and device performance across a wide temperature range.

ORCID

Qalandarova Dildora, https://orcid.org/0009-0005-5130-464X, **M.Sh. Ibragimova,** https://orcid.org/0009-0004-7867-7086
U.G. Salayev, https://orcid.org/0009-0001-8223-1114; **I.B. Sapaev,** https://orcid.org/0009-0004-3125-3112;
D.S. Mamarajabov, https://orcid.org/0009-0003-6043-2331; **A.M. Madolimov,** https://orcid.org/0009-0000-4645-740X
F.O. Tokhirova, https://orcid.org/0009-0005-3087-5400; **O.A. Sattarova,** https://orcid.org/0009-0006-3263-4640

REFERENCES

[1] T. Maeda, T. Narita, S. Yamada, T. Kachi, T. Kimoto, M. Horita, & J. Suda, "Impact ionization coefficients and critical electric field in GaN," Journal of Applied Physics, **129**(18), 185702 (2021). https://doi.org/10.1063/5.0050793
[2] S.J. Pearton, R. Deist, F. Ren, L. Liu, A.Y. Polyakov, & J. Kim, "Review of radiation damage in GaN-based materials and devices," Journal of Vacuum Science & Technology A, **31**(5), 050801 (2013). https://doi.org/10.1116/1.4799504
[3] N. Donato, & F. Udrea, "Static and dynamic effects of the incomplete ionization in superjunction devices," IEEE Transactions on Electron Devices, **65**(10), 4469–4475 (2018). https://doi.org/10.1109/TED.2018.2867058
[4] S.J. Pearton, Y.-S. Hwang, & F. Ren, "Radiation effects in GaN-based high electron mobility transistors," Journal of Materials, **67**, 1601–1611 (2015). https://doi.org/10.1007/s11837-015-1401-2
[5] A.T. Neal, S. Mou, R. Lopez, J.V. Li, D.B. Thomson, K.D. Chabak, & G.H. Jessen, "Incomplete ionization of a 110 meV unintentional donor in β-Ga_2O_3 and its effect on power devices," Scientific Reports, **7**, 13218 (2017). https://doi.org/10.1038/s41598-017-13341-8
[6] J.Sh. Abdullayev, & I.B. Sapaev, "Optimization of the influence of temperature on the electrical distribution of structures with radial p-n junction structures," East European Journal of Physics, (3), 344–349 (2024). https://doi.org/10.26565/2312-4334-2024-3-39
[7] Sh.B. Utamuradova, Sh.Kh. Daliev, J.J. Khamdamov, Kh.J. Matchonov, A.Kh. Khaitbaev, East Eur. J. Phys. (4), 484 (2025), https://doi.org/10.26565/2312-4334-2025-4-49
[8] J.Sh. Abdullayev, & I.B. Sapaev, "Factors influencing the ideality factor of semiconductor p-n and p-i-n junction structures at cryogenic temperatures," East European Journal of Physics, (4), 329–333 (2024). https://doi.org/10.26565/2312-4334-2024-4-37
[9] M. Phifer, S. Hossain, J. Osborne, Z. Xie, & M. Alam, "Demonstration of TCAD modeling for GaN devices," in: *IEEE SoutheastCon 2025*, (Concord, NC, USA, 2025), (pp. 1–6). https://doi.org/10.1109/SoutheastCon56624.2025.10971621
[10] H. Shang, & Y. Jiang, "A physical model of a diamond vertical Schottky diode including incomplete ionization and thermal effects," Journal of Physics D: Applied Physics, **58**(15), 155104 (2025). https://doi.org/10.1088/1361-6463/adb9fb
[11] C. Onwukaeme, & H.-Y. Ryu, "Design of GaN-based laser diode structures with nonuniform doping distribution in a p-AlGaN cladding layer for high-efficiency operation," Crystals, **15**(3), 259 (2025). https://doi.org/10.3390/cryst15030259
[12] J. Wei, J. Hao, Q. Zhao, J. Fan, F. Zhang, & Z. Dong, "Comparative study of wide-bandgap materials for neutron detection: GaN and 4H-SiC," Nuclear Technology, **211**(12), 3080–3093. https://doi.org/10.1080/00295450.2025.2462444
[13] J.F. Lozano, N. Seoane, J.M. Guedes, E. Comesaña, J.G. Fernandez, F.M. Almonacid, E.F. Fernández, & A. García-Loureiro, "Gallium nitride: A strong candidate to replace GaAs as base material for optical photovoltaic converters in space exploration," Optics & Laser Technology, **192**(Part A), 113447 (2025). https://doi.org/10.1016/j.optlastec.2025.113447
[14] J.Sh. Abdullayev, & I.B. Sapaev, "Modeling and calibration of electrical features of p-n junctions based on Si and GaAs," Physical Sciences and Technology, **11**(3–4), 39–48 (2024). https://doi.org/10.26577/phst2024v11i2b05
[15] J.Sh. Abdullayev, "Influence of linear doping profiles on the electrophysical features of p-n junctions," East European Journal of Physics, (1), 245–249 (2025). https://doi.org/10.26565/2312-4334-2025-1-26

[16] J.Sh. Abdullayev, & I.B. Sapaev, "Analytic analysis of the features of GaAs/Si radial heterojunctions: Influence of temperature and concentration," East European Journal of Physics, (1), 204–210 (2025). https://doi.org/10.26565/2312-4334-2025-1-21
[17] J.Sh. Abdullayev, I.B. Sapaev, N. Esanmuradova, S. Kadirov, & S. Kuliyev, "Mathematical analysis of the features of radial p-n junction: Influence of temperature and concentration," East European Journal of Physics, (2), 220–225 (2025). https://doi.org/10.26565/2312-4334-2025-2-24
[18] S. Chatterjee, and M. Mukherjee, "Electrical Characterization in Ultra-Wide Band Gap III-Nitride Heterostructure IMPATT/HEMATT Diodes: A Room-Temperature Sub-Millimeter Wave Power Source," J. Electron. Mater. **52**, 1552–1563 (2023). https://doi.org/10.1007/s11664-022-10090-2
[19] J.Sh. Abdullayev, I.B. Sapaev, & S.R. Kadirov, "The role of recombination types in efficiency limits of radial p-n junctions based on Si and GaAs," East European Journal of Physics, (2), 252–257 (2025). https://doi.org/10.26565/2312-4334-2025-2-30
[20] D.B. Abdirimova, F.O. Quryozov, and R.O. Ozodov, "Critical behavior of the specific heat of $Ga_{1-x}Mn_xAs$ ferromagnetic semiconductors," AIP Conference Proceedings, **2647**(1), 020033 (2022). https://doi.org/10.1063/5.0124323
[21] J.S. Abdullayev, I.B. Sapaev, J.S. Abdullayev, D.A. Juraev, M.J. Jalalov, & E.E. Elsayed, "Mathematical Modeling of Incomplete Ionization in Radial p-Si/n-GaAs Heterojunctions: Temperature and Doping Effects," J. Electron. Mater. **54**, 10484–10492 (2025). https://doi.org/10.1007/s11664-025-12391-8
[22] Sh.B. Utamuradova, Sh.Kh. Daliev, J.J. Khamdamov, Kh.J. Matchonov, M.K. Karimov, Kh.Y. Utemuratova, East Eur. J. Phys. (1), 276 (2025), https://doi.org/10.26565/2312-4334-2025-1-32
[23] J.Sh. Abdullayev, L. Abdullayeva, L. Agamalieva, & R. Ismailova, "Correlating Ni microstructure with Schottky barrier homogeneity in monolayer MoS_2 field-effect transistors," Advanced Physical Research, **7**(3), 350–357 (2025). https://doi.org/10.62476/apr.73350
[24] P. Murugapandiyan, K. Sri Rama Krishna, A. Revathy, and A. Fletcher, "Enhancement Mode AlGaN/GaN MISHEMT on Ultra-Wide Band Gap β-Ga_2O_3 Substrate for RF and Power Electronics," J. Electron. Mater. **53**, 2973–2987 (2024). https://doi.org/10.1007/s11664-024-11005-z
[25] J.S. Abdullayev, I.B. Sapaev, S.R. Kadirov, & J.Sh. Abdullayev, "Modeling of optoelectronic properties in pSi/n-$CdmZn_{1-m}S$ heterojunctions: Effects of composition and temperature," Journal of Electronic Materials, **54**(10), 11607–11617 (2025). https://doi.org/10.1007/s11664-025-12480-8
[26] I.B. Sapaev, J.I. Razzokov, J.S. Abdullayev, D.A. Qalandarova, & M.S. Ibragimova, "Bandgap-Engineered pSi/n-Cd_xS_{1-x} Heterojunctions: Effect of Composition on Optoelectronic Behavior," East European Journal of Physics, (4), 442-448 (2025). https://doi.org/10.26565/2312-4334-2025-4-44
[27] J.S. Abdullayev, D.A. Qalandarova, M.S. Ibragimova, I.B. Sapaev, & J.I. Razzokov, "Experimental and Simulation-Based Investigation of p-Si/n-CdS Heterojunctions: From Cryogenic Freeze-Out to Room Temperature Operation," J. Electron. Mater. **55**, 2229–2239 (2026). https://doi.org/10.1007/s11664-025-12642-8
[28] B. Rakhimov, F. Rakhimova, R. Ozodov, A. Saidov, and Z. Saidova, "GPU-based implementation of object detection algorithms using CUDA Vision Workbench," in: *Hybrid methods for modeling and optimizing complex systems* (HMMOCS 2024, Lecture Notes in Networks and Systems, Vol. 1481), edited by P. S. Stanimirović, S. D. Mourtas, and J. K. Sahoo, (Springer, Cham. 2024). https://doi.org/10.1007/978-3-031-95649-2_9
[29] A. Kumar, G. Kumar, & C. Kumar, "Design and Performance Evaluation of a $Ge_{1-x}Sn_x$/Ge Multiple Quantum Well Heterojunction Phototransistor for Long-Haul DWDM Optical Communication Systems," J. Electron. Mater. **55**, 3185–3202 (2026). https://doi.org/10.1007/s11664-025-12653-5
[30] J. Sadullayev, M. Akhmedov, M. Vapayev, I. Davletov, and G. Boltaev, "Modeling of Thermal Effects in a Polyimide Target Under Pulsed Laser Irradiation," East European Journal of Physics, (1), 274-280 (2026). https://doi.org/10.26565/2312-4334-2026-1-31

ВПЛИВ НЕПОВНОЇ ІОНІЗАЦІЇ ДОМІШОК У GaN ОПТИЧНИХ ФОТОПЕРЕТВОРЮВАЧАХ У ДІАПАЗОНІ 4-400 К ДЛЯ КОСМІЧНИХ СОНЯЧНИХ ЕНЕРГЕТИЧНИХ ЗАСТОСУВАНЬ

Д.А. Каландарова[1], М.Ш. Ібрагімова[1], У.Г. Салаєв[1], І.Б. Сапаєв[2], Д.С. Мамараджабов[4], А.М. Мадолімов[3], Ф.О. Тохірова[4], А.І. Юсупов[5], О.А. Саттарова[6]
[1]Ургенчський державний університет, вулиця Хаміда Олімджона, 14, Ургенч, 220100 Узбекистан
[2]Національний дослідницький університет TIIAME, кафедра фізики та хімії, Ташкент, Узбекистан
[3]Кафедра травматології та ортопедії, Ферганський медичний інститут громадського здоров'я, Фергана, Республіка Узбекистан
[4]Самаркандський державний медичний університет. вул. Аміра Темура, 18, 140100, Самарканд, Узбекистан
[5]Ташкентський державний технічний університет, Ташкент, Узбекистан
[6]Ургенчський державний медичний інститут, 220100, вул. Аль-Хорезмі, 28, Ургенч, Узбекистан

Ми представляємо комплексне числове дослідження температурно- та концентраційно-залежної іонізації легуючих домішок в оптичних фотоелектричних перетворювачах (ОФП) на основі GaN, що охоплює діапазон температур від 4 до 400 K та рівні легування від 1×10^{14} до 1×10^{18}см$^{-3}$. Акцепторні легуючі домішки (Mg, Zn, Be) демонструють неповну іонізацію за кімнатної температури, причому Mg досягає рівня $P_A \approx 0.60$ при 300 K, а нижче 50 K спостерігається сильне замерзання $P_A < 1$. Донорні легуючі домішки (Si, O, S) майже повністю іонізуються при 300 K $P_D > 0.95$ та підтримують високу електронну щільність навіть за кріогенних температур. Збільшення концентрації легуючої домішки зменшує замерзання акцептора, але не може подолати внутрішні межі активації за низьких температур. Ці результати підкреслюють асиметрію між GaN p- та n-типу, важливість стратегій спільного легування та надають кількісні рекомендації для прогнозування щільності носіїв заряду, питомого опору та продуктивності пристроїв у потужних космічних ОПК на основі GaN.

Ключові слова: *GaN; іонізація домішок; оптичні фотоперетворювачі; температурна залежність; концентрація носіїв; неповна іонізація; космічна сонячна енергія*

East European Journal of Physics. **2.** 239-244 (2026)
DOI:10.26565/2312-4334-2026-2-25 ISSN 2312-4334

DETERMINATION OF THE ENERGY SPECTRUM OF THE DENSITY OF STATES UNDER UNIAXIAL PRESSURE

M.A. Rakhmanov[1], I.G. Tursunov[1], O.O. Mamatkarimov[2], N.Yu. Sharibaev[2], S.S. Sharipbaev[2]*
[1]Chirchik State Pedagogical University, 111702, Tashkent, Uzbekistan
[2]Department of Energy Engineering, Namangan State Technical University, Namangan, Uzbekistan
**Corresponding Author email: sharipbaev1999@gmail.com*
Received January 29, 2026; revised April 8, 2026; accepted April 12, 2026

This paper considers the influence of hydrostatic pressure on the energy spectrum of the density of localized states in doped silicon n-Si, n-Si⟨Ni⟩ and p-Si⟨B,Mn⟩. Based on the experimental dependence of the relative resistivity ρ_p/ρ_0 on pressure, a model is constructed in which pressure enters via the deformation energy Ed = κP, yielding a linear shift of the trap levels $E_i(P) = E_i(0)+\alpha_i Ed$. It is shown that for different impurity centers (Mn, Ni) the deformation sensitivity of the levels differs in both sign and magnitude, which is manifested in qualitatively different behavior of $\rho_p/\rho_0(P)$. A procedure is proposed for reconstructing the relative electron concentration $N(P)/N_0$ and the associated spectrum $N_{ss}(E,P)$ from the experimental $\rho_p/\rho_0(P)$ curves. A comparison is made with the conventional temperature DLTS model, and the possibility of using a "tenso-DLTS" approach to identify donor and acceptor centers, their deformation potentials and symmetry is substantiated. The results demonstrate that hydrostatic pressure is not only an external perturbation, but also an effective spectrum-forming parameter for controlling the electronic properties of doped silicon.
Keywords: *Doped silicon; Hydrostatic pressure; Deformation energy; Density-of-states spectrum; Localized levels; Tenso-DLTS; Resistivity; n-Si⟨Ni⟩; p-Si⟨B,Mn⟩; Transition-metal impurity centers*
PACS: 71.55.Cn, 72.20.Fr, 73.40.Qv

INTRODUCTION

The study of the influence of mechanical pressure on energy levels in silicon has been actively developing for the past several decades. In the literature, several directions can be distinguished that are directly related to the problem of determining the spectrum $N_{ss}(E,X)$.

The first experiments on recording DLTS spectra under uniaxial stress showed that mechanical stress causes splitting and linear shifts of trap peaks, thereby enabling the determination of their symmetry and pressure sensitivity [1–4]. These works laid the foundation of a method in which the derivative with respect to stress X is measured and the distribution $N_{ss}(E)$ is reconstructed by analogy with temperature DLTS.

A number of studies [4–7] have shown that mechanical stresses, including hydrostatic pressure, accelerate the formation of oxygen thermal donors and change the concentration of oxygen clusters. This explains the decrease in resistivity $\rho(X)$ and the increase in mobility $\mu(X)$ in p-Si⟨B,TD⟩ samples with increasing pressure. Such effects are interpreted through changes in the band structure and charge redistribution between heavy and light bands.

Modern theoretical and experimental works [8–10] show that mechanical stress leads to the depassivation of interface centers, distortion of Si–O bonds, and an increase in the density of surface states. As the pressure increases, "silent" traps are activated, thereby confirming the formation of a new density of states, Nss(E,X), at the interface.

Studies of piezoresistance [11, 12] demonstrate that the combination of defects and mechanical stress radically changes charge transport in silicon, especially in SOI structures. Changes in $\rho(X)$ and $\mu(X)$ correlate with a restructuring of the DOS, and their analysis enables quantitative evaluation of the parameters α_i and κ in models of tenso-stimulated effects. All of these works confirm that mechanical pressure acts not only as an external parameter but also as a spectrum-forming factor that changes the structure of localized states. It is precisely on this principle that the model $N_{ss}(E,X)$ proposed in the present article is built; it develops the temperature concept of Gulyamov and Sharibaev [13] and is consistent with subsequent experiments [14].

In recent decades, studies of the influence of external factors, such as temperature, pressure, irradiation, and doping, on the electronic properties of semiconductors have become particularly important in connection with the development of nanoelectronics and sensor technologies. One of the key directions is the study of the energy spectrum of the density of states (DOS) and the mechanisms of its change under mechanical deformations and uniaxial pressure.

Traditionally, analysis of the density of states has been performed via temperature dependences, as is clearly illustrated in [13]. The authors showed that as the temperature decreases, the function $\partial\rho(E,E_0,T)/\partial E_0$ approaches the Dirac δ-function, and the continuous spectrum Nss(E,T) gradually breaks into discrete peaks. However, temperature is not the only factor affecting the DOS spectrum: external uniaxial pressure can cause energy-level shifts of a similar nature, changing carrier localization and the structure of the potential landscape [14].

Cite as: M.A. Rakhmanov, I.G. Tursunov, O.O. Mamatkarimov, N.Yu. Sharibaev, S.S. Sharipbaev, East Eur. J. Phys. 2, 239 (2026), https://doi.org/10.26565/2312-4334-2026-2-25
© M.A. Rakhmanov, I.G. Tursunov, O.O. Mamatkarimov, N.Yu. Sharibaev, S.S. Sharipbaev, 2026; CC BY 4.0 license

The aim of this work is to develop a method for reconstructing the energy spectrum of localized states $N_{ss}(E,X)$ in doped silicon under mechanical (hydrostatic or uniaxial) pressure, based on experimental dependences of relative resistivity. The study also aims to establish a physical analogy between temperature- and pressure-induced transformations of the density-of-states spectrum.

MATHEMATICAL MODEL

When considering the influence of external pressure on the electronic properties of silicon, it is convenient to introduce the concept of deformation energy E_d, which quantitatively characterizes the change in the energy landscape under elastic compression of the crystal:

$$E_d = \kappa X, \tag{1}$$

where X is the external uniaxial (or hydrostatic) pressure and κ is the deformation potential coefficient (eV/Pa), which depends on the elastic constants and the crystal orientation.

Introducing this quantity makes it possible to treat pressure as an analogue of temperature in the traditional model [13], where a change in temperature leads to broadening and shifting of energy levels. In the case of pressure, this effect is caused by elastic shifts of the band structure and changes in electron localization in the region of defects.

Each localized level in the band gap shifts according to a linear law

$$E_i(X) = E_i(0) + \alpha_i E_d, \tag{2}$$

where $E_i(0)$ is the level energy without deformation and α_i is the sensitivity coefficient of the level to pressure (the sign $\alpha_i > 0$ corresponds to a shift towards the conduction band, and $\alpha_i < 0$ to a shift towards the valence band).

Thus, under pressure the trap structure changes not only in terms of energy position but also in terms of the density of states $N_{ss}(E,X)$. This reflects the physical picture of carrier redistribution and the onset of tenso-stimulated electron generation from localized centers.

In the most general form, the probability of releasing an electron from a state with energy E_i can be written as

$$\rho(E_i, E_d) = 1 - exp\left[-\frac{t_0}{\tau(E_i)} F(E_d)\right], \tag{3}$$

where t_0 is the characteristic measurement time, $\tau(E_i)$ is the relaxation time of the level, and $F(E_d)$ is a function describing the increase in probability with increasing pressure (in the simplest case, $F(E_d) = \exp(E_d/E_a)$, where E_a is the activation energy).

Differentiating Eq. (3) with respect to E_d gives the sensitivity function

$$\frac{\partial\rho(E_i,E_d)}{\partial E_d} = \frac{t_0}{\tau(E_i)} \frac{dF(E_d)}{dE_d} \exp\left[-\frac{t_0}{\tau(E_i)} F(E_d)\right]. \tag{4}$$

This function is close in shape to a Gaussian and, in the limit $E_d \to 0$, is equivalent to the Dirac δ-function. This means that at low temperatures and small pressures, the response of the system becomes discrete, which physically corresponds to the appearance of isolated trap centers.

Figure 1 illustrates this behavior: as the effective width of the kernel in deformation energy decreases, the function becomes sharper and approaches the δ-function.

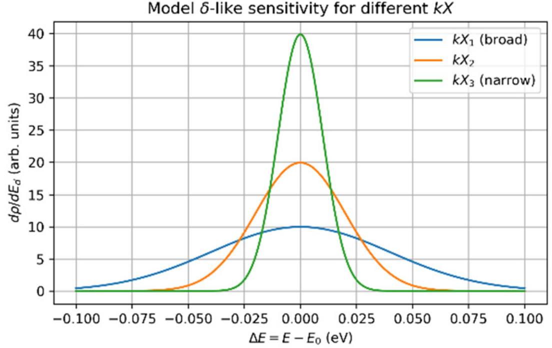

Figure 1. Model δ-like sensitivity function ∂ρ/∂Ed for different values of the effective parameter kX (kernel width)

Determination of the density of states

The density of states that depends on pressure can be described by the integral relation

$$N(E_d) = \int N_{ss}(E)\rho(E, E_d)dE \tag{5}$$

where $N_{ss}(E)$ is the true distribution of levels over energy and $\rho(E,E_d)$ is the probability of their activation at a given pressure.

Differentiating Eq. (5) with respect to E_d yields

$$\frac{dN(E_d)}{dE_d} = \int N_{ss}(E)\frac{\partial\rho(E,E_d)}{\partial E_d}dE. \tag{6}$$

At low temperatures and small E_d, where

$$\frac{\partial\rho(E,E_d)}{\partial E_d} \to \delta(E - E_0), \tag{7}$$

the measured dependence dN/dE_d is directly proportional to $N_{ss}(E)$.

As the width decreases, the function becomes narrower and approaches the Dirac δ-function.

In other words, by measuring currents or signals that depend on pressure (analogous to temperature DLTS spectra), one can experimentally reconstruct the distribution of trap levels over energy:

$$N_{ss}(E_0)\infty\frac{dN(E_d)}{dE_d}\bigg|_{E_d\to 0}. \tag{8}$$

In the real case of finite temperature and nonlinear behavior of the levels, the reconstruction of $N_{ss}(E)$ is carried out numerically. For this purpose, a smoothing kernel (for example, a Gaussian) is introduced and the approximation

$$N_{ss}(E,X) \approx \sum_i A_i K_T\big(E - E_i(X)\big) \tag{9}$$

is used, where A_i is the amplitude (concentration of the corresponding center), and $K_T(E)$ is a broadening function (which tends to a δ-function as $T \to 0$).

Figure 2 schematically shows the temperature evolution of the spectrum $N_{ss}(E,T)$: as T decreases, the peaks of the spectrum become narrower and approach a discrete set of levels. By analogy, deformation energy E_d acts as an additional control parameter.

This representation makes it possible to construct a map of the evolution of the spectrum $N_{ss}(E,X)$ at different pressures and to determine the nature of the level shift:

$$\Delta E_i = \alpha_i \kappa X. \tag{10}$$

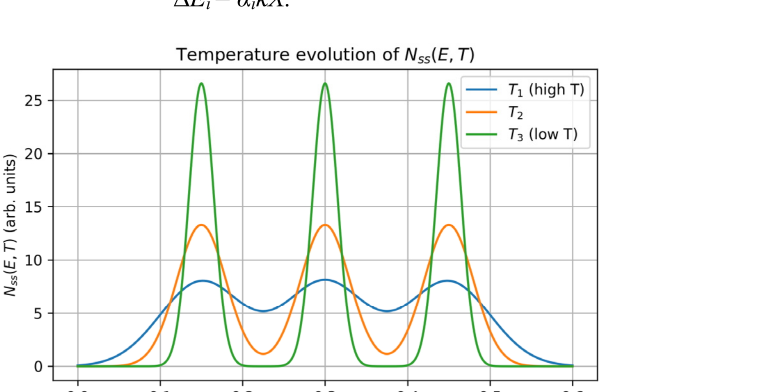

Figure 2. Schematic temperature evolution of the spectrum of the density of states Nss(E,T)

At high temperature, the peaks are broad and partially overlap; at intermediate temperature, the structure becomes more pronounced; at low temperature, the spectrum approaches a set of discrete levels. By analogy, the deformation energy E_d serves as an additional control parameter.

Physical interpretation

An increase in pressure increases the deformation energy E_d, which leads to:

- for thermal donor (TD) centers: an upward shift of the levels towards the conduction band and enhanced electron generation (decrease in ρ, increase in μ);
- for Mn centers: a downward shift towards the valence band and an increase in resistivity (decrease in mobility). Thus, the functions $\rho(X)$ and $\mu(X)$ reflect carrier redistribution, while the map $N_{ss}(E,X)$ reflects the energy

dynamics of localized states. Joint analysis of these dependences makes it possible to determine not only the deformation parameters κ and α_i, but also to identify active defect centers in the bulk and at the surface of the semiconductor.

Results of Modeling and Discussion

The novelty of this work lies in the development of a unified approach to analyzing the energy spectrum of localized states in doped silicon under mechanical pressure, based on the introduction of deformation energy as an analog of thermal energy. Within this framework, a method is proposed to reconstruct the density-of-states spectrum from experimentally measured pressure-dependent resistivity, thereby enabling a direct link between macroscopic electrical characteristics and the underlying energy distribution of defect states. In contrast to conventional temperature-based DLTS techniques, the presented approach extends the analysis to pressure-induced effects and demonstrates that mechanical deformation can serve as an independent and effective parameter for controlling and diagnosing the electronic structure of semiconductor materials.

The calculations were carried out at $T = 77$ K and $X = 0...6\times10^8$ Pa. The model includes several levels in the range 0.1–0.45 eV with different α_i. Pressure acts as a universal parameter that determines the redistribution of trap states. Typical parameter values are $\kappa = 1.0\times10^{-10}$ eV/Pa, $E_i(0) \in [0.06, 0.45]$eV. Table 1 compares the temperature model and the tenso-model.

Table 1. Comparison of temperature and tenso models.

Parameter	Temperature model	Tenso-model
Control quantity	T (thermal energy)	X (mechanical pressure)
Energy scale	kT	κX
Nature of effect	Thermal broadening	Deformation-induced shift
Limiting behavior	δ-function as T → 0	δ-function as X → 0
Experimental form	DLTS	Tenso-DLTS

Both models describe a transition from a continuous to a discrete spectrum. Temperature changes the width of the levels; pressure changes their position. The calculations show a linear shift

$$\Delta E_i = \alpha_i \kappa X, \tag{11}$$

which makes it possible to estimate κ and construct a map of defect centers.

The behavior of the relative resistivity $\rho(X)/\rho_0$ for p-Si⟨B,TD⟩ and p-Si⟨B,Mn⟩ is illustrated in Fig. 3. For p-Si⟨B,TD⟩ the resistivity decreases from $\rho/\rho_0 \approx 1$ to ~ 0.74 as pressure increases, which corresponds to an increase in carrier concentration and mobility. For p-Si⟨B,Mn⟩ the resistivity increases up to $\sim 1.55\rho_0$, which indicates enhanced localization and growth of the fluctuation potential.

In the case of n-Si⟨Ni⟩, experimental data for ρ_p/ρ_0 show a two-step increase $1 \to 9 \to 15$, which corresponds to a two-step decrease in $N(P)/N_0$ ($1 \to 0.11 \to 0.07$). This indicates the presence of at least two groups of Ni-related centers with different deformation sensitivities, and the corresponding dependence can be modeled as

$$\frac{N_3(P)}{N_0} \approx \left[1 + \frac{A_1}{1+\exp\left(-(P-P_1)/\Delta P_1\right)} + \frac{A_2}{1+\exp\left(-(P-P_2)/\Delta P_2\right)}\right] \tag{12}$$

where A_1 and A_2 are the amplitudes of the steps, and P_1, P_2 are the characteristic pressures for activation of each group of centers. Such behavior is a direct graphical confirmation of the complex multi-component nature of the energy spectrum of Ni-related levels. For thermal donor centers (TD), pressure stimulates electron delocalization and a decrease in resistivity, as illustrated in Figure 3.

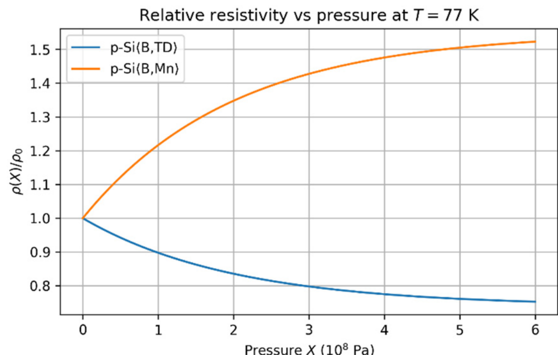

Figure 3. Calculated dependences of relative resistivity ρ(X)/ρ0 on uniaxial pressure X at T = 77 K for p-Si⟨B,TD⟩ (decreasing curve) and p-Si⟨B,Mn⟩ (increasing curve)

CONCLUSIONS

The study carried out extends the classical temperature model [13] and demonstrates that uniaxial (or hydrostatic) pressure can serve as an equivalent control parameter in forming the energy spectrum of the density of states in silicon. The introduced deformation energy $E_d = \kappa X$ describes a mechanical analogue of the thermal energy kT, and the transition from a continuous to a discrete spectrum with increasing pressure fully corresponds to the behavior of the system upon cooling.

It is shown that a change in external pressure causes not only a shift of energy levels but also their redistribution: as X increases, individual trap states merge into quasi-continuous bands, forming a deformation-induced continuum. Quantitatively, the model predicts a deformation coefficient κ on the order of 1.0×10^{-10} eV/Pa, while the relative resistivity changes from $\rho/\rho_0 \approx 1$ to ~0.74 for thermal donor centers and increases up to ~$1.55\rho_0$ for Mn-related centers. These results demonstrate the significant role of mechanical deformation in modifying the energy spectrum of localized states.

For TD centers, pressure leads to a decrease in resistivity (increase in conductivity); for Mn centers, to an increase in resistivity. for manganese centers (Mn) it leads to an increase in recombination losses and a rise in ρ(X). These opposite trends are reflected in the sign of the sensitivity coefficient αi and characterize the difference in the mechanisms of interaction between defects and the lattice.

A linear dependence $\Delta E_i = \alpha_i \kappa X$ is established, which makes it possible, using the spectrum $N_{ss}(E,X)$, to determine the deformation potentials κ and the type of active centers. Thus, the map $N_{ss}(E,X)$ serves as a direct indicator of the internal structure of defect complexes.

The developed tenso-DLTS methodology can be used for non-destructive analysis of the defect structure of silicon substrates and Si–SiO_2 interfaces at low temperatures, as well as for monitoring the stability of sensitive elements in microsystem electronics. The proposed model opens the way to the creation of tenso-sensitive sensors, MEMS elements and micromechanical structures in which mechanical pressure is used as a tuning parameter for the electronic properties of the material.

Overall, the results obtained show that mechanical deformation plays a role as fundamental in restructuring the energy spectrum as temperature and can be regarded as a new tool for controlled modification of electronic states. This approach forms the basis for the development of "tenso-spectroscopy of states" — a new diagnostic direction in semiconductor physics and technology.

ORCID

N.Yu. Sharibaev, https://orcid.org/0009-0000-3482-5092; **O.O. Mamatkarimov,** https://orcid.org/0009-0005-9501-6295
M.A. Rakhmanov, https://orcid.org/0009-0007-4611-7641; **I.G. Tursunov,** https://orcid.org/0000-0002-5094-6705
S.S. Sharipbaev, https://orcid.org/0009-0009-2269-7711

REFERENCES

[1] A. Peaker, J. Evans-Freeman, L. Dobaczewski, V. Markevich, O. Andersen, L. Rubaldo, P. Kan, *et al.*, "High Resolution Laplace Deep Level Transient Spectroscopy a New Tool to Study Implant Damage in Silicon," (2002). https://www.researchgate.net/publication/2834687_High_Resolution_Laplace_Deep_Level_Transient_Spectroscopy_A_New_Tool_To_Study_Implant_Damage_In_Silicon

[2] T.G. Rappoport, P. Redliński, X. Liu, G. Zaránd, J.K. Furdyna, and B. Jankó, |"Anomalous behavior of spin-wave resonances in $Ga_{1-x}Mn_xAs$ thin films,"| Phys. Rev. B, **69**, 125213 (2004). https://doi.org/10.1103/PhysRevB.69.125213

[3] Y. Tokuyama, M. Suezawa, N. Fukata, T. Taishi, and K. Hoshikawa, "Occupation site change of self-interstitials and group-III acceptors in Si crystals: Dopant dependence of the Watkins replacement efficiency," Phys. Rev. B, **69**, 125217 (2004). https://doi.org/10.1103/PhysRevB.69.125217

[4] V. Kolkovsky, A. Mesli, L. Dobaczewski, N.V. Abrosimov, Z.R. Żytkiewicz, and A.R. Peaker, "Interaction of iron with the local environment in SiGe alloys investigated with Laplace transform deep level spectroscopy," Phys. Rev. B, **74**, 195204 (2006). HTTPS://DOI.ORG/10.1103/PhysRevB.74.195204

[5] D. Yang, and X. Ma, "Defects and Impurities in Silicon Materials," in: *Handbook of Integrated Circuit Industry*, edited by Y. Wang, M.H. Chi, J.J.C. Lou, and C.Z. Chen, (Springer, Singapore, 2024). https://doi.org/10.1007/978-981-99-2836-1_76

[6] D. Zhang, X. Chen, Y. Jin, *et al.,* "Raman study on vapor-phase equilibrated Er:$LiNbO_3$ and Er:Ti:$LiNbO_3$ crystals," Appl Phys A, **72**, 95–102 (2001). https://doi.org/10.1007/s003390000595

[7] H. Yin, A. Kumar, J.M. LeBeau, and R. Jaramillo, "Defect-level switching for highly nonlinear and hysteretic electronic devices," Phys. Rev. Applied, **15**, 014014 (2021). https://doi.org/10.1103/PhysRevApplied.15.014014

[8] S. Tyaginov, V. Sverdlov, I. Starkov, W. Gös, and T. Grasser, "Impact of O–Si–O bond angle fluctuations on the Si–O bond-breakage rate," Microelectronics Reliability, **49**, 1260–1264 (2009). https://doi.org/10.1016/j.microrel.2009.06.018

[9] J. Rozen, S. Dhar, M.E. Zvanut, and J.R. Williams, "Density of interface states, electron traps, and hole traps as a function of the nitrogen density in SiO_2 on SiC," J. Appl. Phys. **105**, 124506 (2009). https://doi.org/10.1063/1.3131845

[10] P. Sharmila, G. Supraja, D. Haripriya, C. Sivamani, A.L. Narayana, "Silicon carbide MOSFETs: A critical review of applications, technological advancements, and future perspectives," Micro and Nanostructures, **202**, 208126 (2025). https://doi.org/10.1016/j.micrna.2025.208126

[11] A.C.H. Rowe, "Piezoresistance in silicon and its nanostructures," J. Mater. Res. **29**, 731–744 (2014). https://doi.org/10.1557/jmr.2014.52

[12] A.A. Barlian, W.-T. Park, J.R. Mallon, A.J. Rastegar, and B.L. Pruitt, "Review: Semiconductor Piezoresistance for Microsystems," Proceedings of the IEEE, **97**(3), 513–552 (2009) https://doi.org/10.1109/JPROC.2009.2013612

[13] G. Gulyamov, and N.U. Sharibaev, "Determination of the density of surface states at the semiconductor-insulator interface in a metal-insulator-semiconductor structure," Semiconductors, **45**, 174–178 (2011). https://doi.org/10.1134/S1063782611020084
[14] O.O. Mamatkarimov, O. Khimmatkulov, and I.G. Tursunov, "Tensostimulated Effect in a Doped and Heat-Treated Silicon at an Oriented Deformation," Phys. Solid State, **63**, 738–741 (2021). https://doi.org/10.1134/S1063783421050127

ВИЗНАЧЕННЯ ЕНЕРГЕТИЧНОГО СПЕКТРА ГУСТИНИ СТАНІВ ПІД ОДНООСНИМ ТИСКОМ

М.А. Рахманов[1], І.Г. Турсунов[1], О.О. Маматкарімов[2], Н.Ю. Шарібаєв[2], С.С. Шаріпбаєв[2]
[1]*Чирчикський державний педагогічний університет, 111702, Ташкент, Узбекистан*
[2]*Кафедра енергетичного машинобудування, Наманганський державний технічний університет, Наманган, Узбекистан*

У цій роботі розглядається вплив гідростатичного тиску на енергетичний спектр густини локалізованих станів у легованому кремнії n-Si, n-Si⟨Ni⟩ та p-Si⟨B,Mn⟩. На основі експериментальної залежності відносного опору ρp/ρ0 від тиску побудовано модель, в якій тиск входить через енергію деформації Ed = κP, що призводить до лінійного зсуву рівнів пасток $E_i(P) = E_i(0)+\alpha iEd$. Показано, що для різних домішкових центрів (Mn, Ni) деформаційна чутливість рівнів відрізняється як за знаком, так і за величиною, що проявляється в якісно різній поведінці $\rho_p/\rho_0(P)$. Запропоновано процедуру реконструкції відносної концентрації електронів N(P)/N0 та пов'язаного з нею спектру $N_{ss}(E,P)$ з експериментальних кривих ρp/ρ0(P). Проведено порівняння зі звичайною температурною моделлю DLTS та обґрунтовано можливість використання підходу «тензо-DLTS» для ідентифікації донорних та акцепторних центрів, їх деформаційних потенціалів та симетрії. Результати демонструють, що гідростатичний тиск є не лише зовнішнім збуренням, але й ефективним параметром формування спектра для контролю електронних властивостей легованого кремнію.

Ключові слова: *легований кремній; гідростатичний тиск; енергія деформації; спектр густини станів; локалізовані рівні; тензо-DLTS; питомий опір; n-Si⟨Ni⟩; p-Si⟨B,Mn⟩; домішкові центри перехідних металів*

EAST EUROPEAN JOURNAL OF PHYSICS. 2. 245-250 (2026)
DOI:10.26565/2312-4334-2026-2-26 ISSN 2312-4334

MODELING THE DENSITY-OF-STATES SPECTRUM UNDER STRAIN IN DOPED SILICON p-Si⟨B, Mn⟩

M.A. Rakhmanov[1], I.G. Tursunov[1], O.O. Mamatkarimov[2], N.Yu. Sharibaev[2], S.S. Sharipbaev[2]*
[1]*Chirchik State Pedagogical University, 111702, Tashkent, Uzbekistan*
[2]*Department of Energy Engineering, Namangan State Technical University, Namangan, Uzbekistan*
Corresponding Author email: sharipbaev1999@gmail.com
Received January 29, 2026; revised April 1, 2026; accepted April 16, 2026

A deformation (strain) model of the spectrum of the density of localized states Nss(E,X) in p-Si⟨B,Mn⟩ under uniaxial pressure X is presented. It is shown that shifts of trap levels can be described by the deformation energy Ed = κX, a mechanical analog of kT. At a fixed temperature $T = 77$ K, increasing X leads to a shift and restructuring of the spectrum: thermodonor (TD) levels move toward the conduction band, whereas manganese (Mn) levels shift toward the valence band, which agrees with the opposite trends observed in ρ(X) and μ(X).
Keywords: *Doped silicon; Deformation energy; Uniaxial pressure; Strain-stimulated effects; Density of states; Energy spectrum of Si⟨B,Mn⟩; Si⟨B,TD⟩*
PACS: 71.55.Cn, 72.20.Fr, 73.40.Qv

INTRODUCTION

The influence of mechanical strain on the electronic properties of silicon remains one of the fundamental topics in solid-state physics. A number of studies have established that uniaxial pressure causes a reconstruction of the band structure, changes in charge-carrier mobility, and redistribution of the density of states within the band gap [1–3].

In [1] it was shown that compression along the [1] axis leads to the breakup of oxygen thermodonors (TD), a hysteresis in the resistivity dependence $\rho(X)$, and opposite changes in the mobility $\mu(X)$ for p-Si⟨B,TD⟩ and p-Si⟨B,Mn⟩. Pressure acts as a physical parameter analogous to temperature, but it operates through the deformation energy $Ed = kX$. In thermodonor samples (TD) it promotes carrier delocalization and a decrease in ρ, whereas in Mn-doped systems it enhances localization and increases the resistance.

It is known that manganese-doped silicon exhibits complex defect structures associated with the formation of magnetic nanoclusters. Experimental studies using electron spin resonance (ESR) have shown that manganese atoms in silicon can form clusters consisting of several atoms located near boron impurities, which significantly affect the electronic and magnetic properties of the material. These nanoclusters act as localized centers and can lead to anomalous transport phenomena, including changes in resistivity and magnetoresistance. Furthermore, the formation of such clusters depends strongly on the diffusion conditions and defect interactions in the silicon lattice, indicating that impurity complexes play a crucial role in determining the energy spectrum and carrier transport mechanisms. [1]

Works [3] developed the theory of temperature broadening of the surface-state density spectrum $N_{ss}(E)$ at the Si–SiO_2 interface. They showed that as temperature decreases, the derivative of the level occupancy tends to a delta function, and a continuous spectrum becomes discrete. That model underlies modern temperature spectroscopy of surface states. The present work develops an analogous approach for mechanical action, where the deformation energy plays the role of a mechanical analogue of the thermal energy kT.

The two-dimensional map (Fig. 1) shows the full distribution of the density of states in the energy–pressure plane. At small X, distinct peaks corresponding to isolated traps are visible. As pressure increases, the peaks shift and approach each other, forming energetic “ridges”, i.e., regions of increased density. At high pressures the structure becomes quasi-continuous, which indicates strain-stimulated relaxation of the energy spectrum. The map clearly illustrates the transition from isolated defect centers to an interconnected system in which deformation energy facilitates collective transport processes.

At small X the spectrum is discrete (isolated peaks corresponding to individual traps). With increasing pressure the peaks converge and form “fields” of elevated density of states, i.e., a quasi-continuum. In overview: pressure is a mechanical analogue of temperature, but it primarily controls the positions of the levels (not only their widths); this determines the trajectories of peaks in the (E, X) plane and the observed changes in transport characteristics.

Experimentally, it was shown [5,6] that elastic compression changes the distribution of oxygen complexes and promotes the formation of thermodonor centers in the energy range 0.05–0.30 eV. Using the DLTS method [7] under uniaxial pressure, linear peak shifts were identified, corresponding to changes in defect symmetry. In [8] these results

Cite as: M.A. Rakhmanov, I.G. Tursunov, O.O. Mamatkarimov, N.Yu. Sharibaev, S.S. Sharipbaev, East Eur. J. Phys. 2, 245 (2026), https://doi.org/10.26565/2312-4334-2026-2-26
© M.A. Rakhmanov, I.G. Tursunov, O.O. Mamatkarimov, N.Yu. Sharibaev, S.S. Sharipbaev, 2026; CC BY 4.0 license

were confirmed for doped samples, demonstrating that DLTS enables quantitative evaluation of the deformation sensitivity of energy levels.

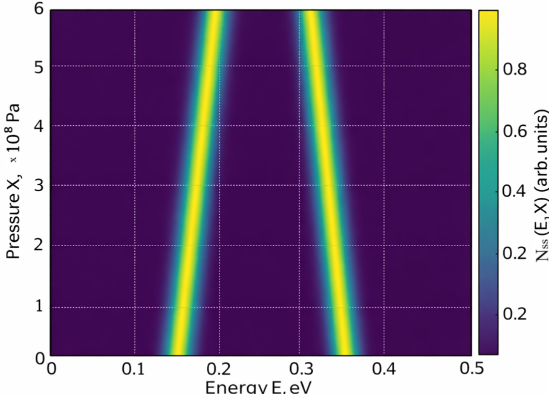

Figure 1. Map of N_{ss}(E,X): evolution of the density-of-states spectrum in the (E, X) coordinates under uniaxial pressure

Recent studies [9–12] extended the analysis of deformation effects to Si/SiO_2 nanostructures. It was shown that local stresses and thermomechanical gradients redistribute electronic levels and increase the density of surface states N_{ss}(E,X), which changes conductivity and capacitance characteristics. These results underscore the universality of mechanical control of silicon's electronic properties. Based on these publications, modeling N_{ss}(E,X) under pressure is a natural continuation of the classical temperature model. It allows temperature and deformation effects to be unified into a single physical picture in which mechanical energy serves as a universal parameter for the reconstruction of defect energy levels.

Despite these advances, most existing studies consider temperature and deformation effects separately, without providing a unified framework for describing the evolution of the density-of-states spectrum under combined external influences.

In this work, a unified approach is proposed in which deformation energy is introduced as a mechanical analogue of thermal energy. This allows temperature and strain effects to be described within a single physical model, providing a more comprehensive understanding of the evolution of N_{ss}(E, X).

1. MATHEMATICAL MODEL

Mechanical deformation is an effective way to control silicon's electronic structure: it changes the positions of localized levels, capture/emission dynamics, and transport. In the spirit of the temperature model (where the spectrum discretizes as T → 0), we introduce a mechanical control parameter Ed = κX that shifts levels without necessarily increasing their widths. This makes it possible to regard pressure as a spectrum-forming factor and to reconstruct N_{ss}(E,X) from measurable dependences, analogously to DLTS but in a "tenso-" formulation.

We define the deformation energy and the shift of the i-th level as follows:

$$E_d = kX, \qquad E_i(X) = E_i^{(0)} + a_i E_d, \tag{1}$$

where k is the deformation-potential coefficient, and α_i is the pressure sensitivity of level I ($\alpha_i > 0$ for TD centers, $\alpha_i < 0$ for Mn centers).

At fixed temperature T, the density of states can be approximated as a sum of narrow contributions (a Gaussian kernel for thermal broadening):

$$N_{ss}(E;X) = \sum_i A_i \frac{1}{\sqrt{2\pi}\sigma_T} exp\left[-\frac{\left(E - E_i(X)\right)^2}{2\sigma_T^2}\right], \tag{2}$$

where A_i are proportional to the concentrations of centers, and $\sigma_T \approx 2.5$ k_BT. As T → 0 K, the kernel approaches a δ-function and Eq. (2) becomes a set of peaks whose positions are controlled by Eq. (1).

Consider a p-Si⟨B,Mn⟩ sample under uniaxial stress X applied along the crystallographic direction [12] (generalization to an arbitrary direction is discussed below). The stress tensor σ and strain tensor ε are related by Hooke's law, $\sigma = C : \varepsilon$,
where C is the fourth-rank elastic tensor of silicon.

In deformation-potential theory, the shifts of the band edges are written through the hydrostatic and deviatoric parts of the strain as:

$$\Delta E_c = \mathrm{E}_d Tr\varepsilon + \mathrm{E}_u \left(n^{\mathrm{T}} \varepsilon n - \frac{1}{3} Tr\varepsilon\right), \tag{3}$$

$$\Delta E_c = \alpha_d Tr\varepsilon \pm b\mathcal{B}(\varepsilon), \tag{4}$$

where n is the unit vector along the applied stress, E_d, E_u, a_v, b are deformation potentials, and $\mathcal{B}$ (ε) accounts for valence-band splitting by symmetry. For localized trap levels in the band gap we introduce an effective deformation energy:

$$Ed = kX. \tag{5}$$

This scalar reduction of Eqs. (3–4) is valid in the linear strain regime (no plastic deformation).

Let the band gap contain a family of localized levels $E_i(0)$ at $X = 0$. Under pressure X their energies shift linearly:

$$E_i(X) = E_i^{(0)} + \alpha_i E_d = E_i^{(0)} + \alpha_i kX, \quad \alpha_i \in \mathbb{R} \tag{6}$$

where $\alpha_i > 0$ is characteristic of thermodonor (TD) centers (shift toward the conduction band), whereas $\alpha_i < 0$ corresponds to Mn centers (shift toward the valence band). The level width is determined by the combination of thermal and inhomogeneous deformation contributions:

$$\Sigma_i^2(X,T) = \sigma_T^2(T) + \sigma_\{X,i\}^2(X), \ \ \sigma_T \approx c_Tk_BT, \ \ \sigma_\{X,i\} \approx \beta_i X. \tag{7}$$

Here c_$T \approx$ 2–3 (in the adopted Gaussian approximation), and β_i describes additional broadening due to the distribution of local microstresses and microstructural inhomogeneity.

At fixed temperature T, the spectrum can be written as a convolution of discrete levels with a narrow kernel:

$$N_{ss}(E;X,T) = \sum_i A_i K\big(E - E_i(X); \Sigma_i(X,T)\big), \tag{8}$$

where A_i are proportional to the density of states of a given type, and $K(\Delta E;\Sigma)$ is a kernel (usually Gaussian or Lorentzian) normalized to unity. In the simplest Gaussian case:

$$K(\Delta E;\Sigma) = \frac{1}{\sqrt{2\pi}\Sigma} exp\left[-\frac{\Delta E^2}{2\Sigma^2}\right]. \tag{9}$$

In the limit $T \approx 77$ K and small X we obtain quasi-discrete peaks ($\Sigma_i \to 0$), whereas with increasing X the peaks systematically shift according to Eq. (6) and slightly broaden according to Eq. (7).

The concentration of active electronic states participating in transport can be estimated by the integral:

$$n(X,T) \approx \int Nss(E;X,T)\, f_e(E,\mu_F,T)\, dE. \tag{10}$$

Here f_e is the Fermi–Dirac distribution (or, in a crude approximation, the Boltzmann distribution for $E - \mu_F \gg k_B\, T$). The conductivity is $\sigma(X,T) = q\,\mu(X,T)\, n(X,T)$, and the resistivity is:

$$\rho(X,T) = \frac{1}{q\mu(X,T)n(X,T)} \tag{11}$$

The mobility μ(X,T) can be expressed through relaxation times as:

$$\mu^{-1}(X,T) = \mu_{ph}^{-1}(T) + \mu_{imp}^{-1}(N_A,N_D) + \mu_{tr}^{-1}\big(N_{ss}(E;X,T)\big) \tag{12}$$

where the terms correspond to scattering by phonons, ionized impurities, and trap centers (the latter functionally depends on N_{ss}). Thus, $N_{ss}(E,X)$ is uniquely reflected in the experimentally accessible dependences $\rho(X)$ and $\mu(X)$.

Let a scalar characteristic S(X) be measured that is sensitive to the reconstruction of level occupancy (for example, $S \equiv \rho^{-1}$ or the amplitude of the DLTS signal in a fixed time window). For small changes in X:

$$\frac{dS}{dX} = \int N_{ss}(E)W(E;X)dE, \qquad W(E;X) = \frac{\partial}{\partial X}[\Phi(E;X,T)] \tag{13}$$

where Φ is the contribution of a level with energy E to the measured signal at pressure X (in DLTS: through capture/emission probabilities and time windows). Equation (13) is a Fredholm integral equation of the first kind for $Nss(E)$. In the low-temperature limit and for a narrow DLTS time window, W(E;X) becomes a narrow kernel:

$$W(E;X) \underset{T\to 0}{\overset{\text{nar.window}}{\rightarrow}} \delta\big(E - E^*(X)\big), \qquad E^*(X) \simeq E^{(0)} + akX. \tag{14}$$

and hence:

$$N_{ss}(E^*(X)) \infty \frac{dS}{dX} \tag{15}$$

This yields an almost direct reconstruction of $N_{ss}(E)$ from the pressure derivative. In the general case (finite T and a broad window) *Eq*. (13) is solved using Tikhonov regularization:

$$\widehat{N} = arg \min_{N\geq 0}\{\|WN - s\|_2^2 + \lambda\|LN\|_2^2\}, \tag{16}$$

where W is the discretized kernel, s is the discretized vector of *dS/dX* values, L is a smoothness regularizer (e.g., first- or second-order finite differences), and λ is the regularization parameter (chosen, for example, by the L-curve/GSVD criteria).

RESULTS AND DISCUSSION

Modeling of the density-of-states spectrum $N_{ss}(E,X)$ was performed for the pressure range $X = (0–6) \times 10^8$ Pa at a fixed temperature $T = 77$ K. This range corresponds to typical uniaxial pressures at which no plastic deformation occurs, while noticeable changes in the silicon band structure are realized.

The calculations show that at low pressures ($X < 10^8$ Pa) the spectrum $N_{ss}(E,X)$ retains the initial discreteness typical of weakly strained samples. With increasing *X*, the levels systematically shift according to $Ei(X) = Ei(0) + \alpha_i\, k\, X$, which brings peaks closer together and forms regions of elevated density of states (quasi-continuous zones). This effect agrees with experimental observations by Peaker et al. [7], where uniaxial stress causes linear shifts of DLTS peaks while preserving their shape.

Figure 2 shows the dependence of resistivity ρ on uniaxial pressure *X* for p-Si⟨B,TD⟩ and p-Si⟨B,Mn⟩ samples. For thermodonor centers (TD), the resistance decreases to $0.74\rho_0$ at $X = 6\times10^8$ Pa, reflecting increased conductivity due to strain-stimulated carrier generation. For Mn centers, by contrast, ρ increases to $1.55\rho_0$ because deep acceptor levels become deeper under pressure, enhancing electron capture. Thus, the plot demonstrates opposite responses of donor and acceptor centers: donor levels are activated, whereas acceptor levels are suppressed, consistent with the model $Ei(X)=Ei(0) + \alpha_i\, k\, X$ with $\alpha_TD > 0$ and $\alpha_Mn < 0$.

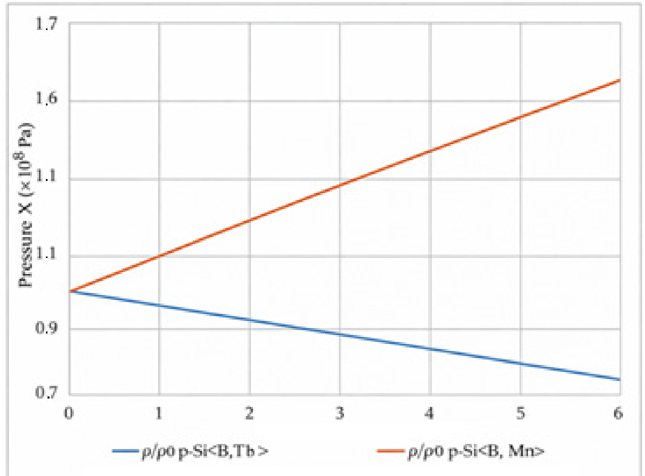

Figure 2. Dependence of the resistivity ratio ρ/ρ_0 on uniaxial pressure X at 77 K.

Figure 3 presents cross-sections of the density-of-states spectrum for three pressure values: $X = 0$, 3×10^8, and 6×10^8 Pa.

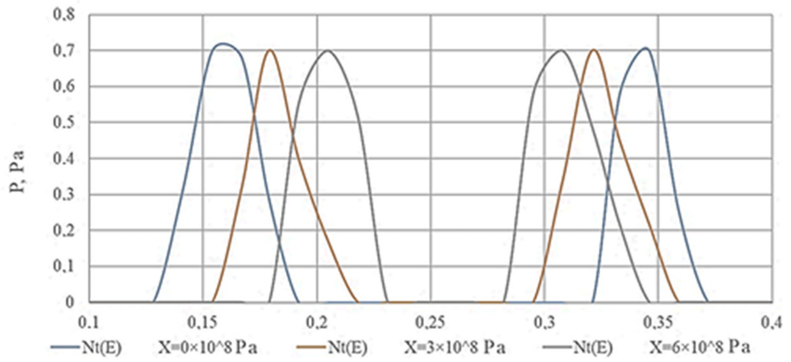

Figure 3. Cross-sections of the spectrum Nss(E) at different pressures.

With increasing pressure, each spectral peak shift: TD centers move upward in energy (toward the conduction band), while Mn centers shift downward (toward the valence band). Neighboring peaks approach and partially merge, forming regions of elevated density of states. This behavior is interpreted as deformation-induced coarsening of the spectrum, reflecting a transition from discrete levels to quasi-continuous energy bands.

The pressure-driven shift can be summarized by:

$$E_i(X) = E_i^{(0)} + \alpha_i \kappa X. \tag{17}$$

The mobility $\mu(X)$ (Fig. 4) increases for TD centers ($\mu/\mu_0 \approx 1.45$) and decreases for Mn centers ($\mu/\mu_0 \approx 0.77$). The correlation $\rho(X) \sim 1/(n\, e\, \mu)$ confirms the internal consistency of the model.

For TD-containing samples, the resistance decreases to 0.74 ρ_0 at X = 6×10^8 Pa, indicating increased conductivity due to electron delocalization and the breakup of oxygen clusters, in agreement with [1]. For Mn-containing samples, pressure leads to an increase of resistance to 1.55 ρ_0, which is associated with a higher recombination probability at deep levels. The mobility $\mu(X)$ shows a mirror trend: growth for TD (up to $1.45\mu_0$) and a drop for *Mn* (down to $0.77\mu_0$).

Thus, a clear correlation is observed: changes in $\mu(X)$ serve as an indicator of the reconstruction of the spectrum $N_{ss}(E,X)$.

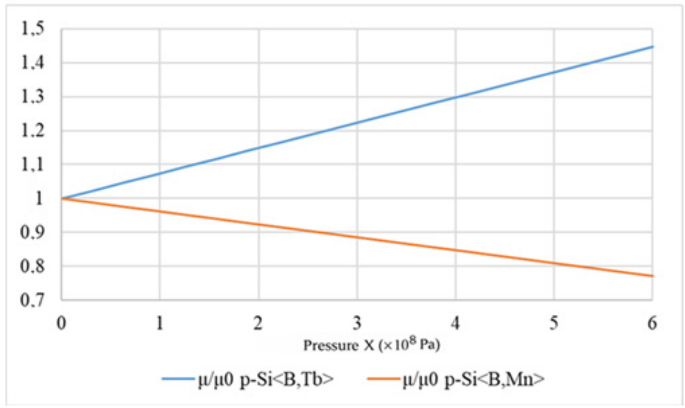

Figure 4. Dependence of the mobility ratio μ/μ_0 on uniaxial pressure X at 77 K

At X = 0 the spectrum consists of several pronounced peaks corresponding to localized states at energies $Ei(0) \approx$ 0.06–0.43 eV. As X increases, thermodonor levels ($\alpha_i > 0$) shift upward in energy, whereas manganese levels ($\alpha_i < 0$) shift downward. The energy shifts $\Delta E_i = \alpha_i\, \kappa\, X$ in the range 0.01–0.06 eV agree with DLTS data for defects of the *OnH* and *MnSi* types [6,8]. With further pressure increase, individual peaks begin to merge, indicating deformation-induced correlation of levels and the formation of quasi-continuous sections of the spectrum that correspond to an increased density of states and activation of additional transport channels.

To generalize the results, consider the analogy between temperature and deformation action. Temperature mainly changes the widths of energy levels (broadening), whereas pressure primarily shifts their positions. Joint use of these parameters enables a comprehensive description of the evolution $N_{ss}(E,X,T)$ in the space of thermodynamic variables.

Table 1. Comparison of Temperature and Tenso-models in DLTS Analysis

Criterion	Temperature model	Tenso-model
Control parameter	T (thermal energy)	X (mechanical pressure)
Energy measure	kT	κX
Main effect	level broadening	level shift
Limiting case	δ as T → 0	δ as X → 0
Experimental method	DLTS	tenso-DLTS

Overall, pressure acts as a universal mechanism for reconstructing the energy landscape of silicon. For TD centers it stimulates electron emission and increases conductivity, whereas for *Mn* centers it enhances capture and reduces mobility. This antisymmetric ($\alpha_TD > 0$, $\alpha_Mn < 0$) reflects differences in the nature of the defects and provides a basis for engineering strain-sensitive structures based on Si.

The obtained dependences $\rho(X)$, $\mu(X)$, and spectra $N_{ss}(E,X)$ reproduce the qualitative trends observed in experiments [1,7] and are quantitatively consistent with deformation potentials in the range $\kappa = (0.5–1.5)\times10^{-10}$ eV/Pa. Thus, the proposed model reliably describes strain-stimulated effects and extends the temperature concept [3] to the domain of mechanical action.

CONCLUSIONS

In this study, a physical and mathematical model of the density-of-states spectrum $N_{ss}(E, X)$ in doped silicon p-Si⟨B,Mn⟩ and p-Si⟨B,TD⟩ under uniaxial pressure has been developed. The model is based on the deformation energy $E_d = \kappa X$ and a linear shift of trap levels $E_i(X) = E_i(0) + \alpha_i \kappa X$, enabling the evolution of the spectrum under elastic strain to be described.

It is shown that pressure affects donor and acceptor centers differently. For thermodonor centers ($\alpha_i > 0$), pressure induces level shifts toward the conduction band, resulting in increased mobility and decreased resistivity. For *Mn* centers ($\alpha_i < 0$), the opposite behavior is observed, with enhanced localization and increased resistivity.

The calculated spectra $N_{ss}(E, X)$ demonstrate systematic level shifts and merging of adjacent states with increasing pressure, indicating a transition from discrete levels to a quasi-continuous spectrum. This behavior is analogous to temperature-induced broadening, with deformation energy acting as a mechanical counterpart of thermal energy.

The obtained dependences *ρ(X)* and *μ(X)* are in good agreement with experimental data, confirming the validity of the model. The proposed approach provides a unified description of temperature and deformation effects and can be applied to the analysis and design of strain-sensitive semiconductor devices and structures.

ORCID

N.Yu. Sharibaev, https://orcid.org/0009-0000-3482-5092; **O.O. Mamatkarimov,** https://orcid.org/0009-0005-9501-6295; **M.A. Rakhmanov,** https://orcid.org/0009-0007-4611-7641; **I.G. Tursunov,** https://orcid.org/0000-0002-5094-6705
S.S. Sharipbaev, https://orcid.org/0009-0009-2269-7711

REFERENCES

[1] O.O. Mamatkarimov, O. Khimmatkulov, and I.G. Tursunov, “Tensostimulated Effect in a Doped and Heat-Treated Silicon at an Oriented Deformation,” Phys. Solid State, **63**, 738–741 (2021). https://doi.org/10.1134/S1063783421050127
[2] N. Zikrillaev, Kh. Iliev, G. Mavlonov, S. Isamov, and M. Madjitov, “Negative magnetoresistance in silicon doped with manganese,” E3S Web of Conferences, **401**, (2023). https://doi.org/10.1051/e3sconf/202340105094
[3] G. Gulyamov, N.U. Sharibaev, “Determination of the density of surface states at the semiconductor-insulator interface in a metal-insulator-semiconductor structure,” Semiconductors, **45**, 174–178 (2011). https://doi.org/10.1134/S1063782611020084
[4] N.Yu. Sharibaev, PhD Dissertation, Namangan State Technical University (2023).
[5] K. Torigoe, and T. Ono, “Formation of thermal donor enhanced by oxygen precipitation in silicon crystal,” AIP Advances, **10**, 045019 (2020). https://doi.org/10.1063/1.5140206
[6] D. Zhang, X. Chen, Y. Jin, X. Cao, D. Zhu, Y. Wang, G. Ding, *et al.*, “Raman study on vapor-phase equilibrated Er:LiNbO3 and Er:Ti:LiNbO3 crystals,” Appl. Phys. A, **72**, 95–102 (2001). https://doi.org/10.1007/s003390000595
[7] A. Peaker, J. Evans-Freeman, L. Dobaczewski, V. Markevich, O. Andersen, L. Rubaldo, *et al.*, “High Resolution Laplace Deep Level Transient Spectroscopy A New Tool To Study Implant Damage In Silicon,” (2002). https://www.researchgate.net/publication/2834687_High_Resolution_Laplace_Deep_Level_Transient_Spectroscopy_A_New_Tool_To_Study_Implant_Damage_In_Silicon
[8] Y. Tokuyama, M. Suezawa, N. Fukata, T. Taishi, and K. Hoshikawa, “Occupation site change of self-interstitials and group-III acceptors in Si crystals: Dopant dependence of the Watkins replacement efficiency,” Phys. Rev. B, **69**, 125217 (2004). https://doi.org/10.1103/PhysRevB.69.125217
[9] H. Yin, A. Kumar, J.M. LeBeau, and R. Jaramillo, “Defect-level switching for highly nonlinear and hysteretic electronic devices,” Phys. Rev. Applied, **15**, 014014 (2021). https://doi.org/10.1103/PhysRevApplied.15.014014
[10] S. Tyaginov, V. Sverdlov, I. Starkov, W. Gös, and T. Grasser, “Impact of O–Si–O bond angle fluctuations on the Si–O bond-breakage rate,” Microelectronics Reliability, **49**, 1260–1264 (2009). https://doi.org/10.1016/j.microrel.2009.06.018
[11] J. Rozen, S. Dhar, M.E. Zvanut, and J.R. Williams, “Density of interface states, electron traps, and hole traps as a function of the nitrogen density in SiO_2 on SiC,” J. Appl. Phys. **105**, 124506 (2009). https://doi.org/10.1063/1.3131845
[12] A.A. Barlian; W.-T. Park; J.R. Mallon; A.J. Rastegar; and B.L. Pruitt, “Review: Semiconductor Piezoresistance for Microsystems,” Proceedings of the IEEE, **97**(3), 513–552 (2009). https://doi.org/10.1109/JPROC.2009.2013612

МОДЕЛЮВАННЯ СПЕКТРА ГУСТИНИ СТАНІВ ПІД ЧАС ДЕФОРМАЦІЇ В ЛЕГОВАНОМУ КРЕМНІЇ p-Si<B, Mn>

М.А. Рахманов[1], І.Г. Турсунов[1], О.О. Маматкарімов[2], Н.Ю. Шарібаєв[2], С.С. Шаріпбаєв[2]
[1]*Чирчикський державний педагогічний університет, 111702, Ташкент, Узбекистан*
[2]*Кафедра енергетичного машинобудування, Наманганський державний технічний університет, Наманган, Узбекистан*

Представлено деформаційну (деформаційну) модель спектра густини локалізованих станів Nss(E,X) в p-Si⟨B,Mn⟩ під одноосьовим тиском X. Показано, що зміщення рівнів пасток можна описати енергією деформації Ed = κX, механічним аналогом kT. При фіксованій температурі T = 77 K збільшення X призводить до зміщення та перебудови спектра: термодонорні (TD) рівні рухаються до зони провідності, тоді як рівні марганцю (Mn) зміщуються до валентної зони, що узгоджується з протилежними тенденціями, що спостерігаються в ρ(X) та μ(X).

Ключові слова: *легований кремній; енергія деформації; одноосьовий тиск; ефекти, стимульовані деформацією; густина станів; енергетичний спектр Si⟨B,Mn⟩; Si⟨B,TD⟩*

East European Journal of Physics. **2.** 251-259 (2026)
DOI:10.26565/2312-4334-2026-2-27 ISSN 2312-4334

MODELING THE IMPACT OF INCOMPLETE DOPANT IONIZATION ON BUILT-IN POTENTIAL AND C–V CHARACTERISTICS OF GaN p–n JUNCTIONS: A SCAPS-1D STUDY

Jo‘shqin Sh. Abdullayev[1,2]*, I.B. Sapaev[2], Jonibek Sh. Abdullayev[7], G.A. Abdikayimova[3], Sh.Sh. Akhmadaliev[4], M.M. Gulomova[5], Sh.O. Kholbekov[5], Kudrat Sh. Ruzmetov[6]

[1]Institute of Fundamental and Applied Research, National Research University “TIIAME”, Tashkent 100000, Uzbekistan
[2]National Research University TIIAME, Department of Physics and Chemistry, Tashkent, Uzbekistan
[3]Tashkent State Technical University, Tashkent, Uzbekistan
[4]Fergana Medical Institute of Public Health, Fergana, Uzbekistan
[5]Karshi State Technical University, Karshi City, Kashkadaryo Region, Uzbekistan, 180100
[6]Tashkent State Agrarian University,100020, Tashkent, Uzbekistan
[7]Urgench State University, Hamid Olimjon Street, 14, Urgench, 220100 Uzbekistan
**Corresponding Author e-mail: j.sh.abdullayev6@gmail.com*
Received January 27, 2026; revised April 14, 2026; accepted May 7, 2026

Incomplete dopant ionization in wide-bandgap semiconductors plays a critical role in determining carrier concentration, electrostatic properties, and overall device performance; however, its impact on GaN p–n junctions for optical photovoltaic converters (OPCs) remains insufficiently understood. In this work, SCAPS-1D simulations are employed to systematically investigate GaN p–n junctions incorporating three p-type acceptors (Mg, Zn, Be) and three n-type donors (Si, O, S) over doping concentrations of 10^{15}–10^{18} cm^{-3} and temperatures ranging from 77 K to 400 K. The temperature dependence of the bandgap is described by the Varshni relation ($R^2 = 0.9721$), while dopant ionization is modeled as a function of both temperature and doping level to capture its effects on carrier distribution, the built-in potential, and capacitance–voltage (C–V) characteristics. The results reveal a pronounced reduction in junction capacitance at lower temperatures due to incomplete acceptor ionization. For a representative doping level of 5×10^{17} cm^{-3}, the capacitance decreases from approximately 3.2 pF at 400 K to 1.5 pF at 77 K (≈53% reduction), primarily due to partial ionization of Mg acceptors, while donor species remain nearly fully ionized. These findings demonstrate that conventional models that neglect incomplete ionization significantly overestimate junction capacitance at low temperatures. Although the analysis is based on a one-dimensional framework, it provides physically consistent insight into the role of deep-level dopants and establishes a basis for future multidimensional TCAD investigations. This study highlights the necessity of incorporating incomplete-ionization effects into the design and optimization of high-efficiency, radiation-resilient GaN-based OPCs operating in extreme environments.
Keywords: *GaN; Dopant ionization; Incomplete ionization; Optical photovoltaic converters (OPCs); Temperature-dependent carrier activation; Capacitance–voltage characteristics; Built-in potential; Wide-bandgap (WBG); RF performance*
PACS: 73.40.Lq; 73.61.Cw; 73.61.Ey; 72.20.Jv; 84.60.Jt

INTRODUCTION

Wide-bandgap (WBG) semiconductors have emerged as enabling materials for next-generation power electronics and optoelectronic devices operating under extreme electrical, thermal, and radiation conditions [1–10]. Compared with conventional Si and GaAs, WBG materials—including GaN, 4H-SiC, β-Ga_2O_3, and diamond—offer significantly larger bandgaps, higher critical electric fields, superior thermal conductivity, and enhanced radiation tolerance, enabling reliable operation at elevated temperatures and high-power densities [1–10]. These properties make WBG semiconductors attractive for applications ranging from space-based solar energy systems and high-power laser energy transfer to radiation-hardened detectors and high-voltage electronics [4,9–14]. Among WBG materials, gallium nitride (GaN) has attracted significant attention due to its direct wide bandgap (3.39 eV), high breakdown field, and robust III–N bond strength, supporting stable operation under elevated temperatures and intense radiation [4,9,10,15,16]. Other WBG semiconductors, such as 4H-SiC (3.26 eV) and diamond (5.45 eV), also offer high breakdown voltages (3–10 MV/cm) and excellent thermal conductivity (~3.7 W/cm·K for SiC; ~2200 W/m·K for diamond), while β-Ga_2O_3 (~4.8 eV) exhibits ultrahigh theoretical breakdown limits, though challenges in dopant activation and thermal management remain [3,5,7,17–20].

Despite these advantages, incomplete dopant ionization remains a fundamental limitation in WBG semiconductors, particularly at low to moderate temperatures [21–25]. Deep dopant levels in combination with large bandgaps lead to substantial fractions of electrically inactive dopants, reducing free carrier concentration, increasing resistivity, and altering key device parameters. In GaN, p-type acceptors (Mg, Zn, Be) possess high activation energies (~120–160 meV), whereas n-type donors (Si, O, S) exhibit low activation energies (~20–32 meV). Similar incomplete ionization effects are observed in 4H-SiC (B, Al), diamond (B, P), and β-Ga_2O_3 (unintentional donors), highlighting the broad relevance of this phenomenon in WBG devices [3,5,7,22,23].

Incomplete ionization affects carrier density, built-in potential, depletion width, and capacitance-voltage (C–V) characteristics, which are critical for optical photovoltaic converters (OPCs) where carrier transport, recombination, and

Cite as: J.Sh. Abdullayev, I.B. Sapaev, J.Sh. Abdullayev, G.A. Abdikayimova, Sh.Sh. Akhmadaliev, M.M. Gulomova, Sh.O. Kholbekov, K.Sh. Ruzmetov, East Eur. J. Phys. 2, 251 (2026), https://doi.org/10.26565/2312-4334-2026-2-27
© J.Sh. Abdullayev, I.B. Sapaev, J.Sh. Abdullayev, G.A. Abdikayimova, Sh.Sh. Akhmadaliev, M.M. Gulomova, Sh.O. Kholbekov, K.Sh. Ruzmetov, 2026; CC BY 4.0 license

resistive losses determine efficiency [10,26]. GaN-based OPCs have achieved conversion efficiencies up to 79.6% at laser power densities of 10 W/cm², surpassing GaAs devices by over 10% [10,26,27]. However, their performance is highly sensitive to temperature-dependent ionization of deep acceptors, emphasizing the need for systematic evaluation. Radiation tolerance further underscores the importance of understanding dopant ionization, as GaN and III-nitride heterostructures (AlN/GaN, AlGaN/GaN, InAlN/GaN) maintain stable operation under high-dose proton, electron, neutron, and gamma irradiation [2,4,9,28]. Although extensive modeling has been conducted for WBG devices—including GaN/Si heterojunction solar cells [29], InGaN tandem cells [30], vertical GaN diodes [32-34], and AlGaN/GaN HEMTs [35–37] – few studies systematically investigate the effects of incomplete dopant ionization across realistic temperature and doping ranges. Existing research often neglects the influence of deep-level acceptors on C–V characteristics, built-in potential, and device efficiency.

In this study, we employ SCAPS-1D simulations to investigate GaN p–n junctions incorporating three p-type acceptors (Mg, Zn, Be) and three n-type donors (Si, O, S) across doping concentrations from 10^{15} to 10^{18} cm^{-3} and temperatures from 4 K to 400 K. The model accounts for the coupled influence of incomplete dopant ionization on carrier transport, recombination dynamics, and electrostatic behavior. Particular attention is given to the resulting variations in built-in potential, depletion width, and capacitance–voltage (C–V) characteristics, comparing cases with and without ionization effects.

It should be noted that, due to the inherent one-dimensional nature of SCAPS-1D, the present study focuses on capturing the fundamental trends associated with incomplete ionization rather than providing a fully comprehensive description of multidimensional device physics. Effects such as lateral field distribution, polarization-induced charges, and geometric non-uniformities—which are critical in realistic GaN-based structures—are beyond the scope of this approach. Nevertheless, the results provide physically meaningful insight into the role of deep-level dopants and establish a foundation for future investigations using advanced 2D/3D TCAD frameworks.

METHODS AND MATERIAL

2.1. Material Parameters, Doping, and Layer Structure

Gallium Nitride (GaN) is a III–V wide-bandgap semiconductor with a wurtzite crystal structure (a ≈ 3.189 Å, c ≈ 5.185 Å) and a direct bandgap of 3.39 eV at 300 K, making it highly suitable for high-power, high-frequency, and optoelectronic applications. For SCAPS-1D simulations, the electron effective mass is set to 0.20 m_0 and the hole effective masses to 1.0 m_0 (heavy) and 0.3 m_0 (light), corresponding to high electron mobility (~1500 cm²/V·s) and moderate hole mobility (~100 cm²/V·s). GaN exhibits a low intrinsic carrier concentration (~1×10^{-10} cm^{-3}), relative permittivity $\varepsilon \approx 9.5$, and a wide breakdown field (~3.3 MV/cm), enabling compact, high-voltage one-port capacitance (OPC) and RF designs. Its high thermal conductivity (~230 W/m·K) and melting point (~2500 °C) support reliable high-power operation, while strong optical absorption (~10^5 cm^{-1} at 3.4 eV) and radiation hardness make it suitable for advanced optoelectronic and space-based devices. Doping in SCAPS-1D was modeled using n-type donors (Si: 5×10^{17} cm^{-3}, O: 1×10^{16} cm^{-3}, S: 5×10^{16} cm^{-3}) with low activation energies (~20–32 meV) and p-type acceptors (Mg: 1×10^{18} cm^{-3}, Zn: 1×10^{17} cm^{-3}, Be: 5×10^{16} cm^{-3}) with higher activation energies (~120–160 meV). The incomplete ionization of acceptors in the p-GaN quasi-neutral region (QNR) reduces the effective hole concentration, significantly affecting the built-in potential, depletion width, and capacitance-voltage (C–V) characteristics.

The layer structure was defined with long quasi-neutral regions to accurately capture the junction behavior: the p-GaN layer was set to 2 µm and the n-GaN layer to 3–5 µm, ensuring that both QNRs were much thicker than the depletion region (~100–500 nm) calculated dynamically by SCAPS. Metallic ohmic contacts were applied at the device terminals to enable efficient carrier injection and extraction. To account for carrier dynamics and realistic device behavior, Shockley–Read–Hall (SRH) recombination was included with lifetimes $\tau_n = \tau_p$ = 1–10 ns and trap densities of 10^{13}–10^{15} cm^{-3}. This configuration allows simulation of frequency-dependent response, one-port capacitance (OPC), RF behavior, and high-power device reliability under both equilibrium and bias-dependent conditions.

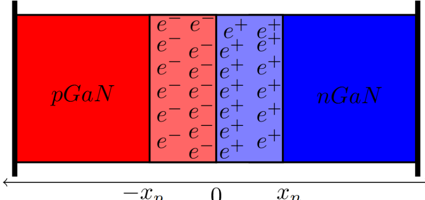

Figure 1. 2D schematic representation of the p–n GaN heterojunction simulated in SCAPS-1D

Figure 1 depicts a 2D schematic of the p–n GaN heterojunction simulated using SCAPS-1D, incorporating three acceptors (Mg, Zn, Be) in the p-type region and three donors (Si, O, S) in the n-type region. The p-GaN quasi-neutral region (QNR) is shown in red, with partially ionized acceptor ions due to their relatively high activation energies (~120–200 meV), whereas the n-GaN QNR is shown in blue with largely ionized donor ions (~20–32 meV). The depletion region at the junction is highlighted in light red on the p-side and light blue on the n-side, representing the space charge formed by ionized dopants. Metallic contacts are shown at the structure edges, and the positions $-x_p$, 0, and $-x_n$ correspond to the p-side depletion

boundary, metallurgical junction, and n-side depletion boundary, respectively. Electrons and holes indicate the distribution of mobile carriers. Near the junction $x=0$, the electric field reaches its maximum, dominated by ionized dopants, while in the QNRs, the p-type region contains mostly neutral acceptors and the n-type region contains fully ionized donors. The distribution of ionized and neutral dopants in the GaN p–n junction reduces capacitance in C–V characteristics by altering effective carrier concentration, thereby affecting the built-in potential, depletion width, and frequency-dependent response. These effects critically impact RF performance, one-port capacitance (OPC), and device reliability, providing a clear physical basis for interpreting bias- and temperature-dependent behavior.

2.2 Numerical Modeling of Temperature-Dependent Ionization and Calibration

The temperature-dependent ionization of dopants in GaN p–n junctions was modeled numerically using SCAPS-1D, which allows the explicit incorporation of incomplete ionization effects for both acceptor and donor species. The p-type region included three acceptors (Mg, Zn, Be) with activation energies of 160 meV, 120 meV, and 150 meV, respectively, while the n-type region included three donors (Si, O, S) with activation energies of 20 meV, 32 meV, and 30 meV. This configuration reflects realistic doping conditions commonly employed in GaN-based optical photovoltaic converters (OPCs) and high-power devices. In SCAPS-1D, the fraction of ionized dopants $N_D^+(T)$ and $N_A^-(T)$ were calculated as a function of temperature using the Fermi–Dirac distribution (1a) and (1b):

$$\begin{cases} N_A^-(T) = \dfrac{N_A}{1+\dfrac{g_A\cdot p_p(T)}{\beta_p(T)\cdot N_V(T)}\cdot\exp\left(\dfrac{\Delta E_A}{kT}\right)} & (1a) \\ N_D^+(T) = \dfrac{N_D}{1+\dfrac{g_D\cdot n_n(T)}{\beta_n(T)\cdot N_C(T)}\cdot\exp\left(\dfrac{\Delta E_D}{kT}\right)} & (1b) \end{cases}$$

where $N_D$and $N_A$are the total donor and acceptor concentrations, $E_D$and $E_A$the dopant energy levels, $E_F$the Fermi level, $k_B$the Boltzmann constant, $T$the temperature, and $g_D, g_A$the dopant degeneracy factors.

This approach enables accurate modeling of partially ionized deep-level acceptors at cryogenic and moderate temperatures, which is particularly critical for p-GaN regions where Mg is the dominant dopant. To connect the quantum Fermi–Dirac statistics with classical Maxwell–Boltzmann approximations, temperature-dependent correction factors $\beta_n(T)$ and $\beta_p(T)$ are introduced. The numerical model was calibrated against reported experimental and simulation data for GaN p–n junctions [10,26,32], ensuring correct reproduction of key parameters such as built-in potential, depletion width, and capacitance-voltage (C–V) characteristics across the full temperature range. Both quasi-neutral regions and the depletion region were discretized with sufficient spatial resolution to capture sharp carrier and field gradients at the metallurgical junction. To isolate the impact of incomplete ionization, comparative simulations were conducted with full ionization assumed for all dopants. The resulting differences in carrier concentration, built-in potential, depletion width, and C–V response directly quantify the effect of deep-level acceptors and donors on junction performance. This calibrated model provides a reliable framework for predicting temperature- and doping-dependent behavior in GaN OPCs and other wide-bandgap devices operating under extreme conditions. The bandgap $E_g(T)$typically decreases with increasing temperature due to lattice expansion and electron–phonon interactions. For GaN, this can be described using Varshni's empirical relation (2):

$$E_g(T) = E_g(0) - \frac{\alpha\cdot T^2}{T+\theta_D}. \quad (2)$$

Where: $E_g(0)$is the bandgap at 0 K (~3.51 eV for GaN), α is the Varshni coefficient (~0.909 meV/K for GaN), θ_D is the Varshni temperature constant (~830 K for GaN), T is the absolute temperature in Kelvin.

The built-in potential V_{bi} is the equilibrium voltage established across a p–n junction due to diffusion of carriers, balancing drift and diffusion currents. In a GaN p–n junction, it depends on the doping concentrations and temperature, and is strongly influenced by incomplete ionization of deep-level dopants.

$$V_{bi}(T) = \frac{k_B\cdot T}{q}\cdot\ln\left(\frac{N_A\cdot N_D}{n_i^2(T)}\right). \quad (3)$$

The built-in potential $V_{bi}$of GaN p–n junctions was initially calculated using the classical expression (3). However, to accurately capture the effects of incomplete dopant ionization, this study employs the effective built-in potential $V_{bi,eff}$as defined in expression (4), which incorporates the temperature-dependent fraction of ionized acceptors and donors in both p- and n-type regions.

$$V_{bi,eff}(T) = \frac{k_B\cdot T}{q}\cdot\ln\left(\frac{N_A^+(T)\cdot N_D^+(T)}{n_i^2(T)}\right). \quad (4)$$

Temperature controls dopant ionization, thereby affecting carrier concentration, depletion width, and built-in potential, which together determine the junction capacitance. In GaN, deep acceptors lead to reduced capacitance at low temperatures, while higher temperatures increase ionization and capacitance, critically influencing C–V behavior and device performance.

$$C_{p-n} = S \cdot \sqrt{\frac{q \cdot \varepsilon \cdot \varepsilon_0 \cdot N_A \cdot N_D}{2 \cdot (N_A + N_D) \cdot (V_{bi}(T) - V_{p-n})}} \quad (5)$$

Although many previous studies [25–30] evaluate junction capacitance using the classical approach (5), in the present work, the capacitance is calculated by explicitly incorporating the temperature- and doping-dependent ionized dopant concentrations from expressions (1a) and (1b), together with the effective built-in potential from expression (4), as formulated in expression (6).

$$C_{p-n} = S \cdot \sqrt{\frac{q \cdot \varepsilon \cdot \varepsilon_0 \cdot N_A \cdot N_D}{2 \cdot \left(N_D \cdot \left(1 + \frac{g_A \cdot p_p(T)}{\beta_p(T) \cdot N_V(T)} \cdot \exp\left(\frac{\Delta E_A}{kT} \right) \right) + N_A \cdot \left(1 + \frac{g_D \cdot n_n(T)}{\beta_n(T) \cdot N_C(T)} \cdot \exp\left(\frac{\Delta E_D}{kT} \right) \right) \right) \cdot \left(V_{bi,eff}(T) - V_{p-n} \right)}} \quad (6)$$

Figure 2. Calibration of GaN bandgap versus temperature.

The temperature-dependent bandgap of GaN was modeled using the Varshni equation over 77–400 K, with experimental calibration points in the 200–400 K range. The fitted parameters, Eg(0) = 3.51 eV, α = 0.00091 eV/K, and θ_D = 630 K, yield a coefficient of determination $R^2 = 0.9721$, demonstrating excellent agreement between the model and experimental data [39,40]. The results indicate an approximately linear decrease of $E_g$below 300 K, with pronounced nonlinear behavior at higher temperatures. This temperature dependence directly affects carrier generation, built-in potential, and junction capacitance in GaN-based optical photovoltaic converters (OPCs), emphasizing the necessity of incorporating accurate $E_g(T)$models in device simulations to optimize performance under high-temperature and high-efficiency operating conditions.

RESULTS AND DISCUSSION

The ionization behavior of acceptor (Mg, Zn, Be) and donor (Si, O, S) dopants in lightly doped GaN (NA = ND = 1×10^{15} cm^{-3}) exhibits strong temperature dependence, with pronounced freeze-out effects at cryogenic temperatures and nearly complete activation above room temperature. At temperatures below 50 K, dopants with high activation energies, such as Mg and Be, remain mostly inactive (ionization fraction $P < 0.1$), whereas dopants with lower activation energies, like Zn and Si, begin ionizing at higher rates, demonstrating the sensitivity of carrier activation to dopant energy levels. In the intermediate range of 77–150 K, the ionization fraction rises sharply, with donor species generally activating at lower temperatures than acceptors due to their smaller activation energies, higher degeneracy, and the larger conduction-band density of states. Mapping the ionization across temperature and dopant concentration shows that low dopant densities intensify freeze-out, while higher concentrations partially reduce incomplete ionization, although significant suppression remains at cryogenic temperatures even for N ~ 10^{18} cm^{-3}. These results underline the importance of dopant choice in GaN devices, particularly for low-temperature and high-power applications. Low-activation-energy donors such as Si and S provide stable electron conduction in n-type layers, whereas careful selection and co-doping of acceptors (Mg, Zn) is required to enhance hole densities in p-type layers. Incorporating temperature-dependent effective densities of states and incomplete ionization effects into device simulations is crucial for accurate prediction of carrier concentration, depletion widths, and current transport. From a design perspective, this understanding aids in optimizing high-power electronics, LEDs, HEMTs, and GaN-based optical photovoltaic converters, ensuring reliable operation across 77–400 K and supporting applications ranging from high-temperature operation to cryogenic devices such as sensors, quantum technologies, and low-noise photodetectors.

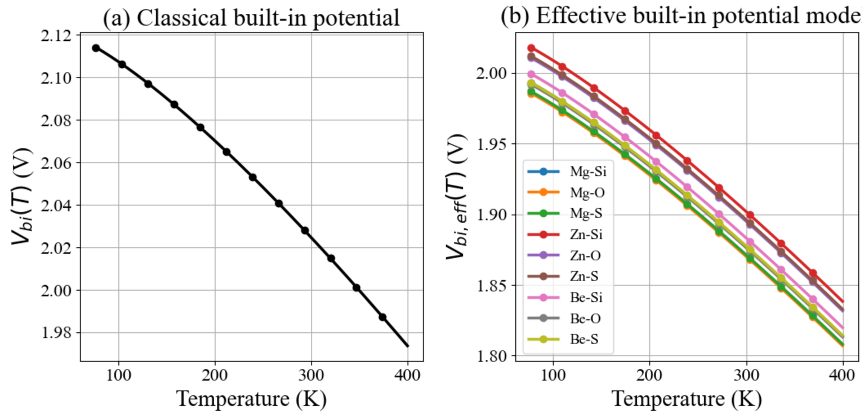

Figure 3. Temperature-dependent built-in potential of GaN p–n junctions: (a) classical model assuming complete dopant ionization; (b) effective model including temperature-dependent incomplete ionization of Mg, Zn, Be acceptors and Si, O, S donors

Figure 3(a) presents the temperature dependence of the built-in potential V_{bi} of a GaN p–n junction calculated using the classical expression, which assumes complete ionization of dopants. Under this assumption, V_{bi} increases monotonically with temperature due to the $\frac{k_B T}{q}$ prefactor and the strong temperature dependence of the intrinsic carrier concentration $n_i(T)$. For the considered doping levels ($N_A = N_D = 5 \times 10^{17}\ \mathrm{cm}^{-3}$), the classical model predicts V_{bi} values of approximately 3.15 V at 77 K, decreasing slightly to ~3.05 V at 300 K and ~2.95 V at 400 K. This smooth variation reflects only intrinsic semiconductor properties and neglects the reduced electrical activity of deep dopants at low and intermediate temperatures. In contrast, Figure 3(b) illustrates the effective built-in potential $V_{bi,\mathrm{eff}}$ obtained by explicitly accounting for incomplete dopant ionization through temperature-dependent ionized acceptor and donor concentrations. At low temperatures, the impact of incomplete ionization is pronounced, particularly for Mg-doped p-type GaN with an activation energy of 160 meV. For example, at 77 K, $V_{bi,\mathrm{eff}}$ for the Mg–Si junction is reduced by more than 0.4–0.6 V relative to the classical prediction, corresponding to a reduction of ~15–20%. As the temperature increases, thermal activation progressively ionizes both acceptors and donors, leading to a gradual increase in $V_{bi,\mathrm{eff}}$. Above ~300 K, the effective built-in potentials for all dopant combinations (Mg–Si, Zn–Si, Be–Si, and corresponding O and S donors) converge toward the classical V_{bi}, with deviations below 5 % at 400 K.

A clear hierarchy among acceptors is observed: Zn-doped GaN (120 meV) exhibits the highest $V_{bi,\mathrm{eff}}$ at low temperatures, followed by Be (150 meV), while Mg shows the strongest suppression due to its deeper acceptor level. Donor choice (Si, O, S) introduces smaller variations (<0.1–0.15 V across the full temperature range), consistent with their relatively shallow activation energies (20–32 meV). These results demonstrate that p-type dopant activation dominates the deviation from the classical model in GaN p–n junctions.

From a device-physics perspective, the reduced $V_{bi,\mathrm{eff}}$ at low temperatures implies wider depletion regions and lower junction capacitance than predicted by classical theory, directly affecting C–V characteristics, RF response, and carrier collection efficiency. This is particularly relevant for GaN-based optical photovoltaic converters (OPCs) and space or cryogenic applications, where devices may operate well below room temperature. The comparison between Figures 3(a) and 3(b) highlights the necessity of incorporating incomplete ionization in quantitative modeling of wide-bandgap devices. Future work should extend this framework to non-uniform doping profiles, polarization-induced charges in III-nitride heterostructures, and high-field operation, as well as experimental validation through temperature-dependent C-V and I–V measurements. Such integrated modeling will be essential for predictive design of high-efficiency, radiation-hard GaN devices operating under extreme thermal conditions.

Figure 4 illustrates the strong asymmetry between acceptor and donor ionization in GaN as a function of temperature and doping concentration. As shown in Fig. 4(a), deep acceptors (Mg, Zn, Be) exhibit severe incomplete ionization, particularly at low temperatures and high doping densities. Magnesium, with an activation energy of 160 meV, is the most affected: at 300 K and $N_A \sim 10^{17}$–$10^{18}\ \mathrm{cm}^{-3}$, only ~10–15 % of Mg atoms are ionized, while below 50 K Mg is almost completely frozen out. Even at elevated temperatures (~400 K), full activation is not achieved, highlighting the intrinsic limitation of p-type GaN. Lower-activation-energy acceptors partially mitigate this effect; at 300 K, Zn (120 meV) and Be (150 meV) reach ionization fractions of ~75 % and ~65 %, respectively, demonstrating improved but still incomplete hole activation. In contrast, Fig. 4(b) shows that n-type donors in GaN are nearly fully ionized across the entire investigated temperature range. Silicon donors (20 meV) exhibit ~85 % ionization already at ~10 K and exceed 99 % ionization at room temperature, with oxygen (32 meV) and sulfur (30 meV) showing similarly high activation (>95 % at 300 K). Donor ionization remains largely insensitive to both temperature and doping concentration, ensuring stable electron densities from cryogenic to high-temperature operation. These results confirm that incomplete ionization is the dominant limitation of p-type GaN and directly governs the built-in potential, depletion width, and capacitance–voltage behavior of GaN p–n junctions. For GaN-based optical photovoltaic converters and high-power devices, the reduced hole density due to incomplete Mg activation increases series resistance, degrades carrier collection, and reduces efficiency,

whereas the fully ionized n-type region ensures robust electron transport. Accurate inclusion of temperature- and concentration-dependent dopant ionization is therefore essential for realistic modeling and optimization of GaN devices operating over the 4–400 K range.

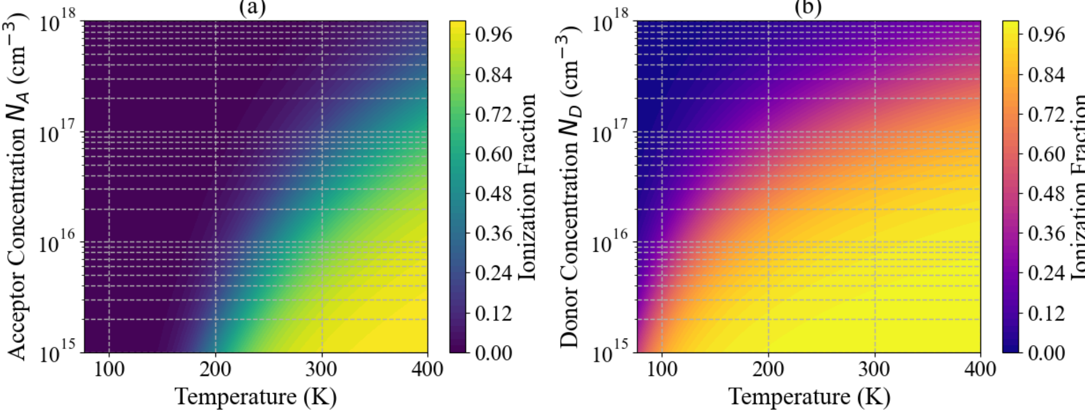

Figure 4. Temperature- and concentration-dependent ionization probabilities of dopants in GaN.
(a) Acceptor ionization probability $P_A(T)$ for Mg, Zn, and Be over 77–400 K and 10^{14}–10^{18} cm^{-3}, (b) Donor ionization probability $P_D(T, N_D)$ for Si, O, and S over the same temperature and concentration ranges.

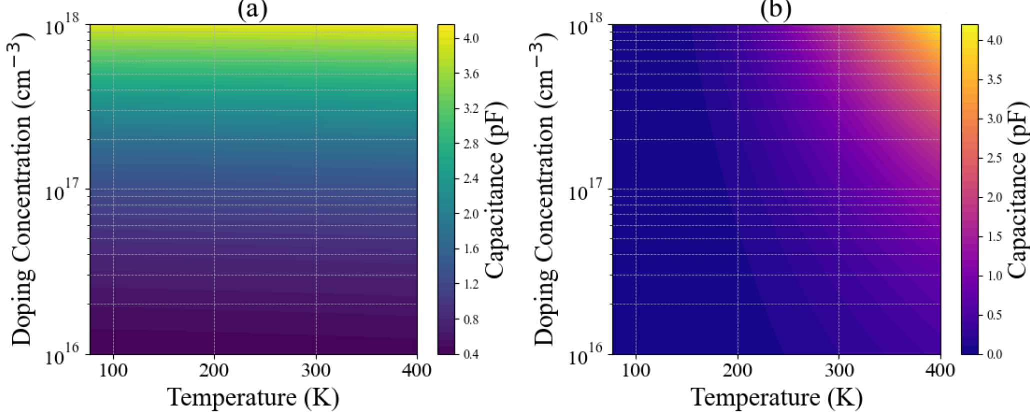

Figure 5. Temperature- and doping-dependent p–n junction capacitance of GaN: (a) classical model assuming full dopant ionization, and (b) effective model accounting for incomplete ionization of Mg acceptors and Si donors, highlighting reduced capacitance at low temperatures and high doping

Temperature- and doping-dependent junction capacitance in GaN. Figure 5 illustrates the calculated p–n junction capacitance of GaN as a function of temperature (77–400 K) and doping concentration (10^{16}–10^{18} cm^{-3}). Figure 5(a) presents the classical capacitance assuming complete dopant ionization, while Figure 5(b) accounts for the incomplete ionization of Mg acceptors (E_A = 160 meV) and Si donors (E_D = 20 meV). In the classical model (Figure 5(a)), the capacitance increases monotonically with doping, reaching up to ~4.5 pF at the highest doping ($N_A = N_D = 10^{18}$ cm^{-3}). Temperature dependence is relatively weak, with $C_{p\text{–}n}$ decreasing slightly at higher temperatures due to the increase in intrinsic carrier concentration and the logarithmic dependence of the built-in potential $V_{bi}(T)$. Across the full temperature range, the variation in capacitance for mid-range doping ($N_A = N_D = 10^{17}$ cm^{-3}) is only ~5%, indicating negligible temperature sensitivity under full ionization assumptions. In contrast, the effective capacitance model (Figure 5(b)) shows a pronounced reduction at low temperatures due to incomplete ionization of Mg. For a typical p-type doping of 5×10^{17} cm^{-3} and n-type doping of 5×10^{17} cm^{-3}, the capacitance drops from ~3.2 pF at 400 K to ~1.5 pF at 77 K, highlighting a ~53% reduction caused by the freeze-out of acceptors. Donor ionization remains nearly complete across the temperature range, so the observed decrease is primarily driven by Mg acceptors. The impact of incomplete ionization is most significant at high doping levels ($N_A \geq 10^{18}$ cm^{-3}), where the capacitance reduction reaches ~60% at cryogenic temperatures. These results emphasize that classical capacitance models overestimate $C_{p\text{–}n}$ at low temperatures, particularly for heavily Mg-doped p-type GaN. The effective model demonstrates that incomplete ionization must be incorporated to accurately predict junction behavior, especially for optical photovoltaic converters, high-power LEDs, and high-voltage GaN devices operating below room temperature. Overall, Figure 5 highlights the asymmetry between acceptor and donor ionization: n-type regions maintain robust capacitance due to nearly complete Si ionization, while p-type regions exhibit strong temperature-dependent reductions in capacitance. This behavior directly impacts depletion width, junction voltage, and charge storage, reinforcing the necessity of including temperature- and dopant-dependent ionization effects in GaN device simulations.

CONCLUSIONS

This study quantitatively demonstrates the critical impact of incomplete dopant ionization on the electrostatic and capacitance–voltage (C–V) characteristics of GaN p–n junctions using SCAPS-1D simulations. The analysis was carried out over doping concentrations ranging from 10^{15} to 10^{18} cm^{-3} and temperatures between 77 K and 400 K, incorporating both deep acceptors (Mg, Zn, Be) and shallow donors (Si, O, S).

The results show that incomplete ionization of deep acceptors, particularly Mg with activation energies of approximately 120–160 meV, leads to significant carrier freeze-out at low temperatures. For a representative doping level of 5×10^{17} cm^{-3}, the junction capacitance decreases from about 3.2 pF at 400 K to 1.5 pF at 77 K, corresponding to a reduction of approximately 53%. In more extreme cases, the overall reduction in capacitance can reach ~60% at cryogenic temperatures. This reduction is accompanied by a decrease in the built-in potential and an increase in the depletion width due to the reduced free-hole concentration.

In contrast, n-type donors with lower activation energies (~20–32 meV) remain nearly fully ionized across the entire temperature range (77–400 K), showing minimal impact on carrier availability. The bandgap variation modeled using the Varshni relation exhibits strong agreement (R^2 = 0.9721), ensuring accurate temperature-dependent simulation results.

Importantly, conventional models that neglect incomplete ionization significantly overestimate junction capacitance, particularly in heavily Mg-doped structures (≥10^{17} cm^{-3}). This leads to inaccuracies in predicting device performance, especially for applications operating under low-temperature or high-radiation conditions.

Although the study is limited to a one-dimensional SCAPS-1D framework, it captures the essential physical trends and provides reliable insight into the role of dopant ionization. The findings clearly indicate that incorporating temperature- and doping-dependent ionization effects is essential for accurate modeling and optimization of GaN-based optical photovoltaic converters, which have demonstrated efficiencies up to 79.6% at 10 W/cm², as well as for high-power and radiation-resilient electronic devices operating across extreme environments.

ORCID

Jo'shqin Sh. Abdullayev, https://orcid.org/0000-0001-6110-6616; **I.B. Sapaev,** https://orcid.org/0000-0003-2365-1554; **Jonibek Sh. Abdullayev,** https://orcid.org/0000-0001-8950-2135; **G.A. Abdikayimova,** https://orcid.org/0000-0003-3739-8430; **Kudrat Sh. Ruzmetov,** https://orcid.org/0009-0002-2575-6827; **Sh.Sh. Akhmadaliev,** https://orcid.org/0000-0003-4830-2887

REFERENCES

[1] T. Maeda, T. Narita, S. Yamada, T. Kachi, T. Kimoto, M. Horita, and J. Suda, "Impact ionization coefficients and critical electric field in GaN," Journal of Applied Physics, **129**(18), 185702 (2021). https://doi.org/10.1063/5.0050793

[2] S.J. Pearton, R. Deist, F. Ren, L. Liu, A.Y. Polyakov, and J. Kim, "Review of radiation damage in GaN-based materials and devices," Journal of Vacuum Science and Technology A, **31**(5), 050801 (2013). https://doi.org/10.1116/1.4799504

[3] N. Donato, and F. Udrea, "Static and dynamic effects of the incomplete ionization in superjunction devices," IEEE Transactions on Electron Devices, **65**(10), 4469–4475 (2018). https://doi.org/10.1109/TED.2018.2867058

[4] S.J. Pearton, Y.-S. Hwang, and F. Ren, "Radiation effects in GaN-based high electron mobility transistors," Journal of Materials, **67**, 1601–1611 (2015). https://doi.org/10.1007/s11837-015-1401-2

[5] A.T. Neal, S. Mou, R. Lopez, J.V. Li, D.B. Thomson, K.D. Chabak, and G.H. Jessen, "Incomplete ionization of a 110 meV unintentional donor in β-Ga_2O_3 and its effect on power devices," Scientific Reports, **7**, 13218 (2017). https://doi.org/10.1038/s41598-017-13341-8

[6] J.Sh. Abdullayev, and I.B. Sapaev, "Factors influencing the ideality factor of semiconductor p-n and p-i-n junction structures at cryogenic temperatures," East European Journal of Physics, (4), 329–333 (2024). https://doi.org/10.26565/2312-4334-2024-4-37

[7] M. Phifer, S. Hossain, J. Osborne, Z. Xie, and M. Alam, "Demonstration of TCAD modeling for GaN devices," in: *SoutheastCon. 2025*, (IEEE, 2025), pp. 1–6. https://doi.org/10.1109/SoutheastCon56624.2025.10971621

[8] H. Shang, and Y. Jiang, "A physical model of a diamond vertical Schottky diode including incomplete ionization and thermal effects," Journal of Physics D: Applied Physics, **58**(15), 155104 (2025). https://doi.org/10.1088/1361-6463/adb9fb

[9] C. Onwukaeme, and H.-Y. Ryu, "Design of GaN-based laser diode structures with nonuniform doping distribution in a p-AlGaN cladding layer for high-efficiency operation," Crystals, **15**(3), 259 (2025). https://doi.org/10.3390/cryst15030259

[10] J. Wei, J. Hao, Q. Zhao, J. Fan, F. Zhang, and Z. Dong, "Comparative study of wide-bandgap materials for neutron detection: GaN and 4H-SiC," Nuclear Technology, **211**(12), 3080–3093 (2025). https://doi.org/10.1080/00295450.2025.2462444

[11] J.F. Lozano, N. Seoane, J.M. Guedes, E. Comesaña, J.G. Fernandez, F.M. Almonacid, E.F. Fernández, and A. García-Loureiro, "Gallium nitride: A strong candidate to replace GaAs as base material for optical photovoltaic converters in space exploration," Optics and Laser Technology, **192**(Part A), 113447 (2025). https://doi.org/10.1016/j.optlastec.2025.113447

[12] J.Sh. Abdullayev, "Influence of linear doping profiles on the electrophysical features of p-n junctions. East European Journal of Physics, (1), 245–249 (2025). https://doi.org/10.26565/2312-4334-2025-1-26

[13] J.Sh. Abdullayev, and I.B. Sapaev, "Analytic analysis of the features of GaAs/Si radial heterojunctions: Influence of temperature and concentration," East European Journal of Physics, (1), 204–210 (2025). https://doi.org/10.26565/2312-4334-2025-1-21

[14] J.Sh. Abdullayev, I.B. Sapaev, N. Esanmuradova, S. Kadirov, and S. Kuliyev, "Mathematical analysis of the features of radial p-n junction: Influence of temperature and concentration," East European Journal of Physics, (2), 220–225 (2025). https://doi.org/10.26565/2312-4334-2025-2-24

[15] S. Chatterjee, and M. Mukherjee, "Electrical Characterization in Ultra-Wide Band Gap III-Nitride Heterostructure IMPATT/HEMATT Diodes: A Room-Temperature Sub-Millimeter Wave Power Source," J. Electron. Mater. **52**, 1552–1563 (2023). https://doi.org/10.1007/s11664-022-10090-2

[16] J.Sh. Abdullayev, I.B. Sapaev, and S.R. Kadirov, The role of recombination types in efficiency limits of radial p-n junctions based on Si and GaAs. East European Journal of Physics, (2), 252–257 (2025). https://doi.org/10.26565/2312-4334-2025-2-30

[17] J.Sh. Abdullayev, I.B. Sapaev, J.S. Abdullayev, D.A. Juraev, M.J. Jalalov, and E.E. Elsayed, "Mathematical Modeling of Incomplete Ionization in Radial *p*-Si/*n*-GaAs Heterojunctions: Temperature and Doping Effects. *J. Electron. Mater.* **54**, 10484–10492 (2025). https://doi.org/10.1007/s11664-025-12391-8

[18] J.Sh. Abdullayev, L. Abdullayeva, L. Agamalieva, and R. Ismailova, "Correlating Ni microstructure with Schottky barrier homogeneity in monolayer MoS_2 field-effect transistors," Advanced Physical Research, **7**(3), 350–357 (2025). https://doi.org/10.62476/apr.73350
[19] P. Murugapandiyan, K. Sri Rama Krishna, A. Revathy, and A. Fletcher, "Enhancement Mode AlGaN/GaN MISHEMT on Ultra-Wide Band Gap β-Ga_2O_3 Substrate for RF and Power Electronics," J. Electron. Mater. **53**, 2973–2987 (2024). https://doi.org/10.1007/s11664-024-11005-z
[20] J.S. Abdullayev, D.A. Qalandarova, M.S. Ibragimova, I.B. Sapaev, and J.I. Razzokov, "Experimental and Simulation-Based Investigation of p-Si/n-CdS Heterojunctions: From Cryogenic Freeze-Out to Room Temperature Operation," J. Electron. Mater. **55**, 2229–2239 (2026). https://doi.org/10.1007/s11664-025-12642-8
[21] A. Kumar, G. Kumar, and C. Kumar, "Design and Performance Evaluation of a $Ge_{1-x}Sn_x$/Ge Multiple Quantum Well Heterojunction Phototransistor for Long-Haul DWDM Optical Communication Systems," J. Electron. Mater. (2026). https://doi.org/10.1007/s11664-025-12653-5
[22] M.A.A. Rosle, and M.Z. Pakhuruddin, "Investigation of gallium nitride emitter thickness in GaN/Si heterojunction solar cell by SCAPS-1D," NanoVol, **20**(09), 2550026 (2025). https://doi.org/10.1142/S1793292025500262
[23] M.K. Omar, M. Rashid, and M.Z. Pakhuruddin, "Investigation on indium concentration in two-terminal tandem indium gallium nitride solar cells by SCAPS-1D," Physica Scripta, **99**(11), 115531 (2024). https://doi.org/10.1088/1402-4896/ad8193
[24] H. Abboudi, W. Belaid, R. En-nadir, I. Ez-zejjari, M. Zouini, A. Sali, and H. El Ghazi, "Optimization of $In_xGa_{1-x}N$ P-I-N solar cells: Achieving 21% efficiency through SCAPS-1D modeling," Crystals, **15**(7), 633 (2025). https://doi.org/10.3390/cryst15070633
[25] Z. Hu, K. Nomoto, B. Song, M. Zhu, M. Qi, M. Pan, X. Gao, *et al.*, "Near unity ideality factor and Shockley-Read-Hall lifetime in GaN-on-GaN p-n diodes with avalanche breakdown featured," Applied Physics Letters, **107**(24), 243501 (2015). https://doi.org/10.1063/1.4937436
[26] J.S. Abdullayev, M.S. Ibragimova, J.Sh. Abdullayev, and I.B. Sapaev, "Cryogenic material and electrophysical changes in Si and GaAs," East European Journal of Physics, (1), 343–350 (2026). https://doi.org/10.26565/2312-4334-2026-1-40
[27] Y.-C. Lai, Y.-N. Zhong, M.-Y. Tsai, and Y.-M. Hsin, "Gate capacitance and off-state characteristics of E-mode p-GaN gate AlGaN/GaN high-electron-mobility transistors after gate stress bias," Journal of Electronic Materials, **50**, 1162–1166 (2021). https://doi.org/10.1007/s11664-020-08949-1
[28] N. Bano, I. Hussain, E.A. Al-Ghamdi, and M.S. Ahmad, "Quantitative analysis of electrically active defects in Au/AlGaN/GaN HEMTs structure using capacitance–frequency and DLTS measurements," Journal of Physics Communications, **5**(12), 125010 (2021). https://doi.org/10.1088/2399-6528/ac41aa
[29] S. Lv, S. Wang, J. Yu, G. Tian, G. Wang, P. An, K. Song, *et al.*, "Wafer scale gallium nitride integrated electrode toward robust high temperature energy storage," Small, **20**(27), 2310837 (2024). https://doi.org/10.1002/smll.202310837
[30] W. Yang, J.-S. Yuan, B. Krishnan, A.J. Tzou, and W.-K. Yeh, "C-V measurement under different frequencies and pulse-mode voltage stress to reveal shallow and deep trap effects of GaN HEMTs," in: *2018 IEEE 6th Workshop on Wide Bandgap Power Devices and Applications (WiPDA)*, (Atlanta, GA, USA, 2018). https://doi.org/10.1109/WIPDA.2018.8569206
[31] J. Park, S.H. Lee, I.M. Kang, and Y.J. Yoon, "Fabrication of AlGaN/GaN HEMT using TMAH pre-treatment and analysis of electrical characteristics by proton irradiation," Current Applied Physics, **75**, 33–39 (2025). https://doi.org/10.1016/j.cap.2025.04.010
[32] H. Sun, Q. Fan, X. Ni, Q. Luo, and X. Gu, "Low-pressure chemical vapor deposition SiNx process study and its impact on interface characteristics of AlGaN/GaN MISHEMTs," Micromachines, **16**(4), 442 (2025). https://doi.org/10.3390/mi16040442
[33] D.A. Qalandarova, M.S. Ibragimova, J.S. Abdullayev, and I.B. Sapaev, "Mathematical modeling of electrostatic potential in radial and planar p–n junctions: A comparative study," East European Journal of Physics, (1), 333–342 (2026). https://doi.org/10.26565/2312-4334-2026-1-39
[34] J.S. Abdullayev, M.S. Ibragimova, J.Sh. Abdullayev, and I.B. Sapaev, "Thermal expansion characteristics of planar and radial Si/GaAs p–n heterojunctions," East European Journal of Physics, (1), 388–395 (2026). https://doi.org/10.26565/2312-4334-2026-1-46
[35] H. Teisseyre, P. Perlin, T. Suski, I. Grzegory, S. Porowski, J. Jun, A. Pietraszko, and T.D. Moustakas, "Temperature dependence of the energy gap in GaN bulk single crystals and epitaxial layer," Journal of Applied Physics, **76**(4), 2429–2434 (1994). https://doi.org/10.1063/1.357592
[36] C. Prall, M. Ruebesam, C. Weber, M. Reufer, and D. Rueter, "Photoluminescence from GaN layers at high temperatures as a candidate for in situ monitoring in MOVPE," Journal of Crystal Growth, **397**, 24–28 (2014). https://doi.org/10.1016/j.jcrysgro.2014.04.001
[37] J.Sh. Abdullayev, D.A. Qalandarova, and M.Sh. Ibragimova, "Impact of incomplete ionization on the critical electric field of p-n junction structures based on Si and GaAs," Low Temperature Physics, **52**(2), 164–169 (2026). https://doi.org/10.1063/10.0042291

МОДЕЛЮВАННЯ ВПЛИВУ НЕПОВНОЇ ІОНІЗАЦІЇ ДОМІШОК НА ВБУДОВАНИЙ ПОТЕНЦІАЛ І ВОЛЬТ-ФАРАДНІ (C–V) ХАРАКТЕРИСТИКИ p–n ПЕРЕХОДІВ GaN: ДОСЛІДЖЕННЯ ЗА ДОПОМОГОЮ SCAPS-1D

Джошкін Ш. Абдуллаєв[2], І.Б. Сапаєв[2], Джонібек Ш. Абдуллаєв[7], Г.А. Абдикаїмова[3], Ш.Ш. Ахмадалієв[4], М.М. Гуломова[5], Ш.О. Холбеков[5], Кудрат Ш. Рузметов[6]
[1]Інститут фундаментальних та прикладних досліджень, Національний дослідницький університет «ТІІАМЕ», Ташкент 100000, Узбекистан
[2]Національний дослідницький університет ТІІАМЕ, фізико-хімічний факультет, Ташкент, Узбекистан
[3]Ташкентський державний технічний університет, Ташкент, Узбекистан
[4]Ферганський медичний інститут громадського здоров'я, Фергана, Узбекистан
[5]Каршинський державний технічний університет, місто Карші, Кашкадарьинська область, Узбекистан, 180100
[6]Ташкентський державний аграрний університет, 100020, Ташкент, Узбекистан
[7]Ургенчський державний університет, вул. Хаміда Олімжона, 14, Ургенч, 220100 Узбекистан

Неповна іонізація домішок у напівпровідниках із широкою забороненою зоною відіграє критичну роль у визначенні концентрації носіїв заряду, електростатичних властивостей і загальної продуктивності пристроїв; однак її вплив на p–n переходи GaN для оптичних фотовольтаїчних перетворювачів (OPC) залишається недостатньо вивченим. У цій роботі використано моделювання SCAPS-1D для систематичного дослідження p–n переходів GaN із трьома p-типовими акцепторами

(Mg, Zn, Be) і трьома n-типовими донорами (Si, O, S) у діапазоні концентрацій легування 10^{15}–10^{18} см$^{-3}$ і температур від 77 K до 400 K. Температурна залежність ширини забороненої зони описується за допомогою співвідношення Варшні ($R^2 = 0,9721$), тоді як іонізація домішок моделюється як функція температури та рівня легування для врахування її впливу на розподіл носіїв, вбудований потенціал і вольт-фарадні (C–V) характеристики. Результати демонструють суттєве зменшення ємності переходу за нижчих температур через неповну іонізацію акцепторів. Для характерного рівня легування 5×10^{17} см$^{-3}$ ємність зменшується приблизно з 3,2 пФ при 400 K до 1,5 пФ при 77 K (≈53% зниження), що переважно зумовлено частковою іонізацією акцепторів Mg, тоді як донорні домішки залишаються майже повністю іонізованими. Ці результати показують, що традиційні моделі, які ігнорують неповну іонізацію, суттєво переоцінюють ємність переходу за низьких температур. Хоча аналіз базується на одновимірній моделі, він надає фізично узгоджене розуміння ролі глибоких домішкових рівнів і закладає основу для майбутніх багатовимірних TCAD-досліджень. Це дослідження підкреслює необхідність урахування ефектів неповної іонізації під час проєктування та оптимізації високоефективних, стійких до радіації OPC на основі GaN, що працюють в екстремальних умовах.
Ключові слова: *GaN; іонізація домішок; неповна іонізація; оптичні фотовольтаїчні перетворювачі (OPC); температурно-залежна активація носіїв; вольт-фарадні характеристики; вбудований потенціал; широкозонні напівпровідники (WBG); радіочастотні характеристики*

DOI:10.26565/2312-4334-2026-2-28 ISSN 2312-4334

INVESTIGATION OF STRUCTURAL, OPTOELECTRONIC AND PHOTOVOLTAIC PERFORMANCE OF Cu_2SnS_3COMPOUND: COMBINED DFT AND SCAPS-1D SIMULATIONS

Boualem Kada[1], Karima Benyahia[1], Nabil Beloufa[2,3], Hamza Rekab-Djabri[2,4], D. Belfennache[5], Abdelkader Bouhenna[1], Samir Bekheira[2], A. Alami[6], Hamad M. Adress Hasan[7], Hamdy A. Khatab Ali[8]

[1]*Materials Science and Applications Laboratory (LSMA), Faculty of Sciences and Technology, University of Ain-Temouchent, Algeria*
[2]*Laboratory of Micro and Nanophysics (LaMiN), National Polytechnic School of Oran, ENPO-MA, BP 1523, El M'Naouer, 31000, Oran, Algeria*
[3]*Hydrometeorological Institute for Training and Research IHFR, Ibnou Rochd.Bp 7019, Oran, Algeria*
[4]*Faculty of Nature and Life Sciences and Earth Sciences, AkliMohand-Oulhadj University, 10000, Bouira, Algeria*
[5]*Research Center in Industrial Technologies (CRTI) P.O. Box 64, Cheraga 16014 Algiers, Algeria*
[6]*Laboratory of Process Engineering, Materials and Environment, Faculty of Technology, University of DjillaliLiabes, P.O. Box 89, Sidi Bel Abbes 22000, Algeria;*
[7]*Chemistry Department, Faculty of Science, Omar Al-Mukhtar University, Libya*
[8]*Chemistry Department Faculty of Education (Al-Marj), Benghazi University, Libya*
**Correspondence Author e-mail: belfennachedjamel@gmail.com*
Received February 12, 2026; revised March 3, 2026; accepted May 6, 2026

Evaluating the structural, optoelectronic, and photovoltaic performance of the Cu_2SnS_3 compound is essential for the development of materials for solar energy. This ternary chalcogenide semiconductor stands out for its strong potential in photovoltaic applications, thanks to its broad light-absorbing range and chemical stability. In this paper, we have examined the structural and optoelectronic properties of copper-based ternary semiconductors, specifically those in the Cu_2SnS_3 compound, and their effectiveness in photovoltaic applications. Since there is significant variation in previous studies on the band gap values (0.65-1.35 eV), an attempt was made to find an appropriate approximation for studying this type of compound. The structural properties were investigated using both the Perdew-Burke-Ernzerhof (PBE) form of the generalized gradient approximation (GGA) and the local density approximation (LDA), allowing a comparative assessment of the effects of different exchange-correlation functionals on the material's structure. Given the important influence that Cu delectrons play in determining their electronic properties, as shown by the results obtained when using different exchange correlation energy functionals. The combined function of the Becke-Johnson potential, modified by Tran and Blaha, and the Hubbard potential (TB-mBJ+U) was employed to systematically optimize the calculated anion displacement. The calculations yielded the band gap values. The semiconductor quasiparticle is 0.7 eV in the monoclinic structure (m-CTS; SG: Cc), and that of the orthorhombic structure (gold-CTS; SG: Imm2) is 0.73 eV, which is largely consistent with experimental values. The study of optical properties, including the dielectric function, also revealed the reflectance, absorption coefficient, and refractive index of the Cu_2SnS_3 compound in its two phases. The latter is considered a promising candidate in optoelectronic applications. To verify this, we used the SCAPS program, and the results were good. When this compound is used as an absorbent layer in a photovoltaic cell, the current density (Jsc) increases, peaking at a thickness of 800 nm.
Keywords: *Cu_2SnS_3; FP-LAPW; LDA; TB-mBJ+U; Photovoltaic cells*
PACS: 73.50.-h, 73.50.Pz

1. INTRODUCTION

Semiconductors are attracting considerable interest due to their strong potential in photovoltaic applications, particularly for thin-film solar cells [1-3]. Among them, the chalcogenide family, especially copper chalcogenides and copper tin sulfide (CTS), is attracting increasing attention for their use in this type of device [4,5]. The preparation of these materials as colloidal inks can enable low-cost manufacturing via solution-based printing and coating processes [6, 7].

Due to the scarcity and rising prices of indium and gallium, there is interest in alternative chalcogenide semiconductors $Cu_2ZnSnSe_4$ (CZTSe) and Cu_2ZnSnS_4 (CZTS) [8,9]. The later solar panels have a relatively optimal efficiency of about 14% [10,11]. In practice, one could reduce the synthesis cost by incorporating tin and zinc at indium and gallium sites, respectively, in the CZTSe quaternary system. These later systems have very attractive applications as near-infrared devices [12], efficient Li-ion batteries [13,14], thermoelectric materials [15], and acousto-optic instrumentation. The CTSe compound is regarded as a promising material for solar panels, with a direct optical gap measured at 1.1-1.5 eV [16]. Several simple ternary systems exist, such as Cu_2SnSe_3, an example of a current low-cost solar cell. [17,18]. Cu_2SnSe_3 (CTSe) is a p-type semiconductor with an absorption coefficient greater than 10^4 cm^{-1} and a direct band gap between 0.8 and 1.1 eV. [19,20]. Compared to other solar cells, those based on CZTS (Cu_2ZnSnS_4) have achieved a maximum photovoltaic conversion efficiency of 12.6%. [21]. The CTS (Cu_2SnS_3) is a semiconductor interlayer compound that can be doped with zinc for the synthesis of CZTS (Cu_2ZnSnS_4). [22, 23]. CTS nanocrystals

Cite as: B. Kada, K. Benyahia, N. Beloufa, H. Rekab-Djabri, D. Belfennache, A. Bouhenna, S. Bekheira, A. Alami, H.M.A. Hasan, A.K.A. Hamdy, East Eur. J. Phys. 2, 260 (2026), https://doi.org/10.26565/2312-4334-2026-2-28
© B. Kada, K. Benyahia, B. Nabil, H. Rekab-Djabri, D. Belfennache, A. Bouhenna, S. Bekheira, A. Alami, H.M.A. Hasan, A.K.A. Hamdy, 2026; CC BY 4.0 license

(NC) can themselves serve as absorbers for thin-film photovoltaic systems. [24] Therefore, the CTS system is composed of non-toxic, naturally abundant elements and is economically viable [25, 26]. Therefore, based on the latter considerations, this material is particularly relevant, both for its elaboration process and its attractive applications, such as solar panel technologies and precise optoelectronic devices. [27]. Actually, more research is focused on studying different absorber materials that exhibit excellent environmental performance and high-efficiency conversion panels [28,29]. Furthermore, the Cu_2SnS_3 (CTS) technology is a viable option, as it is composed of abundant, non-toxic elements. [30]. In the Cu-Sn-Se system, most research has been conducted on the ternary semiconductor Cu_2SnSe_3 [31]. The Cu_2SnSe_3 compound formed has a congruent melting point of 963 K [32] or 968 K [33].

Cu_2SnS_3 (CTS) remains one of the most promising ternary photo absorbing compounds [34, 35]. Because of its wide band gap and high optical absorption coefficient in the visible spectrum, it is a very attractive material for thin-film PV applications [36, 37]. The first PV device using the CTS compound as an absorber material was developed by T. A. Kuku and O. A. Fakolujo [38], with an efficiency of 0.11%. Since then, research on this material has almost stagnated, until a cell with an efficiency of 2.84% was reported by Koike et al. [39]. Studies conducted by Umehara et al. [40] have shown that it is possible to improve the efficiency of the CTS cell to 6.0% by doping it with germanium (Ge) using a $Cu_2Sn_{0.83}Ge_{0.17}S_3$ composition. CTS is a ternary semiconductor belonging to the I-IV-VI group [34]. It is a polymorphic material that crystallizes in various systems, namely cubic (F4-3m) with a=b=c=5.696Å [41], tetragonal I4-2d with a=b=5.689Å and c=11.370Å [42], monoclinic C1c1 with a=6.967Å, b=12.049Å, and c=6.945Å [31], and monoclinic superstructure C1c1 with a=6.961Å, b=12.043Å, and c=26.481Å [32].A hexagonal structure of CTS was reported by Wu et al. [43]. However, to date, no other study has reproduced this structure. Some rare research has been conducted on the synthesis of CTS with a triclinic phase. [44,45], and no detailed crystallographic description of this structure has been provided. Thus, the Cu_2SnS_3 compound exists in cubic, tetragonal, and monoclinic structures [34]. Furthermore, with the identification of copper-rich phases such as Cu_3SnS_4, Cu_4SnS_4, and Cu_2S, we obtain an increase in the conductivity of these materials. [46]. Robles et al. [47] demonstrate that the resistivity of CTS has been increased from 2.10^{-3}Ω.cm to 5.10^{-3}Ω.cm. Bodeux et al. [48] indicated that the variation in component content had an influence on the increase in CTS conductivity. They noted an increase from 0.1 S cm^{-1} to 0.8 S cm^{-1} for a Cu/Sn ratio that increased from 1.9 to 2.2. Thus, it is clear that the presence of secondary phases modifies the optical and electrical properties of the CTS compound and consequently affects the conversion efficiency of PV solar cells.

The thermodynamic study of CTS formation reveals that tetragonal and monoclinic structures form at relatively low temperatures (<750°C), whereas the cubic structure forms at higher temperatures (>750°C) [35]. Furthermore, cubic-structured CTS can also be produced experimentally at low temperatures using chemical synthesis methods by optimizing the experimental conditions [49]. Theoretically, calculations of the electronic density of states have all shown that CTS offers a direct optical aperture with theoretical values ranging from 0.84 eV to 0.88 eV [50, 51], while experimentally, the different optical gap values reported in the literature are in an extremely large range, from 0.83 to 1.77 eV [38,46,52], which are desirable values for PV applications. This compound also exhibits a strong optical absorption coefficient, with values reaching up to $10^5 cm^{-1}$[36, 52].

The originality of this study lies in the evaluation of the structural and optoelectronic properties of the Cu_2SnS_3 compound in both monoclinic (Cc) and orthorhombic (Imm2) structures using DFT and four approaches: LDA, GGA, GGA + U, and (TB-mBJ+U). Solar cell modeling based on CTS was performed using the 1-dimensional solar cell capacitance software (SCAPS-1D) to achieve optimal electrical conversion efficiency. The models studied take into account the influence of the thickness of the absorber coating on the behavior of the back contact, the effect of different parameters such as the thickness and concentration of doping of the various layers, as well as the design of a new Cu_2SnS_3 (CTS) based solar cell with a promising efficiency.

2. COMPUTATIONAL DETAILS

2.1 First-principle calculation of Cu_2SnS_3

Ab initio calculations were performed using the Full-Potential Linearized Augmented Plane Wave (FP-LAPW) method [53], as implemented in the Wien2k code [54], within the density functional theory (DFT) formalism [55]. To accurately model the structural and electronic properties of the Cu_2SnS_3-Cc and Cu_2SnS_3-Imm2 phases, we adopted both the generalized gradient approximation (GGA) according to the Perdew-Burke-Ernzerhof (PBE) formalism [56] and the local density approximation (LDA) [57]. To improve the accuracy of describing band gaps and electronic correlation effects, particularly in d orbitals, the modified Tran-Blaha exchange potential (TB-mBJ) was combined with a Hubbard (U) correction (TB-mBJ + U), thereby providing a more accurate representation of electronic interactions in these complex compounds. [58, 59] for all cited systems. In the FP-LAPW method, the Kohn and Sham wave functions are developed in terms of spherical harmonics within the MT spheres for a maximum value of lmax=10.

The muffin-tin sphere radii (Rmt) for Cu_2SnS_3-Cc of the Cu, Sn, and S atoms are 2.26 u.a., 2.14 u.a., and 1.95 u.a., respectively; for Cu_2SnS_3-Imm2, they are 2.24 u.a., 2.16 u.a., and 1.85 u.a. The size of basis sets was controlled by the parameter RMT. Kmax (where Kmax is the maximum modulus for the reciprocal lattice vector), we have extended the basis function to RMT in our computations. Kmax is equal to 8. The number of k-points in the whole Brillouin zone was chosen as 250 for both systems to converge the total energy, with a mesh of 13×11×13 for the Cu_2SnS_3-Ccand and 11×9×11 for the Cu_2SnS_3-Imm2 compound. The optical properties of both compounds are calculated using a 1000 k-

point mesh in the irreducible Brillouin zone. The self-consistent iterations are repeated until the convergence energy is less than or equal to 10^{-4} Ry.

2.2 SCAPS-1D numerical simulation

To design one-dimensional solar cells, we use SCAPS (Solar Cell Capacitance Simulator), a numerical modeling tool provided by the Electronics and Information Systems (ELIS) department at Ghent University, Belgium [60, 61]. Therefore, the software can easily simulate various energy conversion factors, including power conversion efficiency (PCE), fill factor (FF), energy gap (Eg), short-circuit current density (Jsc), quantum efficiency (QE), and current-voltage characteristics (J-V) [62].

Most studies of semiconductor devices are based on the simultaneous solution of Poisson's equation and the continuity equation. It calculates the concentrations of electrons and holes, as well as the value of the electrostatic potential, at every moment and at every point in space using a sequence of finite elements. The relationship between potential and carrier density is expressed by Poisson's equation. [63]:

$$\Delta V = \frac{-q}{\varepsilon}(N_d - N_a + p - n) \tag{1}$$

where V is the potential, q is the elementary charge of electrons, N_d and N_a are the concentrations of ionized donor and acceptor dopants. n and p are the carrier densities. The equations of continuity define the variations in charge density (electrons, holes) and are formulated by the following equations [64]:

$$\frac{\partial n}{\partial t} = G_n - \frac{\Delta n}{\tau_n} + \mu_n\left(\xi\frac{\partial n}{\partial x} + n\frac{\partial \xi}{\partial x}\right) + D_n\frac{\partial^2 n}{\partial^2 x}, \tag{2}$$

$$\frac{\partial p}{\partial t} = G_p - \frac{\Delta p}{\tau_p} + \mu_p\left(\xi\frac{\partial p}{\partial x} + p\frac{\partial \xi}{\partial x}\right) + D_p\frac{\partial^2 p}{\partial^2 x}, \tag{3}$$

where n and p are the concentrations of electrons and holes, G_n and G_p are the electron and hole generation rates, and τ_n and τ_p are the electron and hole recombination rates, which themselves have complex expressions related in particular to illumination. The charge carriers can be moved by the presence of both an electric field and a concentration gradient. Under the influence of an electric field, a current called drift current (or conduction current) is generated. This current is proportional to the electric field and defined by the following relationship [65].

$$J_n(x) = q\mu_n nE(x) + qD_n\frac{dn(x)}{dx}, \tag{4}$$

$$J_p(x) = q\mu_p pE(x) + qD_p\frac{dp(x)}{dx}. \tag{5}$$

Here n and p are the concentrations of electrons and holes, $J_n(x)$ and $J_p(x)$ are the electron and hole current densities, where E(x) is the electric field and μ_n and μ_p are the mobilities of electrons and holes, respectively.

3. RESULTS AND DISCUSSIONS

3.1 Structural properties

In this study, the crystal structure of the Cu_2SnS_3 compound belongs to the orthorhombic space group (Cc) or monoclinic space group (Imm2), as shown in Figures 1a and 1b. In the unit cell of the CTS compound with the structure, the Cu^+ and Sn^{4+} cations occupy distinct sites in the crystal lattice, while the S^{2-} anions provide the bond between these tetrahedral units. This phase is less common than the monoclinic and cubic phases, whereas in monoclinic CTS, Cu and Sn atoms completely occupy the two separate tetrahedral sites in an orderly manner at the cation positions and do not share the same atomic positions and are distorted with different M-S distances.

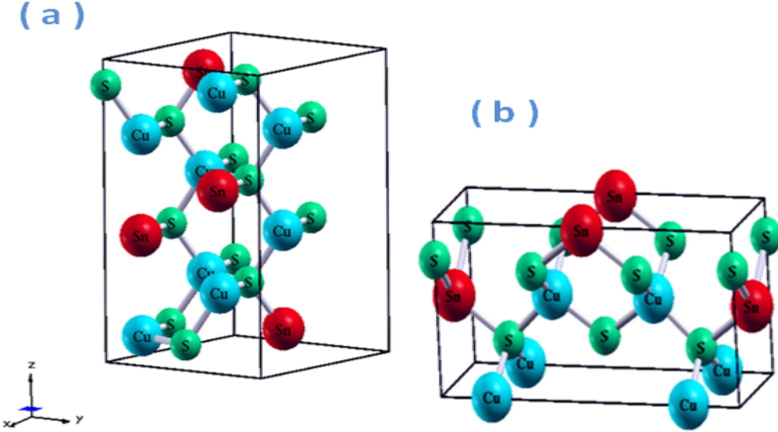

Figure 1. The crystal structure of Cu_2SnS_3 compounds: (a): Monoclinic with Cc symmetry, (b): Orthorhombic with Imm2 symmetry

In the current structural optimization, we aim to determine the ground state of our compound, which was initially required. More than a hundred iterations of the process were done until the total energy calculation converged. The parameters of the network at equilibrium are calculated by adjusting the total energy of the volume using Murnaghan's empirical formula [66], following the well-known relationship:

$$E(V) = E_0 + \left[\frac{B_0 V}{B'(B'-1)}\right] \cdot \left[B'\left(1 - \frac{V_0}{V}\right) + \left(\frac{V_0}{V}\right)^{B'} - 1\right], \tag{6}$$

where B and B' denote the compression modulus and its derivative, respectively. V_0 is the volume of the ground state. The modulus of compressibility (B) and its derivative (B_0') are defined by:

$$B_0 = V\left(\frac{\partial^2 E}{\partial V^2}\right), \tag{7}$$

$$k = \frac{\partial B}{\partial P}. \tag{8}$$

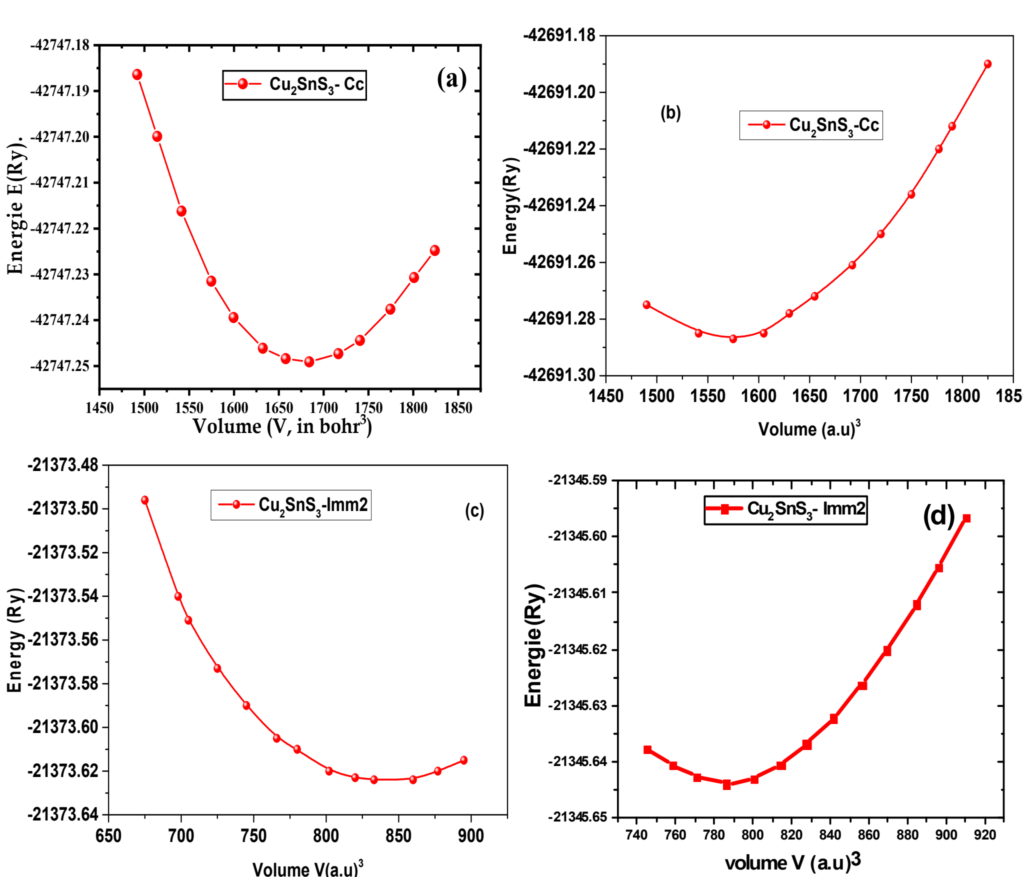

Figure 2. Volume optimization of Cu_2SnS_3-Cc was performed using (a) GGA-PBE and (b) LDA, while Cu_2SnS_3-Imm2 was optimized using (c) GGA-PBE and (d) LDA approximations

As illustrated in Figures 2a, b, c, and d, the predicted variation of the total energy versus the cell volume for Cu_2SnS_3-Cc and Cu_2SnS_3-Imm2 using both well-known exchange and correlation LDA and GGA-PBE functionals. All the obtained results, such as (lattice constants a, bulk modulus B, and its derivative B'), are obtained using the plane wave method and the pseudo potentials are summarized in the Table. 1. One could observe easily that the obtained results according to the GGA functional are the closest ones with an excellent correlation to the experimental counterpart [67-69].

Table 1. Calculated lattices constants (a, b, c) in (Å), bulk modulus B (GPa), the derivative and β (Deg), of Cu_2SnS_3-Cc and Cu_2SnS_3-Imm2

	a(Å)	b(Å)	c(Å)	B (GPa)	B ′	β (Deg)
			Cu_2SnS_3-Cc			
LDA	6.59*	11.41*	6.62*	90.67*	4.94*	111.07*
GGA	6.70*	11.67*	6.73*	68.70*	4.85*	109.37*
Other Calcul	6.65^a, 6.654^b 6.653^c 6.71^d	11.54^a, 11.534^b 11.536^c 11.620^d	6.67^a, 6.654^b 6.665^c 6.74^d	- - - -	- - - -	$109.39^{a,c}$, 109.67^d - -

	a(Å)	b(Å)	c(Å)	B (GPa)	B′	β (Deg)
	Cu_2SnS_3-Cc					
	6.079[e]		6.741[e]	-	-	-
	Cu_2SnS_3-Imm2					
LDA	3.76*	5.18*	11.24*	91.48*	5.52*	-
GGA	3.91*	5.42*	11.65	71.46*	4.47*	-
Other Calcul	3.92[d] 3.923[e]	5.43[d] 5.428 [e]	11.61[d] 11.612[e]	- -	- -	- -

*Present calculations, [a]Ref [67] Experimental (photoreflectance spectroscopy (PR), [b]Ref [68] Experimental, [c]Ref [69] X-ray diffraction method, [d]Ref [50] PBE-GGA and TB-mBJ approximations, [e]Ref [70] TB-mBJ approach and Hubbard potential.

The comparative study is well elucidated in the Table. 1 of the obtained results enables us to employ the PBE-GGA approximation as the practical potential, based on rigorous crystallographic atomic positions, thereby providing our study with an accurate electronic band-gap configuration.

3.2 Electronic properties

3.2.1 Band structure

Based on equilibrium structural parameters for the Cu_2SnS_3-Cc and Cu_2SnS_3-Imm2 structures, we investigate the electronic characteristics of Cu_2SnS_3 compounds. We use the modified Becke Johnson potential (mBJ), the Hubbard formalism (U), and the generalized gradient approximation (PBE-GGA). The Fermi level is referenced at 0 eV. We compute the band structures for our compounds along the directions of symmetry in the first zone of Brillouin (ZB).

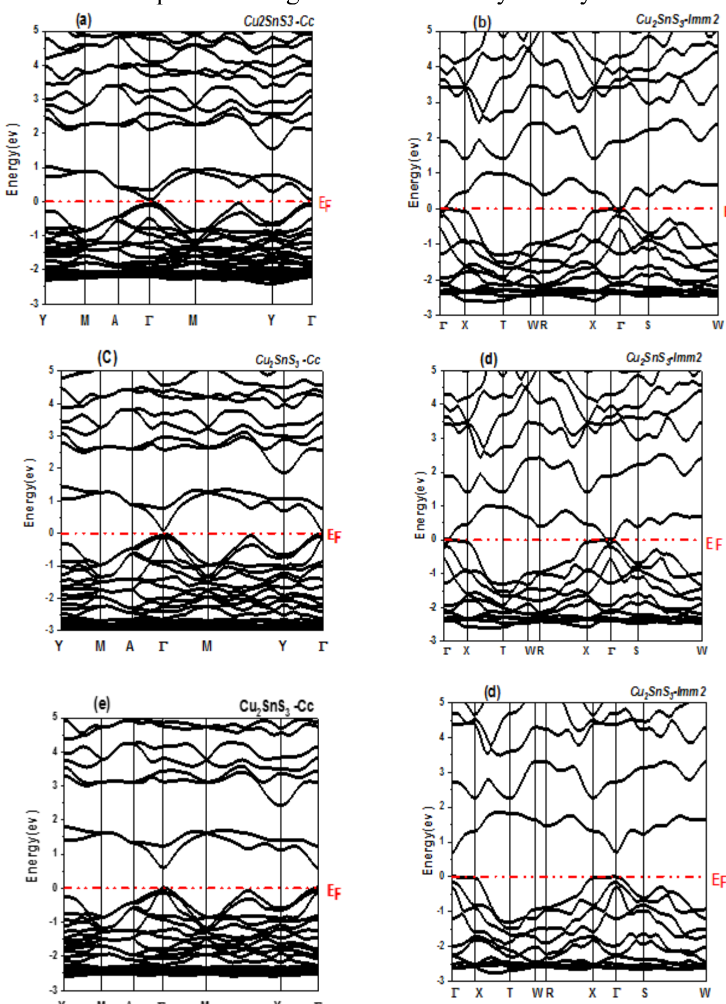

Figure 3. The band structures of Cu_2SnS_3 in the Cc phase (left panel) were computed using: (a) PBE-GGA, (c) Hubbard correction, and (e) TB-mBJ+U, while those of Cu_2SnS_3 in the Imm2 phase (right panel) were obtained using: (b) PBE-GGA, (d) Hubbard correction, and (f) TB-mBJ+U

Initially, we employed the GGA approximation to calculate the band gap, which revealed that the CTS material is a metal, as illustrated in Figs. 3(a) and 3 (b). We note a gap of 0.086 eV for Cu_2SnS_3-Cc-Cc and 0 eV for Cu_2SnS_3-Imm2 at the high symmetry point *Γ*. By comparing our results with the experimental value of 0.92 eV for the monoclinic phase [71, 72], we note a significant discrepancy. For the d-type orbital correction on Cu atoms, we employed the TB-mBJ + U

approximation [73], which accounts for the overlap involving the Cu 3d orbitals that constitute the top of the valence band." To determine the correct Ud (Cu) value, we conducted a series of tests, as shown in Table 2, and recorded the resulting values. Through these tests, we established that Ud (Cu) = 6 eV is the appropriate value to correct this situation.

Table 2 Band gap calculation of Cu_2SnS_3

Compound	Energy gap Eg (eV)									
	GGA	Hubbard				TB-mbj +U				Other Calaculations
		U_d=0	U_d=2	U_d=4	U_d=6	U_d=0	U_d=2	U_d=4	U_d=6	
Cu_2SnS_3-Cc	0.086	0.086	0.13	0.19	0.26	0.29	0.36	0.52	0.70	0.70[70] ,0.88[74] 0.95[75]
Cu_2SnS_3-Imm2	0	-	-	-	.0065	-	-	-	0.73	0.60[70]

The obtained electronic band structures of Cu_2SnS_3-Cc and Cu_2SnS_3-Imm2 structures are shown in Fig. 3 (c, d, e, and f). It is clear that both compounds exhibit p-type semiconductors with direct band gaps (Γ–Γ) of 0.70 eV for Cu_2SnS_3-Cc and 0.732 eV for Cu_2SnS_3-Imm2. The results obtained are consistent with previously reported experimental values. The band gap, as determined by the various approximations employed in this section, is summarized in Table 2.

3.2.2 Density of state

To elucidate the orbital hybridization mechanisms in CTS alloys and clarify the contributions of different atomic states to the electronic band structures, the predicted total density of states (TDOS) and partial density of states (PDOS) were calculated and are shown in Figs. (4a) and (4b), respectively. The Fermi level (EF) was arbitrarily set at 0 eV to serve as an energy reference. We note that there is a similarity in density of states to monoclinic and orthorhombic structures of Cu_2SnS_3, where we find that the energy region between [-14, -6] eV.

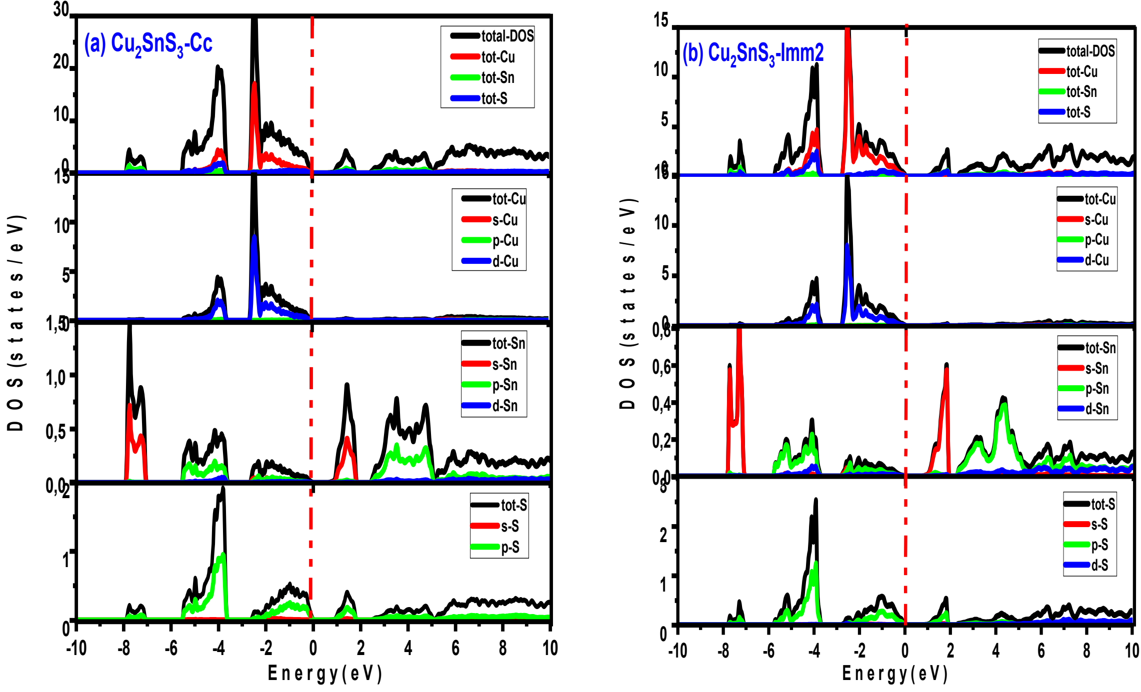

Figure 4. The density of states (DOS) partial and total of Cu_2SnS_3-Cc and Cu_2SnS_3-Imm2 using (GGA-PBE)

The electronic states corresponding to the s and p orbitals of the Sn atom, as well as the s orbitals of the S atom, are confined to an energy band located approximately between -14 eV and -6 eV. The failure of the PBE-GGA approximation to calculate the band gap is further exacerbated by the observation that the conduction band around the Fermi level is primarily composed of Cu (d) with a minor contribution from the p states of (Sn) and (S). The d states of Cu predominate at the maximum of the valence band.

The energy region [0,14] eV is characterized by the significant contribution of the p of (Sn) and the small contribution of the p of (S), which resulted in a gap of 0.7 and 0.73 electron-volts for Cu_2SnS_3-Cc and Cu_2SnS_3-Imm2, respectively. Eventually, the Cu_2SnS_3 compound exhibits semiconductor behavior; this property likely makes it a promising candidate for various applications.

3.3 Optical Properties

The optical properties of solids for the complete range of photon energies can be characterized as the complex dielectric function, defined by the following formula [76]:

$$\varepsilon(\omega) = \varepsilon_1(\omega) + i\varepsilon_2(\omega). \quad (9)$$

The imaginary component $\varepsilon_2(\omega)$ of the dielectric function, at a given angular frequency ω, is determined from the sum of the contributions of all possible electronic transitions between occupied and unoccupied states. It is expressed by the following relation: [77, 78]:

$$\varepsilon_2(\omega) = \frac{8}{3\pi\omega^2}\sum_{ij}\int \left|P_{ij}(k)\right|^2 \frac{dS_k}{\nabla\omega_{ij}(k)}, \tag{10}$$

Where $P_{ij}(k)$ represent the components of the dipole moment matrix between $|nk\rangle$and $|\acute{n}k\rangle$

The indices i and j represent the initial and final states of the system, respectively, and are used to identify the configurations before and after the transition in question. Indeed, the real part of the dielectric function is given by the Kramers-Kronig and can be expressed as [78, 79]:

$$\varepsilon_1(\omega) = 1 + \frac{2}{\pi} P \int_0^\infty \frac{\varepsilon_2(\omega')\omega' d\omega'}{\omega'^2 - \omega^2}, \tag{11}$$

where P the principal part of the Cauchy integral and ω is the frequency. It is possible to use the complex dielectric tensor to calculate various optical constants, such as the refraction coefficient $n(k)$ and the extinction coefficient $k(\omega)$ which are given by the equation:

$$n(\omega) = \frac{1}{\sqrt{2}}[(\varepsilon_1{}^2(\omega) + \varepsilon_2{}^2(\omega))^{\frac{1}{2}} + \varepsilon_1(\omega)]^{1/2}, \tag{12}$$

$$K(\omega) = \frac{1}{\sqrt{2}}[(\varepsilon_1{}^2(\omega) + \varepsilon_2{}^2(\omega))^{\frac{1}{2}} - \varepsilon_1(\omega)]^{1/2}. \tag{13}$$

Other very interesting optical grades that can be deduced from the complex index are the reflection coefficient R and the absorption coefficient $\alpha(\omega)$, which can be expressed by [80]

$$\text{Re}\,\sigma(\omega) = \frac{\omega}{4\pi}\text{Im}\,\varepsilon(\omega), \tag{14}$$

$$\alpha(\omega)\frac{4\pi}{\lambda}\text{k}(\omega). \tag{15}$$

Studying the optical properties of materials allows us to know the way they interact with light as well as their electrical structure in order to know the possibility of their application in the field of optoelectronic applications. In this section, we will investigate the optical properties of the compound Cu_2SnS_3 in its various phases, focusing on key parameters such as the absorption coefficient and refractive index. This analysis aims to describe electronic transitions and vibrations, particularly in the visible, ultraviolet, and infrared regions.

3.3.1 Dielectric function

For Cu_2SnS_3 in both the Cc (red curve) and Imm2 (blue curve) crystal phases, Fig. 5(a) shows the real component of the dielectric function, $\varepsilon_1(\omega)$, and Fig. 5(b) the imaginary part, $\varepsilon_2(\omega)$. The material's dispersion and polarization behavior can be inferred from the $\varepsilon_1(\omega)$ spectrum. Both phases exhibit positive $\varepsilon_1(\omega)$ values in the visible and near-infrared regions (up to ~3.3 eV), which is favorable for optoelectronic applications, as it indicates low absorption and strong dielectric transparency. In the Cc phase, we observe a sharp peak at approximately 5 eV, which can be attributed to the increased polarization of the UV spectrum. However, at high photon energy, where it exceeds 8 eV, the values become negative, and this compound has a reflective property similar to metals.

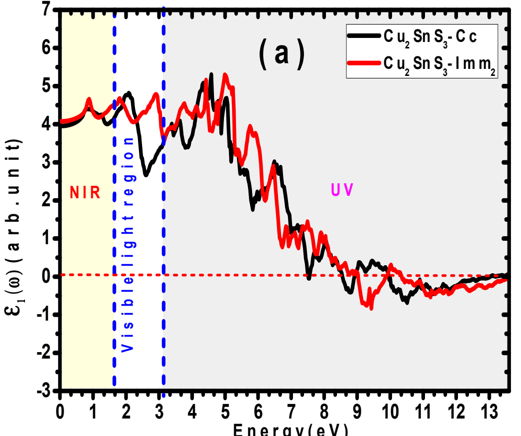

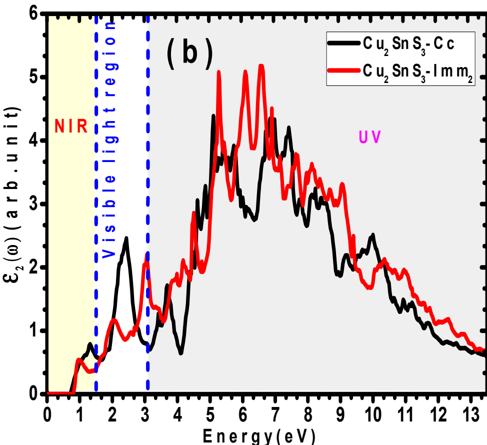

Figure 5. Dielectric function: Real part (a) and Imaginary part (b) of Cu_2SnS_3 in the Cc and Imm2 phases calculated using the TB-mBJ+U method

As for the optical absorption properties related to interband electronic transitions, they are visualized by the $\varepsilon_2(\omega)$ spectrum in Fig. 5(b). There is a great similarity between the spectra in the two phases, with the $\varepsilon_2(\omega)$ values of the Imm2 phase usually appearing at slightly larger values. The onset of absorption (first non-zero ε_2 values) occurs at about 1 eV, which means a comparable band gap. It also includes many peaks between 3 and 8 eV, indicating excellent absorption properties in the UV spectrum, which means more effective absorption of photons. This feature allows use in the field of photocatalysis and photovoltaic applications.

Ultimately, it can be said that the Cu_2SnS_3 compound is a good absorber of UV-visible, as both phases exhibit unique dielectric responses. These discoveries open up new possibilities for designing materials with adjustable optical properties that can be utilized in optoelectronic devices and solar energy conversion applications.

3.3.2 Absorption coefficient, reflectivity, refraxion and extinction index

The absorption coefficient enables us to describe a material's ability to absorb incident photons, thereby evaluating its performance in optoelectronic and photovoltaic applications. The optical absorption coefficient of Cu_2SnS_3 for the Cc (red curve) and Imm2 (blue curve) crystal structures is shown in Fig. 6 (a) as a function of photon energy. As the photon energy moves into the visible and ultraviolet (UV) ranges, both phases show a dramatic rise in absorption, which is negligible in the near-infrared region (below ~1.5 eV).

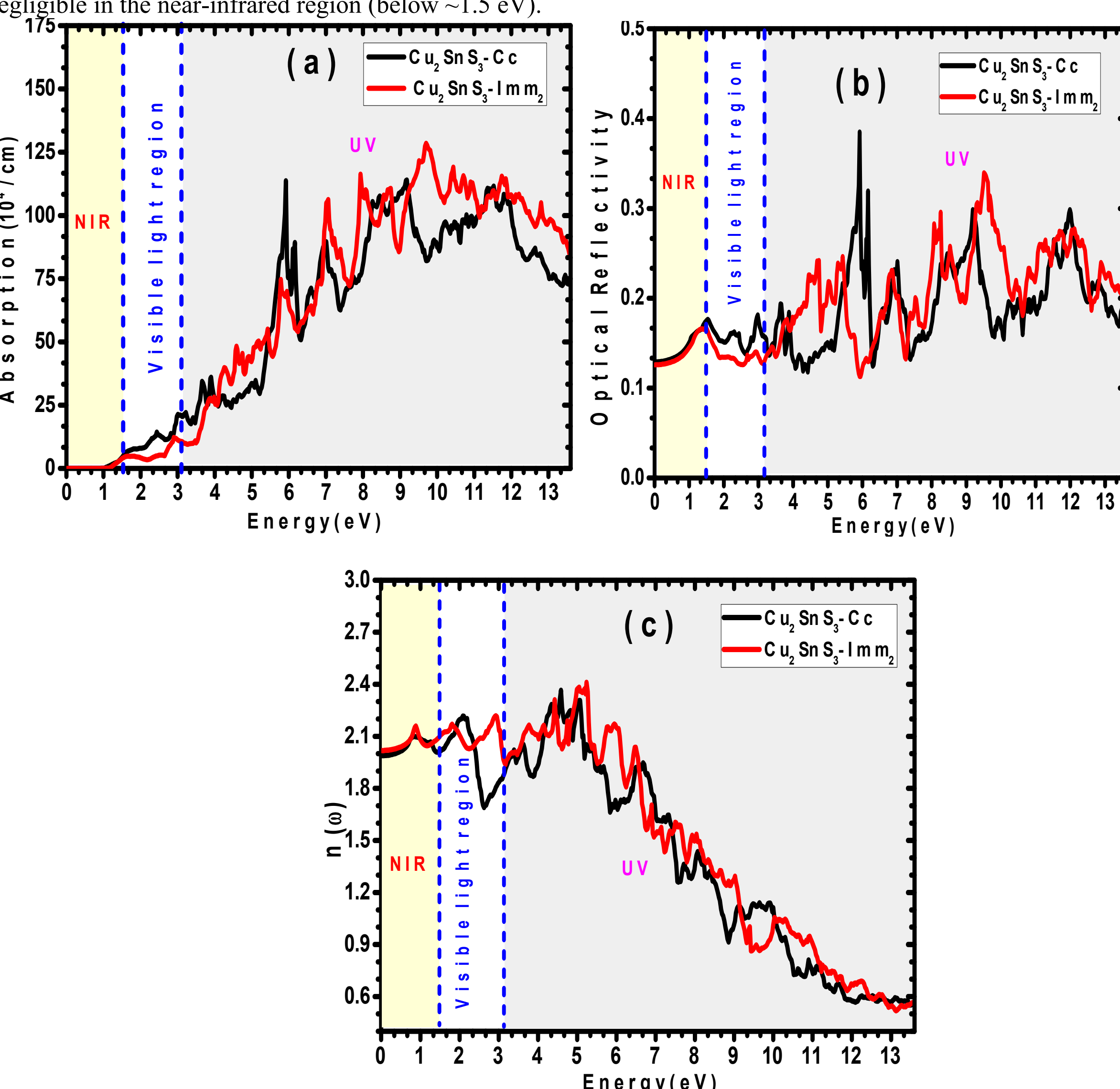

Figure 6. Absorption coefficient (a), reflectivity (b) and refraxion(c) of Cu_2SnS_3-Cc and Cu_2SnS_3-Imm2 using TB-mBJ+U

There is a comparable band gap, as evidenced by the onset of absorption at 1 eV. Both structures also show significant absorption accompanied by prominent peaks in the UV region, reaching limit values above 10^5 cm^{-1}. This suggests that there are numerous permitted electronic transitions. In the region of 8–11 eV, the Cc phase exhibits somewhat greater absorption values compared to the Imm2 phase, indicating a stronger interaction with high-energy photons.

Optical reflectivity indicates the amount of incident light reflected from the surface of a material. It is an important metric for applications such as sensors, photovoltaics, and optical coatings. We plotted the optical reflectivity of Cu_2SnS_3 in the Cc (red line) and Imm2 (blue line) phases against photon energy in Fig. 6 (b). Both phases show comparatively low reflectivity, typically below 0.2, in the visible and near-infrared ranges (0–3.3 eV), suggesting that the majority of incident light in this range is either absorbed or transmitted. This is a beneficial characteristic for light-harvesting devices such as solar cells. Reflectivity rises and exhibits multiple noticeable oscillations that correspond to interband transitions as photon energy increases into the ultraviolet (UV) range. The Imm2 phase shows somewhat higher and more variable reflectance values in the UV spectrum, especially between 5 and 8 eV, due to its unique electronic band structure. As for the Cc phase, the reflectivity remains relatively smoother.

The graph with the sign 6 (c) expresses the change in the refractive index value of the Cu_2SnS_3 compound in its Cu_2SnS_3-Cc and Cu_2SnS_3-Imm2 phases across the spectra of visible light, ultraviolet, and near-infrared light spectrums. Both phases exhibit comparable and consistent refractive indices (1.8-2.1) in the near infrared. The index rises for both in the visible zone. The refractive index exhibits more intricate behavior in the UV spectrum, with peaks and valleys that correspond to different electronic transitions. Interestingly, Cu_2SnS_3-Cc typically exhibits sharper features and significantly higher indices in the 3.0-6.0 eV range, indicating variations in its optical sensitivity to higher-energy photons.

3.4 Numerical device modelling

The one-dimensional software SCAPS-1D allows the modeling of any photovoltaic structure using the materials listed in its data files, while offering the possibility of modifying various parameters, such as layer thickness, surface area, and doping level. This simulator relies on an iterative and self-consistent numerical solution of a system of coupled differential equations, including Poisson and continuity equations for majority and minority carriers (electrons and holes), in order to predict the electrical behavior and performance of photovoltaic devices [81].

The structure analyzed is a planar configuration shown in Fig. 7, consisting of an n-type indium gallium zinc oxide (IGZO) layer, which serves as both the electron transport layer (ETL) and the front contact (anode). It also incorporates p-type material ($CuSnS_3$), used as an absorbing material, as well as different materials placed as p-type layers that act as hole transport material (HTL) to the gold (Au) metal electrode, such as Cu_2O, which is known for its wide bandgap, giving it transparency in the visible spectrum. P3HT is an organic conductor sensitive to visible light. DPBTTT-14 is commonly used as a hole transport material (HTM) due to its superior electrical conductivity and high charge carrier mobility.

The studied structure is a planar structure with the configuration FTO/$CuSnS_3$/HTL, as shown in Fig 7. The simulation was performed under standard conditions, with lighting of 1000 W/m² at 300 K and an air mass of AM 1.5G. The simulation was performed using parameters specific to each material purposes are listed in Table 3.

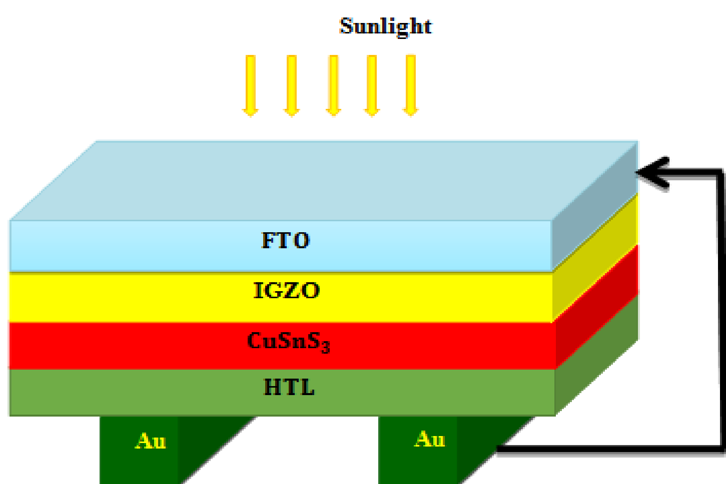

Figure 7. Architecture of the primary p-i-n type perovskite solar cell device

Table 3. The parameters for each material were used for simulation.

Parameters	FTO [76]	IGZO [77]	Cu_2SnS_3	Cu_2O [78]	D-PBTTT-14 [78]	P3HT [79]
Eg (eV)	3.5	3.05	0.88	2.17	2.16	2
χ, (eV)	4	4.16	3.9 - 4.3	3.2	3.2	3.2
ε	9	10	10^{-20}	7.11	10	3
Nc (cm^{-3})	2.2×10^{18}	5×10^{18}	2.2×10^{18}	2.02×10^{17}	2.8×10^{19}	10^{20}
Nv (cm^{-3})	1.8×10^{19}	5×10^{18}	2.9×10^{18}	1.1×10^{19}	2.5×10^{21}	10^{20}
μ_n ($cm^2 V^{-1} s^{-1}$)	20	15	10^1 - 10^3	200	10^{-4}	10^{-4}

Parameters	FTO [76]	IGZO [77]	Cu_2SnS_3	Cu_2O [78]	D-PBTTT-14 [78]	P3HT [79]
μ_h ($cm^2 V^{-1} s^{-1}$)	10	0.1	10 - 100	80	10^{-4}	10^{-4}
ND (cm^{-3})	2×10^{19}	10^{18}	10^{16} - 10^{19}	0.0	0.0	0.0
NA (cm^{-3})	0.0	0.0	10^{18} - 10^{20}	10^{18}	10^{18}	10^{16}
Nt(cm^{-3})	10^{15}	2.0×10^{15}	10^{14}	10^{14}	10^{14}	10^{15}

3.4.1 Influence of ETL materials

We modified the hole transport layer (HTL) in this cell and analyzed the impact of different hole transport materials on the current-voltage (J_V) properties using IGZO as the electron transport layer (ETL). Show Table 4. According to these results, PSCs with a Cu_2O HTL have the best energy conversion efficiency (PCE). Thedifferenceof bandgap between perovskite and the Cu_2O layer is significant; however, it is possible to achieve high conversion efficiency (P_{CE}) through effective contact between the active layer and the metal electrode.

Table 4. Comparative analysis of hole transport materials in structures incorporating IGZO as the ETL layer.

	Cu_2O	P3HT	D-PBTTT-14
Voc (V)	0.833	0.824	0.831
Jsc (mA/cm²)	49.44	94,44	49,44
FF (%)	84.40	79 .05	84.36
PCE (%)	34.79	32 ,21	34.68

3.4.2 Influence of absorbing layer thickness

The absorber layer plays a crucial role in the cell's performance [82]. To achieve this role, we will vary the absorber layer thickness from 100 nm to 800 nm. The simulation results are shown in Fig. 8. We can see that the variation in the thickness of the $CuSnS_3$ affects all the parameters of the cell. The current density Jsc increases with the increase in the thickness of the absorber ($CuSnS_3$), which is due to the latter's high absorption coefficient. For the others, an increase in the form factor, especially for Cu_2O, justifies the latter as a candidate promoter in this device. This simulation study, therefore, confirms that the film must have an optimal thickness of 800 nm. This demonstrates that perovskite is a material capable of achieving better light absorption and higher efficiency, even with thicknesses of a few hundred nanometers.

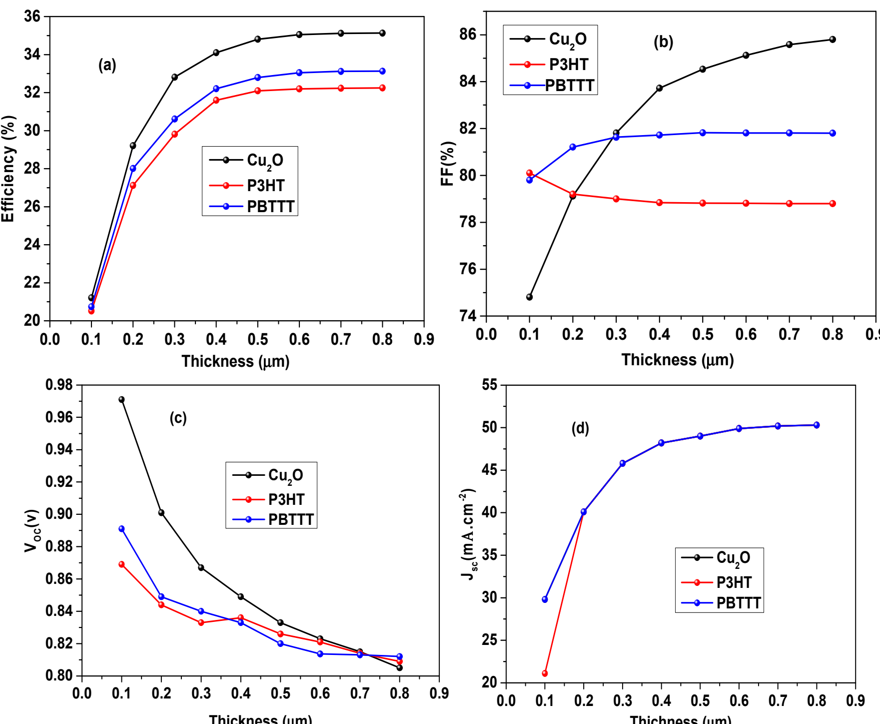

Figure 8. Variation of photovoltaic parameters as a function of the thickness of Cu_2SnS_3: a) Conversion efficiency (P_{CE}), b) Fill factor (FF), c) Open-circuit voltage (V_{oc}), and d) Short-circuit current density (J_{sc})

3.4.3 Effect of Doping on Various Device Components

Doping plays a crucial role in the performance variations of solar cells, as it directly influences the electrical properties of different regions of the device and allows for the optimization of charge carrier generation and collection [83,84]. In this section, we propose a study of optimal properties for the active layer and observe that the impact of doping absorbers with p-type carriers manifests itself in a range from 10^{12} to 10^{21} cm^{-3}, as illustrated in Fig. 9.

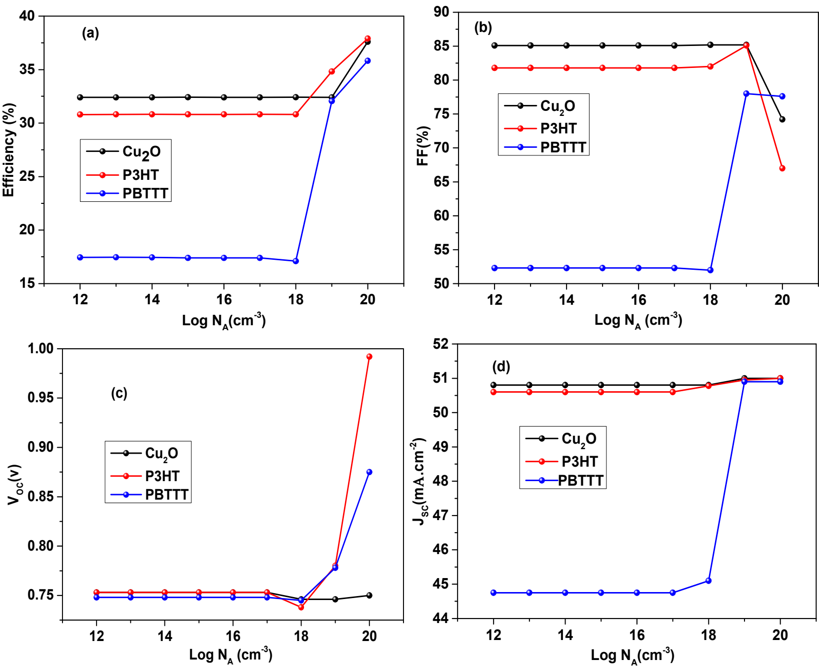

Figure 9. Impact of doping on variations in solar cell performance: a) PCE, b) FF, c) V_{OC} and d) J_{sc}

The results reveal that efficiency increases with dopant concentration up to 10^{20} cm^{-3}. Notably, in the cases of P_3HT and Cu_2O, the values reach 37.85% and 37.3%, respectively. The fill factor (FF) increases slightly to 10^{19} cm^{-3} for D-PBTTT-14, while for P_3HT and Cu_2O, it remains almost constant at 10^{19} cm^{-3}, then decreases sharply beyond this doping density. As N_A increases, the Fermi energy level of the holes approaches the valence band (VB), resulting in an increase or constancy of V_{OC} and J_{SC}.

The stability in J_{SC} for solar cells with Cu_2O and P_3HT as HTLs, for D-PBTTT-14, exhibits a crossover up to 10^{20}cm^{-3}. The V_{OC} is stable between 10^{12} and 10^{18} cm^{-3}, then increases for HTL P3HT and D-PBTTT-14, and remains stable for HTL Cu_2O. This indicates that a higher dopant concentration was ineffective and led to deep defects.

3.4.4 Effect of External Operating Temperature

The performance of solar cells is significantly affected by operating temperature [85]. We utilized the SCAPS-1D solar cell simulator to investigate the temperature-dependent variability in the device's performance. 300 K to 400 K, in 10°C increments, under standard 1 sun illumination conditions, as described in our previous work [80].

As shown in Fig. 10, both the fill factor (FF) and the power conversion efficiency (P_{CE}) of the hole transport layer decrease as temperature increases. According to Equation 16, this behavior is attributed to the temperature-dependent rise in the dark saturation current (J_0). This leads to a decrease in open-circuit voltage (V_{OC}). This finding corresponds well with our simulation results.

$$V_{OC} = \frac{AKT}{e} Ln\left[\frac{J_{ph}}{J_0} + 1\right]. \tag{16}$$

Furthermore, as temperatures rise, internal resistance decreases due to the low resistivity of the materials. This promotes better current flow, which reduces energy losses and increases the fill factor (FF).

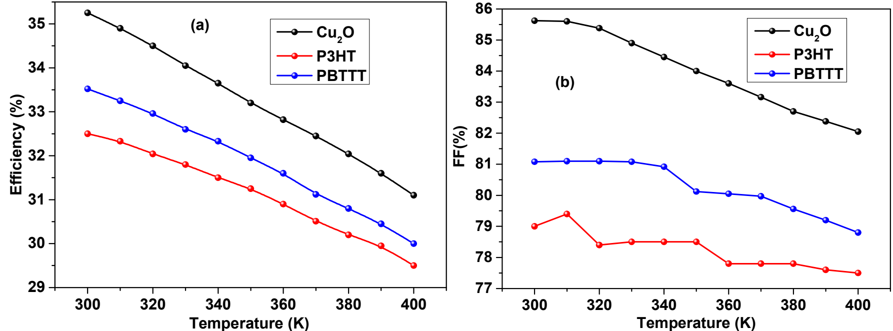

Figure 10. Influence of operating temperature on the performance parameters of solar cells, namely: (a) power conversion efficiency (PCE), (b) fill factor (FF), (c) open-circuit voltage (Voc), and (d) short-circuit current density (Jsc)

(*continued on next page*)

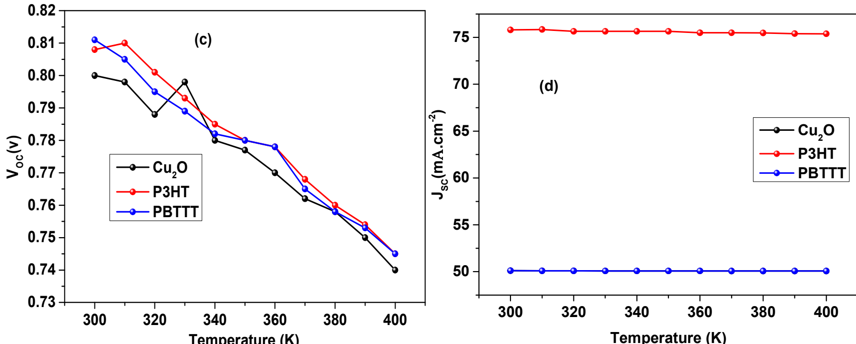

Figure 10. Influence of operating temperature on the performance parameters of solar cells, namely: (a) power conversion efficiency (PCE), (b) fill factor (FF), (c) open-circuit voltage (Voc), and (d) short-circuit current density (Jsc)

5. CONCLUSIONS

This work has enabled the achievement of the objectives set for studying the structural, optoelectronic, and photovoltaic performance of the Cu_2SnS_3 compound, through a combined simulation process based on density functional theory (DFT) and the SCAPS-1D software. A comparative analysis of the structural, electronic, and optical properties of CTS (Cu_2SnS_3) was performed to evaluate its potential for photovoltaic applications. Our calculations were performed using direct LDA (or GGA) methods, but the values obtained suggested that the compound Cu_2SnS_3 is a metal, contrary to what experimental studies have demonstrated. This is because this type of semiconductor is based on copper. We note that the Cud electrons possess a dual nature, enabling them to hybridize with Sn *s* electrons. Therefore, this compound appeared to be metallic in nature. In order to displace the anion, The TB-mBJ+U functional, which combines the Tran and Blaha modified Becke–Johnson potential with a Hubbard U term, was introduced to better account for electron correlation effects, as the results were largely consistent with the experiment, as both structures, Cc and Imm2, appeared as p-type semiconductors with direct gaps (Γ-Γ) of 0.7 eV and 0.7 eV, respectively. Regarding the study of optical properties, the compound Cu_2SnS_3 exhibits increased polarization in the ultraviolet spectrum at high photon energies in both phases. It is also characterized by positive $\varepsilon_1(\omega)$ values up to 3 eV, making this compound, in both phases, a candidate for electronic applications. In the last part of this work, we proved the effectiveness of the Cu_2SnS_3 compound in the field of photovoltaic cells, where, using the SCAPS program, we took this compound as an absorption layer, where the simulation showed that the current density Jsc increases even to its peak, which leads to an increase in the absorption coefficient, and this is at a thickness of 800 nanometers. Several questions remain to be explored to fully understand how structural, optoelectronic, and photovoltaic properties influence the behavior of the Cu_2SnS_3 compound. The results presented in this study make a significant contribution to this understanding and provide valuable insights for the development of high-performance materials for solar energy.

ORCID

Boualem Kada, https://orcid.org/0009-0007-2817-4167; **Benyahia Karima,** https://orcid.org/0000-0001-8690-8949
Beloufa Nabil, https://orcid.org/0009-0004-8612-3948; **Hamza Rekab Djabri,** https://orcid.org/0000-0002-2458-1335
Djamel Eddine Belfennache, https://orcid.org/0000-0002-4908-6058; **Alami Ahmed,** https://orcid.org/0000-0001-7000-8292
Hamad M. Adress Hasan, https://orcid.org/0000-0002-6739-8311

REFERENCES

[1] R. Ouldamer, D. Madi, and D. Belfennache, in: *Advanced Computational Techniques for Renewable Energy Systems. IC-AIRES 2022. Lecture Notes in Networks and Systems*, vol. 591, edited by M. Hatti, (Springer, Cham. 2023). pp. 700-705, https://doi.org/10.1007/978-3-031-21216-1_71
[2] S. Mahdid, D. Belfennache, D. Madi, M. Samah, R. Yekhlef, and Y. Benkrima, J. Ovonic. Res. **19**(5), 535-545 (2023). https://doi.org/10.15251/JOR.2023.195.535
[3] D. Belfennache, N. Brihi, and D. Madi, in: *Proceedings of the IEEE xplore, 8th (ICMIC)* (IEEE, 2017). pp. 497–502. https://doi.org/10.1109/ICMIC.2016.7804164
[4] A.C. Lokhande, P.T. Babar, V.C. Karade, M.G. Gang, V.C. Lokhande, C.D. Lokhande, and J.H. Kim, J. Mater. Chem. A, **7**, 17118–17182 (2019). https://doi.org/10.1039/C9TA00867E
[5] C. Xing, Y. Lei, M. Liu, S. Wu, W. He, and Z. Zheng, Phys. Chem. Chem. Phys. **23**, 16469 (2021). https://doi.org/10.1039/D1CP02067F
[6] F. Saker, L. Remache, D. Belfennache, K.R. Chebouki, and R. Yekhlef, Chalcogenide Lett. **22**(2), 151 (2025). https://doi.org/10.15251/CL.2025.222.151
[7] Q. Zhao, R. Han, A.R. Marshall, S. Wang, B.M. Wieliczka, J. Ni, J. Zhang, *et al.*, Adv Mater. **34**, 2107888 (2022). https://doi.org/10.1002/adma.202107888
[8] F. A. Boukhelkhal, N. Selmane, A. Cheknane, M. Noureddine, A. Zoukel, N. Baydogan, B. Günalan, and H. S. Hilal, Chem. Phys., **601**,112952 (2026), https://doi.org/10.1016/j.chemphys.2025.112952
[9] A. Saoudi, Y. Bouznit, F. Chouikh, and G. Leroy, Chem. Phys. **600**, 112894 (2026). https://doi.org/10.1016/j.chemphys.2025.112894

[10] J. Chi, H. Wei, L. Chu, L. Han, T. Liu, X. Zhong, D. Kou, *et al.*, Energy Environ. Sci. **18**, 8366 (2025). https://doi.org/10.1039/D5EE02706C
[11] S. Tao, H. Wang, M. Jia, J. Han, Z. Wu, J. Zhou, M. Baranova, *et al.*, Adv. Funct. Mater. **35**(23), 2423251 (2025). https://doi.org/10.1002/adfm.202423251
[12] P.A. Fernandes, P.M.P. Salomé, and A.F. Da Cunha, J. Phys. D: Appl. Phys. **43**, 215403 (2010). https://doi.org/10.1088/0022-3727/43/21/215403
[13] A.G. Chronis, E. Karantagli, F.I. Michos, C.S. Garoufalis, and M.M. Sigalas, Solid. State. Commun. **332**, 114326 (2021). https://doi.org/10.1016/j.ssc.2021.114326
[14] X. Wu, Z. Zhang, and H. Soleymanabadi, Solid. State. Commun. **306**, 11377 (2020). https://doi. /10.1016/j.ssc.2019.113770
[15] E.J. Skoug, J.D. Cain, D.T. Morelli, J. Alloys. Compd. **506**, 18 (2010). https://doi.org/10.1016/j.jallcom.2010.06.182
[16] L.K. Samanta, Phys. Status Solidi a, **100**, K93 (1987). https://doi.org/10.1002/pssa.2211000165
[17] G. Marcano, C. Rincon, L.M. De Chalbaud, D.B. Bracho, and G.S. Perez, J. Appl. Phys. **90**, 1847 (2001). https://doi.org/10.1063/1.1383984
[18] S.K. Biswas, M.M. Ahmed, M.F. Orthe, M.S. Sumon, and K. Sarker, Eur. J. Electr. Eng. Comput. Sci. **7**, 63 (2023). https://doi.org/10.24018/ejece.2023.7.5.558
[19] P.P.J. Helan, K. Mohanraj, G. Sivakumar, Iran. J. Sci. Technol. Trans. A Sci. **42**, 1677 (2018). https://doi.org/10.1007/s40995-017-0355-1
[20] G.H. Chandra, O.L. Kumar, R.P. Rao, and S. Uthanna, J. Mater. Sci. **46**, 6952 (2011). https://doi.org/10.1007/s10853-011-5661-y
[21] T.J. Huang, X. Yin, G. Qi, Phys. Status. Solidi RRL, **8**, 735 (2014). https://doi.org/10.1002/pssr.201409219
[22] A. Ali, J. Jacob, M.I. Arshad, M.A. Nabi, A. Ashfaq, K. Mahmood, N. Amin, *et al.*, Solid. State Sci. **103**, 106198 (2020). https://doi.org/10.1016/j.solidstatesciences
[23] U.V. Ghorpade, M.P. Suryawanshi, S.W. Shin, I. Kim, S.K. Ahn, J.H. Yun, and J.H. Kim, Chem. Mater. **28**, 3308 (2016). https://doi.org/10.1021/acs.chemmater.6b00176
[24] B. Saparov, Chem. Rev. **122**, 10575 (2022). https://doi.org/10.1021/acs.chemrev.2c00346
[25] U.A. Shah, A. Wang, M.I. Ullah, M. Ishaq, I.A. Shah, Y. Zeng, and K. Sun, Small, **20**, 2310584 (2024). https://doi.org/10.1002/smll.202310584
[26] Lalarukh, S.M. Hussain, S. Ali, A.F. Zahoor, H. Azmat, N. Nazish, M.A. Alshehri, *et al.*, Polym. Adv. Technol. **35**, e6471 (2024). https://doi.org/10.1002/pat.6471
[27] H. Zhou, W.C. Hsu, H.S. Duan, B. Bob, W. Yang, T.B. Song, and Y. Yang, Energy Environ. Sci. **6**, 2822 (2013). https://doi.org/10.1039/C3EE41627E
[28] Y. Bellal, A. Bouhank, D. Belfennache, R. Yekhlef, East Eur. J. Phys. (1), 170 (2025). https://doi.org/10.26565/2312-4334-2025-1-16
[29] A. Urbina, J Phys Energy, **2**, 022001 (2020). https://doi.org/10.1088/2515-7655/ab5eee
[30] M.F. Islam, N.M. Yatim, P. Chelvanathan, M.T. Ferdaous, M.A. Hashim, A.K. Modak, N. Amin, Malaysian J. Sci. Health. Technol. **7**, 110 (2020). https://doi.org/10.33102/mjosht.v7io.117
[31] M. Wang, M. He, L. Zhu, B. Ma, F. Zhang, P. Liang, X. Chao, *et al.*, J. Mater. Chem. A., **10**, 12946 (2022). https://doi.org/10.1039/D2TA02888C
[32] M.H. Sayed, M.M. Gomaa, and M. Boshta, Results. Opt. **12**, 100499 (2023). https://doi.org/10.1016/j.rio.2023.100499
[33] O.V. Parasyuk, L.D. Olekseyuk, and O.V. Marchuk, J. Alloys Compd. **287**, 197 (1999). https://doi.org/10.1016/S0925-8388(99)00047-X
[34] S.B. Jathar, S.R. Rondiya, Y.A. Jadhav, D.S. Nilegave, R.W. Cross, S.V. Barma, M.P. Nasane, *et al.*, Chem. Mater. **33**, 1983 (2021). https://doi.org/10.1021/acs.chemmater.0c03223
[35] A.C. Lokhande, R.B.V. Chalapathy, M. He, E. Jo, M. Gang, S.A. Pawar, and J.H. Kim, Sol. Energy. Mater. Sol. Cells, **153**, 84 (2016). https://doi.org/10.1016/j.solmat.2016.04.003
[36] A.C. Lokhande, K.V. Gurav, E. Jo, C.D. Lokhande, and J.H. Kim, J. Alloys. Compd. **656**, 295 (2016). https://doi.org/10.1016/j.jallcom.2015.09.232
[37] A.C. Lokhande, K.V. Gurav, E. Jo, M. He, C.D. Lokhande, and J.H. Kim, Opt. Mater. **54**, 207 (2016). https://doi.org/10.1016/j.optmat.2016.02.040
[38] T.A. Kuku, and O.A. Fakolujo, Energy Mater. **16**, 199 (1987). https://doi.org/10.1016/0165-1633(87)90019-0
[39] J. Koike, K. Chino, N. Aihara, H. Araki, R. Nakamura, K. Jimbo, and H. Katagiri, Jpn. J. Appl. Phys., **51**, 10 (2012). https://doi.org/10.1143/JJAP.51.10NC34
[40] M. Umehara, Y. Takeda, T. Motohiro, T. Sakai, H. Awano, and R. Maekawa, J. Neurol. Sci. **146**, 167 (1997). https://doi.org/10.1016/S0022-510X(96)00301-2
[41] G.E. Delgado, A.J. Mora, G. Marcano, and C. Rincón, Mater. Res. Bull. **38**, 1949 (2003). https://doi.org/10.1016/j.materresbull.2003.09.017
[42] A.D. Dugarte, N.R. Pineda, L. Nieves, J.A. Henao, G.D. Delgado, and J.M. Delgado, Acta. Cryst. B, **77**, 158 (2021). https://doi.org/10.1107/S2052520620016571
[43] C. Wu, Z. Hu, C. Wang, H. Sheng, J. Yang, and Y. Xie, Appl. Phys. Lett. **91**, 143104 (2007). https://doi.org/10.1063/1.2790491
[44] D. Avellaneda, M.T.S. Nair, and P.K. Nair, J. Electrochem. Soc. **157**, D346 (2010). https://doi.org/10.1149/1.3384660
[45] M. Adelifard, M.M.B. Mohagheghi, and H. Eshghi, Phys. Scr. **85**, 035603 (2012). https://doi.org/10.1088/0031-8949/85/03/035603
[46] X. Chen, H. Wada, A. Sato, and M. Mieno, J. Solid. State. Chem. **139**, 144 (1998). https://doi.org/10.1006/jssc.1998.7822
[47] V. Roblés, J.F. Trigo, C. Guillén, and J. Herrero, J. Alloys. Compd. **642**, 40 (2015). https://doi.org/10.1016/j.jallcom.2015.04.104
[48] R. Bodeux, J. Leguay, and S. Delbos, Thin Solid Films, **582**, 229 (2015). https://doi.org/10.1016/j.tsf.2014.09.023
[49] J. Chang, and E.R. Waclawik, Cryst. Eng. Comm. **15**, 5612 (2013). https://doi.org/10.1039/C3CE40284C
[50] Y.T. Zhai, S. Chen, J.H. Yang, H.J. Xiang, X.G. Gong, A. Walsh, J. Kang, *et al.*, Phys. Rev. B, **84**, 075213 (2011). https://doi.org/10.1103/PhysRevB.84.075213
[51] Y. Dong, J. He, X. Li, W. Zhou, Y. Chen, L. Sun, P. Yang, *et al.*, Mater. Lett. **160**, 468 (2015). https://doi.org/10.1016/j.matlet.2015.08.028

[52] Q. Chen, X. Dou, Y. Ni, S. Cheng, and S. Zhuang, J. Colloid Interface Sci. **376**, 327 (2012). https://doi.org/10.1016/j.jcis.2012.03.015
[53] Y. Benkrima, D. Belfennache, R. Yekhlef, and A.M. Ghaleb, Chalcogenide Lett. **20**, 609-618 (2023). https://doi.org/10.15251/CL.2023.208.609
[54] K. Schwarz, P. Blaha, Comput. Mater. Sci. **28**, 259 (2003). https://doi.org/10.1016/S0927-0256(03)00112-5
[55] Y. Achour, Y. Benkrima, I. Lefkaier, and D. Belfennache, J. Nano- Electron. Phys. **15**(1), 01018(5pp) (2023). https://doi.org/10.21272/jnep.15(1).01018
[56] Y. Benkrima, D. Belfennache, R. Yekhlef, M.E. Soudani, A. Souiga, and Y. Achour, East Eur. J. Phys. (2), 150 (2023). https://doi.org/10.26565/2312-4334-2023-2-14
[57] Y. Benkrima, S. Benhamida, and D. Belfennache, Dig. J. Nanomater. Bios. **18**(1), 11 (2023) https://doi.org/10.15251/DJNB.2023.181.11
[58] Y. Benkrima, M.E. Soudani, D. Belfennache, H. Bouguettaia, and A. Souigat, J. Ovonic. Res. **18**(6), 797 (2022). https://doi.org/10.15251/JOR.2022.186.797
[59] A. Djemli, M. Reffas, K. Bouferrache, F. Benlakhdar, R. Yekhlef, D. Belfennache, S.I. Ahmed, *et al*., Phys. Solid State, **67**(5), 356 (2025). https://doi.org/10.1134/S1063783425600499
[60] K. Madoui, A Ghechi, S. Madoui, R. Yekhlef, D. Belfennache, S. Zaiou, and M.A. Ali, East Eur. J. Phys. (3), 390 (2024). https://doi.org/10.26565/2312-4334-2024-3-48
[61] E. Danladi, M. Kashif, A. Ichoja, and B.B. Ayiya, Trans. Tianjin. Univ. **29**, 62 (2023). https://doi.org/10.1007/s12209-022-00343-w
[62] A. Maoucha, T. Berghout, F. Djeffal, and H. Ferhati, Sol. Energy, **287**, 113251 (2025). https://doi.org/10.1016/j.solener.2025.113251
[63] I.D. Mayergoyz, J. Appl. Phys. **59**, 195 (1986). https://doi.org/10.1063/1.336862
[64] P. Lazzeretti, J. Chem. Phys. **151**, 114108 (2019). https://doi.org/10.1063/1.5124250
[65] A.N. Tuama, L.H. Alzubaidi, M.H. Jameel, K.H. Abass, M.Z.H. Mayzan, and Z.N. Salman, J. Sol-Gel. Sci. Technol. **110**, 792 (2024). https://doi.org/10.1007/s10971-024-06385-x
[66] F.D. Murnaghan, **30**, 244 (1944). https://doi.org/10.1073/pnas.30.9.244
[67] T. Raadik, M. Grossberg, J. Krustok, M. Kauk-Kuusik, A. Crovetto, R.B. Ettlinger, O. Hansen, *et al*., Appl. Phys. Lett. **110**, 261105 (2017). https://doi.org/ 10.1063/1.4990657
[68] T. Nomura, T. Maeda, T. Wada, Prog. Photovolt. Res. Appl. **20**, 520 (2012). https://doi.org/10.1002/pip.2183
[69] M. Onoda, X.A. Chen, A. Sato, and H. Wada, Mater. Res. Bull. **35**, 1563 (2000). https://doi.org/10.1016/S0025-5408 (00)00347-0
[70] M. Mesbahi, M.L. Benkhedir, UPB Sci. Bull. Ser. A, **79**, 293 (2017). https://doi.org/10.1103/PhysRevResearch.4.033067
[71] A. Kanai, K. Toyonaga, K. Chino, H. Katagiri, and H. Araki, Jpn. J. Appl. Phys. **54**, 08KC06 (2015). https://doi.org/10.7567/JJAP.54.08KC06
[72] J.D. De Wild, E.V.C. Robert, B.E. Adib, D. Abou-Ras, and P.J. Dale, Sol. Energy. Mater. Sol. Cells. **157**, 259 (2016). https://doi.org/10.1016/j.solmat.2016.04.039
[73] V.I. Anisimov, J. Zaanen, and O.K. Andersen, Phys. Rev. B, **44**, 943 (1991). https://doi.org/10.1103/PhysRevB.44.943
[74] A. Shigemi, T. Maeda, and T. Wada, Phys. Status Solidi B, **252**, 1230 (2015). https://doi.org/10.1002/pssb.201400346
[75] V.L. Shaposhnikov, A.V. Krivosheeva, V.E. Borisenko, and J.L. Lazzari, Sci. Jet. **1**, 1–4 (2012).
[76] T. Ouslimane, L. Et-taya, L. Elmaimouni, and A. Benami, Heliyon, **7**, e06379 (2021). https://doi.org/10.1016/j.heliyon.2021.e06379
[77] A.A. Kanoun, M.B. Kanoun, A.E. Merad, and S. Goumri-Said, Sol. Energy. **182**, 237 (2019). https://doi.org/10.1016/j.solener.2019.02.041
[78] M.K. Das, S. Panda, and N. Mohapatra, Mater. Today Proc. **74**, 756 (2023). https://doi.org/10.1016/j.matpr.2022.11.031
[79] S. Ahmed, F. Jannat, M.A.K. Khan, and M.A. Alim, Optik, **225**, 165765 (2021). https://doi.org/10.1016/j.ijleo.2020.165765
[80] A.N. Abena, A.T. Ngoupo, F.A. Abega, and J.M.B. Ndjaka, Chinese J. Phys. **76**, 94 (2022). https://doi.org/10.1016/j.cjph.2021.12.024
[81] M. Burgelman, P. Nollet, and S. Degrave, Thin Solid Films, **361–362**, 527 (2000). https://doi.org/10.1016/S0040-6090(99)00825-1
[82] F.E. Ikuemonisan, Y.O. Kayode, and O.B. Odubote, Next Materials, **8**, 100870 (2025). https://doi.org/10.1016/j.nxmate.2025.100870
[83] D. Belfennache, D. Madi, N. Brihi, M.S. Aida, and M.A. Saeed, Appl. Phys. A, **124**, 697 (2018). https://doi.org/10.1007/s00339-018-2118-z
[84] R. Ouldamer, D. Belfennache, D. Madi, R. Yekhlef, S. Zaiou, and M.A. Ali, J. Ovonic. Res. **20**(1), 45 (2024). https://doi.org/10.15251/JOR.2024.201.45
[85] D. Belfennache, D. Madi, R. Yekhlef, L. Toukal, N. Maouche, M.S. Akhtar, and S. Zahra, Semicond. Phys. Quant. Optoelectron. **24**(4), 378 (2021). https://doi.org/10.15407/spqeo24.04.378

ДОСЛІДЖЕННЯ СТРУКТУРНИХ, ОПТОЕЛЕКТРОННИХ ТА ФОТОВОЛЬТАЇЧНИХ ХАРАКТЕРИСТИК СПОЛУКИ Cu_2SnS_3: КОМПЛЕКСНЕ DFT ТА SCAPS-1D МОДЕЛЮВАННЯ

Буалем Када[1], Каріма Беньяхія[1], Набіл Белуфа[2,3], Хамза Рекаб-Джабрі[2,4], Д. Белфеннаше[5], Абделькадер Бухенна[1], Самір Бекхейра[2], А. Аламі[6], Хамад М. Адресс Хасан[7], Хамді А. Хатаб Алі[8]
[1]Лабораторія матеріалознавства та застосувань (LSMA), Факультет наук і технологій, Університет Айн-Темушент, Алжир
[2]Лабораторія мікро- та нанофізики (LaMiN), Національна політехнічна школа Оран, ENPO-MA, BP 1523, Ель-М'Науер, 31000, Оран, Алжир
[3]Гідрометеорологічний інститут навчання та досліджень IHFR, Ібну Рошд. Bp 7019, Оран, Алжир
[4]Факультет наук про природу та життя та наук про Землю, Університет АкліМоханд-Ульхадж, 10000, Буйра, Алжир
[5]Дослідницький центр промислових технологій (CRTI), поштова скринька 64, Черага 16014, Алжир, Алжир
[6]Лабораторія технологічних процесів, матеріалів та навколишнього середовища, Технологічний факультет, Університет Джиллалі Ліабес, поштова скринька A/c 89, Сіді-Бель-Аббес 22000, Алжир
[7]Кафедра хімії, факультет природничих наук, Університет Омара аль-Мухтара, Лівія
[8]Кафедра хімії, факультет освіти (Аль-Мардж), університет Бенгазі, Лівія

Оцінка структурних, оптоелектронних та фотоелектричних характеристик сполуки Cu_2SnS_3 є важливою для розробки матеріалів для сонячної енергетики. Цей потрійний халькогенідний напівпровідник вирізняється сильним потенціалом у фотоелектричних застосуваннях завдяки широкому діапазону поглинання світла та хімічній стабільності. У цій статті ми дослідили структурні та оптоелектронні властивості потрійних напівпровідників на основі міді, зокрема тих, що входять до складу сполуки Cu_2SnS_3, а також їхню ефективність у фотоелектричних застосуваннях. Оскільки в попередніх дослідженнях існували значні відмінності щодо значень ширини забороненої зони (0,65-1,35 еВ), було зроблено спробу знайти відповідне наближення для вивчення цього типу сполуки. Структурні властивості досліджувалися з використанням як форми узагальненого градієнтного наближення (GGA) Пердью-Берка-Ернцергофа (PBE), так і наближення локальної густини (LDA), що дозволяє провести порівняльну оцінку впливу різних обмінно-кореляційних функціоналів на структуру матеріалу. Враховуючи важливий вплив, який деелектрони Cu відіграють на визначення їхніх електронних властивостей, як показано результатами, отриманими при використанні різних функціоналів обмінної кореляції енергії, для систематичної оптимізації розрахованого зміщення аніонів було використано комбіновану функцію потенціалу Бекке-Джонсона, модифікованого Траном та Блахою, та потенціалу Хаббарда (TB-mBJ+U). Розрахунки дали значення ширини забороненої зони. Енергія напівпровідникової квазічастинки в моноклінній структурі (m-CTS; SG: Cc) становить 0,7 еВ, а в орторомбічній структурі (золото-CTS; SG: Imm2) – 0,73 еВ, що значною мірою узгоджується з експериментальними значеннями. Дослідження оптичних властивостей, включаючи діелектричну функцію, також виявило коефіцієнт відбиття, коефіцієнт поглинання та показник заломлення сполуки Cu_2SnS_3 у двох її фазах. Останню вважають перспективним кандидатом для оптоелектронних застосувань. Для перевірки цього ми використали програму SCAPS, і результати були хорошими. Коли ця сполука використовується як абсорбуючий шар у фотоелектричному елементі, густина струму (Jsc) збільшується, досягаючи піку при товщині 800 нм.
Ключові слова: *Cu_2SnS_3; FP-LAPW; LDA; TB-mBJ+U; фотоелектричні елементи*

EAST EUROPEAN JOURNAL OF PHYSICS. **2.** 275-279 (2026)
DOI:10.26565/2312-4334-2026-2-29 ISSN 2312-4334

RESISTIVE SWITCHING BEHAVIOR OF Si/TiO THIN FILMS FOR NON-VOLATILE MEMORY APPLICATIONS

Muradulla T. Normurodov[1], Odil Ochilov[2], Ozodbek Y. Yuldashev[2]*, Zarnigor A. Karshieva[2], Nurbek U. Toshboyev[2]
[1]Karshi State University, Uzbekistan
[2]Center of Nanotechnology Development, National University of Uzbekistan, Tashkent, Uzbekistan
**Corresponding Author e-mail: ozodbekyoldoshev997@gmail.com*
Received December 16, 2025; revised March 26, 2026; accepted April 1, 2026

This study presents the fabrication of Si/TiO thin films deposited in DC mode via magnetron sputtering onto p-type silicon substrates and investigates their temperature-dependent resistive switching (RS) and low-resistance state (LRS) characteristics. The nanostructures were annealed at 420°C to improve crystallinity and interfacial contact. Electrical characterization through I–V measurements revealed clear bipolar RS behavior without the need for an initial forming process. The devices exhibited stable high-resistance (HRS) and low-resistance (LRS) states over multiple cycles. The switching mechanism is explained by the formation and rupture of conductive filaments induced by oxygen vacancies at the Si/TiO interface. Bandgap values obtained from Tauc plots were approximately 3.24 eV for TiO and 3.41 eV for SnO_2. These results confirm that Si/TiO nanothin films are promising materials for next-generation fast, energy-efficient, and rewritable memory devices.
Keywords: *TiO; Magnetron Sputtering; Memristor; Rapid Thermal Annealing (RTA)*
PACS: 85.50-n

INTRODUCTION

In recent years, memristors have emerged as one of the most dynamic and influential research directions, driven by their promising applications in neuromorphic computing, advanced artificial intelligence hardware, and next-generation non-volatile memory technologies. Recognized as the fourth fundamental passive circuit element—alongside resistors, capacitors, and inductors—memristors uniquely possess the ability to retain a memory of their resistance state based on the prior flow of electrical charge. This intrinsic memory effect enables them to store information even without external power, positioning memristors as highly attractive candidates for low-power, high-density memory architectures.

Among the various material platforms, metal-oxide-based memristors—particularly those employing binary oxides such as TiO and SnO_2—have gained substantial attention due to their low fabrication cost, straightforward synthesis routes, and excellent compatibility with flexible electronic substrates. Both TiO and SnO_2 are wide-bandgap n-type semiconductors, with bandgap energies of approximately 3.4 eV and 3.6 eV, respectively. TiO is known for its high electron mobility and pronounced surface reactivity, whereas SnO_2 demonstrates remarkable chemical stability and exhibits enhanced electrical conductivity when appropriately doped [4,5]. When these oxides are engineered into nanolayered or nanostructured forms, they can exhibit additional resistive switching pathways, including interface-controlled filament formation and oxygen-vacancy-driven migration processes.

Pant et al. [6] reported pronounced bipolar resistive switching and clearly defined negative differential resistance (NDR) behavior in Si/TiO nanostructures synthesized via magnetron sputtering. These features were attributed to enhanced grain-boundary diffusion and quantum confinement effects at nanoscale interfaces. More recently, Saha and co-workers [7] demonstrated reliable, sharply defined switching characteristics in one-dimensional TiO nanofiber-based memristors, revealing that artificial neural networks (ANN) can accurately model and predict switching dynamics. Additionally, the NDR behavior observed in Co-doped SnO_2 memristors deposited on p-type silicon substrates highlights the profound influence of dopants on the electronic properties of oxide nanostructures [8]. In the present work, we examine the resistive-switching characteristics of a p-Si/TiO nanofilm fabricated by magnetron sputtering (MS). The TiO layers were sequentially deposited onto p-type silicon and quartz substrates and subsequently annealed at 420 °C. Current–voltage (I–V) measurements performed with a Keithley 2460 SourceMeter revealed a distinct hysteresis loop characteristic of memristive behavior. However, due to the close similarity in the bandgap energies of TiO and SnO_2, the resulting switching contrast may be relatively limited, as both oxide layers tend to exhibit p-type semiconductor characteristics. Overall, this study contributes to ongoing efforts to optimize binary oxide nanostructures for implementation in low-power, non-volatile memory devices

METHODS

Thin nanostructured p-Si/TiO films were fabricated using the magnetron sputtering (MS) technique. This method is known for its low cost, convenience, and high suitability for oxide film formation. In this study, p-type silicon substrates

Cite as: M.T. Normurodov, O. Ochilov, O.Y. Yuldashev, Z.A. Karshieva, N.U. Toshboyev, East Eur. J. Phys. 2, 275 (2026), https://doi.org/10.26565/2312-4334-2026-2-29
© M.T. Normurodov, O. Ochilov, O.Y. Yuldashev, Z.A. Karshieva, N.U. Toshboyev, 2026; CC BY 4.0 license

were used. Prior to deposition, the substrates were sequentially cleaned by rinsing in deionized (DI) water, followed by ethanol and acetone, and then rinsed again in DI water. Additionally, they were treated with argon plasma inside the magnetron sputtering system. This multistep cleaning procedure was carried out to completely remove inorganic and organic contaminants and to ensure uniform film formation with good adhesion. After cleaning, the substrates were dried in a nitrogen flow and kept under vacuum in the magnetron sputtering system.

The schematic structure of the fabricated memristor device is shown in Figure 1. The device consists of a p-Si/TiO nanostructure deposited on a p-type silicon substrate. Tin oxide (SnO_2) contacts were used as the top electrode. The TiO layer serves as an intermediate interface layer, while SnO_2 acts as the top oxide electrode, and the p-Si substrate functions as the bottom electrode. This vertical "sandwich-like" configuration enables charge transport through the oxide layers under an applied electric field and allows investigation of resistive switching behavior.

The applied multistep cleaning procedure reduces surface contamination, thereby promoting the formation of uniform films with good adhesion and, consequently, improving the stability and reproducibility of the electrical characteristics of the memristor devices [9].

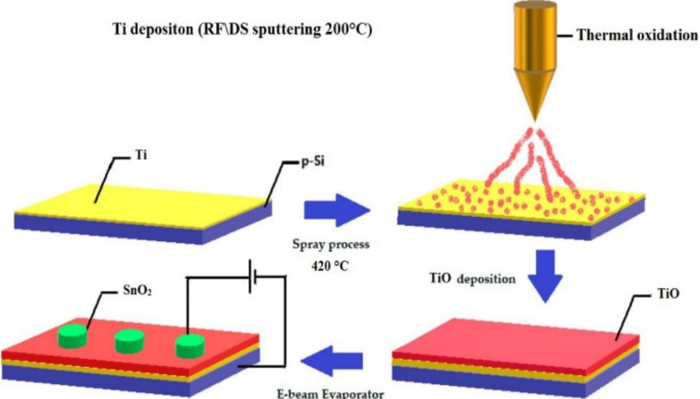

Figure 1. Schematic illustration of the SnO_2/TiO/p-Si memristor device structure

To obtain the SnO_2 electrodes, a contact pattern was created using a mask in the magnetron sputtering system, with oxygen gas as the carrier gas directed toward the heated substrate.

The deposition process was carried out at a temperature of 420°C, monitored using a controlled display. The TiO layer was deposited first, followed by the SnO_2 electrode through a mask to form the nanostructure. This sequence was chosen to ensure proper band alignment and good interfacial contact between the n-type semiconductors. After deposition, the films were annealed at 420°C with oxygen flow to enhance crystallinity and stabilize the interface. For electrical measurements, tin oxide (SnO_2) contacts were applied, and the p-Si substrate served as the bottom electrode electrical characterization of the memristor devices was performed using a Keithley 2460 SourceMeter. A voltage sweeps sequence of 0 → +3 V → 0 → –3 V → 0 was applied to investigate the current–voltage (I–V) characteristics. The hysteresis loop observed in the I–V curve confirmed the presence of resistive switching behavior in the fabricated structures transducer and carried toward the heated substrates using oxygen gas as the carrier.

The deposition process was conducted at a substrate temperature of 450 °C, which was maintained using a controlled hotplate. The SnO_2 was deposited first, followed by the ZnO layer, forming a bilayer heterostructure. This sequence was designed to promote appropriate band alignment and interfacial contact between the n-type semiconductors. Following deposition, the films were annealed in ambient air at 450 °C to improve crystallinity and stabilize the interface. Silver (Ag) top contacts were applied using silver paste for electrical measurements, and the p-Si substrate served as the bottom electrode in the case of silicon-based structures.

Electrical characterization of the memristor devices was performed using a Keithley 2460 SourceMeter. A voltage sweeps protocol of 0 → +3 V → 0 → –3 V → 0 was applied to examine the current–voltage (I–V) characteristics. The presence of a hysteresis loop in the I–V curve confirmed the resistive switching behavior of the fabricated structures.

RESULTS

A. Current–Voltage (I–V) Characteristics

The I–V characteristics of TiO thin films treated in air by Rapid Thermal Annealing (RTA) at 500°C, 600°C, 700°C, 800°C, and 900°C for 10 minutes are shown. It was observed that the memristive behavior of the TiO thin films improved as the annealing temperature increased. To initiate the formation of a conduction path in the metal oxide, the forming voltage was set to 3 V. Bipolar resistive switching behavior was observed for these samples.

Initially, the current increased linearly with voltage according to Ohm's law, then entered a quasi-saturation region. This quasi-saturation stage is explained by the space-charge-limited conduction (SCLC) mechanism, in which charge carriers experience delayed transport [11]. Subsequently, the current increased abruptly, showing a rapid transition from the high-resistance state (HRS) to the low-resistance state (LRS). This sudden increase in current is associated with the formation of conductive filaments (CFs) in TiO induced by oxygen vacancies. Well-defined memory windows were

observed for the samples annealed at higher temperatures (up to 900°C). Kars *et al.* [7] reported that the formation of oxygen vacancies during low-temperature annealing is related to the breaking of Ti–O bonds.
At the same time, atmospheric oxygen attaches to the surface of the TiO film, forming Ti–O bonds [2]. Thus, there is a competition between the breaking of Ti–O bonds in the bulk and the formation of Ti–O bonds at the surface.

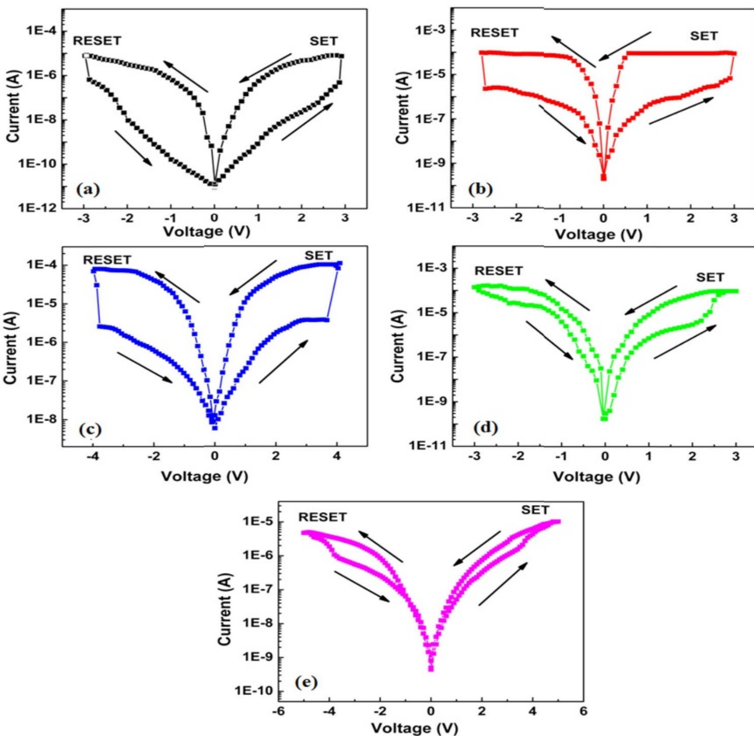

Figure 2. I–V curves of dip-coated TiO thin films processed for 10 min in air ambient with various Rapid Thermal Annealing (RTA) a) 500°C, b) 600°C, c) 700°C, d) 800°C, and e) 900°C

B. Optical Bandgap Estimation

The optical bandgaps of the individual TiO and SnO_2 layers were estimated using Tauc plot analysis derived from UV–Vis absorbance spectra (see Figure 3). By plotting $(\alpha h\nu)^2$ versus photon energy ($h\nu$) and extrapolating the linear region to the energy axis, the direct bandgap values were determined. The estimated optical bandgaps were found to be approximately: TiO layer (3.17 eV), SnO_2 layer (3.41 eV)

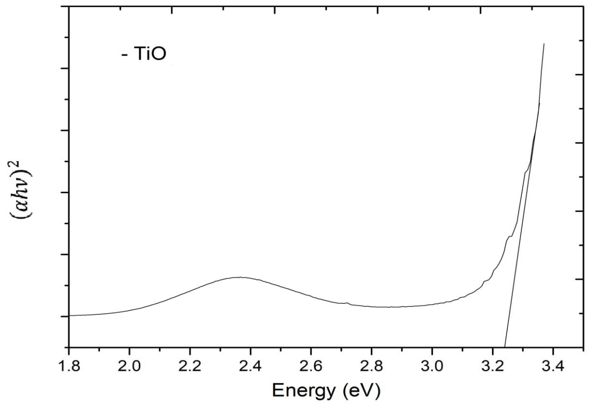

Figure 3. Tauc plot used for bandgap estimation of TiO (3.24 eV)

These values closely match literature-reported data confirming the successful synthesis of phase-pure oxide layers. The slight narrowing of the SnO_2 bandgap compared to the nominal 3.6 eV may be attributed to oxygen vacancy-related subgap states, which can affect the switching performance by serving as electron trapping centers.

C. Structural Characterization (XRD analysis)

Figure 4 shows the XRD patterns of TiO thin nanoplanes processed in air at 500 °C for different durations (1, 5, and 10 min). The XRD peaks at 26.7° and 49.1° correspond to the (101) and (200) planes of the anatase phase, respectively, which are consistent with literature reports. The intensity of the (101) peak decreases with increasing annealing duration.

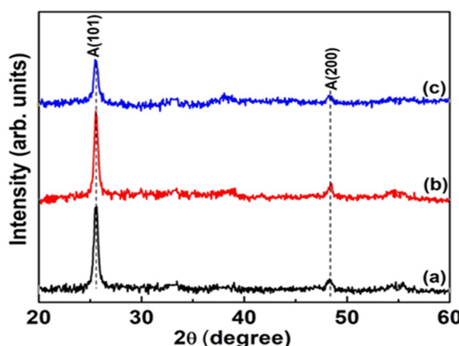

Figure 4. XRD patterns of dip-coated TiO thin films processed at 500°C in air ambient for different RTA duration a) 1min, b) 5min, and c) 10min (the abbreviation stands for: A anatase)

D. Mechanism Interpretation

To identify the charge transport mechanism in the TiO layer for the LRS (Low Resistance State) and HRS (High Resistance State), we monitored the temperature dependence of the electrical conductivity in both states. These results are presented in Figure 5, where the thermally activated behavior of the LRS and HRS within the TiO layer is clearly visible.

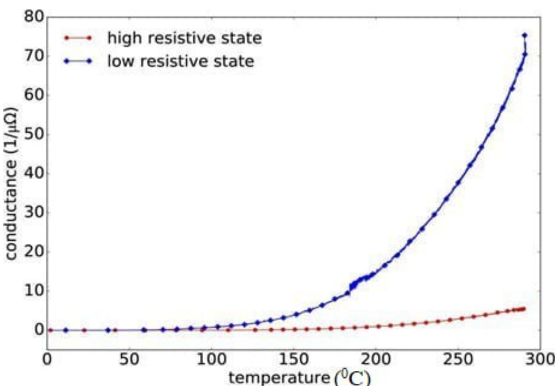

Figure 5. To determine the charge transport mechanism in the LRS and HRS states of the TiO layer, we monitored the temperature dependence of the conductivity in both states. This is shown in the figure, where the thermally activated behavior of the LRS and HRS within the TiO layer is clearly visible

CONCLUSIONS

In this study, a p-Si/TiO thin film was successfully fabricated using the magnetron sputtering technique. Electrical analysis of the device revealed clear bipolar resistive switching behavior accompanied by a stable hysteresis loop in the I–V characteristics. The fact that the switching occurred without the need for a forming step indicates that oxygen vacancies and interface effects play a major role in the resistive switching (RS) mechanism. Tauc plot analysis showed that the optical bandgaps of TiO and SnO_2 were approximately 3.24 eV and 3.41 eV, respectively, which are consistent with values reported in the scientific literature. Although both oxides are n-type semiconductors and the small band offset between them may slightly reduce the overall switching contrast, the device exhibited repeatable SET/RESET cycles and sufficient separation between the resistance states.

These results confirm that the p-Si/TiO nanostructure is a promising platform for exploring low-cost, oxide-based memristors. Future studies may focus on interface engineering, doping, or incorporating buffer layers to further enhance RS characteristics and improve device scalability for neuromorphic and non-volatile memory applications.

ORCID

Muradulla X. Normurodov, https://orcid.org/0000-0003-1771-0853; **Odil O. Ochilov,** https://orcid.org/0000-0002-9319-0143; **Ozodbek Y. Yuldashev**, https://orcid.org/0009-0000-6464-3484; **Zarnigor A. Karshieva,** https://orcid.org/0009-0005-3837-538X; **Nurbek U. Toshboyev,** https://orcid.org/0009-0008-0057-5433

REFERENCES

[1] D. Ielmini, "Resistive switching memories based on metal oxides: Mechanisms, reliability and scaling," Semiconductor Science and Technology, **31**(6), 063002 (2016). https://doi.org/10.1088/0268-1242/31/6/063002

[2] B. Cao, H. Liu, T. Li, J. Gong, S. Zhang, and M.T. Dove, "Synthesis of composite films for ZnO-based memristors with superior stability," Materials Research Express, **11**, 056302 (2024). https://doi.org/10.1088/2053-1591/ad4777

[3] P.D. Walke, *et al.*, "Memristive Devices from CuO Nanoparticles," Nanomaterials, **10**(9), 1677 (2020). https://doi.org/10.3390/nano10091677

[4] P.A. Hind, P. Kumar, U.K. Goutam, and B.V. Rajendra, "Impact of deposition temperature on persistent photoconductivity of SnO_2 thin films deposited using spray pyrolysis technique suitable in optoelectronic synaptic devices," Optical Materials, **146**, 115579 (2024). https://doi.org/10.1016/j.optmat.2024.115579
[5] N.U. Rehman, R. Khan, N. Rahman, I. Ahmad, A. Ullah, M. Sohail, S. Iqbal, et al., "Dual-doped ZnO-based magnetic semiconductor resistive switching response for memristor-based technologies," Journal of Materials Science: Materials in Electronics, **35**, 1557 (2024). https://doi.org/10.1007/s10854-024-13318-5
[6] R. Pant, N. Patel, K.K. Nanda, and S.B. Krupanidhi, "Negative differential resistance and resistive switching in SnO_2/ZnO interface," Journal of Applied Physics, **122**(12), (2017). https://doi.org/10.1063/1.5004969
[7] I. Kars, S.Ş. Çetin, B. Kinaci, B. Sarikavak, A. Bengi, H. Altuntaş, M.K. Öztürk, and S. Özçelik, "Influence of thermal annealing onthe structure and optical properties of d.c. magnetron sputteredtitanium dioxide thin films," Surf Interface Anal. **42**, 1247-1251 (2010). https://doi.org/10.1002/sia.3373
[8] S. Saha, *et al*. "Experimental demonstration of SnO_2 nanofiber-based memristors and their data-driven modeling for nanoelectronic applications," Chip, **2**, 100075 (2023). https://doi.org/10.1016/j.chip.2023.100075
[9] J.X. Murodov, Sh.U. Yuldashev, M.S. Mirkamilova, and U.E. Jurayev, "Tunable Negative Differential Resistance in SnO_2:Co Memristors on p-Si," East European Journal of Physics, (2), 211-214 (2025). https://doi.org/10.26565/2312-4334-2025-2-22
[10] A. Arslanov, Sh. Yuldashev, N. Botirova, R. Nusretov, J. Murodov, and J. Xudoyqulov, "Impact of precursor molar concentration on the structural and optical properties of ZnO thin films synthesized by ultrasonic spray pyrolysis," Physical Science International Journal, **29**(1), 29–35 (2025). https://doi.org/10.9734/psij/2025/v29i1871
[11] P. Chowdhury, H.C. Barshilia, N. Selvakumar, B. Deepthi, K.S. Rajam, A.R. Chaudhuri, and S.B. Krupanidhi, "The structural and electrical properties of TiO2 thin films prepared by thermal oxidation," Phys. B Condens. Matter. **403**, 3718–3723 (2008). https://doi.org/10.1016/j.physb.2008.06.02
[12] D. Regonini, V. Adamaki, C.R. Bowen, S.R. Pennock, J. Taylor, and A.C.E. Dent, "AC electrical properties of TiO_2 and Magnéli phases, Ti_nO_{2n-1}," Solid State Ionics, **229**, 38–44 (2012). https://doi.org/10.1016/j.ssi.2012.10.003
[13] Y. Le Page, and P. Strobel, "Structural chemistry of the Magnéli phases Ti_nO_{2n-1}, $4 \leq n \leq 9$. II. Refinements and structural discussion," J. Solid State Chem. **44**, 273–281 (1982). https://doi.org/10.1016/0022-4596(82)90374-7
[14] L. Liborio, and N. Harrison, "Thermodynamics of oxygen-defective Magnéli phases in rutile: a first-principles study," Phys. Rev. B, **77**, 1–10 (2008). https://doi.org/10.1103/PhysRevB.77.104104
[15] Y. Abbas, I.S. Han, A.S. Sokolov, Y.R. Jeon, and C. Choi, "Rapid thermal annealing on the atomic layer-deposited zirconia thin filmto enhance resistive switching characteristics," J. Mater. Sci. Mater. Electron. **31**, 903–909 (2020). https://doi.org/10.1007/s10854-019-02598-x
[16] X.Y. Yang, Y.K. Zhu, H. Miura, and T. Sakai, "Static recrystallization behavior of hot-deformed magnesium alloy AZ31 during isothermal annealing," Trans. Nonferrous Met. Soc. China. **20**, 1269–1274 (2010). https://doi.org/10.1016/S1003-6326(09)60289-2
[17] M. Tian, M. Mahjouri-Samani, K. Wang, A.A. Puretzky, D.B. Geohegan, W.D. Tennyson, N. Cross, *et al*., "Black anatase formation by annealing of amorphous nanoparticles and the role of the Ti_2O_3 shell in self-organized crystallization by particle attachment," ACS Appl Mater. Interfaces, **9**, 22018–22025 (2017). https://doi.org/10.1021/acsami.7b02764
[18] Z.N. Jameel, A.J. Haider, and S.Y. Taha, "Synthesis of TiO_2 nanoparticles by using sol-gel method and its applications as antibacterial agents," Eng. Tech. J. **32**, 418–426 (2014). https://doi.org/10.30684/etj.32.3B.4
[19] N. Gergel-Hackett, B. Hamadani, B. Dunlap, J. Suehle, S. Member, C. Richter, S. Member, *et al*., "A flexible solution-processed memristor," IEEE Electron Device Lett. **30**, 706–708 (2009). https://doi.org/10.1109/LED.2009.202141
[20] K.N. Pham, V.D. Hoang, C.V. Tran, and B.T. Phan, "TiO_2 thin filmbased transparent flexible resistive switching random access memory," Adv. Nat. Sci. Nanosci. Nanotechnol. **7**, (2016). https://doi.org/10.1088/2043-6262/7/1/015017
[21] C. Ye, T. Deng, J. Zhang, L. Shen, P. He, W. Wei, and H. Wang, "Enhanced resistive switching performance for bilayer HfO_2/TiO_2resistive random access memory," Semicond. Sci. Technol. **31**, 1–7 (2016). https://doi.org/10.1088/0268-1242/31/10/105005
[22] C.H. Huang, T.S. Chou, J.S. Huang, S.M. Lin, and Y.L. Chueh, "Self-selecting resistive switching scheme using TiO_2 nanorod arrays," Sci. Rep. **7**, 1–9 (2017). https://doi.org/10.1038/s41598-017-01354-7

РЕЗИСТИВНА ПОВЕДІНКА ПЕРЕМИКАННЯ ТОНКИХ ПЛІВОК Si/TiO ДЛЯ ЗАСТОСУВАННЯ ЕЛЕКТРОНЕЗАЛЕЖНОЇ ПАМ'ЯТІ

Мурадулла Т. Нормуродов[1], Оділ Очілов[2], Озодбек Ю. Юлдашев[2], Зарнігор А. Каршієва[2], Нурбек У. Тошбоєв[2]
[1]*Каршинський державний університет, Узбекистан*
[2]*Центр розвитку нанотехнологій, Національний університет Узбекистану, Ташкент, Узбекистан*

У цьому дослідженні представлено виготовлення тонких плівок Si/TiO, нанесених у режимі постійного струму за допомогою магнетронного напилення на кремнієві підкладки p-типу, а також досліджено їх температурно-залежні характеристики резистивного перемикання (RS) та низькоомного стану (LRS). Наноструктури були відпалені при 420°C для покращення кристалічності та міжфазного контакту. Електрична характеристика, отримана за допомогою вольт-амперних вимірювань, виявила чітку біполярну поведінку RS без необхідності початкового процесу формування. Пристрої демонстрували стабільні стани високого (HRS) та низького (LRS) опору протягом кількох циклів. Механізм перемикання пояснюється утворенням і розривом провідних ниток, індукованих вакансіями кисню на межі розділу Si/TiO. Значення ширини забороненої зони, отримані з графіків Тауца, становили приблизно 3,24 еВ для TiO та 3,41 еВ для SnO_2. Ці результати підтверджують, що нанотонкі плівки Si/TiO є перспективними матеріалами для швидких, енергоефективних і перезаписуваних пристроїв пам'яті наступного покоління.

Ключові слова: *TiO; магнетронне розпилення; мемристор; швидкий термічний відпал (RTA)*

EAST EUROPEAN JOURNAL OF PHYSICS. 2. 280-291 (2026)
DOI:10.26565/2312-4334-2026-2-30 ISSN 2312-4334

STRUCTURAL, OPTOELECTRONIC AND MECHANICAL PROPERTIES OF $AHgCl_3$ (A=Rb, Cs) PEROVSKITES: A FIRST-PRINCIPLES GGA AND TB-mBJ ANALYSIS

Habiba Bouheraoua, El-Djemai Belbacha*
Laboratory of Physico-Chemical Studies of Materials (LEPCM), Department of Physics, Faculty of Matter Sciences, University of Batna 1, 05000 Batna, Algeria
**Corresponding Author e-mail: eldjemai.belbacha@univ-batna.dz*
Received January 27, 2026; revised April 14, 2026; accepted April 25, 2026

The structural, mechanical, and optoelectronic properties of cubic halide perovskites $AHgCl_3$ (A = Rb, Cs) were investigated using density functional theory (DFT) within the full-potential linearized augmented plane wave (FP-LAPW) method, as implemented in the WIEN2k code. The structural stability of the cubic phase was confirmed using the Goldschmidt tolerance factor and the octahedral factor, while the negative formation energies verified their thermodynamic stability. The calculated elastic parameters, including Poisson's ratio, Pugh's ratio, and Cauchy pressure, indicate that both compounds are mechanically stable, ductile, and exhibit a predominantly ionic bonding nature. The optoelectronic properties were examined using the Tran–Blaha modified Becke–Johnson (TB-mBJ) potential. The results reveal that $RbHgCl_3$ and $CsHgCl_3$ are indirect-band-gap semiconductors with band gaps of 1.25 eV and 1.16 eV, respectively. Furthermore, the optical properties were analyzed over the photon energy range of 0–20 eV. Both compounds exhibit strong absorption in the ultraviolet region and low reflectivity at zero photon energy, indicating favorable performance for optoelectronic applications. Overall, these findings suggest that $AHgCl_3$ (A = Rb, Cs) halide perovskites are promising candidates for applications in photovoltaic devices and ultraviolet photodetectors.
Keywords: *Halide perovskite $KZnX_3$; FP-LAPW; Ab-initio; Wien2k; Opto-electronic properties; TB-mBJ*
PACS: 71, 20.Gj, 81.30.-t

1. INTRODUCTION

The exceptional optoelectronic, magnetic ordering, giant magnetoresistance, and thermoelectric properties of perovskites make them intriguing candidates for diverse applications, such as sensors, microelectronics, solar cells, light-emitting diodes, spintronic devices, photovoltaics, and telecommunications devices [1]. In 1839, Gustav Rose discovered the first perovskite, $CaTiO_3$, and the renowned scientist Count Lev Alexeevich von Perovski, after whom the material was named [2]. Consequently, any material exhibiting a comparable structure and employing the chemical formula ABX_3 is designated as a perovskite. This material family comprises conductors, insulators, semiconductors, and superconductors [2].

The cubic perovskite structure has the chemical formula ABX_3, where cations A and B represent alkali and alkaline earth metals, respectively, and X is an anion. Perovskites can be classified into three main groups according to the anion type: oxide (ABO_3), nitride (ABN_3), and halide perovskites ABX_3 (X = F, Cl, Br, I) [3]. To maintain charge neutrality, halide perovskites typically accommodate divalent metal cations in the +2-oxidation state, such as Pb^{2+}, Sn^{2+}, and Ge^{2+} [4]. In addition, halide perovskites can be readily processed into polycrystalline thin films, making them well-suited for optoelectronic applications across various substrates [5]. The remarkable optical and charge-transport properties of halide perovskites have made them widely sought-after light-harvesting materials with appropriate band gaps, high optical absorption coefficients, long charge-carrier diffusion lengths, high external quantum efficiency, and a notable defect tolerance [6]. In addition, several halide perovskite crystallographic phases have been identified at different temperatures, and cubic, tetragonal, and orthorhombic are the most prevalent phases [7]. Chloroperovskites$ABCl_3$ have a wide band gap, which qualifies them for use in numerous contemporary energy storage devices. Moreover, the broad band gap energy enables chloroperovskites to effectively emit or absorb ultraviolet radiation, rendering them desirable for optoelectronic devices [8-10].

Some examples of cubic halide perovskites are $CsZnCl_3$ and $KHgCl_3$. These compounds were theoretically studied by Aqili et al. [11] and Ullah et al [12]. Their findings indicated that these cubic halide perovskites are indirect band gap semiconductors with band gaps of 3.628 and 1.11 eV, respectively, and might be viable candidates for UV optoelectronic applications [11-12]. M. Arif et al. [13] examined the physical properties of cesium-based cubic halide perovskites, $CsHgX_3$ (X = F, Cl), employing the full potential linearized augmented plane wave (FP-LAPW) approach under the generalized gradient approximation (GGA). Their findings, which include electronic band structure and density of states calculations, revealed that $CsHgF_3$ has an indirect band gap and behaves as a semiconductor, whereas $CsHgCl_3$ exhibits metallic behavior. In the same vein, we have thoroughly investigated the perovskites $RbHgCl_3$ and $CsHgCl_3$. These compounds are documented as stable in the Open Quantum Materials Database (OQMD) [14-15]. We present theoretical calculations on $AHgCl_3$ (where A = Rb or Cs) halide perovskite compounds, providing us with important information about their structural, elastic, and optoelectronic properties, employing the full potential

Cite as: H. Bouheraoua, El-D. Belbacha, East Eur. J. Phys. 2, 280 (2026), https://doi.org/10.26565/2312-4334-2026-2-30
©H. Bouheraoua, El-D. Belbacha, 2026; CC BY 4.0 license

linearized augmented plane wave (FP-LAPW) method within the generalized gradient approximation (GGA) and the Tran and Blaha modified Becke Johnson (TB-mBJ) approach for optoelectronic characteristics. The following is the structure of the study: Section 1 presents a concise introduction, and Section 2 delineates the computational methodologies employed in this investigation. Further, we present our findings in Section 3. Finally, we summarize our results and provide the conclusions.

2. COMPUTATIONAL DETAIL

The physical properties of halide perovskites with a cubic structure, $AHgCl_3$ (A=Rb, Cs), were calculated using the Wien2k package [16] based on the full potential linearized augmented plane wave (FP-LAPW) method [17] to solve the Kohn–Sham equations [18]. This approach is predicated on density functional theory (DFT) [19]. To determine the most stable ground state of the compounds, we optimized the structures using different exchange correlation potentials, including PBE [20], WC [21], and PBE-sol [22]. The Murnaghan equation of state [23] was employed to determine the equilibrium lattice parameters by fitting the total energy–volume data points. The optoelectronic properties were investigated using the Tran–Blaha modified Becke–Johnson (TB-mBJ) [24] and GGA-PBE [20] potentials. The shifted k-point mesh was set to 14×14×14, which corresponds to a dense mesh of 3000 k-points in the first Brillouin zone. The cutoff of the plane waves, RMT×Kmax = 8, was chosen for the interstitial area, whereas the maximum value for the wave function expansion inside spheres was Lmax = 10. In addition, the Fourier charge density inside the atomic sphere was set to Gmax = 12 $(a.u.)^{-1}$, and the cutoff energy was chosen to be − 6.00 Ryd. The self-consistent cycles converged when the total energy was stable within 10^{-5} Ryd. Moreover, the elastic constants examined in this study were obtained using the IRelast [25] method integrated into the Wien2k software [16].

3. RESULTS AND DISCUSSION

3.1 Structural Properties

The perovskite $AHgCl_3$ (A = Rb, Cs) crystallizes in space group 221 (Pm-3m), with lattice properties detailed in Table 1. The A atom is located at (0, 0, 0), the Hg atom is positioned at the center, and the Cl atoms are placed at the face centers (0.5, 0.5, 0), (0, 0.5, 0.5), and (0.5, 0, 0.5) of the lattice. Figure 1 illustrates the crystal structures of $AHgCl_3$ (A = Rb, Cs) perovskites.

Table 1. Computed lattice parameters (A°), volume V ($a.u^3$), bulk modulus B (GPa), pressure derivative B', minimum energy E_0 (Ryd), formation energy E_{form} (eV/atom) values for $AHgCl_3$ (A= Rb, Cs)

Compound	XC	a	V	B	B'	E_0	E_{form}	t	μ
$RbHgCl_3$	PBE	5.37	1045.14	28.43	5.25	-48056.066643	-0.63	0.832	0.657
	WC	5.26	986.13	33.17	5.33	-48050.776143			
	PBE-sol	5.25	979.85	34.51	5.39	-48037.487811			
Other works	[14-15]	5.32							
$CsHgCl_3$	PBE	5.41	1068.74	27.74	5.31	-57673.688577	-0.57	0.870	0.657
	WC	5.28	998.93	33.63	5.50	-57667.866339			
	PBE-sol	5.28	995.65	34.34	5.16	-57652.563214			
Other works	[14-15]	5.38							
	[13]	5.40							

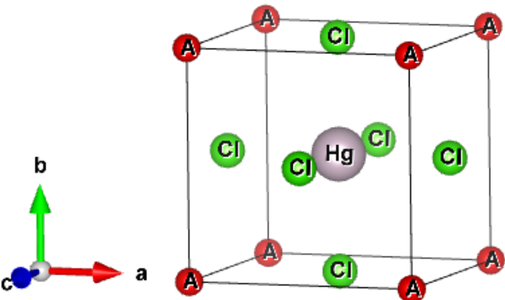

Figure 1. Crystal structure of cubic halide perovskites $AHgCl_3$ (A=Rb, Cs)

Furthermore, to validate the structural stability of these perovskites, we employed the tolerance factor t and the octahedral factor μ. These two quantities are related to the ionic radii using the following equations [26, 27]:

$$t = \frac{R_A + R_X}{\sqrt{2}(R_B + R_X)} \tag{1}$$

$$\mu = \frac{R_B}{R_X} \tag{2}$$

For the cubic perovskite structure, the tolerance factor must lie within the range of $0.8 \leq t \leq 1.0$, and μ is known to be between 0.377 and 0.895 [26, 27]. The values of t and μ are presented in Table 1, which demonstrates that all crystal structures are stable and have cubic symmetry. We computed the formation energy using Equation (3) [28] to discuss the thermodynamic stability.

$$E_f = \frac{1}{5}\left[E_{tot}^{AHgCl_3} - \left(E_a^A + E_a^{Hg} + 3E_a^{Cl}\right)\right], \quad (3)$$

where $E_{tot}^{AHgCl_3}$represent the total energy of the $AHgCl_3$ compound and $E_a^A, E_a^{Hg} and E_a^{Cl}$ are the total energies of A, Hg, and Cl, respectively.

The calculated formation energies of $RbHgCl_3$ and $CsHgCl_3$ are listed in Table 1 and obey the criterion of $Ef < 0.2$ eV/atom [1], ensuring that these formation materials can be formed experimentally. In addition, negative formation energies indicate thermodynamic stability.

The calculated values of the lattice parameters, volume, bulk pressure, derivative, ground state, and formation energies for the compounds are listed in Table 1. This table shows that the minimum energy for $AHgCl_3$perovskites corresponds to the GGA-PBE, that is, − 48056.066643 Ryd ($RbHgCl_3$) and − 57673.688577 Ryd ($CsHgCl_3$), indicating that RbHgCl3 and $CsHgCl_3$ remain stable in the GGA-PBE. Fig. 2 illustrates the structural optimization curves for $RbHgCl_3$ and $CsHgCl_3$ compounds using a GGA-PBE approximation.

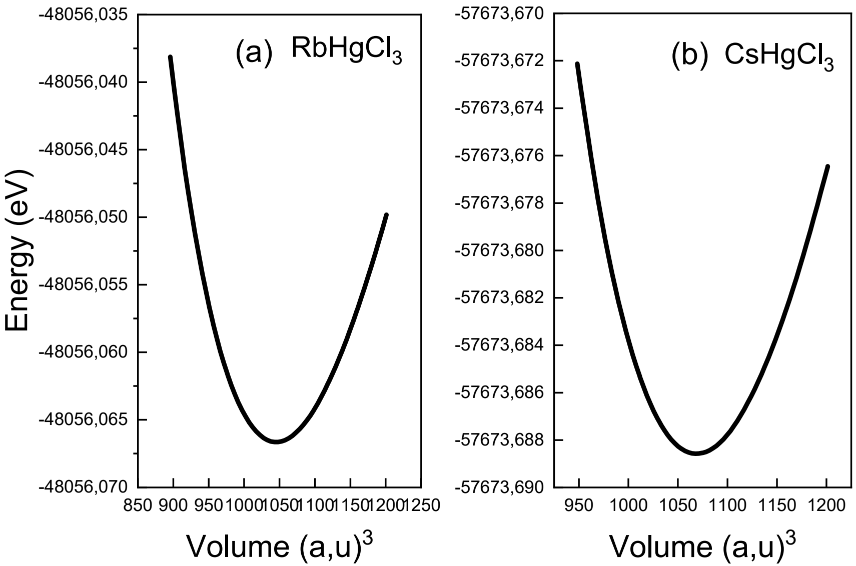

Figure 2. The variation of the total energy as a function of volume for (a) $RbHgCl_3$, (b) $CsHgCl_3$ with GGA-PBE

3.2 ELECTRONIC PROPERTIES

To investigate the electronic properties of cubic halide perovskites $AHgCl_3$ (A = Rb, Cs), we computed the energy band structure (BS), total density of states (TDOS), and partial density of states (PDOS) along high-symmetry directions within the first Brillouin zone over an energy range of −14 to 14 eV using both the GGA-PBE and TB-mBJ approximations. Figures 3(a) and (b) present the band structures of both compounds, with the Fermi level indicated by a horizontal red dashed line at 0 eV.

The GGA-PBE results indicate metallic behaviour in both $RbHgCl_3$ and $CsHgCl_3$, as the valence and conduction bands overlap at the Fermi level, resulting in no band gap. Although these findings are consistent with the values reported in the OQMD database [14,15], this metallic prediction highlights a well-known limitation of GGA, which systematically underestimates band gaps in semiconductors and insulators.

To address this limitation, the TB-mBJ potential was applied, which yielded a more accurate depiction of the electronic structure. The TB-mBJ calculations revealed that both compounds are indirect semiconductors, with the valence band maximum (VBM) at the L point and the conduction band minimum (CBM) at the Γ point (L–Γ). The band gap values listed in Table 2 underscore the substantial improvement provided by the TB-mBJ in accurately capturing the semiconducting nature of these halide perovskites.

The analysis of the total and partial densities of states provides valuable insights into the bonding properties and the nature of the electronic band structure. The total (TDOS) and partial (PDOS) densities of states for $RbHgCl_3$ and $CsHgCl_3$ were calculated using the TB-mBJ potential, as shown in Figs. 3(a, b) and 4(a–f), respectively. The TDOS profiles of all compounds clearly reveal the bandgap (Eg), confirming their semiconducting nature. For $AHgCl_3$ (A = Rb, Cs), the valence band primarily originates from A(p), Hg(d), and Cl(s+p) orbitals, whereas the conduction band is mainly composed of A(d) states, with significant contributions from Hg(d).

Table 2. Calculated indirect band gaps (eV) for $RbHgCl_3$ and $CsHgCl_3$ using GGA-PBE and TB-mBJ

Compound	XC	Bandgap	Other works
$RbHgCl_3$	PBE	0.00	0.00[14-15]
	TB-mBJ	1.25	
$CsHgCl_3$	PBE	0.00	0.00[13-14-15]
	TB-mBJ	1.16	

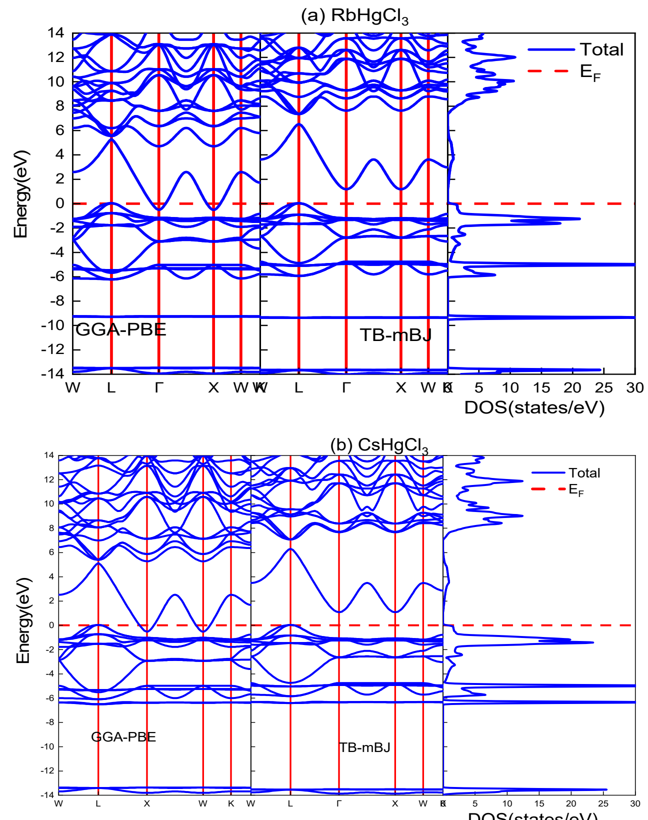

Figure 3. Band structure and DOS for(a) $RbHgCl_3$and (b) $CsHgCl_3$compounds

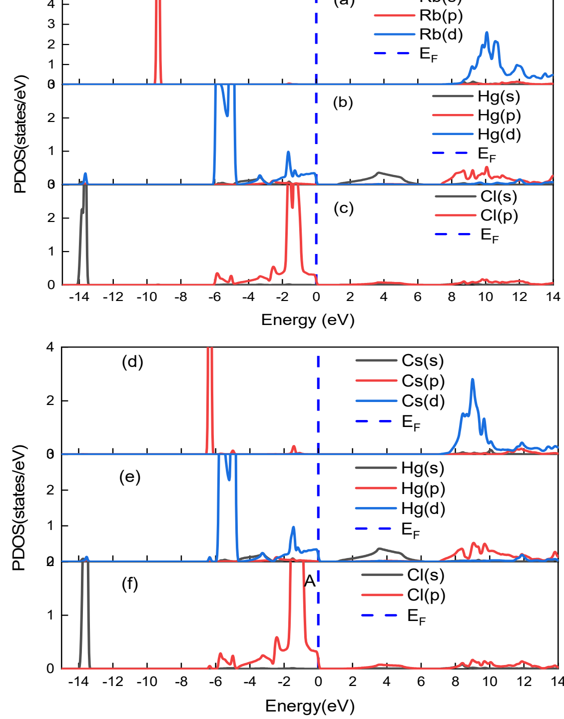

Figure 4. Computed partial densities of states of $AHgCl_3$ compound with TB-mBJ

3. MECHANICAL PROPERTIES

Elastic constants (Cij) are fundamental parameters for describing the mechanical properties of materials. These constants characterize the response of a crystal to external forces. A material is considered mechanically stable if it satisfies the Born stability criteria [29–31]: $C_{11} - C_{12} > 0$, $C_{44} > 0$, $C_{11} > 0$, $(C_{11} + 2C_{12}) > 0$, and $C_{12} < B < C_{11}$. The results presented in Table 3 satisfy these stability criteria, indicating that all the compounds are mechanically stable. Furthermore, the elastic constants can be used to evaluate key mechanical parameters, such as the bulk modulus (B), shear modulus (G), and Young's modulus (E). The relationships between these parameters and the elastic constants are expressed in Eqs. (4)–(8).

$$B = \frac{C_{11} + 2C_{12}}{3} \tag{4}$$

$$G_V = \frac{C_{11} + 3C_{44} - C_{12}}{5} \tag{5}$$

$$G_R = \frac{5(C_{11} - C_{12})C_{44}}{3(C_{11} - C_{12}) + 4C_{44}} \tag{6}$$

$$G = \frac{1}{2}(G_V + G_R) \tag{7}$$

$$E = \frac{9BG}{3B + G} \tag{8}$$

The shear modulus (G) characterizes the stiffness of a material and is defined by Eqs. (5) – (7), where G_V, G_R, and G represent the Voigt [32], Reuss [33], and Hill average shear moduli, respectively. A low value of G indicates that the material is more flexible and easily deformed under shear stress.

The bulk modulus (B) measures the resistance of a material to compression, as expressed in Eq. (4). The relatively low values of B suggest the softness and flexibility of the studied compounds. As shown in Table 3, the bulk modulus (B) values for all compounds are low and of similar magnitude, which further confirms their mechanical softness. Consequently, the shear modulus G is lower than the bulk modulus B, indicating that the analyzed compounds exhibit greater resistance to volumetric compression than to shear deformation.

Young's modulus (E), which depends on both the bulk modulus (B) and shear modulus (G), as given in Eq. (8), provides a measure of the stiffness of the material. The rigidity of a compound increases with increasing Young's modulus. The calculated values of B, G, and E, presented in Table 3, indicate that the ternary chloroperovskite compounds $AHgCl_3$ (A = Rb, Cs) possess moderate rigidity.

To further evaluate the ductile or brittle nature of these compounds, additional mechanical parameters, including Poisson's ratio, Pugh's ratio, and Cauchy pressure, were determined, as listed in Table 3. According to Eq. (9), a material is considered more stable against external deterioration and less compressible when the Poisson's ratio lies between 0.25 and 0.5 [1,34–35].

$$\upsilon = \frac{1}{2}\left[\frac{3B - 2G}{3B + G}\right] \tag{9}$$

Poisson's ratio typically takes values of approximately 0.33 for ionic bonding, 0.25 for metallic bonding, and 0.1 for covalent bonding [1]. Furthermore, Frantsevich et al. [36] reported that a material is classified as ductile if its Poisson's ratio exceeds 0.26 and as brittle if it is below this threshold. The calculated Poisson's ratio values are greater than 0.26, suggesting that the studied compounds exhibit ductile behavior and a predominantly ionic bonding characteristics.

The ratio of the bulk modulus to the shear modulus (B/G), known as Pugh's ratio (K) [37], is another important ductility indicator. A material is considered brittle when (B/G) < 1.75; otherwise, it is considered ductile. In the present study, the calculated Pugh's ratio exceeded 1.75, further confirming the ductile nature of the compounds.

The Cauchy pressure ($CP = C_{12} - C_{44}$) [38] is also used to distinguish between ductile and brittle behaviors. Negative CP values indicate brittleness, whereas positive values suggest ductility. The calculated CP values (Table 3) were positive, indicating that all compounds exhibited ductile behavior.

Another important parameter used to evaluate the presence of microcracks and the mechanical stability of materials is the elastic anisotropy, as determined using Eq. (10).

$$A = \frac{2C_{44}}{(C_{11} - C_{12})} \tag{10}$$

For an isotropic material, A = 1, whereas values of A greater than or less than 1 indicate anisotropic behavior. The calculated values of A, presented in Table 3, show that all compounds exhibit significant anisotropy.

Table 3. Elastic constants C_{11}, C_{12}, and C_{44} (GPa); bulk modulus B (GPa); the shear modulus G (GPa); Young's modulus E (GPa); anisotropic parameter A; Paugh's ratio K; Cauchy pressure C_P; and Poisson's ratio υ for $AHgCl_3$ (A= Rb, Cs) compounds

Compound	C_{11}	C_{12}	C_{44}	B	G	E	A	B/G	C_P	υ
$RbHgCl_3$	46.04	19.71	8.31	28.49	10.00	26.85	0.63	2.84	11.40	0.34
$CsHgCl_3$	45.10	19.41	10.03	27.98	11.07	29.35	0.78	2.52	9.38	0.32
Other works	44.90	18.70	7.56	27.43	9.43	25.40	0.57	2.90	/	0.49

The isotropic and anisotropic characteristics of materials can be elucidated through three-dimensional (3D) representations of the directional dependence of the Young's modulus, shear modulus, and Poisson's ratio. The degree of anisotropy is reflected by the extent to which the resulting closed three-dimensional (3D) surface deviates from an ideal spherical shape. The ELATE tool [39] was used to generate the 3D distributions of Young's modulus (E), shear modulus (G), and Poisson's ratio for $AHgCl_3$ (A = Rb, Cs), as shown in Fig. 5. The studied halide perovskites $AHgCl_3$ (A = Rb, Cs) exhibit anisotropic behavior.

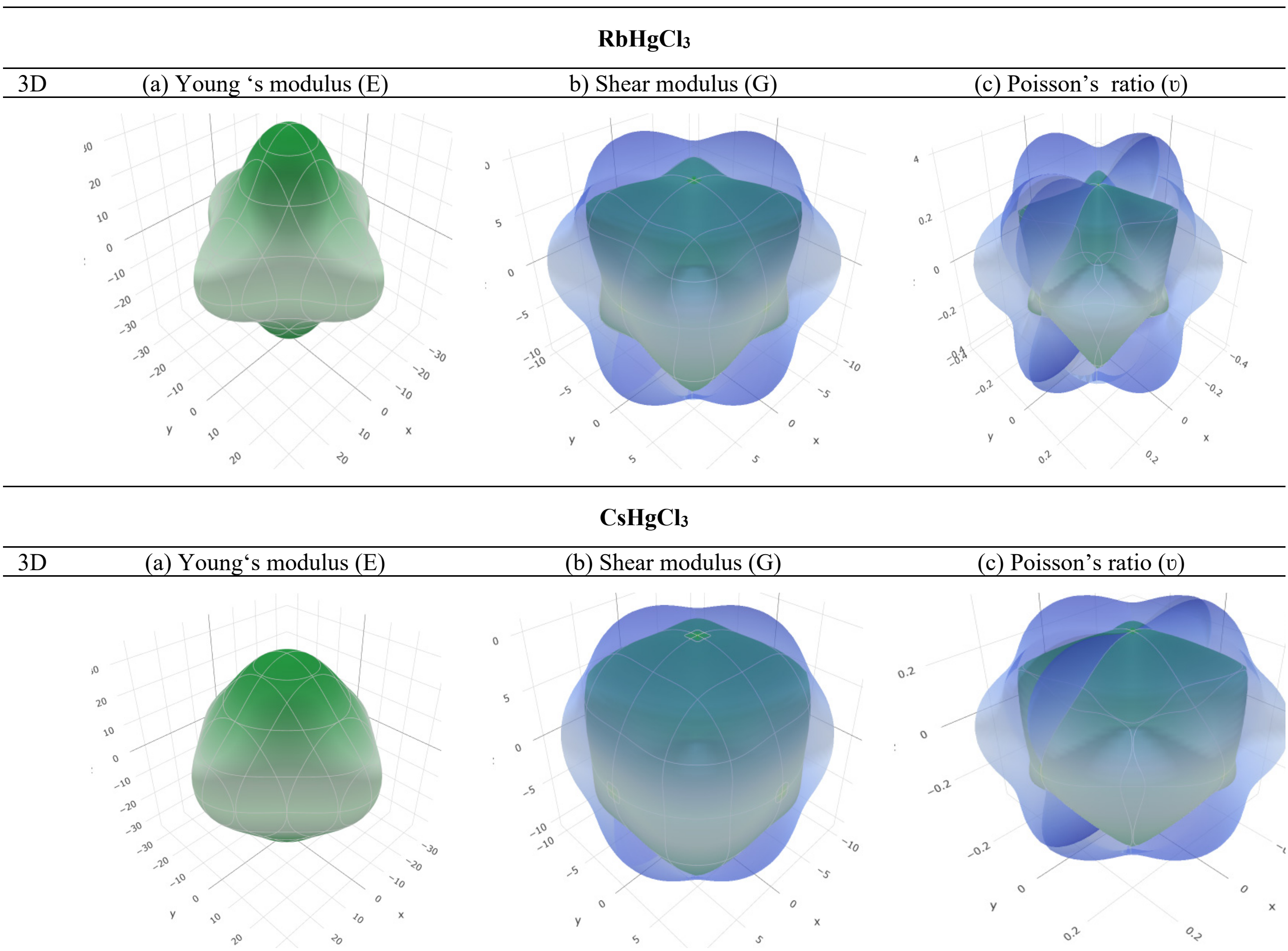

Figure 5. (3D): Young's modulus (a) (E(GPa)), shear modulus (b) (G(GPa)), and Poisson's ratio υ (d) for $AHgCl_3$ (A= Rb, Cs) compounds

3. 4 THERMAL PROPERTIES

Comprehending the velocity of sound, melting point, and Debye temperature is crucial for numerous applications. The computed values of these parameters are presented in Table 4.

Table 4. The calculated values of longitudinal velocity v_l(m/s), transverse velocity v_t,(m/s), sound velocityv_m(m/s), melting temperature T_m,(°K), and Debye temperature θ_D(°K)

Compound	v_l	v_t	v_m	T_m	θ_D
$RbHgCl_3$	3135.04	1541.77	1731.78	825.13	164.16
$CsHgCl_3$	3044.35	1549.69	1736.58	819.58	163.41

The longitudinal and transverse elastic wave velocities [40] were used to estimate the sound velocity [41] using the following equations:

$$\begin{cases} v_l = \sqrt{\dfrac{G}{\rho}} \\ v_l = \sqrt{\dfrac{3B+4G}{3\rho}} \\ v_m = \left[\dfrac{1}{3}\left(\dfrac{2}{v_l^3}+\dfrac{1}{v_l^3}\right)\right]^{-\frac{1}{3}} \end{cases} \tag{11}$$

Where ρ is the mass density of the material, and G and B are the shear and bulk modulus. The data presented in Table 4 indicate that the sound velocity in $RbHgCl_3$ is higher than that in $CsHgCl_3$, which can be attributed to the lower atomic mass of Rb relative to that of Cs.

The thermodynamic properties of a material, including the longitudinal and transverse sound velocities, specific heat, and thermal expansion coefficient, can be correlated with the Debye temperature. The Debye temperature is calculated using the following expression [41]:

$$\theta_D = v_m \frac{h}{K_B}\left[\frac{3n\rho N_A}{4\pi M}\right]^{\frac{1}{3}} \tag{12}$$

Where N_A is Avogadro's number, K_B is Boltzmann's constant, h is Planck's constant, and ρ is the density of thesolid's molecular mass.

The lower sound velocity in $RbHgCl_3$ and $CsHgCl_3$ leads to a corresponding decrease in the Debye temperature. Another important property that can be estimated from the elastic constants is the melting temperature, which can be calculated using the relationship proposed by Fine et al. [42].

$$T_m = \left[553(K) + \left(5.911\left(\frac{K}{GPa}\right)\right)C_{11}\right] \pm 300K \tag{13}$$

3.5 OPTICAL PROPERTIES

Understanding optical parameters, such as the absorption coefficient, refractive index, reflectivity, energy-loss function, extinction coefficient, and optical conductivity, is essential for characterizing interactions between materials and electromagnetic radiation.

The optical properties of the $AHgCl_3$ (A = Rb, Cs) halide perovskites were calculated using the TB-mBJ potential. The analysis begins with a fundamental optical quantity, namely, the complex dielectric function, which is expressed as follows:

$$\varepsilon(\omega) = \varepsilon_1(\omega) + i\varepsilon_2(\omega) \tag{14}$$

For incident photon energies ranging from 0 to 20 eV, the dielectric function ε(ω) was employed to determine the fundamental optical properties using the following relations:

$$\alpha(\omega) = \left[\sqrt{\varepsilon_1^2(\omega)+\varepsilon_2^2(\omega)-\varepsilon_1(\omega)}\right]^{\frac{1}{2}} \tag{15}$$

$$n(\omega) = \frac{1}{\sqrt{2}}\left[\sqrt{\varepsilon_1^2(\omega)+\varepsilon_2^2(\omega)}+\varepsilon_1(\omega)\right]^{\frac{1}{2}} \tag{16}$$

$$R(\omega) = \frac{(1-n)^2+k}{(1+n)^2+k} \tag{17}$$

$$L(\omega) = \frac{\varepsilon_1(\omega)}{\varepsilon_1^2(\omega)+\varepsilon_2^2(\omega)} \tag{18}$$

$$K(\omega) = \frac{(\sqrt{2}\omega)}{c}\left[\sqrt{\varepsilon_1^2(\omega)+\varepsilon_2^2(\omega)}-\varepsilon_1(\omega)\right]^{\frac{1}{2}} \tag{19}$$

$$\sigma(\omega) = \frac{\omega\varepsilon_2(\omega)}{4\pi} \tag{20}$$

Fig. 6 presents our results concerning the real part of the dielectric function, the imaginary part of the dielectric function, the absorption coefficient, the refractive index, the reflectivity, the energy loss, the extinction coefficient, and the optical conductivity.

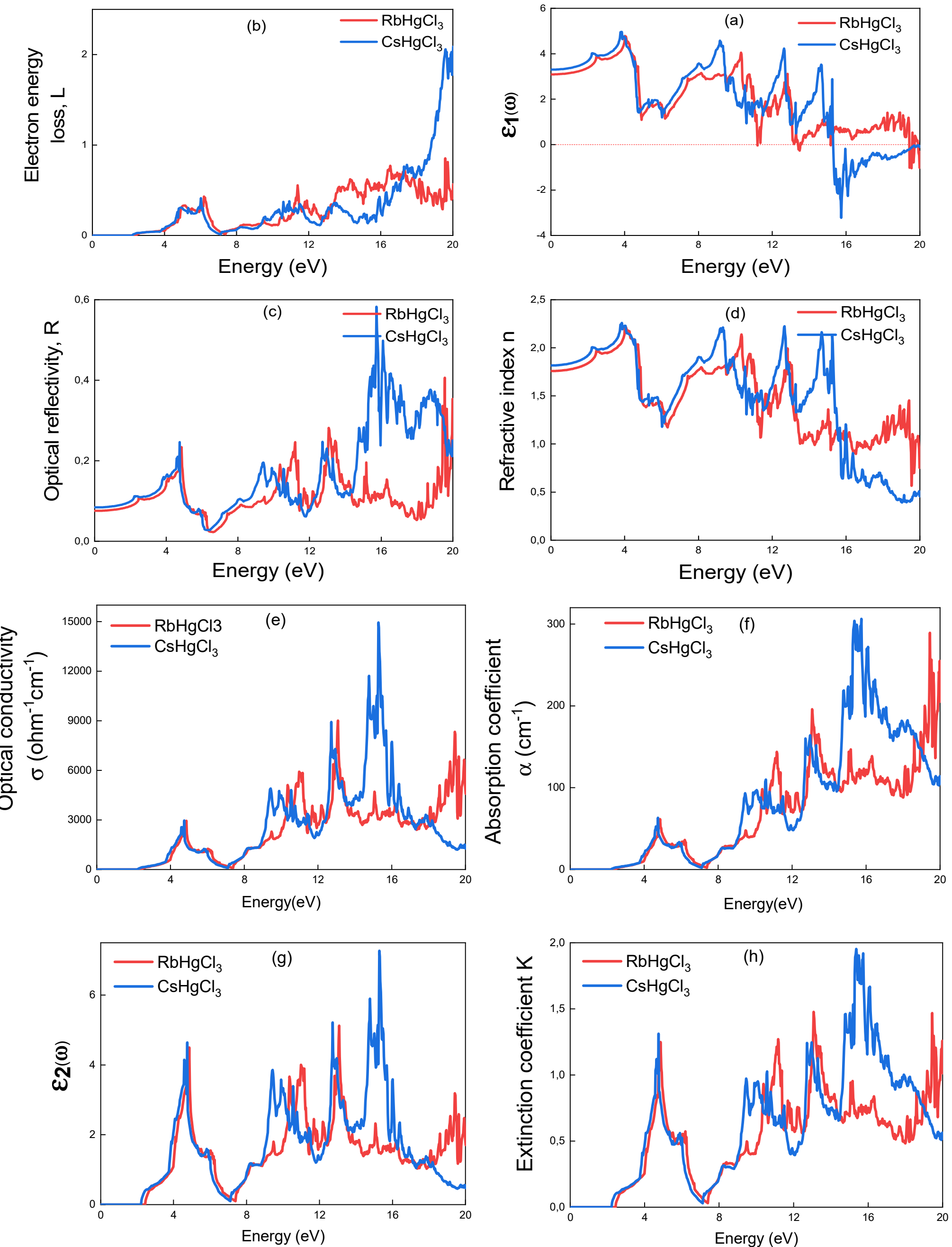

Figure 6. The curve of (a) the imaginary part ε2(ω) of the dielectric, (b) optical conductivity σ(ω), (c) absorption coefficient α(ω), (d) extinction coefficient K(ω), (e) the real part ε1(ω) of the dielectric, (f) refractive index n(ω), (g) optical reflectivity R(ω), and (h) loss function L(ω) of AHgCl3 (A=Rb, Cs).

3.5.1 The real $\varepsilon_1(\omega)$ and imaginary $\varepsilon_2(\omega)$ part of the dielectric function.

The real part of the dielectric function (Fig. 6a) describes the dispersion behavior of the material as well as its polarization capability. The calculated values for $AHgCl_3$ (A = Rb, Cs) halide perovskites are summarized in Table 5, indicating that $RbHgCl_3$ and $CsHgCl_3$ exhibit nearly identical polarization values.

Table 5. Computed the static dielectric function ε1 (0), static refractive index n (0), and reflective index R(0) for $RbHgCl_3$ and $CsHgCl_3$ utilizing the TB-mBJ approximation

Compound	ε1(0)	ε1(0)	*R(0)*
$RbHgCl_3$	3.09	1.75	0.075
$CsHgCl_3$	3.30	1.81	0.084

This behavior can be attributed to the inverse relationship between the band gap and the dielectric response, as described by Penn's model [43], wherein a smaller band gap corresponds to a higher dielectric constant. For both $RbHgCl_3$ and $CsHgCl_3$, the values remain nearly constant throughout the visible region (1.58–3.26 eV). Beyond this range, they increase and reach their maximum values in the ultraviolet region. As illustrated in Fig. 6a, the peak values are 4.78 and 4.96 at photon energies of 4.01 eV and 3.82 eV for $RbHgCl_3$ and $CsHgCl_3$, respectively.

Moreover, within specific energy ranges, the real part becomes negative for both compounds, indicating metallic behavior in these regions.

The imaginary part of the dielectric function is closely related to the electronic band structure and accounts for the absorptive behavior of the material. As shown in Fig. 6g, the imaginary dielectric function of $AHgCl_3$ (A = Rb, Cs) exhibits multiple peaks corresponding to electronic transitions from the valence band to the conduction band. The critical (threshold) energies are determined to be 2.46 eV and 2.24 eV for $RbHgCl_3$ and $CsHgCl_3$, respectively.

The maximum peak values reach 5.12 at 13.07 eV for $RbHgCl_3$ and 7.27 at 15.27 eV for $CsHgCl_3$. These results indicate that absorption begins at approximately 2.46 eV and 2.24 eV for $RbHgCl_3$ and $CsHgCl_3$, respectively, with the strongest absorption occurring in the ultraviolet region.

3.5.2 The absorption coefficient $\alpha(\omega)$

The absorption coefficient, which quantifies the attenuation of light intensity per unit length within a material, exhibits behavior similar to that of the imaginary part of the dielectric function, $\varepsilon_2(\omega)$, as illustrated in Fig. 6f.

For $RbHgCl_3$ and $CsHgCl_3$, absorption begins at 2.46 eV and 2.24 eV, respectively, with maximum values of 289.93 cm^{-1} at 19.44 eV and 306.28 cm^{-1} at 15.74 eV.

These results suggest that both compounds are promising candidates for optoelectronic applications in the ultraviolet region.

3.5.3 Optical conductivity $\sigma(\omega)$

The electrical conductivity of the material is described in terms of its optical conductivity, which characterizes its response to electromagnetic radiation. Figure 6(e) shows the optical conductivity $\sigma(\omega)$, which begins at 2.46 eV for $RbHgCl_3$ and 2.24 eV for $CsHgCl_3$.This behavior reflects the strong correlation between $\sigma(\omega)$, the absorption coefficient $\alpha(\omega)$, and the imaginary part of the dielectric function $\varepsilon_2(\omega)$. The maximum optical conductivity reaches 9012.45 $\Omega^{-1}\cdot cm^{-1}$ at 13.07 eV for $RbHgCl_3$, while for $CsHgCl_3$ it reaches 9893.50 $\Omega^{-1}\cdot cm^{-1}$ at 15.74 eV.
These results indicate that the ternary $AHgCl_3$ (A = Rb, Cs) perovskite compounds are promising candidates for ultraviolet optoelectronic device applications.

3.5.4 The extinction coefficient $K(\omega)$ and refraction index $n(\omega)$

The propagation of electromagnetic radiation through a material can be described using the complex refractive index [44]:

$$N(\omega) = n(\omega) + iK(\omega) \tag{21}$$

where $K(\omega)$ denotes the extinction coefficient and $n(\omega)$ represents the refractive index. The extinction coefficient quantifies the attenuation of light intensity in a material owing to absorption and scattering effects.

As illustrated in Fig. 6h, the spectrum of $K(\omega)$ for both compounds closely follows that of the imaginary part of the dielectric function, $\varepsilon_2(\omega)$, owing to their strong correlation, as expressed by the relation $2n(\omega)K(\omega) = \varepsilon_2(\omega)$ [6] .The $K(\omega)$ spectra exhibit several pronounced peaks in the ultraviolet region, indicating enhanced optical absorption in this energy range.

The refractive index $n(\omega)$ describes the phase velocity of light within the material. Furthermore, as shown in Fig. 6d, the behavior of $n(\omega)$ is consistent with that of the real part of the dielectric function, $\varepsilon_1(\omega$, presented in Fig. 6a. The static values of $n(\omega)$ and $\varepsilon_1(\omega)$ listed in Table 5 further support this relationship [45–46].

$$n_0(\omega) = \sqrt{\varepsilon_1}(\omega) \tag{22}$$

3.5.5 The energy loss function $L(\omega)$

Figure 6(b) depicts the energy-loss function, which describes the energy dissipation of fast electrons in the material owing to electromagnetic radiation and provides insight into the plasmonic response of the system.

The energy-loss spectrum indicates that the dominant losses occur in the ultraviolet region, wherein $RbHgCl_3$ and $CsHgCl_3$ exhibit their maximum peak values. Negligible losses are observed in the visible region and at lower photon energies, indicating reduced plasmonic excitations in these energy ranges.

3.5.6 The optical reflectivity $R(\omega)$

Figure 6(c) illustrates the optical reflectivity, $R(\omega)$, indicating that most of the reflectivity peaks occur in the ultraviolet region at higher photon energies. This behavior corresponds to energy regions where the real part of the dielectric function, $\varepsilon_1(\omega)$, decreases and becomes negative.

The static reflectivity values R(0)for $RbHgCl_3$ and $CsHgCl_3$ are listed in Table 5. The maximum reflectivity values are 0.50 and 0.58 for $RbHgCl_3$ and $CsHgCl_3$, respectively. A low R(0) value for both compounds indicates weak reflectivity and strong absorption in the low-photon-energy region, which is characteristic of semiconductor materials.

This optical behavior suggests that both halide perovskite compounds exhibit similar properties and are promising candidates for optoelectronic applications, particularly in photovoltaic devices and ultraviolet photodetectors.

4. CONCLUSIONS

In this work, the structural, electronic, mechanical, and optical properties of cubic halide perovskites $AHgCl_3$ (A = Rb, Cs) were systematically investigated using density functional theory (DFT) within the FP-LAPW method as implemented in the WIEN2k package.

The structural stability of the cubic phase was confirmed through tolerance and octahedral factor analyses, while the negative formation energies further verified their thermodynamic stability. The mechanical properties indicate that both compounds are mechanically stable, ductile, anisotropic, and predominantly ionic in nature.

Electronic structure calculations using the TB-mBJ potential reveal that $RbHgCl_3$ and $CsHgCl_3$ are indirect band gap semiconductors, with band gap values of 1.25 eV and 1.16 eV, respectively.

The optical analysis demonstrates strong absorption in the ultraviolet region, low reflectivity at zero photon energy, and consistent behavior across key optical parameters, indicating favorable optoelectronic performance.

Overall, the obtained results suggest that both $AHgCl_3$ (A = Rb, Cs) halide perovskites are promising candidates for optoelectronic applications, particularly in photovoltaic devices and ultraviolet photodetectors.

Data Availability
The corresponding author, El-Djemai Belbacha, is available to provide the data supporting this study's findings upon reasonable request.
Conflicts of Interest
The authors of this work (Habiba Bouheraoua and El-Djemai Belbacha) declare that they have no conflicts of interest.

ORCID
Habiba Bouheraoua, https://orcid.org/0009-0008-1254-1943; **Belbacha El-Djemai,** https://orcid.org/0000-0002-2875-1266

REFERENCES

[1] P. Kumari, R. Sharma, U. Lilhore, R. Khenata, and V. Srivastva, "First-principles study on structural, electronic, elastic, mechanical, thermodynamic, and thermoelectric properties of $RbSnX_3$(X= F, Cl, and Br) perovskites," J. Energy Research, **46**, 23893 (2022). https://doi.org/10.1002/er.8687
[2] S. Gupta, S. Singh, R.R. Chaudhary, D. Shikha, and V. Singh, "Review: perovskite materials, properties, and their multifunctional applications," J. Mech. Eng. **7**, 44 (2022).
[3] S.C. Mouna, M. Radjai, A. Bouhemadou, D. Houatis, D. Allali, S.S. Essaoud, and S. Bin-omran, "Structural, elastic, and thermodynamic properties of $BaXCl_3$(X=Li, Na) perovskites under pressure effectab-initio exploration," Physica Scripta, **98**, 065949 (2023).https://doi.org/10.1088/1402-4896/acd3c4
[4] S. Seok, and T.F. Guo, "Halide perovskite materials and devices," MRS Bulletin, **45**, 427 (2020). https://doi.org/10.1557/mrs.2020.140
[5] F. Erdinc, E.K. Dogan, and H. Akkus, "Investigation of structural, electronic, optic, and elastic properties of perovskite $ReGeCl_3$ crystal: a first principles study," Gaz University Journal of science, **32**, 1008 (2019). https://doi.org/10.35378/gujs.448378
[6] S. Naseem, N.A. Noor, R. Ashraf, F. Alresheedi, M. Laraib, A. Rehman, and S. Raiz, "DFT based study of copper calcium halide perovskite nanomaterials for optoelectronic and energy applications," Results in Physics, **58**, 107485 (2024). https://doi.org/10.1016/j.rinp.2024.107485
[7] S. Bouchikhi, K. Benyahia, R. Mehyaoui, and A. Touia, "First principles calculations of the inorganic halide perovskite $RbSnBr_3$: optical and thermoelectric properties of its three phases," Computational Condensed Matter, **33**, e00761 (2022). https://doi.org/10.1016/j.cocom.2022.e00761
[8] M. Husain, N. Rahman, M. Albalawi, S. Ezzine, M. Amami, T. Zaman, A. Rehman, *et al*., "Examining computationally the structural, elastic, optical and electronic properties of $CaQCl_3$(Q=Li and K) Chloroperovskites using DFT framework," RSC advances, **12**, 32338 (2022). https://doi.org/10.1039/d2ra05602j
[9] A. Jehan, M. Husain, V. Tirth, A. Algahtani, M. Uzair, N. Rahman, and S.N. Khan, "Investigation of the structural, electronic, mechanical, and optical properties of $NaXCl_3$(X=Be, Mg) using density functional theory," RSC Advances, **13**, 28395 (2023).https://doi.org/10.1039/d3ra04922a
[10] A. Jehan, M. Husain, N. Sfina, S.N. Khan, N. Rahman, V. Tirth, R. Khan, *et al*., "First principles calculations to investigate structural, elastic, electronic, and optical properties of $XSrCl_3$(X=Li, Na)," Optik, **287**, 171088 (2023). https://doi.org/10.1016/j.ijleo.2023.171088
[11] A. Aqili, A.Y. Al-Reyahi, S.M. Al-Azar, S.S. Essaoud, M.E. Ketfi, M.E. Maghrabi, N. Al-Aqtash, and A. Mufleh, "Investigation the physical characteristics of inorganic cubic perovskite $CsZnX_3$(X=F, Cl, Br, and I): An extensive ab-initio study towards devices," Computational and Theoretical Chemistry, **1238**, 114721 (2024). https://doi.org/10.1016/j.comptc.2024.114721
[12] S. Ullah, M. Alshahrani, D. Alshehri, S. Tirth, V. Algahtani, A. Almalki, N. Rahman, *et al*., "First-principles insights into the structural, elastic, electronic, and optical properties of KHgX3 (X= F, Cl) novel halide perovskites," Indian Journal of Physics, 1-15 (2025). https://doi.org/10.1007/s12648-025-03878-5

[13] M. Arif, A. Reshak, S. Zaman, M. Hussain, N. Rahman, S. Ahmad, M. Saqib, *et al.*, "Density functional theory based study of the physical properties of cesium based cubic halide perovskites $CsHgX_3$ (X=F, Cl)," International Journal of Energy Research, **46**, 2467-2476 (2022). https://doi.org/10.1002/er.7321
[14] S. Kirklin, J.E. Saal, B. Meredig, A. Thompson, J.W. Doak, M. Aykol, S. Rühl, and C. Wolverton, "The open quantum materials database (OQMD): assessing the accuracy of DFT formation energies," Nbj Comput. Mater. **1**, 1 (2015). https://doi.org/10.1038/npjcompumats.2015.10
[15] J. Saal, S. Kirklin, M. Aykol, B. Meredig, and C. Wolverton, "Materials design and discovery with high-throughput density functional theory: the open quantum materials database (OQMD)," JOM, **65**, 1501-1509 (2013). https://doi.org/10.1007/s11837-013-0755-4
[16] P. Blaha, K. Schwarz, G.A.H. Medsen, D. Kvasnicka, and J. Luitz, *WIEN2K: An Augmented Plane Wave Local Orbitals Program for Calculating Crystal Properties*, (Techn University, Wien, 2001).
[17] P. Blaha, K. Schwarz, P. Sorantin, and S.B. Trickey, "Full- Potential Linearized Augmented Plane Wave Program for Crystalline Systems," Comput. Phys. Commun. **59**, 399 (1990). https://doi.org/10.1016/0010-4655(90)90187-6
[18] W. Kohn, and L.J. Sham, "Self-consist equations including exchange and correlation effects," Phys. Review, **140**, A1133 (1965). https://doi.org/10.1103/physrev.140.a1133
[19] P. Hohenberg, and W. Kohn, "Density functional theory (DFT)," Phys. Review B, **136**, 864 (1964). http://dx.doi.org/10.1103/PhysRev.136.B864
[20] J.P. Perdew, S. Burke, and M. Ernzerhof, "Generalized gradient approximation made simple," Phys. Review. Lett. **77**, 3865 (1996). https://doi.org/10.1103/physrevlett.77.3865
[21] Z. Wu, and R.E. Cohen, "More accurate generalized gradient approximation for solids," Phys. Review B, **73**, 235116 (2006). https://doi.org/10.1103/physrevb.73.235116
[22] J.P. Perdew, A. Ruzsinszky, G.I. Csonka, O.A. Vydrov, G.E. Scuseria, L.A. Constantin, X. Zhou, *et al.*, "Restoring the density-gradient expansion for exchange in solids and surfaces," Phys. Review Lett. **100**, 136406 (2008). https://doi.org/10.1103/physrevlett.102.039902
[23] F.D. Murnaghan, "The Compressibility of Media Under Extreme Pressure," Proc. Natl. Acad. Sci. USA, **30**, 244 (1944). https://doi.org/10.1073/pnas.30.9.244
[24] F. Tran, and P. Blaha, "Accurate band gaps of semiconductors and insulators with a semilocal exchange-correlation potential," Phys. Review. Lett. **102**, 226401 (2009). https://doi.org/10.1103/physrevlett.102.226401
[25] M. Jamal, S.J. Asadabadi, I. Ahmed, and H.R. Aliabad, "Elastic constants of cubic crystals," Comput. Mater. Sci. **95**, 592 (2014). https://doi.org/10.1016/j.commatsci.2014.08.027
[26] R. Ali, G.J. Hou, Z.G. Zhu, Q.B. Yan, Q.R. Zheng, and G. Su, "Stable mixed group II (Ca, Sr) and XIV(Ge, Sn) Lead-free perovskite solar cells," J. Mater. Chem. **6**, 9220 (2018). https://doi.org/10.1039/c8ta01490f
[27] Y. Zhou, and Y. Zhao, "Chemical stability and instability of inorganic halide perovskites," Energy & Environmental Science, **12**, 1495 (2019). https://doi.org/10.1039/c8ee03559h
[28] Y. Nassah, A. Benmakhlouf, L. Hadjeris, T. Helaimia, R. Khenata, A. Bouuhemadon, S. Bin-omran, *et al.*, "Electronic, band structure, mechanical and optical characteristics of new lead-free halide perovskites for solar cell applications based on DFT computation," Bull. Mater. Sci. **46**, 55 (2023). https://doi.org/10.1007/s12034-023-02890-x
[29] F. Mouhat, and F.X. Coudert, "Necessary and sufficient elastic stability conditions in various crystal systems," Phys. Review, **90**, 224104 (2014). https://doi.org/10.1103/physrevb.90.224104
[30] J. Wang, S. Yip, S.R. Phillpot, and D. Wolf, "Crystal instabilities et finit strain," Phys. Review Lett. **71**, 4182 (1993). https://doi.org/10.1103/physrevlett.71.4182
[31] A.A. Mousa, M.S. Abu-Jafar, D. Dahbiah, R.M. Shaltaf, and J.M. Khalifeh, "Investigation of the perovskite $KSrX_3$(X=Cl and F) Compounds, Examining the optical, Elastic, Electronic, and Structural Properties: FP-LAPW Study," J. Electron. Mater. **47**, 641 (2018). https://doi.org/10.1007/s11664-017-5817-x
[32] W. Voight, *Lehrbuch des Kristallphysik*, (Teubnes, Leipzig, 1928).
[33] A. Reuss, "Berechnung der Fließgrenze von Mischkristallen auf Grund der Plastizitätsbedingung für Einkristalle," Z. angew. Math. Mech. **9**, 49 (1929). https://doi.org/10.1002/zamm.19290090104
[34] H. Fu, D. Li, F. Peng, T. Cao, and X. Cheng. "Ab initio calculations of elastic constants and thermodynamicproperties of NiAl under high pressures," Comput. Mater. Sci. **44**, 774 (2008). https://doi.org/10.1016/j.commatsci.2008.05.026
[35] G. Murtaza, R. Khenata, S. Mohamed, S. Naeem, M.N. Khalid, and A. Manzar, "Structural, elastic, electronic, and optical properties of $CsMCl_3$(M=Zn, Cd)," Physica B: Condensed Matter. **420**, 15 (2013). https://doi.org/10.1016/j.physb.2013.03.011
[36] I.N. Frantsevich, F.F. Voronov, and S.A. Bokuta, *Elastic Constants and Elastic Moduli of Metals and Insulators*, *Handbook*, (Naukuva Dumka, Kiev, 1983). pp. 60. (in Ukrainian)
[37] S.F. Pugh, "XCII. Relations between the elastic moduli and plastic properties of polycrystalline pure metals," (London, Edinburgh Dublin Philos. Mag. J. Sci. **45**, 823 (1954). https://doi.org/10.1080/14786440808520496
[38] D.G. Pettifor, "Theoretical predictions of structure and related properties of intermetallics," Mater. Sci. Techno. **8**, 345 (1992). https://doi.org/10.1179/mst.1992.8.4.345
[39] R. Gaillac, P. Pullumbi, F.-X. Coudert, "ELATE: an open-source online application for analysis and visualization of elastic tensors," J. Phys. Condens Matter, **28**, 275201 (2016). https://doi.org/10.1088/0953-8984/28/27/275201
[40] S.C. Wu, G.H. Fecher, S.S. Naghavi, and C. Felser, "Elastic properties and stability of Hensler compounds: Cubic Co_2YZ compounds with L_21 structure," J. Appl. Phys. **125**, 082523 (2019).https://doi.org/10.1063/1.5054398
[41] E. Schreibes, O.L. Anderson, and N. Soga, *Elastic Constants and Their Measurements*, (McGraw-Hill, NewYork,1996).
[42] L.O. Anderson, "A simplified method for calculating the Debye temperature from elastic constants," J. Phys. Chem. Solids, **24**, 909 (1963). https://doi.org/10.1016/0022-3697(63)90067-2
[43] M.E. Fine, L.D. Brown, and H.L. Marcus, "Electronic constants versus melting temperature in metals," Scr. Metall. **18**, 951 (1984). https://doi.org/10.1016/0036-9748(84)90267-9
[44] D.R. Penn, "Wave- number-dependent dielectric function of semiconductors," Phys. Review, **128**, 2093 (1960). https://doi.org/10.1103/physrev.128.2093

[45] M. Houari, B. Bouadjemi, S. Haid, M. Matoughui, T. Lantn, Z. Aziz, S. Bentata, and B. Bouhafs, "Semiconductors behavior of halide perovskites $AGeX_3$(A=K, Rb and Cs; X=F, Cl, and Br): First-principles calculations," Indian J Phys. **94**, 455 (2020). https://doi.org/10.1007/s12648-019-01480-0
[46] R. Sharma, A. Dey, S.A. Dar, and V. Srivastava, "A DFT investigation of $CsMgX_3$(X=Cl, Br) halide perovskites: Electronic, thermoelectric and optical properties," Computational and Theoretical Chemistry, **1204**, 113415 (2021). https://doi.org/10.1016/j.comptc.2021.113415

СТРУКТУРНІ, ОПТОЕЛЕКТРОННІ ТА МЕХАНІЧНІ ВЛАСТИВОСТІ ПЕРОВСКИТІВ AHgCl3 (A=Rb, Cs): АНАЛІЗ З ПЕРШИХ ПРИНЦИПІВ GGA ТА TB-mBJ

Хабіба Бухерауа, Ель-Джемаї Белбача
Лабораторія фізико-хімічних досліджень матеріалів (LEPCM), кафедра фізики, факультет наук про речовину, Університет Батна 1, 05000 Батна, Алжир

Структурні, механічні та оптоелектронні властивості кубічних галогенідних перовскітів $AHgCl_3$ (A = Rb, Cs) досліджували за допомогою теорії функціоналу густини (DFT) у рамках методу повнопотенціальної лінеаризованої доповненої плоскої хвилі (FP-LAPW), реалізованого в коді WIEN2k. Структурну стабільність кубічної фази підтверджували за допомогою коефіцієнта толерантності Гольдшмідта та октаедричного коефіцієнта, тоді як негативні енергії утворення підтвердили їх термодинамічну стабільність. Розраховані параметри пружності, включаючи коефіцієнт Пуассона, коефіцієнт П'ю та тиск Коші, вказують на те, що обидві сполуки є механічно стабільними, пластичними та переважно демонструють іонну природу зв'язків. Оптоелектронні властивості досліджували за допомогою модифікованого потенціалу Бекке-Джонсона Трана-Блаха (TB-mBJ). Результати показують, що $RbHgCl_3$ та $CsHgCl_3$ є напівпровідниками з непрямою забороненою зоною та шириною забороненої зони 1,25 еВ і 1,16 еВ відповідно. Крім того, оптичні властивості були проаналізовані в діапазоні енергії фотонів 0–20 еВ. Обидві сполуки демонструють сильне поглинання в ультрафіолетовому діапазоні та низьку відбивну здатність за нульової енергії фотонів, що вказує на сприятливі характеристики для оптоелектронних застосувань. Загалом, ці результати свідчать про те, що галогенідні перовскіти $AHgCl_3$ (A = Rb, Cs) є перспективними кандидатами для застосування у фотоелектричних пристроях та ультрафіолетових фотодетекторах.

Ключові слова: *галогенідні перовскіти $KZnX_3$; FP-LAPW; ab-initio; Wien2k; оптоелектронні властивості; TB-mBJ*

EAST EUROPEAN JOURNAL OF PHYSICS. **2.** 292-301 (2026)
DOI:10.26565/2312-4334-2026-2-31 ISSN 2312-4334

A NUMERICAL SIMULATION STUDY INVESTIGATING THE FUNCTIONALITY OF A PEROVSKITE SOLAR CELL BASED ON $FASnI_3$ IN BOTH CONVENTIONAL AND INVERTED CONFIGURATIONS USING COMPATIBLE $Zn(O_{0.3}S_{0.7})$ AS THE ELECTRON TRANSPORT LAYER

M.V. Kavitha[1,2], K.S. Sudheer[1,3]***
[1]*Opto-electronic Device Simulation Research Lab, Department of Physics, Christ College (Autonomous), Irinjalakuda, University of Calicut, Kerala, India, PIN-680125*
[2]*Department of Physics, Sree Narayana College, Nattika, University of Calicut, Kerala, India, PIN-680566*
[3]*Department of Physics, St. Aloysius College, Thrissur, University of Calicut, Kerala, India, PIN-680611*
**Corresponding Author email: sudheersebastian@christcollegeijk.edu.in; **e-mail: kavitha.9667@christci.in*
Received February 1, 2026; revised April 22, 2026; accepted April 24, 2026

Formamidinium Tin Iodide is a promising candidate as an absorber layer in perovskite solar cells due to its tunable bandgap, high absorption coefficient, and good thermal stability. The selection of suitable charge transport layers with the proper band offset can effectively reduce recombination at interfaces and improve solar cell performance. The study focuses on enhancing the performance of a perovskite solar cell in which Formamidinium Tin Iodide ($FASnI_3$) is the absorber layer, $Zn(O_{0.3}S_{0.7})$ is the ETL and Spiro-OMeTAD is the HTL using numeric simulation. These charge-transport-layer materials are selected based on their adequate energy band alignment with the absorber. The structure Glass substrate/FTO/$Zn(O_{0.3}S_{0.7})$(ETL)/$FASnI_3$/Spiro-OMeTAD(HTL)/Au, which is an unexplored combination in n-i-p architecture, is simulated through SCAPS-1D and optimization of cell parameters- absorber thickness, absorber doping concentration, absorber defect density, ETL thickness, ETL defect density, HTL thickness, and HTL defect density- is carried out. The variation of cell performance parameters with interface defect density and temperature is also analyzed. With this optimization, the cell delivers an open circuit voltage (V_{oc}) = 1.0145V, short circuit current density (J_{sc}) = 37.82mA cm^{-2}, fill factor (FF) = 83.31% and Power Conversion Efficiency (PCE) =31.97%. The optimized parameters are used to simulate the p-i-n inverted architecture, and the cell output is as follows.V_{oc} = 1.0919V, J_{sc} = 37.293mA cm^{-2}, FF = 83.01% and Power Conversion Efficiency(PCE) =33.8%.
Keywords: *Perovskite solar cell; SCAPS; Formamidinium Tin Iodide; Spiro-OMeTAD, ZnOS*
PACS: 02.60.Cb, 61.72.-y, 42.79.Ek, 84.60.Jt

1. INTRODUCTION

In the realm of renewable energy, perovskite solar cells have demonstrated immense potential, with efficiency increasing exponentially over the past decade. Their unique opto-electronic properties, excellent absorptivity, simple and low-cost preparation and processing, etc., made them inevitable in the field of photovoltaics [1–3]. Organic and inorganic Lead halide perovskite are highly efficient candidates among perovskite solar cells. Even though Lead-based perovskite solar cells reported a breakthrough advancement in efficiency of 25.7%[4–6], their toxicity hinders large-scale commercialization.

Among the Tin-based perovskite solar cells, $FASnI_3$ possesses an appropriate bandgap (1.41 eV) and high mobility, which are desirable for solar cell applications. The oxidation of Sn^{2+} into $Sn^{4+}$is the major stability problem associated with $FASnI_3$.This increases the p-type conductivity of the material and results in low value of efficiency[7,8]. The incorporation of organic additives can enhance the efficiency and act as passivating agents of defects in $FASnI_3$[9,10]. The addition of SnF_2 is also an efficient method to tackle the problem of Sn^{2+} oxidation in $FASnI_3$[11].The $FASnI_3$ layer fabricated with vertical Sn^{2+} gradient using Lewis base-assisted recrystallization method showed an efficiency of 13.82%[12].

Electron Transport Layer (ETL) and the Hole Transport Layer (HTL) are essential for the extraction and collection of photogenerated electrons and holes produced inside the absorber layer in a solar cell structure. Effective charge transport is the primary factor determining the efficiency of a solar cell. The band offset at the interface of the absorber and charge transport layer plays a crucial role in the extraction of charge carriers[13]. The device modelling and optimization of perovskite solar cell with $FASnI_3$ as absorber material, Spiro-OMeTAD as Hole Transport Layer (HTL) and $Zn(O_{0.3}S_{0.7})$ as Electron Transport Layer forms the basis of the current work. $Zn(O_{0.3}S_{0.7})$ is a worthy candidate as an ETL in perovskite solar cells. It provides a suitable band alignment with FASnI3, thereby reducing charge recombination at the interface. Since $Zn(O_{0.3}S_{0.7})$ has significantly greater electron mobility than the commonly used ETL TiO_2, electrons can be extracted from the perovskite absorber layer more quickly and effectively. This improves current density (J_{sc}) and power conversion efficiency (PCE) by lowering charge accumulation and recombination losses[14]. By reducing interfacial trap states and suppressing charge recombination, a well-matched ETL like $Zn(O_{0.3}S_{0.7})$ can indirectly passivate the perovskite surface defects[15]. $Zn(O_{0.3}S_{0.7})$ as ETL can restrict the amount of oxygen and moisture that can enter from the top contact of the cell and lessen the possibility of Sn oxidation at the interface and improves the chemical stability of the underlying $FASnI_3$[15]. Ayush Tara et al. simulated the structure FTO/$Zn(O_{0.3}S_{0.7})$/$FASnI_3$/CuSCN/Au and attained

Cite as: M.V. Kavitha, K.S. Sudheer, East Eur. J. Phys. 2, 292 (2026), https://doi.org/10.26565/2312-4334-2026-2-31
© M.V. Kavitha, K.S. Sudheer, 2026; CC BY 4.0 license

an efficiency of 25.94%[16]. Au/NiO/$FASnI_3$/$ZnO_{0.25}S_{0.75}$/FTO is simulated by Srinivas Mattaparthi et al. and an efficiency of around 31.57% is obtained[17].

The PV community is searching for hole transport materials that are inexpensive, provide high charge carrier mobility, and stability. Both organic and inorganic materials can be used as HTLs. Even though inorganic materials are abundant, low-cost and stable, they are still behind organic HTLs from the efficiency point of view[18]. For the effective extraction of the carriers, the Highest Occupied Molecular Orbital (HOMO) of HTL should be placed above the HOMO level of absorber and Lowest Unoccupied Molecular Orbital (LUMO)level of ETL should be placed below the absorber LUMO level. The chosen HTL spiro-OMeTAD satisfies this condition. The additive engineering can greatly improve the stability of spiro-OMetAD, which is a major challenge faced by researchers. Also, photo-accelerated oxidation of Spiro-OMeTAD is an efficient and rapid process for the manufacturing and industrial applications of Spiro-OMeTAD[19]. The impact of absorber layer thickness, doping concentration, defect density, ETL thickness, doping concentration, HTL thickness, doping concentration, interface defect density and temperature, on the cell performance parameters is discussed in detail and performance optimization is done in this work.

2. METHODOLOGY AND DEVICE MODELLING

The device simulation and optimization of the structure Glass substrate /FTO/$Zn(O_{0.3}S_{0.7})$(ETL)/$FASnI_3$/Spiro-OMeTAD(HTL)/Au is done with Solar Cell Capacitance Simulator software. A lot of research is being done with this computational software and it is based on solving the Poisson's equation and continuity equations for the charge carriers

$$\frac{\partial}{\partial x}\varepsilon_0\varepsilon\frac{\partial\psi}{\partial x} = -q\left(p - n + N_D - N_A + \frac{\rho_{def}}{q}\right) \tag{1}$$

$$\frac{\partial n}{\partial t} = -\frac{\partial J_n}{\partial x} - U_n + G \tag{2}$$

$$\frac{\partial p}{\partial t} = -\frac{\partial J_p}{\partial x} - U_p + G \tag{3}$$

$$J_n = -\mu_n n q\frac{\partial E_{Fn}}{\partial x} \tag{4}$$

$$J_p = +u_p p q\frac{\partial E_{Fp}}{\partial x} \tag{5}$$

ε stands for the permittivity, ε_0 for the free space permittivity, ψ for the electrostatic potential, and q for the charge. n and p represent the concentration of electrons and holes, whereas N_D and N_A denote the ionized donor and ionized acceptor doping concentrations. ρ_{def} stands for defect distribution, whereas J_n and J_p stand for electron and hole current densities. U_n represents the electron recombination rate, U_p the hole recombination rate, G stands for the generation rate of carriers. Electron and hole mobilities are represented by μ_n and μ_p. E_{Fn} and E_{Fp} represent the electron and hole quasi-Fermi levels[20].

The standardization of the software is done by comparing the simulation results of the structure Glass substrate/FTO/TiO_2(ETL)/$FASnI_3$/Spiro-OMeTAD(HTL)/Au with the experimental data [8,20,21] in our previous work. Figure 1 shows the schematic representation of the structure being studied. Figure 2 shows the HOMO and LUMO levels of the layers. While the LUMO level of $Zn(O_{0.3}S_{0.7})$ is below $FASnI_3$, the HOMO level of Spiro-OMeTAD is in the same level as $FASnI_3$. The offset of valence band (VBO) at the Spiro-OMeTAD/$FASnI_3$ interface is zero and the offset of conduction band (CBO) at this interface is -1.47eV. The CBO at the $FASnI_3$/$Zn(O_{0.3}S_{0.7})$ interface is 0.08 eV and the VBO at this interface is -1.5 eV. For the efficient charge carrier extraction and collection, a small value of VBO and a large value of CBO are preferable at the Spiro-OMeTAD/$FASnI_3$ interface. Also small value of CBO and a large value of VBO are preferable at the $FASnI_3$/$Zn(O_{0.3}S_{0.7})$interface[20].

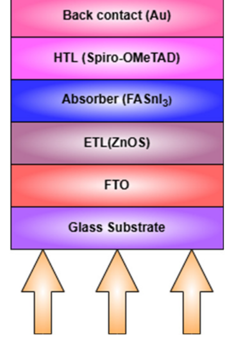

Figure 1. Device configuration

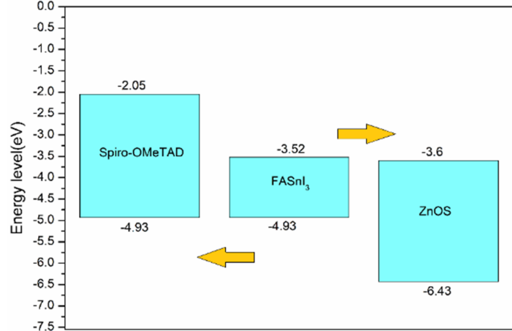

Figure 2. HOMO and LUMO levels of absorber, ETL and HTL

The required simulation parameters are obtained from the published literature. Table 1 lists the parameters needed for simulation. The electron and hole thermal velocities are fixed at 10^7cm/s. The defect density at the Spiro-

OMeTAD/$FASnI_3$ as well as at the $FASnI_3$/$Zn(O_{0.3}S_{0.7})$ interface is set at 10^{16} cm^{-3}. The simulation is performed at an operating temperature of 300K under an illumination of AM1.5G spectrum with an intensity of 1000 mW/cm^2.

Table 1. Simulation parameters of each layer

Parameters	FTO	$Zn(O_{0.3}S_{0.7})$	$FASnI_3$	Spiro-OMeTAD
Thickness (nm)	500[8]	30	350[21]	200[22]
Band gap ,E_g(eV)	3.5[8]	283[16]	1.41[21]	2.88[22]
e-affinity (eV)	4[8]	3.6[16]	3.52[23]	2.05[22]
Dielectric Permittivity, ε_r	9[8]	9[16]	8.2[23]	3[22]
Effective density of states at CB(cm^{-3})	2.2×10^{18}[8]	2.2×10^{18}[22]	1.0×10^{18}[23]	2.2×10^{18}[22]
Effective density of states at VB (cm^{-3})	1.8×10^{19}[8]	1.8×10^{19}[22]	1.0×10^{19}[23]	1.8×10^{19}[22]
e–mobility μ_n,($cm^2V^{-1}S^{-1}$)	20[8]	100	22[23]	2.0×10^{-4}[22]
h^+mobility μ_p, ($cm^2V^{-1}S^{-1}$)	10[8]	25	22[23]	2.0×10^{-4}[22]
Donor density N_D (cm^{-3})	2.0×10^{19}[8]	9.0×10^{16}	-	-
Acceptor density N_A (cm^{-3})	-	-	7.0×10^{16}[23]	2.0×10^{19}[22]
Density of defects, N_t (cm^{-3})	1.0×10^{15}[8]	1.0×10^{15}[13]	2.0×10^{15}[23]	1.0×10^{15}[22]

Figure 3 depicts the structure's energy band diagram. Since Spiro-OMeTAD and $Zn(O_{0.3}S_{0.7})$ provide adequate band offset at the interface of $FASnI_3$, there are no cliffs or peaks found at the interface. The performance parameters- Open circuit Voltage(V_{oc}), short circuit current density (J_{sc}), fill factor (FF) and power conversion efficiency (PCE) -of the device on initial simulation are summarized in Table 2. Figure 4 shows the variation of quantum efficiency with wavelength of radiation. The quantum efficiency curve spans the whole visible spectrum and shows maximum efficiency at 500nm. The cell performance parameters on the initial simulation are listed in Table 2. The variation of cell performance parameters with respect to thickness of absorber, defect density of absorber, doping concentration of absorber, defect density of ETL, thickness of ETL, defect density of HTL, thickness of HTL, defect density at the HTL/absorber interface, defect density at the absorber/ETL interface and temperature etc are analyzed in the next section.

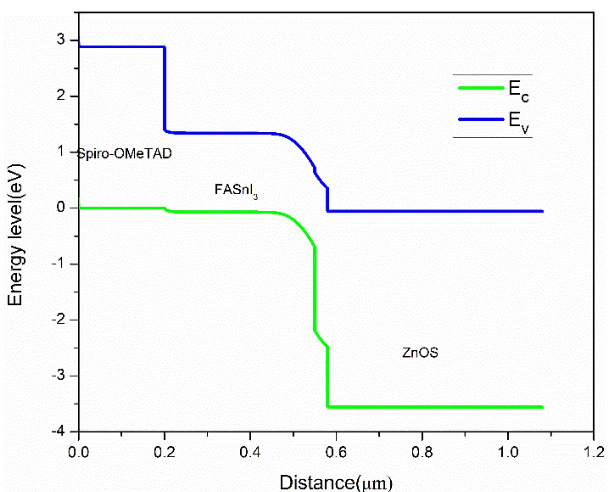

Figure 3. Energy band diagram

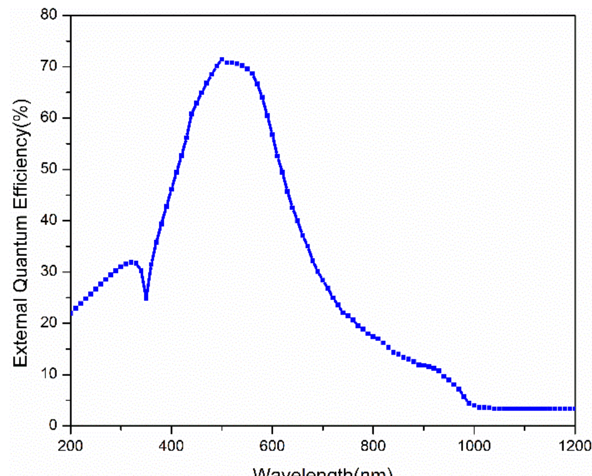

Figure 4. Quantum efficiency curve

Table 2. Initial performance parameters of the cell

V_{oc}(V)	J_{sc}(mA/cm^2)	FF(%)	PCE(%)
0.3464	14.797194	49.35	2.53

3. RESULTS AND DISCUSSION

3.1 Influence of Varying Absorber Layer Thickness

The variation of cell performance parameters with thickness is depicted in Figure 5. Power conversion efficiency increases with thickness from 0 to 1 µm, peaks at 3.26% at 0.75 µm, and then decreases. An increase in thickness leads to greater photon absorption, thereby improving efficiency. However, after saturation, efficiency diminishes because charge carriers may not reach the appropriate electrodes, as the thickness is considerably greater than the diffusion length [4]. J_{sc} also shows the same behaviour. V_{oc} decreases first, becomes constant over a range and slightly decreases after 0.75µm. This could be due to the increase in recombination rate. Fill factor decreases first due to the increase in series resistance [22], becomes constant and increases after 0.75µm. This is because of the decrease in V_{oc} and J_{sc}at this value of thickness.

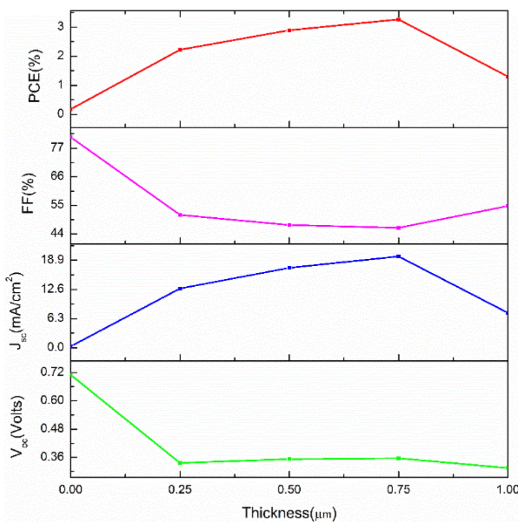

Figure 5. Effect of varying absorber thickness on performance parameters

3.2 INFLUENCE OF VARYING ABSORBER LAYER DEFECT DENSITY

The creation of processing sequences that can reduce harmful impurities, point and cluster defects, is the key task in the production of solar cells. A lot of methods are introduced for passivating unavoidable defects. The defects act as trap states, which can lead to non-radiative SRH recombination[24,25]. Here we study the variation of performance parameters with varying defect density from 10^{14} to 10^{18} cm^{-3}. The results are portrayed in Figure 6. As the defect density increases, the V_{oc}, J_{sc} and efficiency decrease. Fill factor slightly rises first, but this is compensated by the decrease in V_{oc} and J_{sc} and thereby reducing the value of PCE. The defect density and the diffusion length of the carriers are related by the equation

$$L = \sqrt{D\tau} \tag{6}$$

L stands for the diffusion length, D for the diffusion coefficient and τ for the carrier lifetime.

The equation for the diffusion coefficient is

$$D = \frac{\mu k_B T}{q} \tag{7}$$

μ stands for charge carrier mobility, K_B for the Boltzmann constant, T for the temperature and q for the charge

Relaxation time of carriers is given by the equation

$$\tau = \frac{1}{\sigma N_t V_{th}} \tag{8}$$

σ stands for the capture cross-section of carriers, N_t for the defect density and V_{th} for the thermal velocity of carriers. Figure 7 shows the variation of the generation rate of carriers with depth at different defect densities. It is seen that the generation rate is the same for all defect densities. Figure 8 shows the variation of the recombination rate of carriers with depth at different defect densities. As the defect density rises, so does the recombination rate. Since it offers the highest efficiency of 2.59%, 10^{14} cm^{-3} is selected as the optimum value of defect density. Also, it provides a diffusion length of 1.687μm and the chosen thickness lies within this limit of diffusion length.

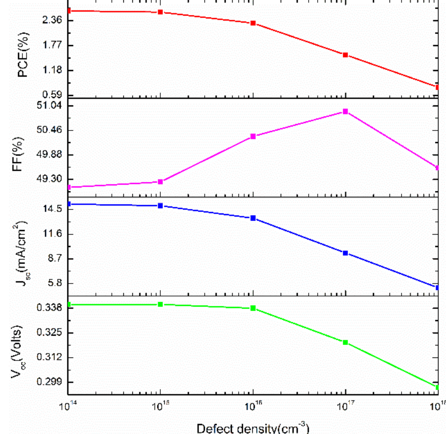

Figure 6. Effect of varying defect density on performance parameter

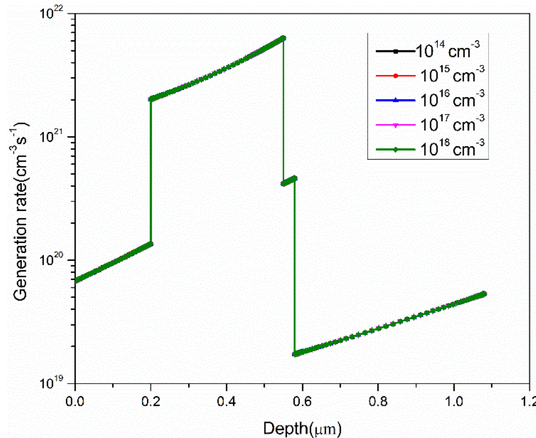

Figure 7. Variation of generation rate with depth at different defect densities

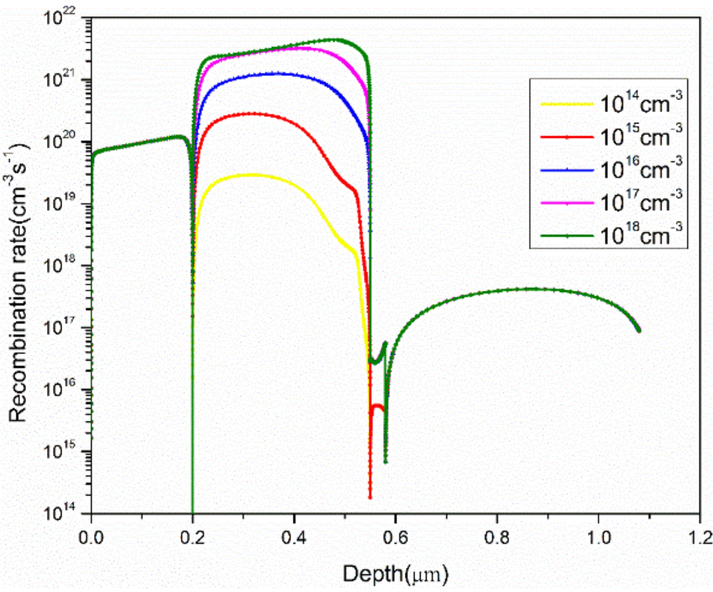

Figure 8. Variation of recombination rate with depth at different defect densities

3.3 INFLUENCE OF VARYING ABSORBER LAYER DOPING CONCENTRATION

The absorber material is a p-type semiconductor and the doping concentration represents the concentration of holes. Generally, increasing the doping level improves the conductivity of the material and hence, the performance parameters increase. Here, the doping concentration is varied from 10^{13} to 10^{17} cm^{-3} and Figure 9 shows the variation of cell performance parameters. The performance parameters remain almost constant with a rise in doping concentration up to 10^{15} cm^{-3} and then decrease. The initial doping concentration is 7×10^{16} cm^{-3}. The doping has a great impact on the cell performance. On reducing the doping concentration to 10^{13} cm^{-3}, the efficiency increases to 8.18%. The decrease in performance at high doping concentration can be attributed to the increase in Auger recombination [26–28].

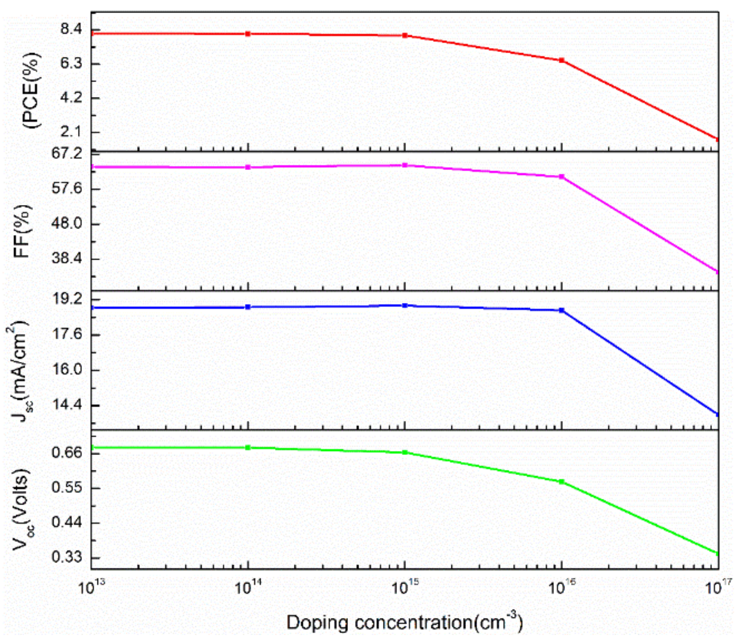

Figure 9. Effect of varying doping concentration on performance parameters

3.4 INFLUENCE OF VARYING ETL AND HTL THICKNESS

The thickness of ETL is varied from 20 to 50nm, whereas the thickness of HTL is varied from 100 to 500nm. The performance parameters obtained are depicted in Figure 10. The figure shows that the HTL thickness does not have much influence on the performance parameters. So, it is optimized at a minimum thickness of 100nm. As the ETL thickness increases, the performance parameters decrease. The efficiency is maximum (3.17%) at an ETL thickness of 20nm. The decrease in efficiency is attributed to the partial absorption of photons by ETL at high thickness[20,29].So the optimum ETL thickness is selected as 20nm.

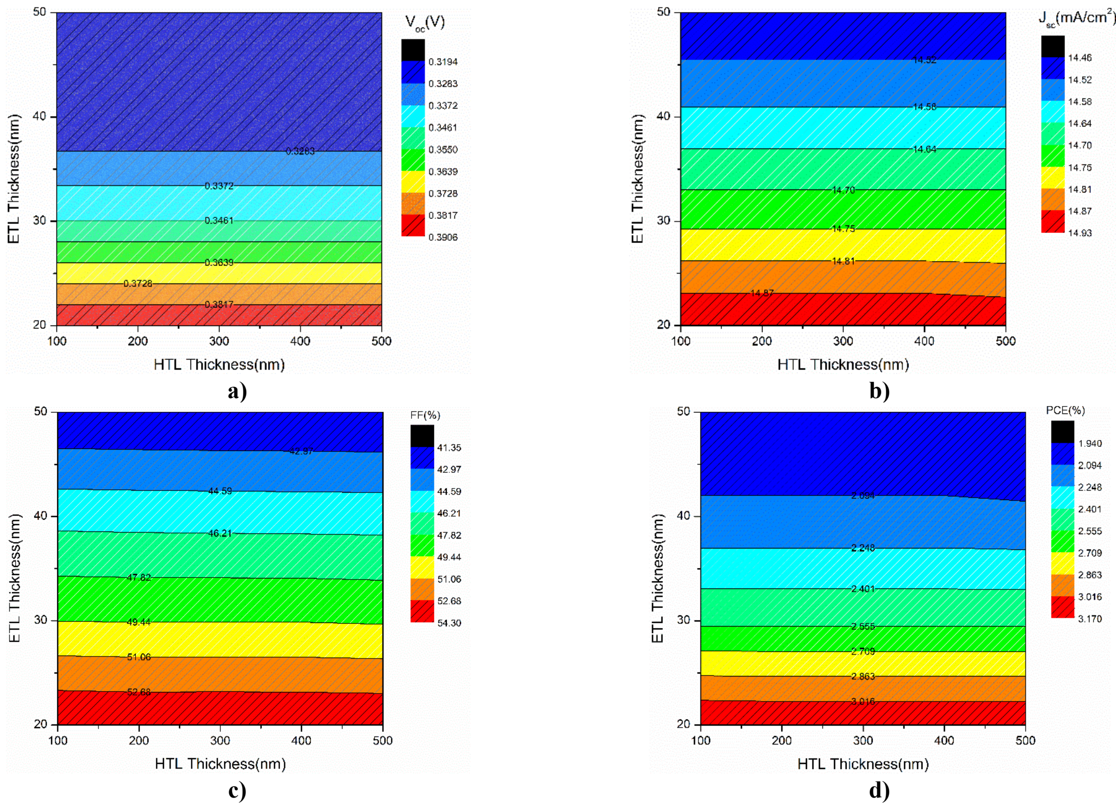

Figure 10. Effect of varying ETL and HTL thickness on a) V_{oc}; b) J_{sc}; c) FF; d) PCE

3.5 INFLUENCE OF VARYING ETL AND HTL DOPING CONCENTRATION

ETL and HTL are necessary for the extraction and transport of charge carriers to the respective electrodes. The increase in doping concentration of ETL and HTL improves the performance parameters. This is because of the increase in the electric field at the interface[30,31].The results of varying doping concentration on the performance parameters are portrayed in Figure 11.

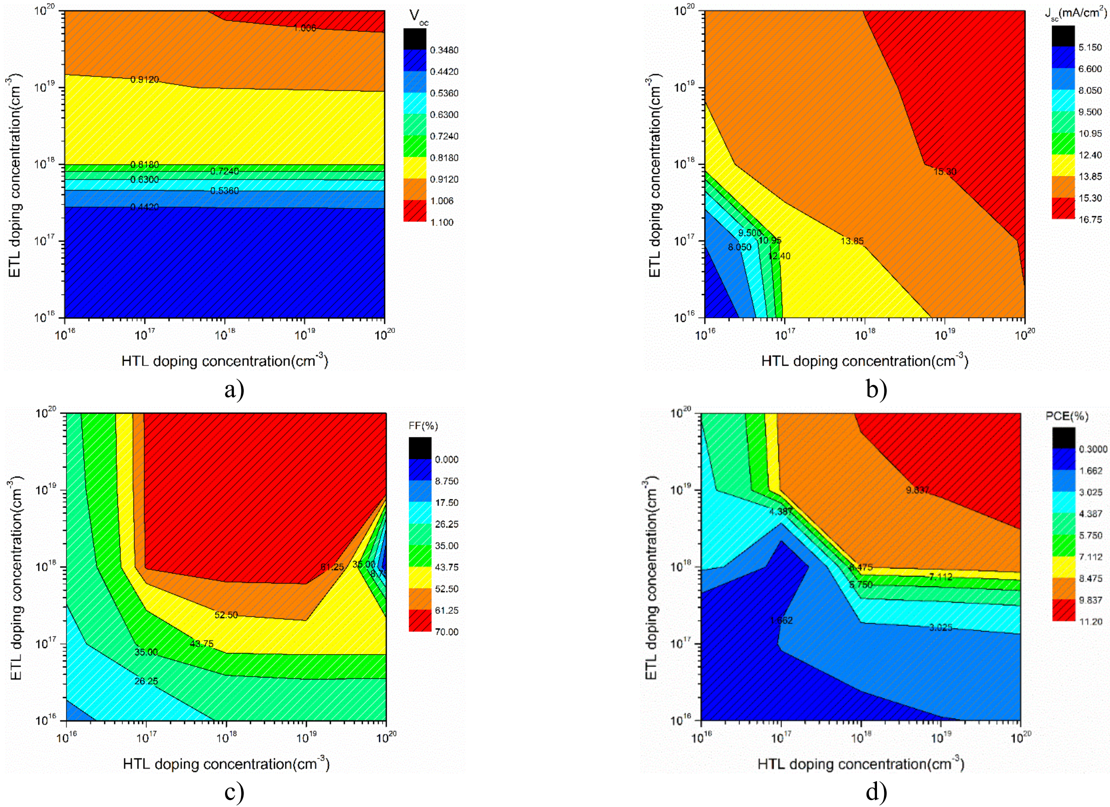

Figure 11. Effect of varying ETL and HTL doping concentration on a) V_{oc}; b) J_{sc}; c) FF; d) PCE

Both the ETL and HTL doping concentrations are varied from 10^{16} to 10^{20} cm^{-3}. All the performance parameters increase with the ETL and HTL doping concentration. The performance parameters yield the maximum value at a doping concentration of 10^{20} cm^{-3} for both the transport layers. The efficiency reaches a maximum value of 11.2% at this doping concentration.

3.6 INFLUENCE OF VARYING INTERFACE DEFECT DENSITY AT THE HTL/ABSORBER INTERFACE AND ETL/ABSORBER INTERFACE

The defect density at both the HTL/absorber and ETL/absorber interface is varied from 10^{10} to 10^{17} cm^{-3}. The variation of performance parameters is depicted in Figure 12 and Figure 13. The defects at the interfaces are common because it is the junction between two structurally different layers. As the interface defect density increases, the performance parameters decrease. The efficiency varies from 3.09 to 2.52% with the variation of HTL/absorber defect density. The efficiency varies from 10.57 to 2.52% with the variation of ETL/absorber defect density. The ETL/absorber interface defect density has a much higher impact on performance parameters. At the interfaces, minority charge carrier recombination occurs and the recombination rate increases with an increase in interface defect density. So, interface modification to control the defect density is very essential in the fabrication of highly efficient perovskite solar cells[32,33].The optimum value of defect density is chosen as 10^{10} cm^{-3} at both the interfaces.

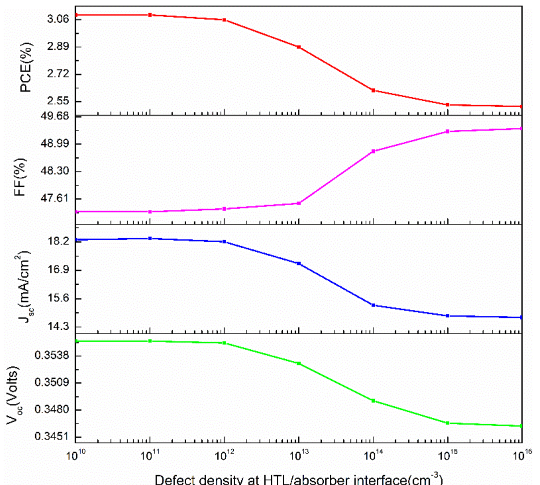

Figure 12. Effect of varying HTL/absorber interface defect density on the performance parameters

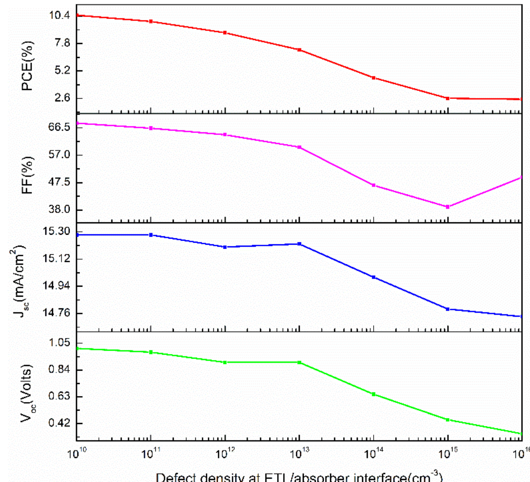

Figure 13. Effect of varying ETL/absorber interface defect density on the performance parameters

3.7 INFLUENCE OF VARYING TEMPERATURE

Figure 14 shows how the performance parameters vary with the operating temperature. The range of temperature variation is from 280K to 320K. As the temperature increases, the performance parameters decrease. V_{oc} varies from 0.39 to 0.30V. J_{sc} slightly decreases from 14.74 to 14.71mA/cm². The Fill factor decreases from 52.07 to 45.54% and the efficiency decreases from 3.06 to 2.01%. The increase in series resistance owing to the increased recombination rate accounts for the observed behaviour of performance parameters[20,34,35].

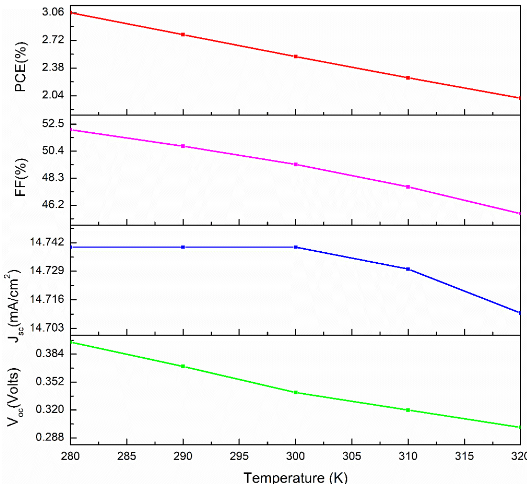

Figure 14. Effect of varying temperature on the performance parameters

The simulation is again performed with the optimized parameters such as absorber thickness of 750nm, absorber defect density of $10^{14}cm^{-3}$, absorber doping concentration of $10^{14}cm^{-3}$, ETL thickness of 20nm, ETL doping concentration of $10^{20}cm^{-3}$, HTL thickness of 100nm, HTL doping concentration of $10^{20}cm^{-3}$, interface defect density of $10^{10}cm^{-3}$ at both ETL/absorber interface and HTL/absorber interface and a temperature of 300K. The performance parameters obtained after optimization are listed in Table 3. All the cell performance parameters show a high improvement on optimization. The cumulative effect of all optimized parameters improves the efficiency to 31.97%.

Table 3. Cell performance parameters after optimization

V_{oc} (V)	J_{sc} (mA/cm^2)	FF(%)	PCE(%)
1.0145	37.824196	83.31	31.97

3.8 THE INVERTED (p-i-n) STRUCTURE

The optimized parameters are used to investigate the inverted (p-i-n) architecture of the solar cell, in which ETL replaces HTL and vice versa. The simulation of the architecture glass substrate/FTO/Spiro-OMeTAD(HTL)/$FASnI_3$/$Zn(O_{0.3}S_{0.7})$(ETL)/Au is executed, and the performance parameters obtained are listed in Table 4. The inverted structure offers better power conversion efficiency, and this could be due to the better material compatibility.

Table 4. Cell performance parameters of the inverted structure

V_{oc} (V)	J_{sc} (mA/cm^2)	FF(%)	PCE(%)
1.0919	37.29378	83.01	33.8

4. CONCLUSIONS

In this work, the eco-friendly solar cell n-i-p architecture, Glass substrate/FTO/$Zn(O_{0.3}S_{0.7})$(ETL)/$FASnI_3$/Spiro-OMeTAD(HTL)/Au, is simulated using SCAPS-1D software. The impact of cell parameters, including absorber thickness, absorber doping concentration, absorber defect density, ETL thickness, ETL defect density, HTL thickness, HTL defect density, interface defect density, and temperature, on cell performance is investigated. The optimized values of each of these cell parameters have been determined. The optimization resulted in an improved performance with V_{oc} of 1.0145 V, J_{sc} of 37.82mAcm^{-2}, fill factor of 83.31% and PCE of 31.97%. The inverted structure yielded a V_{oc} of 1.0919 V, J_{sc} of 37.293mA cm^{-2}, fill factor of 83.01%, and PCE of 33.8%. The greatest impact on efficiency is achieved by optimizing the absorber doping concentration. ETL doping concentration and interface defect density at the ETL/absorber interface also contribute much to the efficiency. So, careful optimization of cell parameters can significantly improve the performance. The proposed structure is a great option for experimental exploration and can be implemented with minimal performance compromise.

Data availability statement

The data that support the findings of this study are available from the corresponding author upon reasonable request.

Funding

This research did not receive any specific grant from funding agencies in the public, commercial, or not-for-profit sectors.

Acknowledgments

The authors would like to thank Marc Burgelman, Department of Electronics and Information Systems at the University of Gent, Belgium, for providing SCAPS software.

Conflict of interest

The authors declare no conflict of interest.

ORCID

Kavitha M.V., https://orcid.org/0009-0005-8611-6091; **Sudheer Sebastian K.,** https://orcid.org/0000-0002-9019-4405

REFERENCES

[1] S. Imani, S.M. Seyed-Talebi, J. Beheshtian, E.W.G. Diau, “Simulation and characterization of CH3NH3SnI3-based perovskite solar cells with different Cu-based hole transporting layers,” Applied Physics A, **129**, 143 (2023). https://doi.org/10.1007/s00339-023-06428-0
[2] T. Wu, Z. Qin, Y. Wang, Y. Wu, W. Chen, S. Zhang, M. Cai, *et al.*, “The Main Progress of Perovskite Solar Cells in 2020–2021,” Nanomicro Lett. **13**, (2021). https://doi.org/10.1007/s40820-021-00672-w
[3] J.Y. Kim, J.W. Lee, H.S. Jung, H. Shin, and N.G. Park, “High-Efficiency Perovskite Solar Cells,” Chem. Rev. **120**, 7867–7918 (2020). https://doi.org/10.1021/acs.chemrev.0c00107
[4] M. Ismail, M. Noman, S. Tariq Jan, and M. Imran, “Boosting efficiency of eco-friendly perovskite solar cell through optimization of novel charge transport layers,” R. Soc. Open. Sci. **10**, (2023). https://doi.org/10.1098/rsos.230331
[5] L. Lin, L. Jiang, P. Li, B. Fan, Y. Qiu, and F. Yan, “Simulation of optimum band structure of HTM-free perovskite solar cells based on ZnO electron transporting layer,” Mater. Sci. Semicond. Process. (2019). https://doi.org/10.1016/j.mssp.2018.10.003
[6] M.V. Kavitha, C.K. Anjali, and K.S. Sudheer, “Device simulation and optimization of HTL-free perovskite solar cell with CH3NH3SnBr3 as the absorber layer using solar cell capacitance simulator software,” Journal of Ovonic Research, **20**, 245–254 (2024). https://doi.org/10.15251/JOR.2024.202.245

[7] X. Meng, T. Wu, X. Liu, X. He, T. Noda, Y. Wang, H. Segawa, and L. Han, "Highly Reproducible and Efficient $FASnI_3$ Perovskite Solar Cells Fabricated with Volatilizable Reducing Solvent," J. Phys. Chem. Lett. **11**, 2965–2971 (2020). https://doi.org/10.1021/acs.jpclett.0c00923
[8] S. Abdelaziz, A. Zekry, A. Shaker, M. Abouelatta, Investigating the performance of formamidinium tin-based perovskite solar cell by SCAPS device simulation, Opt Mater (Amst) 101 (2020). https://doi.org/10.1016/j.optmat.2020.109738
[9] S. Galve-Lahoz, J. Sánchez-Diaz, C. Echeverría-Arrondo, J. Simancas, J. Rodriguez-Pereira, S.-H. Turren-Cruz, J.P. Martinez-Pastor, *et al.*, "Addressing ambient stability challenges in pure $FASnI_3$ perovskite solar cells through organic additive engineering," J. Mater. Chem. A Mater. **12**, 21933–21943 (2024). https://doi.org/10.1039/D4TA03291H
[10] Md.A. Karim, K. Matsuishi, Md.E. Kayesh, Y. He, and A. Islam, "Inhibition of Sn^{2+} Oxidation in $FASnI_3$ Perovskite Precursor Solution and Enhanced Stability of Perovskite Solar Cells by Reductive Additive," ACS Appl. Mater. Interfaces. **15**, 45823-45833 (2023). https://doi.org/10.1021/acsami.3c07903
[11] Z. Chen, and T.P. Dhakal, "Room temperature synthesis of lead-free FASnI3 perovskite nanocrystals with improved stability by SnF_2 additive," Appl. Phys. Rev. **10**, (2023). https://doi.org/10.1063/5.0125100
[12] T. Wu, X. Liu, X. Luo, H. Segawa, G. Tong, Y. Zhang, L.K. Ono, *et al.*, "Heterogeneous $FASnI_3$ Absorber with Enhanced Electric Field for High-Performance Lead-Free Perovskite Solar Cells," Nanomicro Lett. **14**, 99 (2022). https://doi.org/10.1007/s40820-022-00842-4
[13] S.Z. Haider, H. Anwar, and M. Wang, "A comprehensive device modelling of perovskite solar cell with inorganic copper iodide as hole transport material," Semicond. Sci. Technol. **33**, (2018). https://doi.org/10.1088/1361-6641/aaa596
[14] H. Sabbah, J. Arayro, and R. Mezher, "Numerical Simulation and Optimization of Highly Stable and Efficient Lead-Free Perovskite $FA_{1-x}Cs_xSnI_3$-Based Solar Cells Using SCAPS," Materials, **15**, 4761 (2022). https://doi.org/10.3390/ma15144761
[15] T.J. Macdonald, L. Lanzetta, X. Liang, D. Ding, and S.A. Haque, "Engineering Stable Lead-Free Tin Halide Perovskite Solar Cells: Lessons from Materials Chemistry," Advanced Materials, **35**, (2023). https://doi.org/10.1002/adma.202206684
[16] A. Tara, V. Bharti, S. Sharma, and R. Gupta, "Device simulation of $FASnI_3$ based perovskite solar cell with $Zn(O_{0.3}, S_{0.7})$ as electron transport layer using SCAPS-1D," Opt. Mater. (Amst). **119**, 111362 (2021). https://doi.org/10.1016/j.optmat.2021.111362
[17] S. Mattaparthi, D.K. Sinha, A. Bhura, and R. Khosla, "Design of an eco-friendly perovskite Au/NiO/FASnI3/ZnO0.25S0.75/FTO, device structure for solar cell applications using SCAPS-1D," Results in Optics, **12**, 100444 (2023). https://doi.org/10.1016/j.rio.2023.100444
[18] L. Nakka, Y. Cheng, A.G. Aberle, and F. Lin, "Analytical Review of Spiro-OMeTAD Hole Transport Materials: Paths Toward Stable and Efficient Perovskite Solar Cells," Advanced Energy and Sustainability Research, **3**, (2022). https://doi.org/10.1002/aesr.202200045
[19] S.N. Vijayaraghavan, K. Khawaja, J. Wall, W. Xiang, and F. Yan, "Photo-accelerated oxidation of spiro-OMeTAD for efficient carbon-based perovskite solar cells," Energy Advances, **3**, 1054–1061 (2024). https://doi.org/10.1039/D4YA00029C
[20] M.V. Kavitha, and K. Sudheer Sebastian, "Device modelling and performance enhancement of FASnI3-based perovskite solar cell with diverse, compatible charge transport layers," Results in Optics, **18**, 100783 (2025). https://doi.org/10.1016/j.rio.2025.100783
[21] T.M. Koh, T. Krishnamoorthy, N. Yantara, C. Shi, W.L. Leong, P.P. Boix, A.C. Grimsdale, *et al.*, "Formamidinium tin-based perovskite with low Eg for photovoltaic applications," J. Mater. Chem. A Mater. **3**, 14996–15000 (2015). https://doi.org/10.1039/c5ta00190k
[22] M. Kumar, A. Raj, A. Kumar, and A. Anshul, "An optimized lead-free formamidinium Sn-based perovskite solar cell design for high power conversion efficiency by SCAPS simulation," Opt. Mater. (Amst). **108**, (2020). https://doi.org/10.1016/j.optmat.2020.110213
[23] A. Tara, V. Bharti, S. Sharma, and R. Gupta, "Device simulation of FASnI3 based perovskite solar cell with $Zn(O_{0.3}, S_{0.7})$ as electron transport layer using SCAPS-1D," Opt. Mater. (Amst). **119**, (2021). https://doi.org/10.1016/j.optmat.2021.111362
[24] L.K. Ono, S. (Frank) Liu, and Y. Qi, "Reducing Detrimental Defects for High-Performance Metal Halide Perovskite Solar Cells," Angewandte Chemie International Edition, **59**, 6676–6698 (2020). https://doi.org/10.1002/anie.201905521
[25] J. Siekmann, S. Ravishankar, and T. Kirchartz, "Apparent Defect Densities in Halide Perovskite Thin Films and Single Crystals," ACS Energy Lett. **6**, 3244–3251 (2021). https://doi.org/10.1021/acsenergylett.1c01449
[26] M.K. Hossain, G.F.I. Toki, A. Kuddus, M.K.A. Mohammed, R. Pandey, J. Madan, S. Bhattarai, *et al.*, "Optimization of the architecture of lead-free CsSnCl3-perovskite solar cells for enhancement of efficiency: A combination of SCAPS-1D and wxAMPS study," Mater. Chem. Phys. **308**, 128281 (2023). https://doi.org/10.1016/j.matchemphys.2023.128281
[27] E. Danladi, A.C. Egbugha, R.C. Obasi, N.N. Tasie, C.U. Achem, I.S. Haruna, and L.O. Ezeh, "Defect and doping concentration study with series and shunt resistance influence on graphene modified perovskite solar cell: A numerical investigation in SCAPS-1D framework," Journal of the Indian Chemical Society, **100**, 101001 (2023). https://doi.org/10.1016/j.jics.2023.101001
[28] Kavitha M.V., S. Sebastian K., "A numerical study to enhance the performance of $FASnI_3$ -based HTL-free inverted perovskite solar cell with compatible electron transport layers," Phys. Scr. **100**, 075931 (2025). https://doi.org/10.1088/1402-4896/addf1a
[29] M.K. Hossain, M.H.K. Rubel, G.F.I. Toki, I. Alam, Md.F. Rahman, and H. Bencherif, "Effect of Various Electron and Hole Transport Layers on the Performance of $CsPbI_3$ -Based Perovskite Solar Cells: A Numerical Investigation in DFT, SCAPS-1D, and wxAMPS Frameworks," ACS Omega, **7**, 43210–43230 (2022). https://doi.org/10.1021/acsomega.2c05912
[30] A. Ahmed, K. Riaz, H. Mehmood, T. Tauqeer, and Z. Ahmad, "Performance optimization of $CH3NH3Pb(I_{1-x}Br_x)_3$ based perovskite solar cells by comparing different ETL materials through conduction band offset engineering," Opt. Mater. (Amst). **105**, 109897 (2020). https://doi.org/10.1016/j.optmat.2020.109897
[31] K. Hongsith, V. Yarangsi, S. Sucharitakul, S. Phadungdhitidhada, A. Ngamjarurojana, and S. Choopun, "A Multi-Electron Transporting Layer for Efficient Perovskite Solar Cells," Coatings, **11**, 1020 (2021). https://doi.org/10.3390/coatings11091020
[32] A.K. Singh, R. Walia, M.S. Chauhan, R.S. Singh, and V.K. Singh, "Performance analysis of n-TiO_2/p-Cu_2O, n-TiO_2/p-WS_2/p-Cu_2O, and n-TiO_2/p-WS_2 heterojunction solar cells through numerical modelling," Environmental Science and Pollution Research, **30**, 98718–98731 (2022). https://doi.org/10.1007/s11356-022-24236-6

[33] A.S. Yusuf, A.M. Ramalan, A.A. Abubakar, and I.K. Mohammed, "Effect of Electron Transport Layers, Interface Defect Density and Working Temperature on Perovskite Solar Cells Using SCAPS 1-D Software," East European Journal of Physics, (1), 332-341 (2024). https://doi.org/10.26565/2312-4334-2024-1-31
[34] K.S. Nithya, and K.S. Sudheer, "Numerical modelling of non-fullerene organic solar cell with high dielectric constant ITIC-OE acceptor," J. Phys. Commun. **4**, 025012 (2020). https://doi.org/10.1088/2399-6528/ab772a
[35] Y. Gan, X. Bi, Y. Liu, B. Qin, Q. Li, Q. Jiang, and P. Mo, "Numerical Investigation Energy Conversion Performance of Tin-Based Perovskite Solar Cells Using Cell Capacitance Simulator," Energies, (Basel), **13**, 5907 (2020). https://doi.org/10.3390/en13225907

ЧИСЛОВЕ МОДЕЛЮВАННЯ ДОСЛІДЖЕННЯ ФУНКЦІОНАЛЬНОСТІ ПЕРОВСКІТНОГО СОНЯЧНОГО ЕЛЕМЕНТА НА ОСНОВІ FASnI3 У ЗВИЧАЙНІЙ, ТА ІНВЕРТОВАНІЙ КОНФІГУРАЦІЯХ З ВИКОРИСТАННЯМ СУМІСНОГО $Zn(O_{0.3}S_{0.7})$ ЯК ШАРУ ЕЛЕКТРОННОГО ТРАНСПОРТУ

М.В. Кавіта[1,2], К.С. Судхір[1,3]
[1]Дослідницька лабораторія моделювання оптоелектронних пристроїв, кафедра фізики, Коледж Христа (автономний), Ірінджалакуда, Калікутський університет, Керала, Індія, PIN-680125
[2]Кафедра фізики, Коледж Шрі Нараяна, Наттіка, Калікутський університет, Керала, Індія, PIN-680566
[3]Кафедра фізики, Коледж Святого Алоїзія, Тріссур, Калікутський університет, Керала, Індія, PIN-680611

Йодид формамідинію олова є перспективним кандидатом на роль поглинального шару в перовскітних сонячних елементах завдяки регульованій ширині забороненої зони, високому коефіцієнту поглинання та добрій термічній стабільності. Вибір відповідних шарів переносу заряду з належним зміщенням зони може ефективно зменшити рекомбінацію на межі розділу та підвищити продуктивність сонячного елемента. Дослідження зосереджено на підвищенні продуктивності перовскітного сонячного елемента, в якому йодид формамідинію олова ($FASnI_3$) є поглинальним шаром, $Zn(O_{0.3}S_{0.7})$ - ETL, а Spiro-OMeTAD - HTL, за допомогою числового моделювання. Ці матеріали шару переносу заряду вибрані на основі їх адекватного вирівнювання енергетичної зони з поглиначем. Структура скляна підложка/FTO/$Zn(O_{0.3}S_{0.7})$(ETL)/$FASnI_3$/Spiro-OMeTAD(HTL)/Au, яка є недослідженою комбінацією в n-i-p архітектурі, була змодельована за допомогою SCAPS-1D, та проведена оптимізація параметрів комірки – товщини поглинача, концентрації легування поглинача, щільності дефектів поглинача, товщини ETL, щільності дефектів ETL, товщини HTL та щільності дефектів HTL. Також проаналізовано зміну параметрів роботи комірки залежно від щільності дефектів на межі розділу та температури. Завдяки цій оптимізації комірка забезпечує напругу холостого ходу (Voc) = 1,0145 В, щільність струму короткого замикання (Jsc) = 37,82 мА $см^{-2}$, коефіцієнт заповнення (FF) = 83,31% та коефіцієнт перетворення енергії (PCE) = 31,97%. Оптимізовані параметри використовуються для моделювання інвертованої p-i-n архітектури, а вихідна напруга *елемента така: Voc = 1,0919 В, Jsc = 37,293 мА* $см^{-2}$, *FF = 83,01% та ККД перетворення енергії (PCE) = 33,8%.*

Ключові слова: *перовскітний сонячний елемент; SCAPS; формамідиній-олов'яний йодид; спіро-OMeTAD, ZnOS*